



**HAL**  
open science

# Deposition and adsorption of organic matter in the sub-monolayer range studied by experimental and numerical techniques

Canan Turgut

► **To cite this version:**

Canan Turgut. Deposition and adsorption of organic matter in the sub-monolayer range studied by experimental and numerical techniques. Engineering Sciences [physics]. Université de Lorraine, 2015. English. NNT: 2015LORR0012 . tel-02076379

**HAL Id: tel-02076379**

**<https://hal.univ-lorraine.fr/tel-02076379v1>**

Submitted on 22 Mar 2019

**HAL** is a multi-disciplinary open access archive for the deposit and dissemination of scientific research documents, whether they are published or not. The documents may come from teaching and research institutions in France or abroad, or from public or private research centers.

L'archive ouverte pluridisciplinaire **HAL**, est destinée au dépôt et à la diffusion de documents scientifiques de niveau recherche, publiés ou non, émanant des établissements d'enseignement et de recherche français ou étrangers, des laboratoires publics ou privés.



## AVERTISSEMENT

Ce document est le fruit d'un long travail approuvé par le jury de soutenance et mis à disposition de l'ensemble de la communauté universitaire élargie.

Il est soumis à la propriété intellectuelle de l'auteur. Ceci implique une obligation de citation et de référencement lors de l'utilisation de ce document.

D'autre part, toute contrefaçon, plagiat, reproduction illicite encourt une poursuite pénale.

Contact : [ddoc-theses-contact@univ-lorraine.fr](mailto:ddoc-theses-contact@univ-lorraine.fr)

## LIENS

Code de la Propriété Intellectuelle. articles L 122. 4

Code de la Propriété Intellectuelle. articles L 335.2- L 335.10

[http://www.cfcopies.com/V2/leg/leg\\_droi.php](http://www.cfcopies.com/V2/leg/leg_droi.php)

<http://www.culture.gouv.fr/culture/infos-pratiques/droits/protection.htm>

## UNIVERSITE DE LORRAINE

Ecole Doctorale : Énergie Mécanique Matériaux

Institut Jean Lamour

Département Chimie et Physique des Solides et des Surfaces

**THESIS**

presented on 05.03.2015

to obtain the degree of Doctor of the University of Lorraine  
in material science and engineering

by

**Canan TURGUT**Deposition and adsorption of organic matter in the sub-monolayer  
range studied by experimental and numerical techniques**Jury**

President:	<b>Gérard HENRION</b>	Senior researcher (DR) CNRS, IJL, University of Lorraine
Reviewers:	<b>Arnaud DELCORTE</b> <b>Serge DELLA NEGRA</b>	Professor, University Catholique de Louvain, Belgium Senior researcher (DR) CNRS, IPN Orsay, University of Paris-Sud, France
Examiners:	<b>Kai NORDLUND</b>	Professor, University of Helsinki, Finland
Supervisors :	<b>Mohammed BELMAHI</b> <b>Patrick PHILIPP</b>	Professor, University of Lorraine Project leader, Luxembourg Institute of Science and Technology (LIST), Luxembourg

Préambule .....	2
1. Introduction - Contexte.....	2
2. Adsorption d'hexane, et de fragments de chaînes d'hydrocarbures.....	4
3. Collage de polystyrène sur Argent .....	5
4. Adsorption de Polyméthyl méthacrylate (PMMA) sur Ag, Pt, Si et Al <sub>2</sub> O <sub>3</sub> .....	11

# Préambule

Le manuscrit original de cette thèse est écrit en Anglais. Nous présentons ici un résumé étendu, de la thèse. Nous tenons à remercier le président de l'Université de Lorraine ainsi que le conseil scientifique, d'avoir autorisé la publication de ce document en Anglais. Ce travail a été réalisé au Centre de Recherches Public Gabriel - Lippmann du Luxembourg (CRPGL), devenu Luxembourg Institute of Science and Technology (LIST), ainsi que l'Institut Jean Lamour, UMR 7198 Université de Lorraine et Centre National de la Recherche Scientifique. Le travail ainsi que la thèse ont été financé par le Fond National du Luxembourg, dans le cadre d'un contrat regroupant les laboratoires cités et l'Université de Helsinki (Professeur K. Nordlund) ainsi que l'Université Aalto (Professeur J. Lahtinen) de Finlande.

## 1. Introduction - Contexte

La fonctionnalisation des surfaces par plasma est une technique intéressante pour préparer et contrôler l'adhésion sur des surfaces. La maîtrise de cette interface est fondamentale dans de nombreuses applications. Cependant, lorsqu'il s'agit du contrôle à l'échelle de la monocouche, ou de la sub monocouche (sub-ML), il faut développer des techniques adaptées pour faire de tels dépôts, et ensuite les caractériser. La technique de Storing Matter (StoMat)



développée au CRPGL s'avère très utile pour cette approche. Elle a été utilisée dans ce projet pour réaliser des dépôts sub-ML organiques sur des substrats isolants, métalliques et semi-conducteurs. La caractérisation des surfaces a été réalisée par spectrométrie de masse des ions secondaires à temps de vol (TOF-SIMS), et spectroscopie de photoélectrons X (XPS). Les techniques de modélisation telles les simulations de dynamique moléculaire (MD) et la théorie de la densité fonctionnelle (DFT) ont été utilisées et s'avèrent très puissantes également pour accéder aux énergies de collage, et l'obtention des sites d'adsorption privilégiés sur de telles surfaces.

Le manuscrit de cette thèse est organisé en 6 chapitres. Le chapitre 1 est dédié à l'état de l'art et comprend une partie concernant la pulvérisation des éléments par faisceaux d'ions, la spectrométrie TOF-SIMS pour la caractérisation des polymères, tels que le polystyrène (PS) et le poly(méthacrylate de méthyle) (PMMA), la modélisation par MD et DFT de fragments d'hydrocarbures sur des surfaces métalliques, et la technique de StoMat.

Le chapitre 2 est intitulé matériaux et méthodes. Les techniques de déposition et de caractérisation des couches sub-ML y sont décrites, ainsi que les techniques de simulation en MD et DFT utilisées dans cette étude.

Le chapitre 3 est dédié à l'adsorption par MD de fragments d'alcane et de chaînes moléculaires sur des surfaces de Silicium et d'alumine alpha.

Le chapitre 4 traite des études des dépôts de PS sub-ML obtenus par pulvérisation cathodique grâce à la technique StoMat et leur caractérisation par TOF-SIMS, puis de l'effet de l'énergie des ions, et leur flux.

Le chapitre 5 traite des études des dépôts de PMMA sub-ML obtenus par pulvérisation cathodique grâce à la technique StoMat et leur caractérisation par TOF-SIMS, puis de l'effet de l'énergie des ions, et leur flux.

Le chapitre 6 traite des résultats obtenus par DFT de l'adhésion de fragments de PS, et PMMA sur différents types de surfaces telles l'Ag (100) et Ag(111), Pt(111), Si (111),  $\alpha$ -Al<sub>2</sub>O<sub>3</sub> (0001).

Enfin, une conclusion générale, et les perspectives à ce travail sont présentées.

## 2. Adsorption d'hexane, et de fragments de chaines d'hydrocarbures

Dans cette partie, des études par simulation MD et également par DFT ont été réalisées. Les substrats utilisés sont Si (111) et  $\alpha$ -Al<sub>2</sub>O<sub>3</sub> (0001). La limitation à la simulation est liée au fait qu'expérimentalement, il n'a pas été possible d'observer l'adhésion de fragments ou de molécules entières d'hexane.

A température ambiante, il n'a pas été observé de collage d'hexane sur silicium par MD. Cependant pour les radicaux présentés (Figure 1), la probabilité de collage augmente très rapidement lorsque l'angle d'incidence diminue (cf. Figure 1).

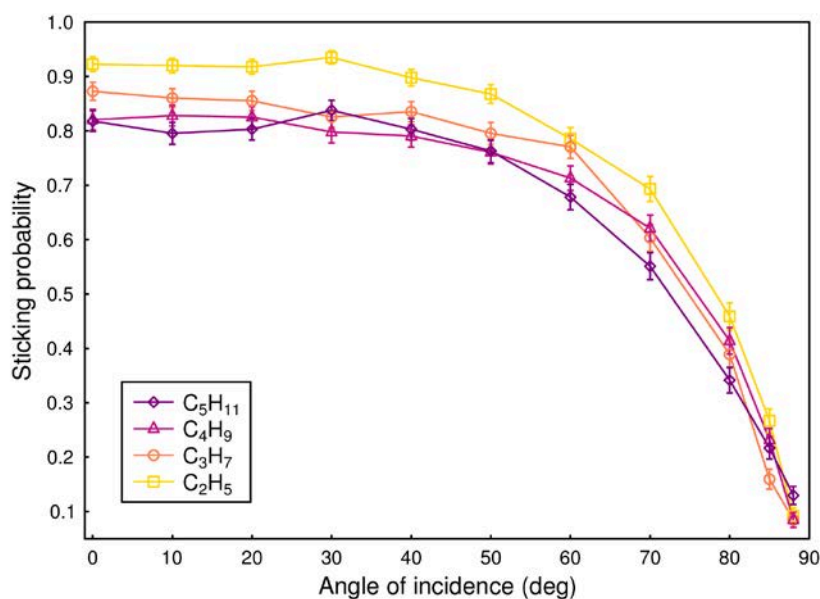


Figure 1: Probabilité de collage pour des fragments d'énergie de 2,5 eV déposés à 300K sur une surface de Si(100).

La probabilité de collage reste constante jusque des angles d'incidence de 40°, pour décroître rapidement ensuite. Pour C<sub>5</sub>H<sub>11</sub> à une énergie de 2,5 eV et à la température de 300 K, environ

80% des radicaux ou des fragments collent à incidence normale. Pour des fragments plus petits, cette probabilité peut être légèrement plus grande (par exemple elle est de 90% pour  $C_2H_5$ ). Cette tendance a été confirmée par des calculs de DFT ab-initio.

La tendance globale peut être expliquée par les liaisons pendantes dans les radicaux qui peuvent réagir avec un atome de silicium ou des dimers reconstruits. En même temps, les énergies de liaison entre les radicaux carbonés et les atomes du substrat augmentent pour des petites chaînes. Par exemple pour  $CH_3$ , on a obtenu une énergie d'adsorption de 1,53eV sur Ag et pour  $C_5H_{11}$  une énergie de 1,03 eV. Cette valeur change avec le nombre d'atomes de carbone. Dans le cas du substrat de  $Al_2O_3$ , pour les mêmes radicaux, les énergies deviennent 0,36 eV et 0,15 eV. Pour les terminaisons oxygène sur  $Al_2O_3$  les liaisons pendantes ne sont pas disponibles, ce qui explique les faibles valeurs des énergies.

Pour les molécules intactes, l'interaction est contrôlée par les interactions de Van der Waals. Pour  $C_6H_{14}$ , elles sont très faibles à la température ambiante. Les calculs par DFT donnent des énergies comprises entre 0,2 et 0,3 eV en fonction de l'orientation des molécules. Pour les surfaces métalliques comme Ag, ces énergies sont encore plus faibles (de l'ordre de 0,01 à 0,02 eV). La situation change pour des molécules d'alcane plus grandes.  $C_8H_{18}$  et  $C_{12}H_{26}$  collent sur l'alumine pour des énergies de 0,1 eV et  $C_{16}H_{34}$  colle pour des énergies de dépôt de 1 eV. Ce n'est pas surprenant qu'en augmentant la longueur de la chaîne carbonée, les interactions de Van der Waals augmentent, et également la probabilité de collage.

### **3. Collage de polystyrène sur Argent**

Ce polymère de composition chimique comparable à celle de l'hexane a permis de développer une étude expérimentale de collage de fragments carbonés sur argent. Le PS a été choisi car il produit sous bombardement ionique des fragments linéaires et cycliques.

Les fragments de PS sont pulvérisés sur un collecteur en Ag pour différents taux de couverture, à savoir (i) la dose locale d'ions primaires est maintenue constante et le taux de couverture est modifié en déplaçant le substrat de PS sous le faisceau d'ions. Après localisation du dépôt en faisant un balayage sur le collecteur, nous avons fait une série de

spectres TOF-SIMS le long du diamètre du collecteur en passant par le centre du dépôt, en utilisant comme ions primaires  $\text{Bi}_3^+$ . Les spectres TOF-SIMS du dépôt de PS sur Ag par Storing Matter montrent des fragments spécifiques qui sont également observés sur le spectre de référence du PS. Dans la figure 2, les rapports des intensités des grands fragments divisés par ceux des plus petits sont présentés pour trois taux de couverture. Il s'agit de  $\text{C}_7\text{H}_7^+ / \text{CH}_3^+$ ,  $\text{C}_7\text{H}_7^+ / \text{C}_3\text{H}_3^+$ , et  $\text{C}_7\text{H}_7^+ / \text{C}_3\text{H}_5^+$ , qui sont présentés. Les données correspondants à  $\text{C}_8\text{H}_9^+ / \text{CH}_3^+$ ,  $\text{C}_8\text{H}_9^+ / \text{C}_3\text{H}_3^+$ ,  $\text{C}_8\text{H}_9^+ / \text{C}_3\text{H}_5^+$ ,  $\text{C}_9\text{H}_7^+ / \text{CH}_3^+$ ,  $\text{C}_9\text{H}_7^+ / \text{C}_3\text{H}_3^+$ , et  $\text{C}_9\text{H}_7^+ / \text{C}_3\text{H}_5^+$  ne sont pas présentés ici.

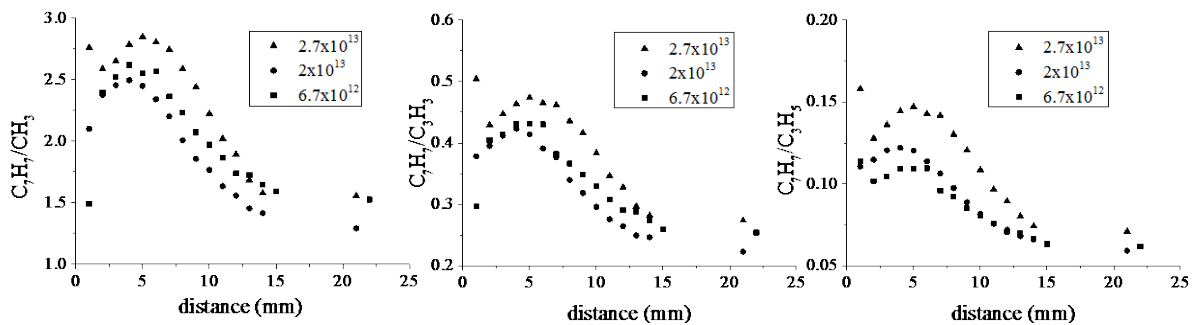


Figure 2 : Rapport des intensités TOF-SIMS des fragments en fonction de la distance pour différent taux de couverture d'ions  $\text{Ar}^+$  (a)  $\text{C}_7\text{H}_7^+ / \text{CH}_3^+$  (b)  $\text{C}_7\text{H}_7^+ / \text{C}_3\text{H}_3^+$  (c)  $\text{C}_7\text{H}_7^+ / \text{C}_3\text{H}_5^+$

La figure 2 montre l'évolution du rapport des intensités de  $\text{C}_7\text{H}_7^+$  sur  $\text{CH}_3^+$ ,  $\text{C}_3\text{H}_3^+$  et  $\text{C}_3\text{H}_5^+$  pour différents taux d'ions primaires  $\text{Ar}^+$  arrivant sur la surface de PS durant le procédé de pulvérisation/dépôt. Nous observons pour toutes les courbes une distribution similaire, avec un maximum au centre du dépôt pour tous les fragments présentés. La comparaison des différentes courbes montre que le rapport le plus élevé est obtenu pour  $\text{C}_7\text{H}_7^+ / \text{C}_3\text{H}_3^+$ .

Une diminution est obtenue pour  $\text{C}_7\text{H}_7^+ / \text{C}_3\text{H}_3^+$  et  $\text{C}_7\text{H}_7^+ / \text{C}_3\text{H}_5^+$ . Comme la distribution de  $\text{C}_7\text{H}_7^+$  est fixée pour un collecteur donné, on peut en conclure que  $\text{C}_3\text{H}_5^+$  et  $\text{C}_3\text{H}_3^+$  sont plus présents sur le collecteur que  $\text{CH}_3^+$  car ils montrent un rapport d'intensités plus faible. Comme tous les autres paramètres demeurent constants, y compris la dose d'ions primaires reçus pour le dépôt /pulvérisation, l'énergie d'impact et les conditions des analyses TOF-SIMS, ces paramètres ne devraient pas induire une modification significative de la fragmentation durant le procédé de dépôt /pulvérisation et pendant l'analyse par TOF-SIMS. Si nous supposons que les mécanismes d'ionisation sont similaires pour les différents fragments, à différents taux de couverture, l'augmentation des rapports en augmentant le taux

de couverture pourrait résulter d'une meilleure probabilité de collage pour les différents fragments sur le collecteur ou bien pourrait résulter de la recombinaison de fragments au moment des analyses TOF-SIMS. Dans les deux cas, l'augmentation du taux de couverture pourrait augmenter la probabilité d'interaction de deux fragments durant le procédé de dépôt ou d'analyse.

Le même type de comportement est observé pour le fragment  $C_9H_7^+$ . Cependant la situation est différente pour le fragment  $C_8H_9^+$  : le maximum du rapport  $C_8H_9^+/CH_3^+$  et  $C_8H_9^+/C_3H_3^+$  décroît avec l'augmentation du taux de couverture de  $Ar^+$  tandis que ce rapport reste constant pour  $C_8H_9^+/C_3H_5^+$ . Une possible contamination par un hydrocarbure ne peut pas être écartée. Il en résulte une augmentation de fragment petits mais elle ne peut être la raison de la décroissance de grands fragments dans le cas de  $C_8H_9^+$  puisque cela devrait être aussi le cas pour  $C_7H_7^+$  et  $C_9H_7^+$  pour lesquels nous observons un comportement opposé.

En effet pour le même taux de couverture, les données proviennent du même collecteur. Le comportement différent pour  $C_8H_9^+$  peut être expliqué par les différents types de fragments tels que classifiés par Vanden Eynde *et al* et les différents processus permettant de former les fragments via la rupture des liaisons C-C, la capture d'un atome d'hydrogène, ou encore la scission de multiples liaisons. Dans le bulk du PS,  $C_7H_7^+$  et  $C_9H_7^+$  sont formés par capture d'hydrogène, réactions d'échange de H et scission de plusieurs liaisons multiples. Pour  $C_8H_9^+$  le mécanisme de capture de H est moins important.

Sur la surface du collecteur, les réactions de fragmentation et de recombinaison sont différentes de ce qui se passe dans le bulk de PS et pourraient changer avec le taux de couverture. Pour les fragments  $C_8H_9^+$  adsorbés sur la surface du collecteur, les atomes de H des groupements alkyl pourraient être perdus plus facilement que pour  $C_7H_7^+$ . Ces atomes d'hydrogène pourraient servir comme une source d'hydrogène pour former d'autres fragments. Ce mécanisme pourrait devenir plus probable en augmentant le taux de couverture et pourrait expliquer la différence entre les fragments  $C_8H_9^+$  et  $C_7H_7^+$  et  $C_9H_7^+$ . Dans le cas de  $C_7H_7^+$  et  $C_9H_7^+$  la perte de H serait moins probable car le groupement alkyl de  $C_7H_7^+$  est plus court et la structure de  $C_9H_7^+$  est polycyclique.

Des études réalisées en changeant la dose d'ions primaires reçue a permis la comparaison entre les expériences réalisées par ToF-SIMS (LIST) et XPS (Aalto University). Le comportement observé précédemment n'est pas obtenu dans ce cas. Normalement en SIMS,

la fragmentation de chaînes de polymère augmente avec la dose d'ions primaires. L'effet observé ici en ToF-SIMS est l'inverse. Le rapport grands/petits fragments augmente avec la dose reçue (Figure 3a). Ici, il faut rappeler que les spectres ToF-SIMS donnent uniquement l'information sur la taille des fragments mais pas sur leur structure. Cette information est obtenue par XPS. L'analyse XPS du substrat de PS montre une diminution de la composante cyclique dans le pic du carbone 1s. L'épaule correspondant à la résonance du noyau phényle (shake-up) décroît également. Ce comportement est attendu et peut être corrélé avec les résultats XPS du dépôt de PS pour lesquels les contributions aromatiques du carbone décroissent alors que les composantes aliphatiques augmentent avec la dose d'ions primaires (Figure 3b). En plus on notera la nécessité d'utiliser des contributions AgC et COCOO et C=OR pour fitter correctement les spectres C 1s. Les fragments réagissent avec l'Ag du substrat et également avec l'oxygène qui a été adsorbé sur la surface de Ag. La comparaison entre les résultats ToF-SIMS et XPS, montre clairement la disparition des fragments contenant beaucoup de carbone en augmentant la dose reçue, et que ceux là ont plutôt une structure linéaire.

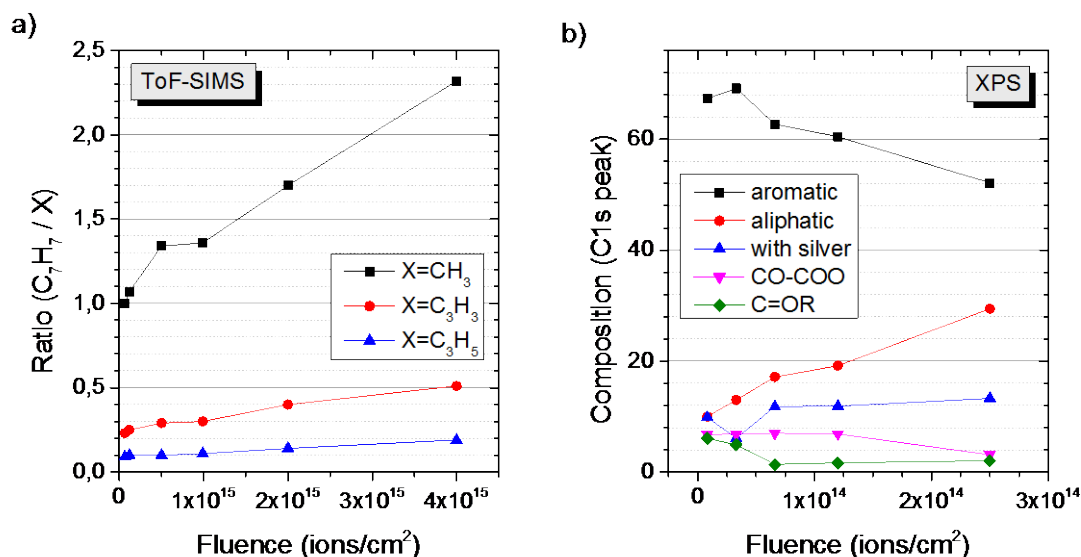


Figure 3: Résultats de dépôts subML de PS sur Ag: a) résultats de ToF-SIMS pour le rapport C<sub>7</sub>H<sub>7</sub><sup>+</sup>/X en fonction de la dose reçue, b) déconvolution du pic C1s obtenu par XPS en fonction de la dose.

Pour avoir une meilleure idée de la fragmentation du dépôt pendant les analyses ToF-SIMS nous avons mené les expériences en comparant les effets de  $\text{Ar}^+$ ,  $\text{Bi}^+$  et  $\text{Bi}_3^+$  (tableau 1) et comparé les résultats correspondant à un substrat de PS obtenu par spin coating et un substrat sub-ML de PS obtenu par Storing Matter.

Rapport des pics	PS référence obtenu par spin coating			PS obtenu par Storing Matter
	$\text{Bi}_1^+$	$\text{Bi}_3^+$	$\text{Ar}^+$	$\text{Ar}^+$ , $N=2.0 \times 10^{13}$ ions
$\text{C}_7\text{H}_7^+ / \text{CH}_3^+$	126.49	1198.00	27.85	2.27
$\text{C}_7\text{H}_7^+ / \text{C}_3\text{H}_3^+$	13.24	26.93	1.63	0.96
$\text{C}_7\text{H}_7^+ / \text{C}_3\text{H}_5^+$	17.03	22.90	7.75	0.28
$\text{C}_8\text{H}_9^+ / \text{CH}_3^+$	21.33	242.85	4.18	1.10
$\text{C}_8\text{H}_9^+ / \text{C}_3\text{H}_3^+$	2.23	5.46	0.24	0.47
$\text{C}_8\text{H}_9^+ / \text{C}_3\text{H}_5^+$	2.87	4.64	1.16	0.14
$\text{C}_9\text{H}_7^+ / \text{CH}_3^+$	15.03	188.16	16.00	0.58
$\text{C}_9\text{H}_7^+ / \text{C}_3\text{H}_3^+$	1.57	4.23	0.93	0.25
$\text{C}_9\text{H}_7^+ / \text{C}_3\text{H}_5^+$	2.02	3.60	4.45	0.07

Tableau 1: Rapport des pics de PS de référence obtenu par spin coating, et celui subML obtenu par Storing Matter lorsqu'ils sont analysés par ToF-SIMS en utilisant les ions primaires  $\text{Bi}_1^+$ ,  $\text{Bi}_3^+$ , et  $\text{Ar}^+$ .

La plus faible fragmentation est obtenue lorsque la surface est analysée par  $\text{Bi}_3^+$ . Une diminution drastique des rapports est obtenue pour l'échantillon sub-ML de PS. Une grande part de la fragmentation apparaît lors du dépôt. Le paramètre important pour la formation des ions secondaires durant l'analyse de la surface du collecteur est lié à l'efficacité du collage et les réactions de recombinaison de petits fragments pour former des fragments plus grands en augmentant le flux d'ions primaires. Cela peut arriver pendant le dépôt ou lors de l'analyse par ToF-SIMS. L'influence du faisceau d'ions primaires pendant les analyses ToF-SIMS de la surface du collecteur est montrée par le rapport entre grands et petits fragments qui est plus élevé pour  $\text{Ar}^+$  que  $\text{Bi}_3^+$ .  $\text{Ar}^+$  a un pouvoir d'arrêt plus faible que  $\text{Bi}_3^+$  qui pourrait favoriser la recombinaison de radicaux sur la surface du collecteur et produire des fragments plus grands, ce qui est contradictoire avec ce que nous observons pour les molécules déposées sur Ag. Ainsi, très probablement, la recombinaison des fragments est induite par le bombardement des ions  $\text{Bi}_3^+$ , plus que par les ions  $\text{Ar}^+$ . Cette explication est soutenue par les calculs de DFT.

Les énergies d'adsorption ont été calculées pour les fragments  $C_3H_3$ ,  $C_3H_5$ ,  $C_6H_5$ ,  $C_7H_7$ ,  $C_8H_9$  et  $C_9H_7$  sur les surfaces de Ag(100) et Ag(111). Ces énergies ne dépendent pas beaucoup des orientations des surfaces d'Ag, ainsi seuls les résultats obtenus sur Ag(111) sont discutés ici. Les fragments sont positionnés sur trois sites de la surface de Ag : (i) contre un atome de Ag, (ii) entre deux atomes de Ag, et (iii) entre trois atomes de Ag. Pour  $C_3H_3$  l'énergie maximale d'adsorption est 1,49 eV pour la position (iii). Pour  $C_3H_5$  on obtient 1,86 eV pour la position (ii). La différence d'énergie pour les différentes positions reste faible et ne dépasse pas 0,15 eV. Pour les grands fragments la position (i) est la plus stable. Les énergies d'adsorption sont de 1,63 eV pour  $C_6H_5$  ; 0,60 eV pour  $C_7H_7$  ; 0,5 eV pour  $C_8H_9$  et 0,61 eV  $C_9H_7$ . Pour  $C_3H_3$  deux atomes de C interagissent fortement avec le substrat en Ag ce qui explique le positionnement du fragment sur la surface (Figure 4b).

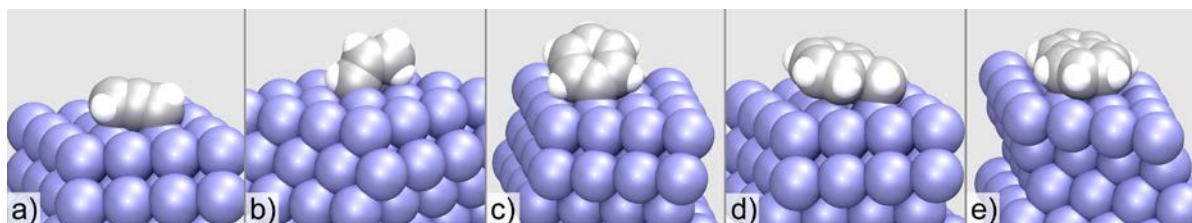


Figure 4: Géométrie d'adsorption pour différents fragments sur la surface de Ag(111): a)  $C_3H_3$ , b)  $C_3H_5$ , c)  $C_6H_5$ , d)  $C_7H_7$ , e)  $C_9H_7$ .

Pour  $C_6H_5$  à  $C_8H_9$ , la liaison C-Ag intervient essentiellement à travers le radical carbone, ce qui explique largement l'angle entre la surface d'Ag et le cycle aromatique (Figure 4 c-d).  $C_9H_7$  a une structure planaire et l'adsorption parallèlement à la surface concerne tous les atomes et les électrons interagissent avec la surface (Figure 4 e). Cela explique la haute valeur de l'énergie d'adsorption en comparaison avec  $C_9H_7$ .

Cela montre que les petits fragments adhèrent plus facilement que les grands fragments observés par ToF-SIMS et qui sont probablement formés par recombinaison qui intervient lors du dépôt et la diffusion sur la surface d'Ag ou pendant le bombardement lors de l'analyse par ToF-SIMS.



## 4. Adsorption de Polyméthyl méthacrylate (PMMA) sur Ag, Pt, Si et Al<sub>2</sub>O<sub>3</sub>.

Ce polymère contient de l'oxygène, et cette étude nous permet de voir comment cet élément influence l'adsorption sur les différentes surfaces.

Les résultats de XPS des dépôts de PMMA sur Ag montrent que les groupes méthyle disparaissent pour des doses élevées d'ions primaires (Figure 5). Pour les groupes oxygénés, la contribution varie peu avec la dose. La contribution C-C augmente avec la dose reçue ce qui montre une perte des autres groupes avec l'augmentation de la dose.

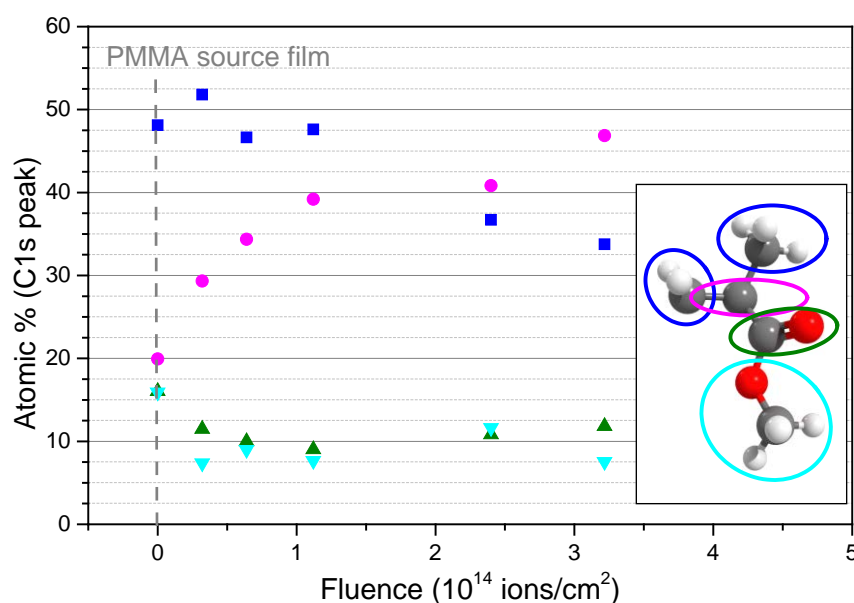


Figure 5: Variation des différentes contributions dans le pic du carbone C1s de films de PMMA analysés par XPS: en bleu les groupes méthyle, en magenta les liaisons C-C, en vert C=O et en bleu clair les liaisons C-O.

Les résultats obtenus par XPS montrent également la présence de fragments caractéristiques observés par ToF-SIMS du bulk de PMMA. Le comportement des petits fragments par rapport aux grands fragments par ToF-SIMS est identique au PS : la quantité des grands fragments est plus importante que ce qui est attendu et peut seulement être expliquée par une

recombinaison de petits fragment pour former des grands. Ceci est soutenu par des calculs de DFT sur de l'Ag.

Des calculs DFT ont également été menés sur différents fragments pour étudier l'influence du substrat sur l'adhésion de fragments pulvérisés dans Storing Matter. Les énergies d'adsorption des différents fragments et les distances sont résumées dans le tableau 2 ci-dessous.

Tableau 2 : Energie d'adsorption de fragments de PMMA et distance de ces fragments avec les différentes surfaces

	<b>E<sub>ads</sub> (eV)</b>			<b>d<sub>ads</sub> (Å)</b>		
	C <sub>2</sub> H <sub>3</sub> O <sub>2</sub>	C <sub>4</sub> H <sub>5</sub> O	C <sub>6</sub> H <sub>11</sub> O <sub>2</sub>	C <sub>2</sub> H <sub>3</sub> O <sub>2</sub>	C <sub>4</sub> H <sub>5</sub> O	C <sub>6</sub> H <sub>11</sub> O <sub>2</sub>
Ag(100)	-1.99	-0.75	-0.88	2.19	2.30	2.24
Al <sub>2</sub> O <sub>3</sub>	-0.81	-0.96	-1.75	1.91	2.18	1.90
Pt	-2.74	-2.6	-2.65	1.99	1.99	2.13
Si	-2.9	-2.2	-4.03	1.95	1.98	1.88

Les énergies d'adsorption les plus élevées sont obtenues pour Si et Pt. Par contre, la nature des interactions fragments – substrat est différente pour les deux surfaces. Pour Si, la liaison se forme entre un atome de Si de la surface et l'atome de carbone portant le radical. Pour Pt, souvent l'interaction fait intervenir plusieurs atomes de Pt et de C ce qui conduit à une densité d'électrons qui est moins localisée et ressemble plus à une structure de bande. Les observations sur les calculs DFT sont également valables pour des fragments de PS et permettent de conclure que les surfaces de Si et Pt sont à privilégier si une forte adhésion est attendue. Par contre une forte adhésion rend la réémission des fragments pour une analyse par ToF-SIMS plus difficile. Dans ce cas, une énergie d'adhésion intermédiaire comme celle trouvée pour l'Ag est à privilégier.

# Conclusions et perspectives

Le but de la thèse était d'étudier les interactions entre des fragments moléculaires avec une énergie de quelques eV avec un substrat métallique. Pour ceci, le dépôt de fragments de deux polymères a été étudié pour le régime de la sous-monocouche sur un collecteur d'argent. Les analyses ToF-SIMS ont montré que la proportion des grands fragments augmente plus vite avec le taux de couverture que celui des petits fragments alors que la fragmentation des polymères augmente avec la dose d'irradiation ionique lors de la préparation des dépôts. Des calculs DFT ont montré que ceci n'est pas dû à l'adhésion préférentielle des grands fragments, qui ont des énergies d'adsorption légèrement plus faible que les petits fragments, mais à une recombinaison des petits fragments pour former des plus grands. La composition du polymère joue aussi un rôle. Pour le PMMA, qui comporte des atomes d'oxygène, la pulvérisation préférentielle de ces derniers peut être observée, ce qui conduit à une baisse des fragments d'hydrocarbures dans une première phase. Pour des taux de couverture plus élevés, la quantité de tous les grands fragments augmente, qu'importe leur composition chimique. Les résultats d'XPS ont surtout permis de quantifier la fragmentation des chaînes de polymères sous le bombardement ionique.

En plus de ces études, les calculs DFT ont été réalisés sur plusieurs substrats afin de pouvoir conclure sur l'influence de ce dernier sur l'adhésion. Les énergies d'adsorption sont de loin les plus faibles sur la surface d'alumine, suivi par la surface d'argent et par les surfaces de silicium et platine, qui montrent des énergies comparables.

Un des problèmes majeurs lors des travaux expérimentaux était la présence de contamination sur la surface des collecteurs. Pour pouvoir contourner ce problème, le développement d'un prototype permettant la préparation et l'analyse des échantillons dans une même enceinte serait l'idéal. La fragmentation des polymères lors du dépôt par bombardement ionique pourrait être réduite par l'utilisation d'agrégats massifs en Argon au lieu d'Argon monoatomique. Des calculs DFT plus poussés permettraient aussi d'étudier la dynamique lors du dépôt des fragments sur les collecteurs et d'obtenir des informations sur le coefficient de collage, ainsi que l'influence de l'orientation des fragments, leur énergie et leur angle d'incidence sur ce dernier. Le calcul des barrières de diffusions de différents fragments sur la

surface des collecteurs permettraient aussi de mieux comprendre les réactions entre les fragments sur la surface du collecteur.

*to Elif, Ece, Rana, Ahmet, Egemen and Ezgi  
Sevgilerimle*



## ACKNOWLEDGEMENTS

It is a pleasure to thank those whose support and contribution made this work possible.

I wish to thank Dr. Tom Wirtz and Dr. Patrick Philipp for providing me with the opportunity to pursue my PhD within their research team.

I extend my gratitude and thanks to my supervisor Prof. Mohammed Belmahi for his invaluable motivation, support and supervision in directing this PhD work. My sincere and special thanks go to my co-supervisor and advisor Dr. Patrick Philipp for his guidance and helpful suggestions he has provided throughout this work.

I kindly thank to Prof. Arnaud Delcorte and Dr. Serge Della Negra for accepting to be my reviewer. I also wish to thank Dr. Gérard Henrion and Prof. Kai Nordlund for being part of my thesis jury.

I would like to kindly acknowledge Prof. Jouko Lahtinen and Dr. Godhuli Sinha from the Aalto University and Prof. Kai Nordlund and Dr. Lotta Mether from the University of Helsinki for their helpful advices and for collaborating in my thesis project.

I am indebted to many of my colleagues at LIST for their unreserved support and friendly cooperation. In this sense, I would like to thank Dr. Nora Becker and Dr. Ben Kasel for introducing me instrumental aspects of the Storing Matter technique. I am grateful as well to Dr. Gilles Frache for his helpful advice and support with ToF-SIMS analysis. Very special thanks to Samir Menaouli, Arnaud Moschetta, and Alain Robert for their engineering and technical assistance. I would like to acknowledge Dr. Ludovic Briquet for his invaluable and constant support and endless patience for teaching me DFT calculations.

My grateful thanks to my colleagues at LIST, who have been close friends as well, and to my lovely friends in Luxembourg who have contributed most in my well-being throughout thesis writing.

Last but not least I would like to thank my parents, grandmother and sisters Sibel, Seçil, and Tuba for the endless love, patience and support they have provided all throughout my life.





# Table of Contents

General context and scope of the thesis .....	23
Chapter I: Literature review .....	25
1. Introduction .....	25
2. Sputtering and ionization models .....	25
2.1. Sputtering theories .....	26
2.2. Ionization Theories .....	31
3. ToF-SIMS for surface characterization of polymers .....	34
3.1. Introduction to ion modification of surfaces .....	34
3.2. Fundamentals of static SIMS .....	35
3.3. MD Simulations for understanding fundamental aspects of static SIMS .....	50
3.4. ToF-SIMS analysis of PS and PMMA .....	60
4. Adsorption of organic molecules and fragments on surfaces .....	66
4.1. MD Simulations of sticking of hydrocarbons on surfaces .....	66
4.2. DFT Calculation studies for the interaction of hydrocarbon fragments with metallic surfaces .....	72
5. Storing Matter Technique .....	74
Chapter II: Materials and Methods .....	77
1. Introduction .....	77
2. Experimental Methods .....	77
2.1. Sputter Deposition Techniques .....	77

2.2. Characterization of Deposits .....	92
3. Simulation Methods .....	94
3.1. Deposition of Organic molecules by Molecular Dynamic (MD) Simulations .....	94
3.2. Deposition of PS and PMMA fragments by DFT Calculations.....	102
Chapter III: Adsorption of alkane fragments and chains on the silicon and $\alpha$ -alumina surface by MD simulations .....	109
1. Introduction.....	109
2. Adsorption of hexane fragments on silicon (University of Helsinki).....	109
3. Adsorption of alkane chains of different lengths on $\alpha$ -alumina (LIST) .....	110
4. Conclusion .....	114
Chapter IV: Sputter deposition of Polystyrene (PS) .....	115
1. Introduction.....	115
2. ToF-SIMS analysis of bulk Polystyrene samples .....	116
2.1. ToF-SIMS spectra of PS analysed by different primary ions.....	116
2.2. Comparison of effects of $\text{Ar}^+$ and $\text{Bi}_1^+$ and $\text{Bi}_3^+$ projectiles on fragmentation of PS	118
3. Development of protocols for ToF-SIMS analysis of PS storing matter deposits.....	120
3.1. Detection and localization of the PS StoMat deposit .....	120
3.2. Comparison of effects of $\text{Ar}^+$ and $\text{Bi}_1^+$ and $\text{Bi}_3^+$ projectiles on fragmentation of PS in case of storing matter deposits.....	124
4. Study of the effect of coverage and primary ion fluence on fragmentation of PS.....	125
4.1. Constant primary ion fluence .....	126

4.2. Varying primary ion fluence.....	131
5. Conclusion .....	140
Chapter V: Sputter deposition of Poly (methyl methacrylate) (PMMA) .....	143
1. Introduction.....	143
2. Analysis of bulk Poly(methyl methacrylate) films .....	143
2.1. Study of the effect of primary ion fluence on fragmentation of PMMA .....	144
3. Analysis of PMMA Storing Matter deposits .....	155
3.1. Detection and localization of the PMMA Storing Matter deposit.....	155
3.2. Study of the effect of coverage and primary ion fluence on fragmentation of PMMA during Storing Matter deposition.....	159
4. Adsorption of PMMA fragments on silver using DFT calculations.....	173
5. Conclusion .....	173
Chapter VI: Adsorption of Polystyrene and Poly(methyl methacrylate) fragments by DFT Calculations	175
1. Introduction.....	175
2. Adsorption of PS fragments on Ag (111) and Ag(100).....	176
2.1. Adsorption sites .....	176
2.2. Adsorption Geometries.....	177
2.3. Adsorption Energies: .....	180
2.4. Adsorption distances.....	183
3. Adsorption of PMMA fragments on Ag(100) .....	190
3.1. Adsorption sites .....	190

3.2.	Adsorption Geometries.....	191
3.3.	Adsorption energies and distances .....	195
4.	Adsorption of PS fragments on Al <sub>2</sub> O <sub>3</sub> (0001), Pt(111) and Si(111).....	196
4.1.	PS fragments on Al <sub>2</sub> O <sub>3</sub> (0001).....	196
4.2.	PS fragments on Pt(111).....	199
4.3.	PS fragments on Si(111).....	201
5.	Adsorption of PMMA fragments on Al <sub>2</sub> O <sub>3</sub> (0001), Pt(111) and Si(111).....	203
5.1.	PMMA fragments on Al <sub>2</sub> O <sub>3</sub> (0001).....	203
5.2.	PMMA fragments on Pt(111).....	204
5.3.	PMMA fragments on Si(111).....	205
6.	Comparison of adsorption of PS and PMMA on different substrates: Al <sub>2</sub> O <sub>3</sub> (0001), Ag(100), Pt(111) and Si(111).....	207
7.	Conclusions.....	211
	Conclusions and Outlook.....	213
	Bibliography .....	219
	Appendix.....	237

# General context and scope of the thesis

This thesis is aimed at contributing to a better fundamental understanding of interactions of organic matter with metal surfaces, since it is crucial for the advance of many industry related processes for improved metal adhesion, protective organic coatings for electronic devices, organic electronics, food packaging, surface modification of medical implants, development of biocompatible materials, etc. For most of these applications, and for a better understanding of interface characteristics, it is important to study the deposition of organic matter during the first monolayers and even in the sub-monolayer range since the interactions during the very first stages of deposition control the final surface and interface properties.

For this purpose, in this study, the experimental deposition of organic matter has been performed using the Storing Matter technique, which was developed at CRP Gabriel Lippmann. The main purpose of this technique has been to obtain an easier quantification in secondary ion mass spectrometry (SIMS) where quantification is difficult due to the dependence of ionization probabilities on the local sample composition. The Storing Matter technique uses a two-step process for the sputtering and analysis of matter: In the first step the matter is sputtered and deposited on a chosen collector and in the second step the collector with deposit is analysed mainly in a SIMS instrument. For its application to the inorganic matter, it has been shown that the technique has a quantitative potential correcting for the matrix effect. Further studies showed that the matrix effect can be avoided when sputtering titanium from different matrices of titanium like  $\text{TiB}_2$ ,  $\text{TiC}$ ,  $\text{TiN}$ , and  $\text{TiO}_2$ . The application of the technique to organic materials is more challenging, since there are more parameters which are contributing to the final results in the case of organics. The technique has been applied to organics first time in a previous PhD work. Experimental conditions, which would lead to high ionization efficiency and low fragmentation, where the molecular information could be preserved to some degree, were investigated. Although promising results have been obtained, the influence of the deposition process on results, including the adsorption and sticking of matter on the collector have not been studied.

The main objective of this thesis is to get insights into sputtering and adsorption mechanisms of organic matter during the Storing Matter deposition process. For this purpose, a multidisciplinary approach has been used. It combines experimental techniques (Storing

matter) for the deposition and the analysis and characterization of deposits (ToF-SIMS, XPS) with advanced numerical simulations (molecular dynamics simulations and density functional theory calculations) to study the deposition of organic molecules and molecular fragments in the sub-monolayer range.

The thesis is organized in six different chapters. The main results of the work are presented in chapters IV, V and VI:

Chapter I: In this chapter a literature review of fundamental processes, which govern the experimental and numerical methods that have been employed in this work, is given. Concerning the experimental work, first, sputtering and ionization models with an emphasis on organics is given. Then, applications of SIMS for the analysis of organics are reviewed. MD and DFT simulation methods for the adsorption of organic matter for a wide range of energies for different applications have been investigated. Finally, state-of-the art of the Storing Matter technique for both inorganic and organic matter is presented.

Chapter II: The experimental and simulations methods that have been used in this work are described in this chapter. The conditions for experiments and simulations are also given.

Chapter III: The third chapter gives the results of MD simulations that guide the choice of appropriate matter for sputter deposition experiments.

Chapter IV: In the fourth chapter, experimental results for the sputter deposition of polystyrene (PS) and also simulation results for the adsorption of some characteristic fragments are presented with the purpose of getting more insights into sputter deposition by the Storing Matter technique.

Chapter V: The sputter deposition technique is applied to a different polymer, poly(methylmethacrylate) (PMMA) and ToF-SIMS and XPS analysis results are presented in combination with simulations results for the adsorption of PMMA molecular fragments.

Chapter VI: The final chapter consists of results of DFT calculations for the adsorption of various PS and PMMA molecular fragments on various substrates. The adsorption characteristics of various fragments and the effects of different substrates on these characteristics are assessed.

# Chapter I: Literature review

## 1. Introduction

In this chapter we will cover literature studies related to deposition and sticking of organic matter in the sub-monolayer range and the characterization of the latter. Special interest will be given to fundamentals which will facilitate to explain processes for the Storing Matter technique developed at CRP Gabriel Lippmann. The technique consists of two steps: first depositing sputtered particles (ions, atoms, molecules, fragments and radicals) on a collector material in the sub-monolayer range and second analysing the deposit by dynamic or static Secondary Ion Mass Spectrometry (SIMS). All related literature will be presented in four sections. In the first section, models for sputtering and ionization processes will be presented, including those of organic matter. In the second section, we will describe the characterization of polymers studies both by experiments and simulations with a special focus on SIMS of organics. Fundamental events of organic SIMS will be explained with the help of existing experimental and simulation data. Example cases of studied polymers with respect to their characterization and modification will be given. The third section explores the sticking of organic matter on surfaces in relation to the deposition process in the Storing Matter technique. MD simulations at low impact energy to get insights into dynamics of hydrocarbon-surface interactions and static DFT calculations to investigate the electronic structure of adsorption processes at the metal-organic interface will be also reviewed. Finally, in the last section, state of the art for the Storing Matter technique is given.

## 2. Sputtering and ionization models

Sputtering is defined as the ejection of surface atoms in the near surface layer by impacting energetic particles on the solid surface.[1] The first evidence for sputtering was observed by W. R. Grove where the matter was deposited on the inside of vacuum chambers as a result of electric discharge between a metal plate and a low pressure mix of several gases.[2] Since then, this phenomenon has been widely used for thin solid film deposition. The main aspects of sputtering has been reviewed by Behrisch and Eckstein.[3]

In sputtering, the incident particles, which can be either electrons, photons or ions, have an energy in the eV to MeV range. In this work, we focus on sputtering by ions. For energies in

the eV to keV range, sputtering is explained by atomic collisions between the impacting particles and surface atoms. For the sputtering with MeV particles, the collision takes place far from thermal equilibrium and some part of the energy is deposited in the electrons. We will limit our discussion to energies from tens of eV to the keV range which is enough to induce collision cascade in the solid as a result of momentum transfer and which is also the energy range used in this work. When the particles leave the surface as a result of this momentum transfer, the process is called “physical sputtering”. If the incident particles (ions) induces a chemical reaction in the surface atoms which results in subsequent desorption of particles, “chemical sputtering” can be mentioned.[4] Being weak in the lower eV region, the physical sputtering is dominated at impact energies of medium eV to the MeV region, whereas chemical sputtering occurs at lower energies.[5]

## 2.1. Sputtering theories

Starting with basic elements of sputtering and accepted sputtering theories, we will continue with the fundamentals for the sputtering of organic matter.

For practical reasons, the most investigated systems for the sputtering studies have been the sputtering of metals by ion bombardment. When an incident ion hits the surface, a series of events start off at the point of impact. The atoms which are knocked off their equilibrium state start to move through the material and may induce further collisions. The impact of an ion on a surface starts a collision cascade which can be defined as a set of energetic collision of nearby atoms induced by an energetic particle in a solid or liquid.[6]

According to classical sputtering theory, three different collision regimes (Fig. I- 1) have been identified by Sigmund[5] depending on the energy of incoming particles and the size of the perturbed volume defined as collision cross section:

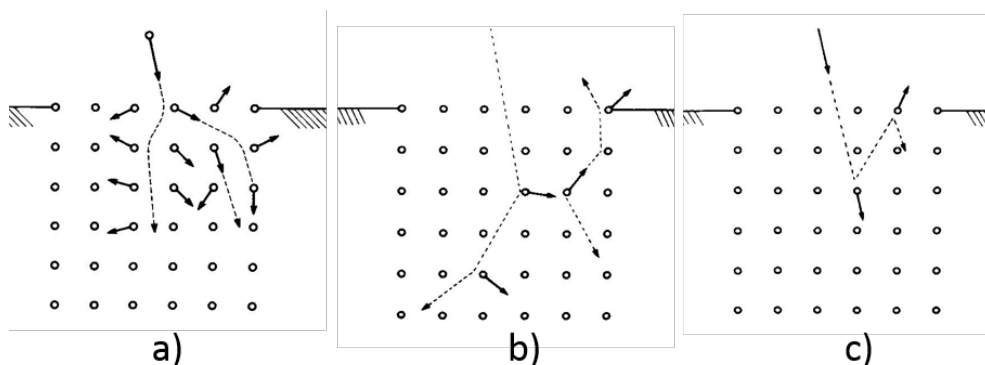


Fig. I- 1: Different collision regimes defined by Sigmund (a) The single-knock-on regime (b) The linear cascade regime (c) The spike regime



1. The single knock-on regime: The incident light ions or low energy heavy ions (lower to medium eV) are energetic enough to sputter surface atoms as a result of incident particle-surface atom collision; however they are not energetic enough to generate a recoil cascade.
2. The linear cascade regime: The energy of the incident particle is high enough (keV and MeV ions) to generate a recoil cascade in the solid and low enough to interact with atoms at rest. The density of the recoil atoms is assumed to be low. Thus, knock-on collisions dominate and the interaction between moving atoms is almost negligible.
3. The spike regime: The heavy and high-energy ions result in a large collision cross-section resulting in the motion of most of the atoms of the recoil in the so-called spike volume.

Within these regimes, the concept of linear cascade regime is well suited to describe some very basic elements of sputtering like sputter yields, angular and energy distributions of the sputtered particles. Sputtering theory is studied both experimentally and by simulations. Some of the experimentally measurable quantities are number of emitted particles, their energy and angular distributions, elemental composition, state of aggregation and charge and excitation states.[7]

The first condition for sputtering is that the beam energy should be higher than the surface binding energy. The difference in between these two energies can vary by several orders of magnitude. For describing high-energy dynamics, kinetic equations of linear transport theory, which Sigmund based his work on, and binary-collision simulation usually suffice. The variables which are governed by high-energy dynamics are the penetration depth of the ion beam, the spatial extension of a cascade and the distribution of the deposited energy. The low-energy regime is usually dealt with molecular-dynamics simulations since existing theories fail to describe the many-body nature of the particle-surface interactions. They help to explain rearrangement processes within the cascade, defect formation and emission of sputtered atoms.[7] Combinations of experimental and simulation studies are rare in literature. Vicanek *et al.* compared energy and angular distributions of matter using linear Boltzmann equations and TRIM simulations.[8]

One important parameter in sputtering theory is the sputter yield, which is defined as the number of atoms ejected from the target per incident ion. It depends on primary ion

properties like their angle, energy and mass and also target atom properties like mass, surface binding energy, crystallinity, density and topography.

Using Boltzmann kinetic equations, Sigmund developed the equation for sputter yield:

$$Y(E,\Theta) = \Lambda F_D(E,\Theta,0) \quad (\text{I-1})$$

where  $F_D(E,\Theta,x)dx$  is the average energy deposited in a layer  $(x,dx)$  in a cascade initiated by a projectile with energy  $E$  at an angle  $\Theta$  to the  $x$ -axis, whereas  $\Lambda$  is a material constant for the surface binding energy and collision cross section.[9]

Using kinetic equations, the angular dependence on the sputter yield can be approximated as[7]:

$$\propto \cos^{-f} \Theta \quad (\text{I-2})$$

with  $1 \leq f \leq 2$

Transport theory for an infinite medium yields a monotonic increase according to equation I-2. Monte Carlo simulation on a semi-infinite medium leads to a maximum at grazing incidence and a subsequent drop.

### 2.1.1. Sputtering of Organics

The Sigmund-Thompson transport theory has always been used for explanation of sputtering phenomena of inorganic materials. However, inorganic materials are much simpler by nature.

Although SIMS has been extensively used for characterization of organics, the mechanisms leading to desorption, ejection and ionization of molecules by energy transfer to the organic/substrate system is complicated. Although it has been used as a model for semi-quantitative descriptions of secondary organic ions, the theoretical model for sputtering of inorganic surfaces developed by Sigmund [5] cannot be directly adapted to sputtering of high mass organic species.[10],[11] It has been shown by Falcone *et al.* that the classical sputtering theory where binary elastic collisions are dominant, cannot be extended to the desorption and ionization of organic ions in all regimes.[11] They suggest a two-step mechanism where first the impact energy by the primary beam is transferred to molecular internal degrees of freedom and this energy is used to desorb organic molecules like ions as well as neutrals. In addition to the secondary particle ejections induced by collision cascades,

some suggest formation of a vibrationally excited region prior to ejection, i.e. some of the energy is transferred to vibrational and rotational modes of molecules.[10],[12]

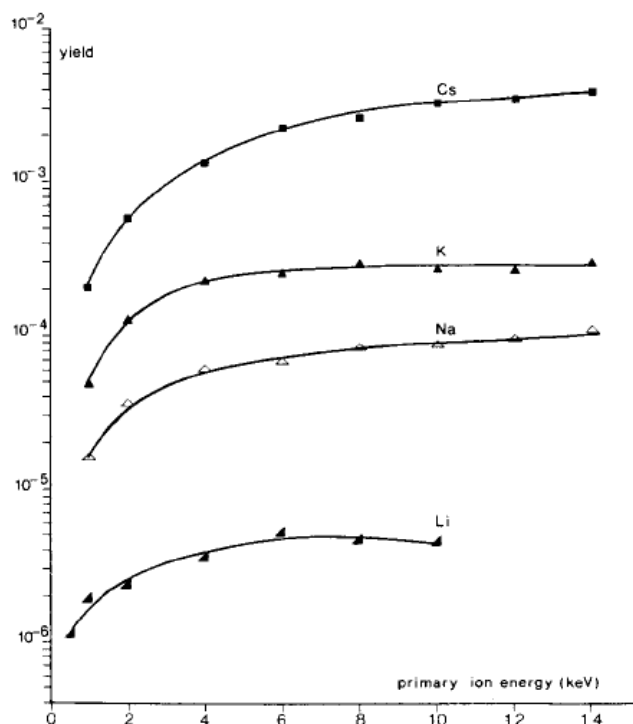


Fig. I-2: Secondary (M+H)<sup>+</sup> ion yields from alanine produced by Cs<sup>+</sup>, K<sup>+</sup>, Na<sup>+</sup> and Li<sup>+</sup> primary ions[13].

In their work for time-of-flight measurements of secondary ions produced by 1-16 keV primary alkali ion bombardment of alanine layers, Standing *et al.* showed that it is mainly nuclear energy loss that governs the secondary ion formation in this energy range.[13] As seen in Fig. I-2, yields increase strongly with increasing mass of the bombarding particle, and also with increasing energy, which suggest that the nuclear stopping power is responsible for this yield increase in this energy range. Fig. I-2 shows it is advantageous to use primary ions with higher masses having larger stopping power. It can be seen that the higher yields are obtained with Cs<sup>+</sup> primary ions at 16 keV. In their work, for the high energy range (MeV), they suggest that it is electronic stopping which is responsible for secondary ion formation, which is consistent with the classical sputtering theory.

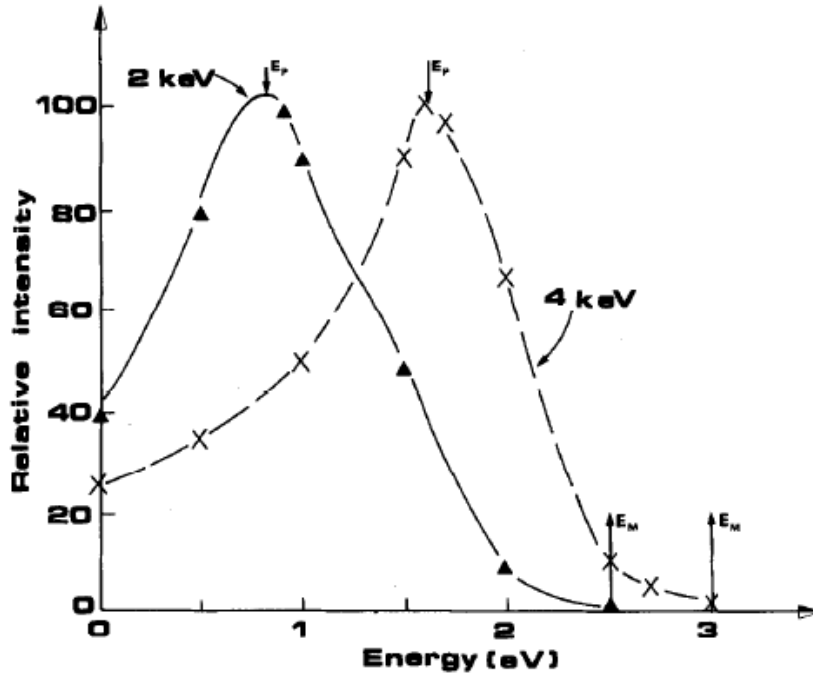


Fig. I-3: Energy distribution of PEG secondary ions after 2 and 4 keV Ar<sup>+</sup> bombardment. E<sub>p</sub>: peak position, E<sub>m</sub>: maximum sputtered energy.[11]

Fig. I-3 shows the energy distributions in case of bombardment of Polyethylene glycol (PEG) with 2 and 4 keV Ar<sup>+</sup> bombardment. The authors do not specify which secondary ions were recorded. It is well known that the peak position is independent of incident energy and ion-target combination in the Sigmund-Thompson model[5] which is shown by the equation[11]:

$$E_p = \frac{U}{2} \quad (I-3)$$

Where U represents the surface potential barrier (surface binding energy) that needs to be overcome for the ejection to happen. Since a peak shift is observed for the energy distribution, the possibility of a linear cascade regime is ruled out.

Assuming the validity of thermal non-linear regime where the atoms in the collision cascade lose the memory of the incident ion, the damage produced in the solid by particle bombardment or the equilibrium reached can be correlated[11] with a Maxwell distribution[14].

$$F \propto E_0^{1/2} \exp\left(-\frac{E_0}{kT}\right) \quad (I-4)$$

Where k is the Boltzmann constant and T is the temperature.

Then, replacing  $E_0$  by  $E+U$ , the following equation is obtained for the energy spectrum.

$$J(E) \propto E(E + U)^{-1/2} \exp[-(E + U)/kT] \quad (I-5)$$

## 2.2. Ionization Theories

One of the earliest models for ionization is bond-breaking model proposed by Slodzian *et al.*[15], which considers the ion emission from materials with ionic bonding is as a result of bond-breaking of a cationic element from anionic groups in the lattice in case of a positive ion emission.

In addition to Slodzian's bond-breaking model Michl assumes that the impacting particle does not only cause bond-breaking, but also produces ionization, fragmentation, electronic excitation or a photochemical reaction. He proposed a two-step mechanism[16] explaining by the primary damage and secondary damage formations. In the primary damage region, both ground-state and electronically excited molecules of the original solid will be formed. The secondary damage formation is a thermal spike regime where the collision cascade develops into a thermal spike where reactions between excited species might occur before, during or after ejection.

In an early study by Grade and Cooks[17], the cationization of organic molecules through attachment to transition or noble metal ions was presented as a new ionization technique. The advantages of this kind of ionization technique are that the ion clusters can be used to characterise the molecular weight, fragmentation patterns can be interpreted easily due to ease of distinguishing cations from other atoms in the organic molecule and the degree of fragmentation can be varied by altering the cation.

Cooks and Bush developed desorption-ionization model for ionization of molecular solids. In the desorption-ionization model developed by Cooks *et al.*, reactions between molecules and fragments are emphasized after being ejected either in the selvedge or by metastable reactions in the field free region of the spectrometer.[18] This model can help to explain ionization in Secondary Ion Mass Spectrometry (SIMS), Fast Atom Bombardment (FAB), Laser desorption (LD) and Plasma Desorption (PD) and can be summarized as in Fig. I-4:

- i. The incoming energy is transformed into vibrational energy, delaying the molecular ion emission. There exists relatively low excess energies in the

desorbed ions due to inefficient coupling between translational energy and internal energies of surface molecules.

- ii. It is not physical factors determining the nature of desorption-ionization spectra and ion yields, but rather chemical factors.
- iii. The association reaction usually occurs in the selvedge and dissociation mainly in free vacuum.

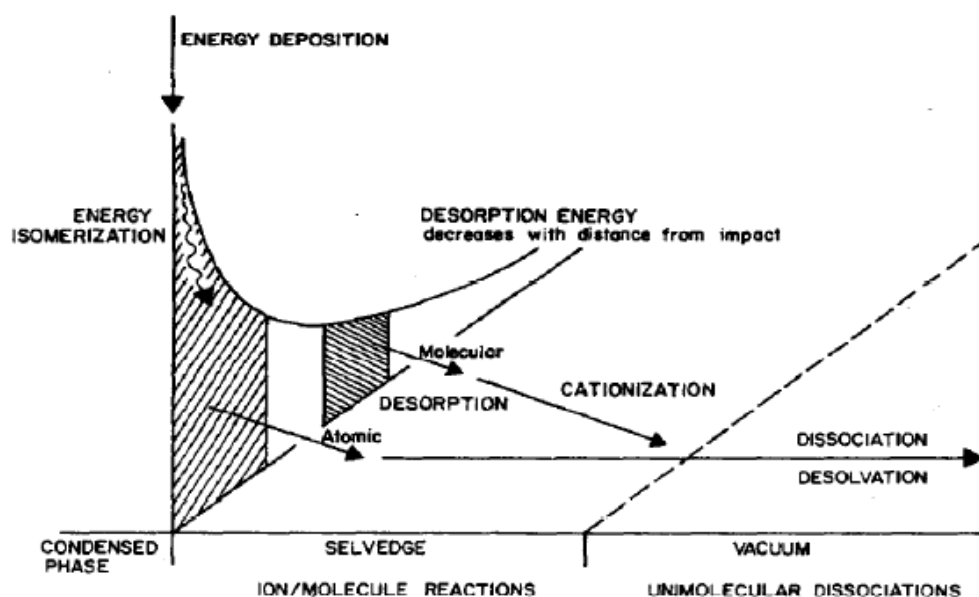


Fig. I-4: Summary of processes occurring in desorption ionization model[18]

A precursor model[19] has been developed by Benninghoven for organic secondary ion formation as a result of bombarding amino acid layers deposited on metals. Fig. I-5 shows the scheme of the secondary ion formation. In agreement with classical sputtering theory by Sigmund[5], the main idea is that the energy and momentum of the impacting particles is transferred to the solid, creating a cascade and an excited area around the point of impact. The sputtering, i.e. the ejection of ions occurs only if sufficient energy is transferred to the solid. For bombardment of molecular solids, the binding state of the precursor and the distribution of energy and momentum in the solid are two main set of parameters important for ion formation. The chemical environment of the precursor determines its binding states, whereas the energy and momentum distribution is governed mainly by the solid lattice and the properties of the primary particles (mass, energy, composition and angle of incidence).

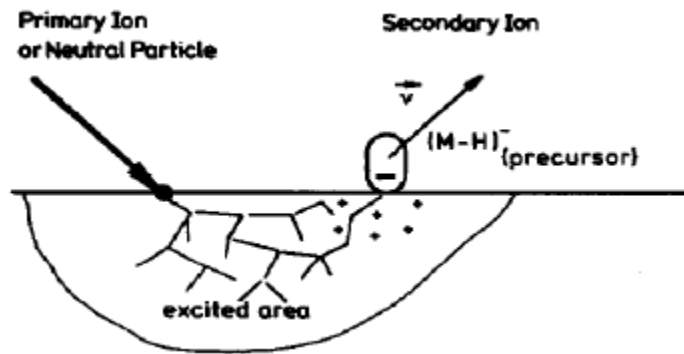


Fig. I-5: Scheme of secondary ion formation[19]

In the precursor model, the ejection mechanisms are correlated with gradual energy decrease with increasing distance from the impact point on the solid. Fig. I-6 shows the distribution of the average energy as a function of distance  $r$  from the impact point. The model assumes that the energy transferred to the molecule is highest at the impact point causing violent ejections resulting in significant fragmentation. In case of an energy under the threshold, no desorption occurs which corresponds to the longer distances from the impact point. There exists only an intermediate region from where intact precursors can be ejected.[19] Larger fragments or whole molecules are sputtering further way from the impact location.

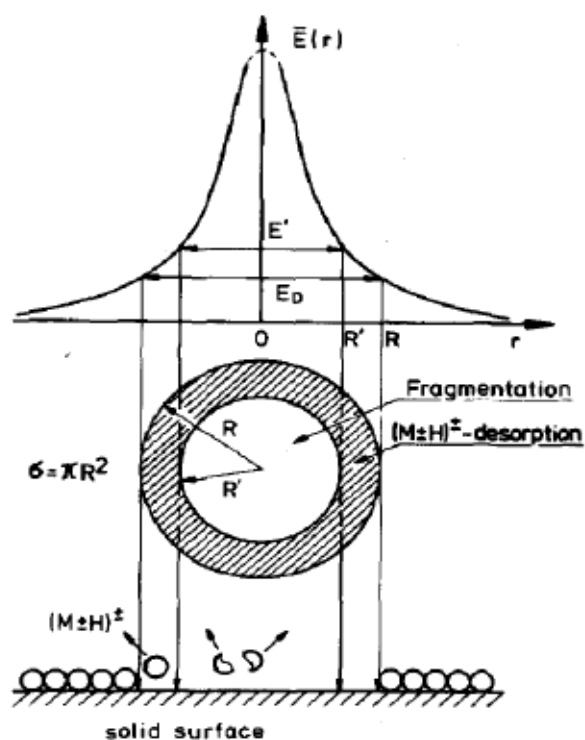


Fig. I-6: The distribution of average energy transferred to a surface particle as a function of distance  $r$  from the impact point[19]

### **3. ToF-SIMS for surface characterization of polymers**

#### **3.1. Introduction to ion modification of surfaces**

Due to their unique advantages, polymers had the interest of various fields of material science. Physical and chemical properties of polymers can be modified by different techniques such as plasma treatments or ion beam irradiation. Plasma treatments are widely used for modification of polymer surfaces and offer many advantageous and unique surface properties through efficient, non-polluting processes. However the complexity of occurring chemical and physical reactions makes it difficult to fully understand the interactions between the plasma and the polymer surface. Compared to plasma processes, ion-beam techniques allow for an easier tuning of the process parameters since ion energy, ion beam current and ion fluence can be adjusted precisely.[20] Moreover, the fast reaction rates in plasmas do not allow for studying the interactions of the matter in the sub-monolayer range. An understanding of sticking and adhesion of molecules and molecular fragments in this regime can be obtained by the ion-beam treatment of polymers. In addition, interactions in the sub-monolayer are important for surface properties in general, since this monolayer defines the (adhesion) properties between the metal and the polymer deposit. For these purposes, molecular fragments can be bombarded by low energy (keV) ions or atoms, or high energy (MeV) ions or photons, desorb, and can be collected to study the sticking in the sub-monolayer range.

Interactions of ion beams with polymers have been studied since several decades and find applications in various areas of interest such as ion beam surface modifications for improved metal adhesion,[21] improved conductivity of polymers,[22] synthesis of novel inorganic films by ion beam irradiation of polymer films,[23] ion beam modification of surface morphology for biocompatibility[24] and ion beam etch resistance of polymers[25].

Two aspects require to be understood regarding ion beam treatments of organic surfaces: the ion beam-solid interaction and characterization of irradiated surfaces. For the interaction of ion beams with organic solids, the particular interest has been the mechanisms for molecular desorption and ejection.[26],[10] The techniques that could be used to understand these mechanisms include Secondary Ion Mass Spectrometry (SIMS), Fast Atom Bombardment Mass Spectrometry (FABMS), Plasma Desorption Mass Spectrometry (PDMS) and Laser Desorption Mass Spectrometry (LDMS). SIMS has proven to be a very efficient technique



for analysis of non-volatile and thermolabile organic compounds among all other desorption-ionization techniques. Its high sensitivity enables analysis of very thin organic layers of monolayer coverages. For characterization of modified polymer surfaces, many techniques can be used including Time-of-Flight Secondary Ion Mass Spectrometry (ToF-SIMS), X-Ray Photoelectron Spectrometry (XPS), Scanning Electron Microscopy (SEM) and Atomic Force Microscopy (AFM). At the same time, modifications of ion beams on surfaces need to be understood in order to characterize them by SIMS.

### **3.2. Fundamentals of static SIMS**

In SIMS, the composition of a solid surface or thin film is determined through sputtering the surface by focused ion beam and collecting and analysing ejected secondary ions. The first SIMS instruments used argon as primary ion beams and were magnetic double focusing sector field mass spectrometer. Later on, SIMS instruments with quadruple mass analysers were developed.[27],[28] Both were developed for inorganic analysis. Static SIMS using time-of-flight analysers, was introduced by Benninghoven for analysis of organic matter. The main difference to the other mass analyzers is that the primary ion current density is so low (thanks to pulsed primary ion beam) that only very low percentage (1%) is enough for analysis of the very first surface layer, so that the organic sample can be analysed without significant damage.[29]

Interactions between ion beams and polymers have been investigated in the field of time-of-flight secondary ion mass spectrometry (ToF-SIMS) which has proven to be a useful technique for the characterization of polymer samples. Its high surface-specific sensitivity, ability to provide direct molecular information and ease of applicability to all types of sample forms have made it attractive for surface analysis of organic matter. Although the use of SIMS for analysis of inorganic matter has been well established, the analysis of organics by static SIMS is still an evolving field. Since the basic processes caused by energetic ion beams in organic samples are not fully understood, data interpretation and quantification is not straightforward.[30] The physical mechanisms underlying the sputtering and ionization of organic molecules is complicated and still to be better understood. In the following sections, we will mention parameters and concepts that are indispensable to static SIMS analysis of organics.

### 3.2.1. Secondary ion yield

The sputter yield was already defined in the previous section as the number of particles ejected from the surface per incident ion. Applied to SIMS, one can define the secondary ion yield which is given by the probability that these ejected particles will be ionized. If we assume the sputtering of a surface particle M, the sputtering particle yield  $Y(X_i^q)$  is related to the sputter yield  $Y_s(M)$  by the ionization probability of particle M,  $P(M \rightarrow X_i^q)$ [31]:

$$P(M \rightarrow X_i^q) = \frac{Y(X_i^q)}{Y_s(M)} \quad (I-6)$$

Sputter yields can be similar for different materials, whereas the secondary ion yields can vary by some orders of magnitude due to ionization or transformation probability defined as the probability that the disappearance of particle M will result in emission of a secondary ionized particle,  $X_i^q$ .

#### 3.2.1.1. Substrate effect

The surface to be analysed has a strong influence on the secondary ion yields as the ionization probabilities are strongly influenced by the local chemical environment of the surface component to be analysed. Unlike sputter yields, the secondary ion yields for different metals can be quite different. When bombarded with 10 keV  $Ar^+$  ions, the sputter yield for metals is typically between 2 and 10 and secondary ion yields are in the range  $10^{-6}$  to  $10^{-4}$ . [31] For molecules, the sputter yields could be similar to those of metals whereas the secondary ion yields can be over ten times greater depending on the environment and the nature and size of the molecule. [31]

The secondary ion yields can be greatly enhanced by the presence of electronegative species, like oxygen on the surface. The sputtering yields for metal oxides can be several orders of magnitude higher than those of metals, which is accompanied with a relatively small change in sputter yields. [31] This is known as matrix effect problem which might cause significant quantification problems in SIMS.

#### 3.2.1.2. Primary ion nature effect

For SIMS of organics, it is known that the secondary ion yields increase with primary ion mass, although not linearly. It has been shown that using primary ions of high masses ( $Xe^+$ ,

$\text{Cs}^+$ ,  $\text{In}^+$ ) compared to low mass ions ( $\text{Ar}^+$ ,  $\text{Ga}^+$ ) can enhance secondary ion yields.[32],[33] It is explained by the increase of stopping power with the ion mass. [30]

Like in the case of going from low mass primary ions to high mass ones, there is a significant increase in secondary ion yields while going from monoatomic projectiles to cluster primary ions. The increase is also nonlinear.[34],[35] The secondary ion yield per atom is higher in case of cluster primary ions. The interest in using cluster projectiles for analysis of organic surfaces is not only due to enhanced secondary ion yields, but also due to reduced chemical damage in the sample which allows emission of intact molecular ions and molecular depth profiling of organics. The damage formed by cluster ions is more surface-localize with rapid sputter removal rates which results in an equilibrated system where the damage created is removed before it can accumulate. [36] New molecular sources like  $\text{C}_{60}^+$ ,  $\text{Au}_3^+$ ,  $\text{SF}_5^+$ ,  $\text{Bi}_3^+$ ,  $\text{Au}_n^+$  and  $\text{Ar}_n^+$  have been used instead of more conventional primary ions like  $\text{Ar}^+$ ,  $\text{Cs}^+$  and  $\text{Ga}^+$  for abovementioned purposes.

For small organic molecules, the increase in secondary ion yields with increasing primary ion energy has been reported.[30]

### 3.2.2. Emission of secondary ions

We know from the previous section that sputtering theory of Sigmund describes well the sputtering event. The collision of primary ions with a surface induces a number of processes described by different collision regimes. [5] In general, the bombarded surface undergoes changes both at the impact point and at the neighbourhood of primary ion trajectory which might include radiation damage, removal of particles by sputtering and ion implantation in deeper layers.[31] In case of SIMS of organics, these processes are more complicated which might lead to fragmentation and dissociation of molecules. [37]

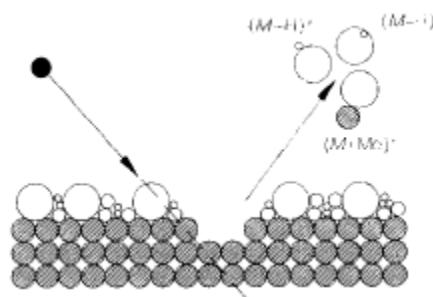


Fig. I-7: Secondary ion formation. [31]

As the primary ion penetrates into the solid, it transfers its kinetic energy to the atoms and after subsequent collisions; some of energy might be directed back, leading to emission of secondary ions. In case of bombardment of organic monolayer on a metal surface, quasi-molecular ions of  $(M+H)^+$ ,  $(M-H)^-$  and  $(M+Me)^+$  can be emitted, where M represents the organic molecule, H hydrogen and Me methyl group. (Fig. I-7) As a result of sputtering, positive, negative secondary ions and neutral particles are emitted as well as electrons and photons. However, the emission of electrons and photons does not provide much information about chemical composition of the surface.

### 3.2.2.1. Kinetic energy distributions of emitted matter

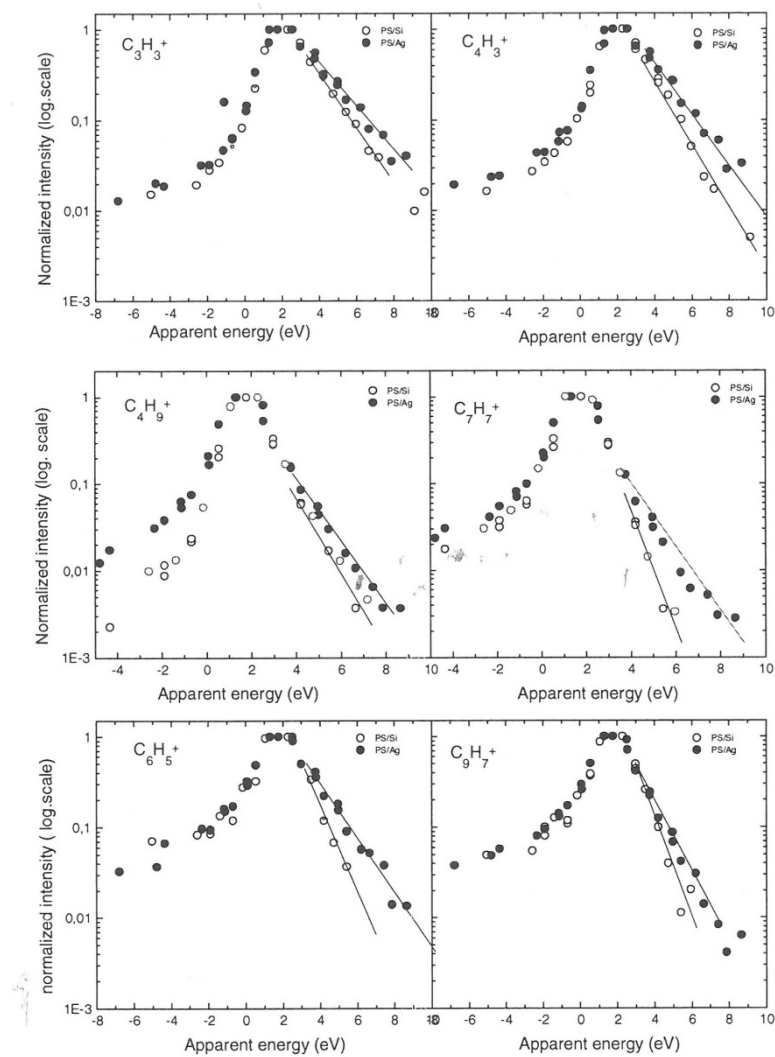


Fig. I-8: KEDs of secondary ions sputtered from polystyrene spin-coated onto Si and Ag[38]

Kinetic energy distributions (KED) of the emitted species have been studied by ToF-SIMS in order to better understand secondary molecular ion formation. Arezki *et al.* studied the effect

of substrate on the KED of organic fragments sputtered from Polystyrene (PS) layers spin-coated on silver (Ag) and silicon (Si).[38] A significant influence of the substrate on the KED of many fragment ions was observed. A narrower KED with a steeper high energy tails was observed for Si compared to Ag. This different behaviour is mainly attributed to the ejection step rather than the ionization step during secondary ion formation.[38] The fact that a similar KED is observed for many fragments shows the negligible effect of ionization on the kinetic energy of sputtered fragments.(Fig. I-8) This was also shown by KED calculations by MD simulations. [39] The differences in KEDs of fragments sputtered from different substrates are related to mechanistic view of the ejection process.[38]

KED studies have been recently complimented with MD simulations to have better insights. More explanations and examples will be given in MD simulations section.

### **3.2.2.2. Fragmentation and reactions**

For bombardment of organics with energetic ions, most of the time the molecules are not desorbed in intact form, they are rather fragmented. Much work in organic SIMS is devoted to interpreting fingerprint spectra (low mass region, up to  $m/z$  of 200) in order to have a better understanding of fragmentation patterns and mechanisms. Having already mentioned some ionization models for sputtering of organics in the previous section, here we will give a brief description of existing fragmentation mechanisms for the SIMS applied to analysis of organic surfaces.

1. Inspired by similarities in fragmentation patterns during SIMS, FABMS, PDMS and LDMS, the desorption ionization model[18] suggests that the energy on the surface is subsequently transferred to a common form and identical fragments are ejected, which are generally the characteristic of the analysed species. Fragmentation occurs through chain scissions in the molecule and it cannot be based on binary collision approximations as more chemistry is involved compared to analysis of inorganics.
2. Based on the work of Hearn and Briggs[40] and Davies *et al.*[41], Leggett and Vickermann developed an empirical model[42] for describing fragment emission from polymer surfaces. In this model, the energy deposited on the surface is transformed into vibrational energy. The fragmentation and unzipping of internally excited polymer chain leads to formation of radicals and molecular ions. The small ions are directly emitted close to the region of primary particle impact.

3. Using the results from kinetic energy distributions of hydrocarbon ions related to their hydrogen content, Delcorte *et al.* proposed a mechanism[43],[44], in which some part of the energy deposited on the surface is transferred to the hydrocarbon as momentum and leads to C-C bond scission. The rest of the energy is distributed in vibrational and rotational forms and the further extents of energy leads to fast decomposition of fragments resulting in hydrogen elimination. The relaxation of characteristic fragments leads to emission of less characteristic fragments. The hydrogen and size effects suggested has been also observed for polymers like polystyrene.[45] Moreover, the kinetic energy distributions of the most characteristic fragment ( $C_7H_7^+$ ) of polystyrene has been predicted by this model.[39]

Apart from all the models for desorption and emission of organic molecules from the surface described above, it is also possible that the molecule might be ejected intact in an excited state and decomposes on its way to the detector in the spectrometer, which are referred to as metastable decay reactions.[30] The products of these reactions can be identified either in the mass spectra or in their kinetic energy distributions. One of the characteristics is that they lack energy compared to fragments directly ionized at the surface since they leave some part of their energy to the parent molecule through decomposition on their way.[45],[46]

### 3.2.2.3. Cationization

Using a metal as substrate is a very common and useful way of identification of organic molecules through forming quasi-molecular secondary ions.[47] This way of forming and detecting quasi-molecular secondary ions is called cationization. For this purpose it is necessary to prepare the organic matter as a thin layer on the metal since the secondary ion yield increases linearly with coverage until a monolayer coverage at which the highest yields are observed.[48] Fig. I-9 shows the secondary ion yields obtained from adenine layers on silver and also from silver. For adenine, the maximum yields are observed at about one monolayer coverage and then the yield decreases for multilayers. For silver, the intensity decreases continuously. No cationization is observed from thick organic layers prepared on metal substrates.

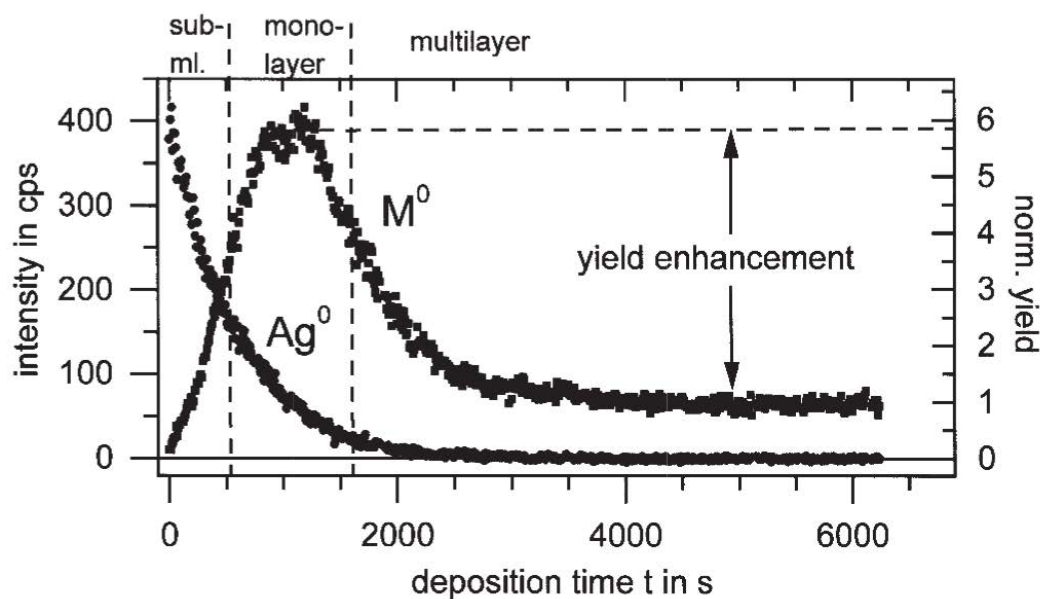


Fig. I-9: Normalized sputter yield of silver ( $\text{Ag}^0$ ) and adenine ( $\text{M}^0$ ) determined by laser post ionization SNMS.[47]

Cationization is not affected by the organic analyte, but rather by the metal used as substrate. It is independent of the structure of the analyte. When prepared on silver as monolayers, almost all materials exhibit cationization. [47] The significant effect of the metal on the secondary ion yields can be observed in Table I-1. For all the polymers mentioned, silver results in the highest secondary ion yields, probably due to the high sputter yield of silver.

Table I-1: Normalized secondary ion yields of polymers prepared as monolayers on metals.[49]

Polymer	Ion	Mass(u)	Ag	Au	Pt	Cu
PS3000	$(\text{M}+\text{Me})^+$	2766	100	16	7	2
PEG1460	$(\text{M}+\text{Na})^+$	1427	100	53	24	1
PMMA1890	$(\text{M}+\text{Me})^+$	1704	100	6	1	4

### 3.2.3. Primary ion related parameters

#### 3.2.3.1. Primary ion charge state

The charge state of the incident ion has no influence on the secondary ion emission. [50] It has also been shown by Della-Negra *et al.* that the memory of the projectile charge state is

lost and the secondary ion yield is almost found independent of the charge state of the primary ion trajectories for grazing incidence angles.[51]

### **3.2.3.2. Primary ion fluence**

For irradiation damage in general, the effect of changing fluence on interactions of Ar<sup>+</sup> ion beam with polyethylene and polystyrene films have been investigated by Calcagno *et al.*[52] It was suggested that at low ion fluences ( $10^{12}$ - $10^{14}$  ions/cm<sup>2</sup>), primary chemical modifications of the polymer film take place (chain scissions, crosslinks, molecular emission and double bonds formation), whereas at higher ion fluences ( $10^{14}$ - $10^{17}$  ions/cm<sup>2</sup>), the polymer does not keep the memory of its initial chemical structure, and a very stable material with properties similar to hydrogenated amorphous carbon is produced.[52] The effect of increasing primary ion fluence on SIMS of organics have been studied by many groups in order to see the limits of ion dose for which the molecular information can still be obtained. It is suggested that for SIMS analysis of organics, primary ion beam fluences above the so called “static limit”, which is often defined to be at or below  $1.0 \times 10^{13}$  ions/cm<sup>2</sup>, causes beam-induced damage effects on the organic matter and limits the secondary ion yields.[53] It was also demonstrated by Ninomiya *et al.* that above the static limit, the sputtering yield of the polymer for atomic primary ion beams decreases.[54] Surface degradation induced by ion beams on several polymers have been studied by Delcorte *et al.* and it was observed that characteristic fragment intensities in the fingerprint SIMS spectra showed a monotonic decay with increasing fluence.[55] Zekonyte *et al.* also studied the interactions of Ar<sup>+</sup> ion beams with PS films from low doses to higher doses of Ar<sup>+</sup> using XPS, and they observed degradation and rearrangement of the polymer chains on the surface.[20]

At low ion doses the interpretation of SIMS spectra is more reliable and easier. Assuming the surface structure is uniform, the primary collision events will be equivalent. At higher ion doses, the structural changes will occur as a result of damage accumulation and the primary collision events might not be equivalent. Time dependent changes will occur in the spectra: it will be more representative of a damaged surface.[37]

### **3.2.4. Substrate related parameters**

#### **3.2.4.1. Coverage**

For ion bombardment (or sputtering) of organic layers on metal surfaces, the total secondary ion yields of ejected molecules and desorption mechanisms strongly depend on the coverage



of the organic molecule.[56] At low coverage, kinetic energy and angular distributions of ejected particles resemble that of the metal, showing that collisions between the metal and adsorbed molecules lead to molecular desorption. At higher coverage, the chemical reactions between organic molecules initiated by the primary ion projectile in the collision cascade reduce the kinetic energy of emitted particles and the kinetic energy distributions of these particles shift toward lower values with a broadening in the angular distributions.

In case of metals and semiconductors, it is well known that atomic species are emitted as a result of collision cascades. In case of organics, it is not fully understood how the primary ion trajectory dissipates energy into the substrate and how molecules are desorbed and ejected. In order to shed light into desorption mechanisms, Chatterjee et al. studied desorption mechanisms of molecules from benzene adsorbed on Ag(111) from submonolayer to multilayer coverages of benzene. The velocity distributions of benzene desorbed as a result of 8 keV Ar<sup>+</sup> bombardment showed a strong dependence on coverage.[56] At very low coverages, the velocity distributions are narrow due to direct collisions between the metal and organic species. At higher coverages of benzene, a wider energy distribution is observed. The shift from low to higher energies is attributed to internal collisions between organic overlayers as a result of energy dissipation into various internal degrees of freedom.[56] This decreases the kinetic energy of the ejected particles. KED peak also shifts from 1.14 to 0.25 eV with increasing coverage. Surface binding energy also changes as the coverage

#### **3.2.4.2. Damage**

When bombarded with keV ions, the energy of the primary ion is transferred to the surrounding medium through collision cascades induced. The modification of the sample surface is not only due to secondary ion emission, but also various radiation effects like primary ion implantation, mixing of atoms, fragmentation and recombination of molecules. As a result, damage in the bombarded area cannot be avoided. The extent of damage by keV primary ions is estimated to be in the order of several nanometers in diameter. The damage cross-section can be defined as the average size of the surface that is modified by the area damaged or from where molecules are ejected by primary ion impact.

For molecular overlayers on metals, Bennighoven *et al.* introduced the concept of damage (or disappearance) cross-section ( $\sigma$ ).[57],[58] They investigated the emission of several parent-like secondary ions bombarding amino acid layers on silver with 2.25 keV Ar<sup>+</sup> primary ion

bombardment. They found different rates of degradation for different secondary ions and defined the damage cross-section,  $\sigma$ , using the following equation[58]:

$$N(t) = N(0)\exp(-\sigma vt) \quad (I-7)$$

where  $N(t)$  is the secondary ion intensity at the time  $t$ ,  $N(0)$  the initial intensity,  $\sigma$  the total cross-section and  $v$  the primary ion flux density. It is assumed that the precursor concentration decay exponentially and the damage rate is constant for the studied primary ion dose range.

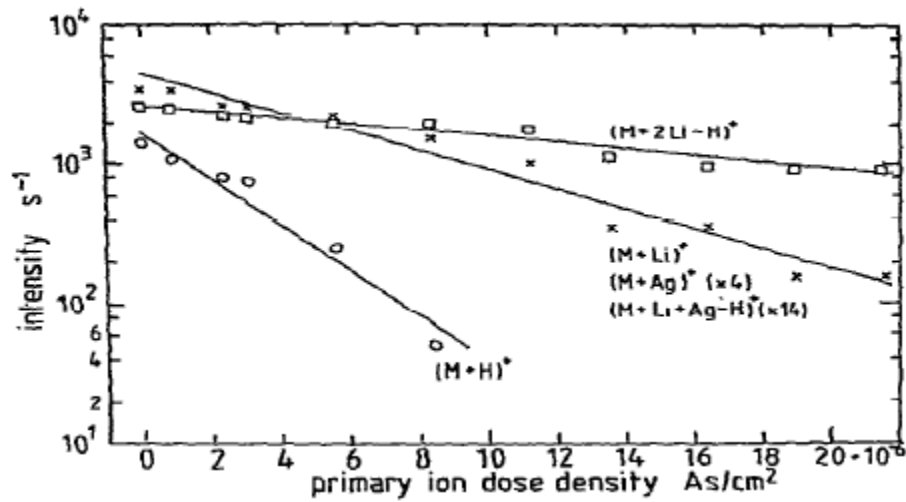


Fig. I-10: the rate of degradation of several parent-like ions of leucine-LiCl mixture on silver[59]

Using this equation and from the data in Fig. I-10, the damage cross-section,  $\sigma$ , may be determined. From complete sputtering on the bombarded area, Sichertmann *et al.* obtained the following equation[58] :

$$N = N(0) \frac{1}{\sigma v} \quad (I-8)$$

Similarly, taking derivative of the equation I-8[60], one can obtain the differential equation for the modification of intensity by time:

$$dN(t) = -\sigma v N(t) dt \quad (I-9)$$

Sichertmann and Benninghoven obtained a value in the range of  $10^{-14} \text{ cm}^2$  for damage cross-sections for various parent like ions of amino acid with 2.25 keV  $\text{Ar}^+$  bombardment.[58] Galera *et al.* found a value in the range  $10^{-13} \text{ cm}^2$  for bombardment of Langmuir-Blodgett (LB) monolayers on gold with 2 keV  $\text{Cs}^+$  ions.[10] Benninghoven reported typical damage

cross sections between  $10^{-13}$  and  $10^{-14}$  cm<sup>2</sup> for heavy particle bombardment of organic molecules.[61]

The extent of damage depends on the primary ion properties (mass, energy, angle of incidence) as well as on the substrate properties (thickness, density).

For bombardments of organic monolayers deposited on metals, the influence of energy, angle of incidence of primary ion, thickness and density of organic layer have been studied by Galera.[10] It has been shown by Benninghoven *et al.* that the damage cross section increases with increasing energy and mass of the primary ion similar to the behaviour of sputter yield, and so the ion emission.[61] Having observed a similar behaviour for the effect of primary ion energy, Galera *et al.* found that the damage cross section increases with increasing angle of incidence for all studied monomolecular films.[10]

The chemical environment has a strong influence on the secondary ion emission, hence on the damage cross section too.

It has also been shown that the disappearance cross-section is correlated with the energy lost in the monolayer rather than in the substrate.[10]

For analysis of bulk polymers (high molecular weight), the damage cross-section concept does not apply as their fragment ions are produced through more complicated processes. Being different to analysis of small molecules like amino acids, formation of fragment ions is involved in case of high molecular weight polymer sputtering. As there are other processes involved (breaking of bonds and rearrangement, etc), a disappearance cross-section cannot be mentioned since the intensity decrease will not be due to some small molecular ions disappearing, but rather modification of the surface as a result of different possible processes involved. In the last two decades experimental studies of organic SIMS utilize high molecular weight polymer in order to understand the mechanisms involved in their sputtering and analysis. There has been many studies to understand physico-chemical processes like bond-scissions, cross-linking, preferential sputtering, etc.[62],[25],[37],[63],[55]

Delcorte *et al.* developed a kinetic model which explains the behaviour of fragments of aliphatic polymers using the direct correlation between the surface degradation and molecular ion emission.[55] This model is based on the intra-cluster phenomenon suggesting that the decay in saturated fragments with higher hydrogen content gives rise to intensity increase of

less saturated fragments with lower hydrogen content. Fig. I-11 shows the decay of secondary ions of  $C_8$  cluster. It can be observed that the decay behaviour evolves from the most saturated to the least saturated fragment: the decrease in intensity of saturated fragments is compensated by an increase in intensity of less saturated fragments in the early stages of increasing ion dose. The degradation of polymers as a result of dehydrogenation phenomenon is explained with this kinetic model with following equations[55]:

$$I_i = \varepsilon_i C_i^* \quad (I-10)$$

Where  $I$  is the intensity of a given ion,  $C$  the surface concentration of its precursor,  $i$  the number of hydrogen atoms and  $\varepsilon$  the sensitivity factor related to physics of interaction and experimental conditions.

Including a decrease rate ( $\alpha$ ) and a probability factor ( $\gamma$ ), the differential equations for the precursor concentration is obtained by[55]:

$$dC_i^* = -\alpha_i C_i^* + \alpha_{i-1} \gamma_{i-1} C_{i-1}^* + \alpha_{i-2} \gamma_{i-2} C_{i-2}^* + \dots \quad (I-11)$$

then combining equations I-10 and I-11, one obtains:

$$dI_i^* = -\alpha_i I_i + \alpha_{i-1} \gamma_{i-1} (\varepsilon_i / \varepsilon_{i-1}) I_{i-1} \quad (I-12)$$

When equation I-12 is applied to the dehydrogenation of  $C_8$  cluster, the following equation is obtained:

$$dI(C_8H_y) = -\alpha_i I(C_8H_y) + \alpha_{i-1} \beta_{i-1} I(C_8H_{y+2}) \quad (I-13)$$

where

$$\beta_i = \gamma_i \varepsilon_{i+1} / \varepsilon_i \quad (I-14)$$

Finally  $\alpha_i$  and  $\beta_i$  values are obtained giving the best fit between the suggested kinetic model and experiments and they found that the model describes correctly the experiments.[55]

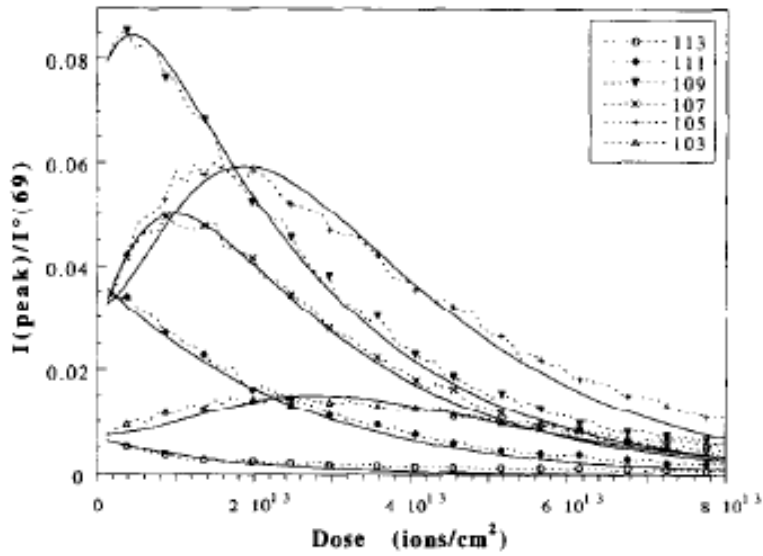


Fig. I-11: Variation of normalized intensities of  $C_8$  cluster ( $C_8H_y^+$ ) with increasing in dose [55]

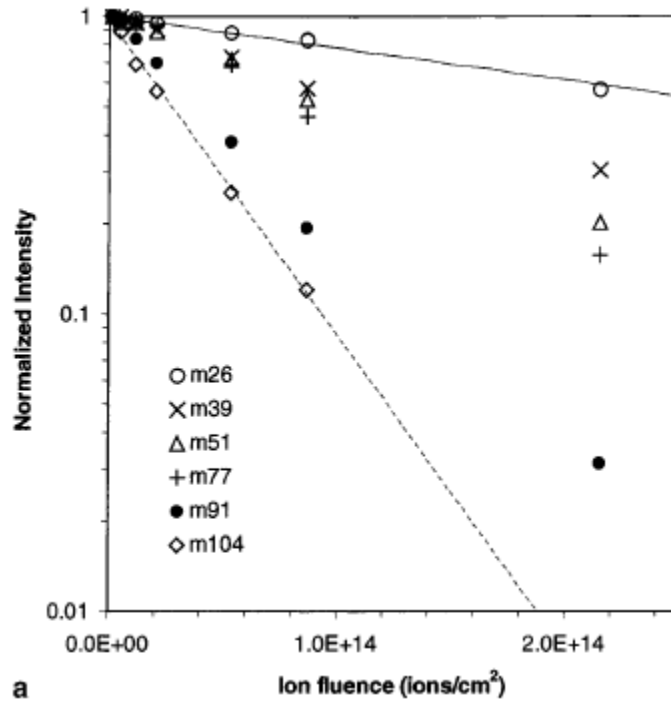


Fig. I-12: Dependence of PS fragment peak intensities on the cumulated ion dose[64]

The rate of decay of several PS fragments is given in Fig. I-12. The decay rate is higher for large fragments ( $C_8H_8^+$ ) which mirror the polymer structure than for small fragments ( $C_2H_2^+$ ). However, the production of these fragments by degradation is assumed to be small since all of these curves can be fit by a single exponential function.[64]

Fig. I-13 shows huge variation in disappearance cross-sections of same fragments of polymer, with a higher cross-section for larger fragments. Both the mass of the fragments and the

amount of hydrogen content might be responsible for the variation in cross-sections.[64] The interpretation of disappearance cross-section for bombardments of polymers with keV ions is not straightforward since it is affected by sputter yields and rate of damage formation of different fragments and the pathways leading to these various fragments are mainly affected by physico-chemical effects like bond-breaking, crosslinking, reorganization, etc. In case of MeV ion bombardment, the damage cross sections are larger than the fragment size which makes the ejection of intact molecules possible. In case of cluster ion bombardment of polymers, the interpretation of damage cross-section is similar: the damage-cross sections are larger than all possible fragments ejected from the surface, so the intact molecules can be observed in the mass spectra.

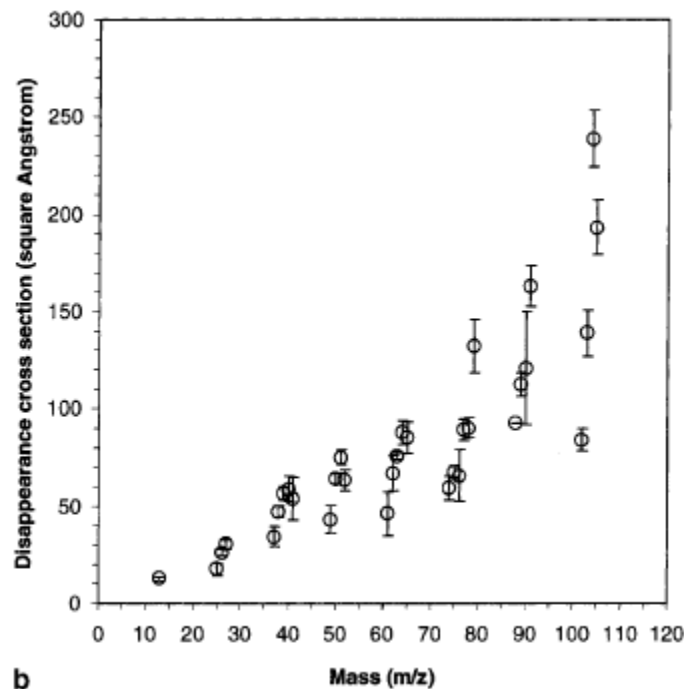


Fig. I-13: Dependence of PS fragment peak intensities on disappearing cross sections obtained from MD simulations[64]

Delcorte *et al.* combined experimental degradation studies with MD simulations in order to have a better understanding of the processes occurring during keV bombardment of polymers.[64] Their MD simulations showed that the disappearance cross-sections and ejection radii are correlated. Moreover, since it was already shown that the kinetic energy distributions is a representation of energy transfer induced by ion-beam at the surface of impact[44] and MD results suggest that the emission mechanisms are directly related to local energy density at the surface[64], the deposited energy profile at the surface can be estimated

by the correlation between the kinetic energies and disappearing (damage) cross-sections of the fragments.

It has been suggested that the intensity of degradation products increase with primary ion dose.[65],[66]. The intensity of fragments which are characteristic of the precursor makes a maximum and then decreases gradually. [25]

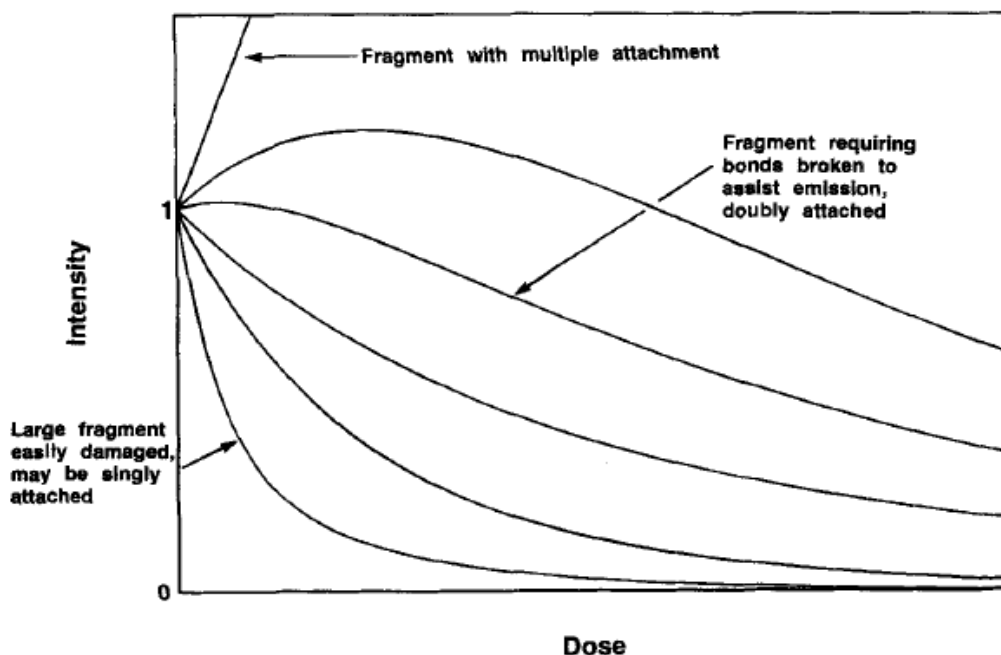


Fig. I- 14: Behaviour of different fragments with ion dose according to bond breaking model[65]

The damage on the impact zone has been described by a bond-breaking model by Gilmore *et al.*[65] The model takes into account the number of bonds to be broken for the ejection of a molecule or fragment, the number of internal bonds in the molecule or fragment and the damage zone. Fig. I- 14 summarizes how the number of these bonds affects the decay rate of the intensity of different fragments with different number of covalent and internal bonds. If the fragment contains more and more bonds to be disrupted, the sum of damage cross-sections will increase and more of these fragments will be released leading to an initial increase in their intensity with increasing ion dose.

This model does not apply to adsorbed overlayers on metals since the molecules are of the monolayer thickness and they are not as strongly bonded to the metal.

### **3.3. MD Simulations for understanding fundamental aspects of static SIMS**

#### **3.3.1. An introduction to simulations of sputtering**

In order to better explain the sputtering events, the experimental studies have been supported by computer simulations, which are mainly based on classic mechanics. Binary collision approximation (BCA) and molecular dynamics (MD) are the main approaches. In the BCA approach, the sputtering is simulated by sequential independent binary collisions between atoms and in MD approach, by multiple interactions as a function of time.

The binary collisions can be calculated by computer programs. However, it would require strong mathematical effort. Thus, in the BCA the trajectories are approximated by their asymptotes between collisions until the energies of incident projectiles and recoils fall below a threshold. The computer programs based on BCA can be categorized into Monte Carlo (MC) and lattice codes with respect to the structure of the solid sputtered (crystalline, polycrystalline or amorphous). MARLOWE[67] is a well-known lattice code which describes sputtering of a crystalline target where only the first impact position on the solid needs to be chosen after which the cascade is completely determined. However, in case of MC programs (TRIM, TRIM.SP)[68], where the target is amorphous, every collision is chosen randomly.

In the BCA based programs (Monte Carlo and lattice codes), the binary collisions are approximated by elastic collisions of atoms using an appropriate interaction potential, which are generally screened Coulomb potentials represented as a sum of exponentials. The potentials are repulsive and are a function of internuclear distance. Inelastic collisions become more significant at higher energies and the electronic energy loss due to inelastic collisions can be incorporated in the program using some theoretical models. This kind of energy loss reduces the energy of the atom, but does not change its direction.

The two weak points of the BCA are the assumption that there is a binary collision between the moving atom and the atom at rest and the concept of asymptotic trajectories. The advantage is that the backscattering, transmission and radiation damage can be determined including sputter yields, reflection coefficients, energy and angle of incidence as well as energy and angular distributions of sputtered atoms without major computational effort.

From the MD simulations, it is possible to obtain positions and velocities of atoms as a function of time. Then, one can obtain information about their energy and angular



distributions, ejection mechanisms and visualize development of atomic positions and important atomic or molecular motions.

In MD approach, sputtering is theoretically explained by classical equations since the effect of quantum mechanical phenomena appears to be insignificant, or computationally too expensive to be taken into account. For solving Newton's equations of motion, interatomic forces between the moving atoms and target atoms and between the target atoms themselves need to be defined. This requires appropriate force field or interaction potentials among the atoms and interatomic potentials to be developed. The best solution to calculate these potentials would be to use quantum chemistry or density functional theory at each time step of the MD simulations, so that interatomic potentials far from equilibrium could be incorporated.[69] However, it would be too complex and computationally costly to do this for large-scale system, therefore instead the interatomic potentials have been approximated.

Molecular dynamics (MD) simulations have been used not only for explaining sputtering events, but also in the fields of thin film growth, ion-implantation, atom scattering, physics of liquids, structure and dynamics of biological molecules, and the motion of galaxies and sand dunes. One of the first applications of MD simulations was by Gibson et al to study the damage by sputtering a Cu target.[70] Following this, Harrison worked more detailed on simulations of sputtering, on which the current ideas and concepts of MD simulations are based on.[71]

### **3.3.2. Potentials used for MD Simulations**

Applied to sputtering of inorganic or organic surfaces, the MD approach is used in order to simulate trajectories of atoms or molecules leaving a surface as a result of bombardment of the surface with energetic particles. For this, the classical equations of motion are integrated for all the particles in the solid. Although MD simulations have been successfully applied to the study of sputtering of atomic solids[72],[73],[74],[75], however its application on sputtering of organic molecules is limited. The lack of many-body interaction potentials for hydrocarbon systems has been the main problem. However, recently there has been a significant advance in development of many body potentials for describing extended systems.[76]

There have been several attempts to include many body interactions in MD simulations using empirical potentials, which would describe the effect of nearby atoms on the interaction of a

pair of atoms. One of the earliest potentials was developed by Stillinger and Weber and Tersoff for describing silicon.[77],[78] The potentials for silicon were further improved to include potentials for SiF.[77],[79]

For the treatment molecular systems, hydrocarbon potentials have been developed. One potential of interest for the SIMS community was developed by Brenner *et al.* for solid carbon and hydrocarbon molecules based on empirical bond order formalism, which allows simulating bond breaking and bond formation[80],[81] This has been possible through incorporating coordination number, bond angles and conjugation effects to account for bond strength.

This potential was initially developed to model diamond film growth, but the potential has been used for systems where reactions occur.[82]

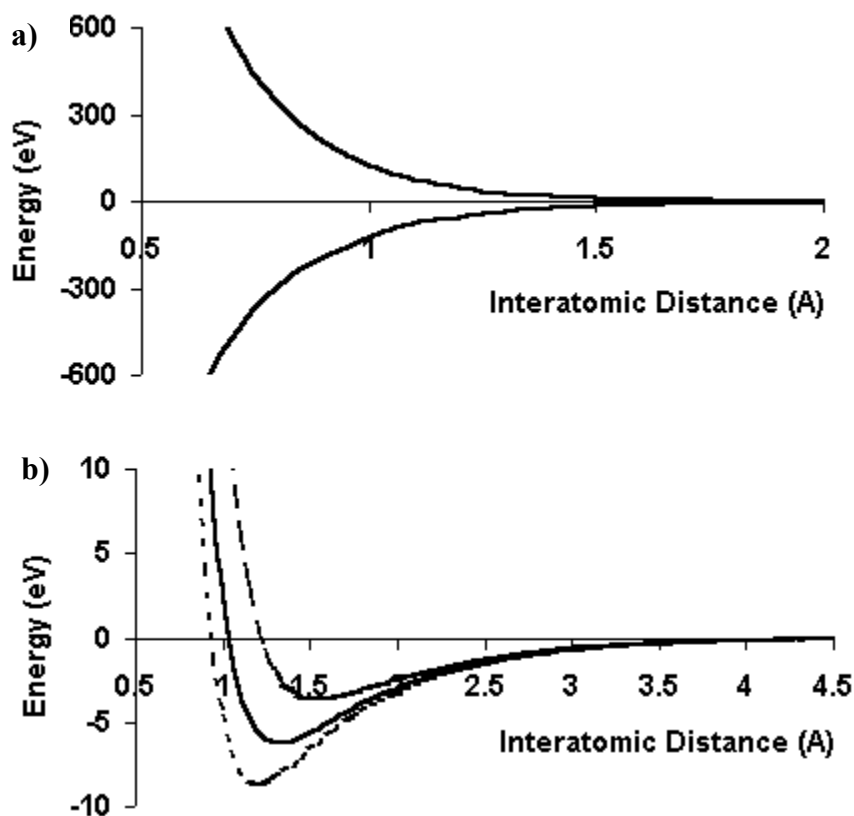


Fig. I-15: Plots for pair potentials using parameters for potential energy expression for hydrocarbons a) the attractive and repulsive pair terms as a function of interatomic distance b) curves corresponding to molecular triple bonds (dotted curve), double bonds (solid curve), and single bonds (dashed curve) [80]

Fig. I-15 shows attractive and repulsive curves as a function of interatomic distances and their corresponding triple, double and single bond curves. The latter curves were obtained by

multiplying the attractive pair term by the appropriate value of the bond order and adding it to the repulsive pair term; [81]

A long range interaction term was incorporated to the Brenner potential by Stuart *et al.* to include interactions between non-bonded species, the AIREBO potential.[83]

### 3.3.3. MD simulations applied to SIMS of organics

MD approach has contributed to fundamental understanding of both sputtering of atomic solids, and more recently of the molecular solids. Molecular solids include both bulk samples and organic overlayers on metallic substrates.

MD results provide useful information about the bombardment process like intact molecular ejection, fragmentation or reactions between the ejected species. Visualizing emission processes by MD simulations and comparing it to experimental results [83],[84],[85],[86],[87], Garrison *et al.* verifies different emission mechanisms for systems where molecules have multiple contacts to the substrate and where they are adsorbed upright to the substrate.[88] For systems with multiple contacts the energy in the substrate is directed upwards resulting in cooperative uplifting of the intact molecules. (Fig. I-16) However, if fragmentation occurs, or not, depends on the collision energy between the substrate atoms and the organic molecule. In case of violent collisions, the momentum is rather directed into the solid, causing fragmentation of the intact molecules. Using MD simulations Garrison *et al.* showed that polyatomic projectiles increase the probability of upward movements of several substrate atoms and their contribution to cooperative uplifting of a molecule from the surface.[87],[89] For the systems with upright chains, the ejection mechanism is affected by the impact location of the incoming particle. If the incoming particle strikes between the bottom atoms of the adsorbate and substrate atoms, intact ejection occurs.[84],[90] If it strikes between the middle of the adsorbate and the substrate atom, in case of small binding energy, intact molecular ejection[91], and in case of large binding energy, fragmentation is observed.

Bombardment of molecular solids with energetic particles induces fragmentation and chemical reactions on the surface. Although it is not possible to predict reaction pathways using classical dynamics, one can gain insights into reactions that might occur. Hydrogen

abstraction reaction [92],[88] or unimolecular reactions that happen in subpicosecond[90] and microsecond time scales are some examples where MD simulations support experiments.

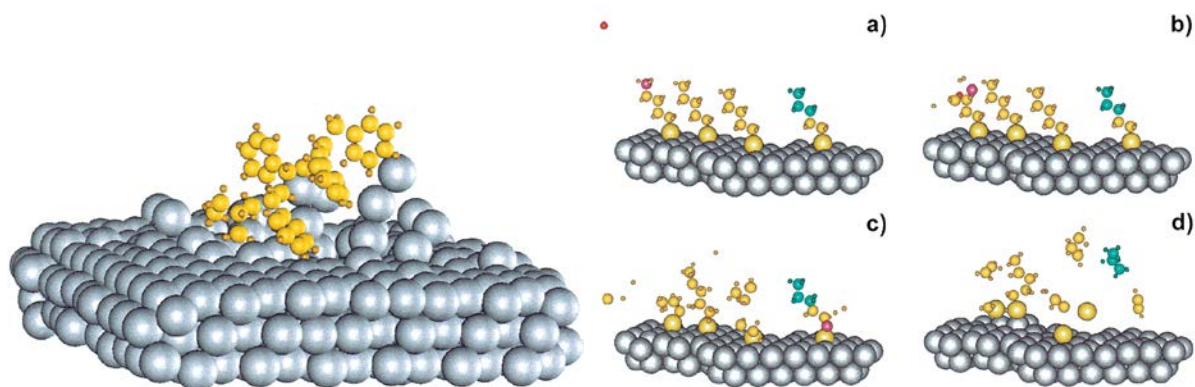


Fig. I-16 : MD simulation visualizations for cooperative uplifting mechanism for a polymer tetramer on Ag and ejection of upright chains [88]

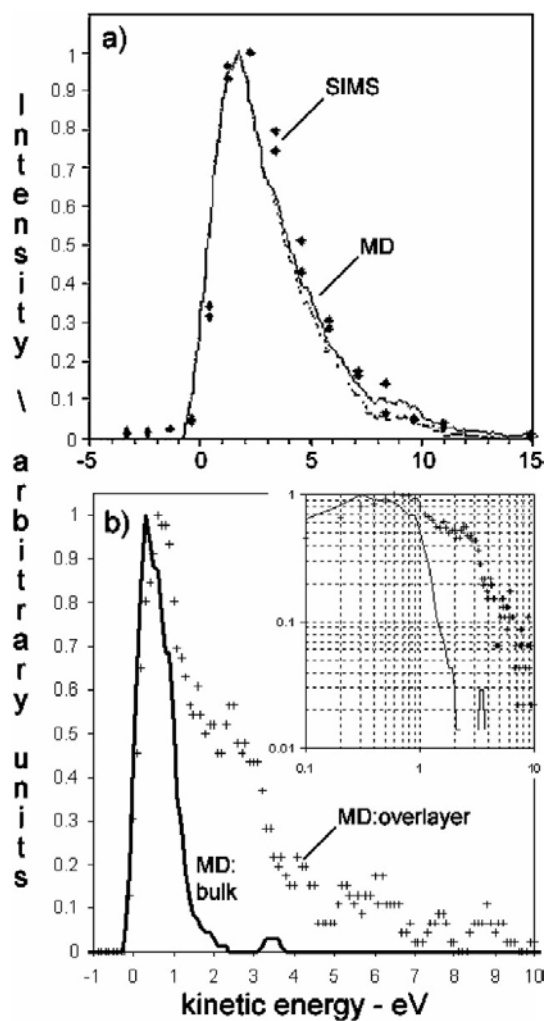


Fig. I-17: KEDs of PS tetramers on Ag measured experimentally (12 keV  $\text{Ga}^+$  bombardment) and calculated by MD simulations (500 eV Ar bombardment) compared to KEDs of a) bulk PS tetramer calculated by b) MD simulations.[93]

MD simulation calculations have also been useful in gaining insights into substrate and matrix effects in case of desorption of large organic molecules. The energy transfer processes, dynamics of the collision cascade, ejection and ionization mechanisms are affected by the environment of the organic molecule and its binding energy with the surroundings. Thus, there have been studies on both the bombardment of bulk organic molecules and organic overlayers of different coverage on metal surfaces. Fig. I-17 shows how MD simulations compare to experimental results for bombardment of organic overlayers on metal and also how MD simulations results differ for calculation of KEDs of molecules ejected from bulk matter and organic matter adsorbed on metal. Calculated KEDs resemble to experimental ones and the narrow distribution of KED for bulk organic molecules is in agreement with soft emission processes described by vibrationally-induced desorption. As the thickness of the organic layer on the metal decreases, the KEDs of ejected matter becomes wider, getting closer to that of obtained from an atomic solid. The increase in the width of KEDs going from bombardment of organic multilayers to monolayer has been observed experimentally.[94]

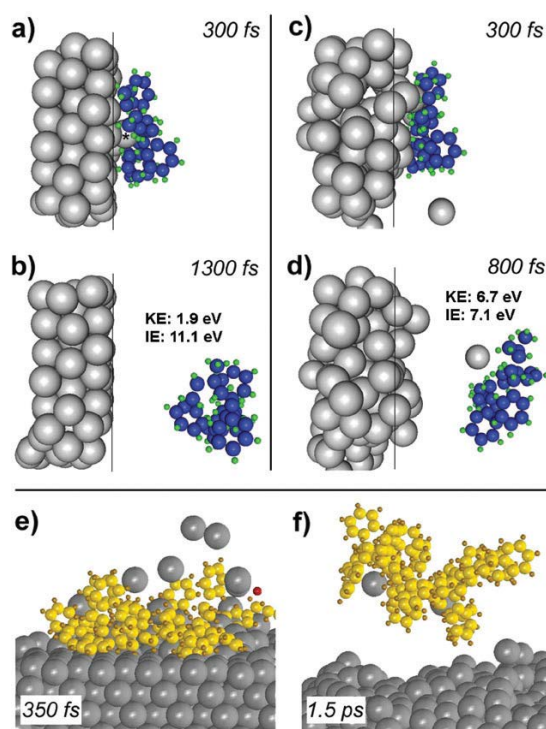


Fig. I-18: for 500 eV Ar bombardment (a-b) single atom-induced desorption of PS tetramer (c-d) cooperative uplifting of PS tetramer and for 5 keV Ar bombardment (e-f) cooperative uplifting of PS hexadecamer [93]

The effect of the substrate on the ejection mechanisms of large organic molecules is further demonstrated in Fig. I-18, where silver atoms facilitate intact emission by a single upward

movement of silver recoil atom (Fig. I-18 a-b), by a collective upward movement of several silver atoms (Fig. I-18 c-d) in case of 500 eV Ar bombardment and in case of 5 keV Ar bombardment.

Restrepo *et al.* used MD simulations in order to understand mechanisms underlying the organic secondary ion yield enhancement in case of MetA-SIMS, where the organic layer is covered with a metallic overlayer.[94] They explained some of the related physical mechanisms in case of bombardment of such prepared samples with mono and poly-atomic projectiles: In case of monoatomic projectiles, energetic recoils of the metallic overlayer, transfer their energy to the underlying organic molecules creating an extended collision cascade increasing the sputtering yield, whereas for polyatomic projectiles the energy of the incoming atoms is used to break the bonds between metallic overlayer and organic molecule, reducing the energy to break covalent bonds in the organic surface and thus reducing the mass of ejected organic molecule.

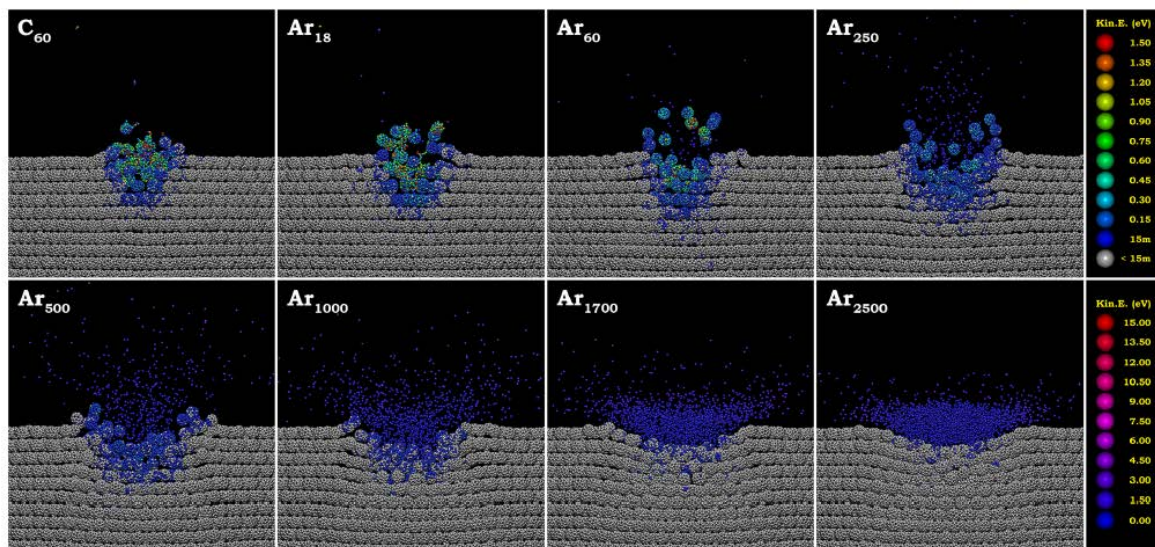


Fig. I-19: Side cross-sectional view of C<sub>60</sub> and Ar cluster bombardment of fullerite sample with indicated kinetic energy scale[95]

Recently Czerwinski *et al.* used MD simulations to elucidate the bond-breaking and crosslinking processes for bombardment of fullerite solid samples by 0.6-50 keV C<sub>60</sub> and Ar<sub>n</sub> clusters.[95] Fig. I-19 shows the views of bombarded samples 3ps after the impact. It is observed that craters formed by C<sub>60</sub> and Ar bombardment have a similar size which indicates that the physics of sputtering process are similar. However, with increasing Ar cluster size, the depth of the crater decrease whereas its lateral size increases, which is explained by the

decrease of kinetic energy per atom resulting from either the increase of the number of atoms or the increase of its lateral size. The difference in bombardment by  $C_{60}$  or Ar clusters is mainly due to chemical effect of the projectile rather than physical.  $C_{60}$  projectile provides highly reactive radicals increasing the efficiency of the cross-linking process, whereas Ar clusters result in a decrease in the number of broken bonds, thus in a decrease in the formation of new intra and intermolecular bonds. [96]

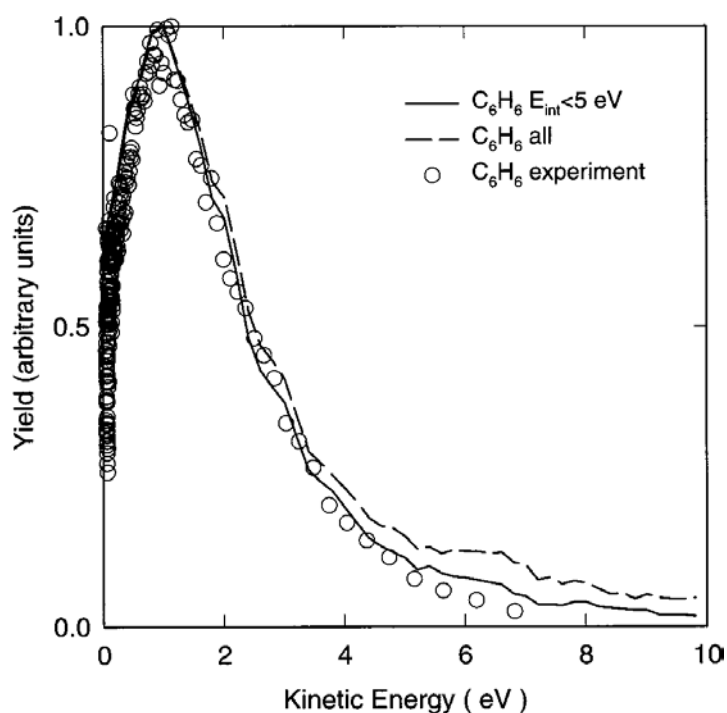


Fig. I-20: Experimental and calculated kinetic energy distributions of  $C_6H_6$  molecules ejected from Ag.[85]

Chatterjee *et al.* studied the energy distributions of molecules ejected from 500 eV Ar bombardment of benzene adsorbed on silver (Ag) both by means of experiments and MD simulations. [85] Fig. I-20 shows there is a good correlation between the results from experiments and simulations, especially for energies smaller than 4 eV. Fig. I- 21 helps to explain the deviation from experimental values in case of higher energies. It can be seen that the kinetic energies of the ejected species increase with their increasing internal energies. The hydrocarbon potentials used for benzene molecule does not take the long-range intermolecular interactions into account, and these interactions become more significant at higher kinetic energies as dissociation and fragmentation of benzene molecules become more pronounced, thus more difficult to explain by simulations.

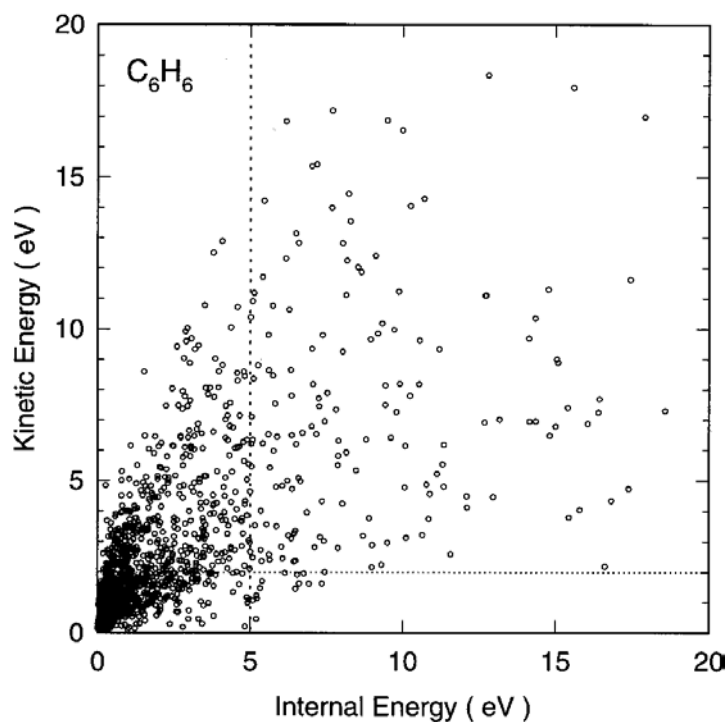


Fig. I- 21: Scatter plot of correlation of kinetic energies of C<sub>6</sub>H<sub>6</sub> molecules ejected from silver with their internal energies.[85]

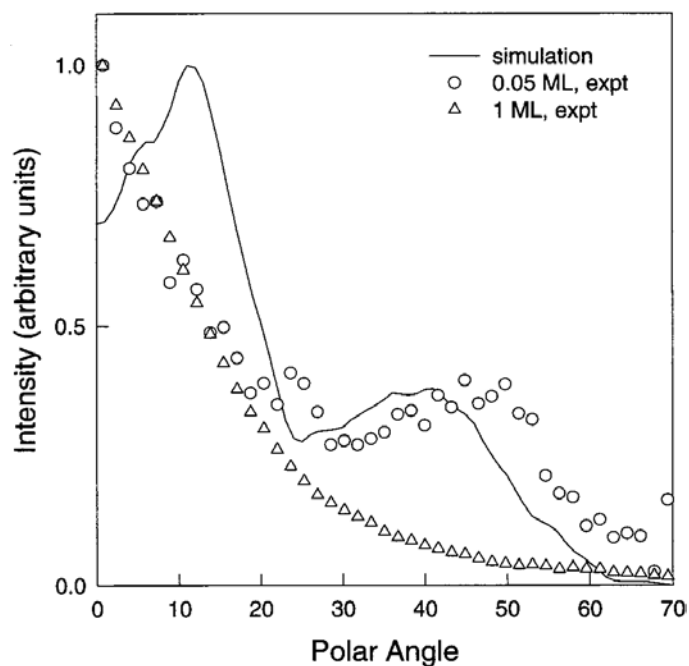


Fig. I- 22: The angular distributions of benzene molecule obtained from simulations and experiments at different coverages. [85]

For the reason that hydrocarbon potentials do not incorporate long-range intermolecular interactions, which helps to explain collisions between benzene molecules, the simulation results should be compared to the experimental results obtained at very low coverage of the benzene on the silver substrate. At lower coverage, the interactions between the benzene



molecules become less significant. It was shown by Chatterjee *et al.* that below 0.2 ML coverage, the distance between the benzene molecules are too large for them to interact. [56]

Angular distributions measured experimentally and calculated by MD simulations are shown in Fig. I- 22. MD simulations reproduce the experimental observations only at low coverage. Both experiment and simulations show a strong off-normal peak at  $40^\circ$ , which is attributed to particles with high energies. Off normal ejection at  $40^\circ$  shows that ejected benzene molecules represent the direction of ejection of the substrate atoms.[97],[98] At high coverages this anisotropic behaviour of the angular distribution is not observed, which is known to be characteristic for ordered metal surfaces. There is a slight discrepancy between experiments and simulations for lower emission angle: the experimental distribution makes a peak normal to the surface, whereas the calculated at  $10^\circ$ .

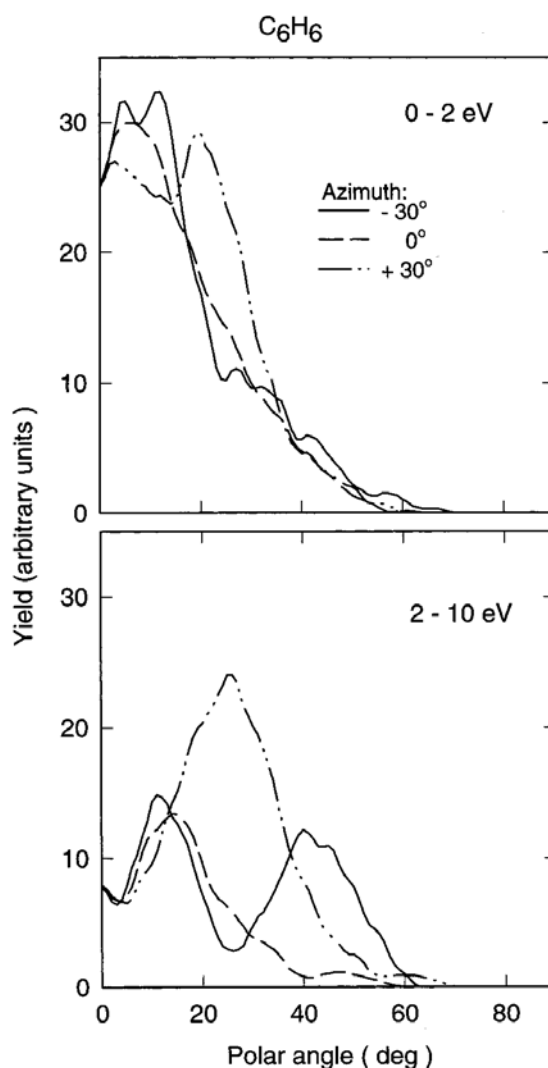


Fig. I-23: The calculated energy resolved angular distributions of benzene molecules below and above 2 eV[98]

Fig. I-23 shows energy resolved angular distributions of benzene molecule for three different azimuthal angles. For an azimuthal angle of  $-30^\circ$ , it is clear that the normal peak ( $10^\circ$ ) is due to the particles with low energies (0-2 eV) and the off-normal peak ( $40^\circ$ ) with higher energies (2-10 eV).

By using MD approach, it has been possible to deduce molecular ejection mechanisms from observed microscopic processes. Chatterjee defines three different mechanisms[85] for  $C_6H_6$  molecular ejection interpreted from their energy resolved angular distributions calculated by MD simulations: first, off-normal ejection at  $-30^\circ$  azimuth due to single collision from an adjacent substrate atom located at the side of the molecule, second off-normal ejection at  $+30^\circ$  azimuth due to single collision from an adjacent substrate atom located right below the molecule and third normal ejection along all azimuths due to multiple collisions from first-layer substrate atoms located below the benzene molecule.

### 3.4. ToF-SIMS analysis of PS and PMMA

#### 3.4.1. Characterization and degradation studies of PS and PMMA`

Damage and degradation rates of polymers during SIMS analysis is an important aspect of ToF-SIMS. In the early studies it has been emphasized that a certain total dose should not be exceeded.[25] The damage threshold for organic materials is usually taken as  $10^{13}$  ions/cm<sup>2</sup> [96] and for obtaining both positive and negative ion spectra an upper dose limit of  $5 \times 10^{12}$  ions/cm<sup>2</sup> is recommended.[66]

Polystyrene (PS) and Poly(methylmethacrylate) (PMMA) are the main polymers used during this PhD work. So, it is important to have a fundamental understanding of their behaviour with ion beam treatments. Theoretical and other spectrometric methods have been employed before using SIMS for ion beam treatments of polymers. Davenas et al. used the evolution of partial pressure as a function of ion fluence and used it as a measure to describe particle-matter interaction for the case of ion bombardment of polymers. The kinetics of gas evolution has been described by an exponentially decreasing law[98]:

$$\frac{dNH_2}{dt} = \frac{\delta j}{2e} nH \exp\left(-\frac{\delta j}{e} t\right) \quad (I-15)$$

Where  $\sigma$  is the radiation damage cross section. The small value of this cross section around  $10^{-15}$  cm<sup>2</sup> means that degradation of the polymer is nearly complete for a fluence of about

$10^{15}$  ions/cm<sup>2</sup>. [99] The optical adsorption studies agree with same order of magnitude at which polymers completely degrade. [98] A faster degradation rate was obtained for PMMA compared to other polymers like Polyethylene (PE), polystyrene, polyimide (PI) and polyphenylquinoxaline (PPQ). [99]

The main difference between PS and PMMA lie in their structure: PS is a polymer with a linear saturated chain with an aromatic pendant group and PMMA with a nonaromatic pendant group. [100] In a work of Davenas *et al.* Rutherford Backscattering Spectroscopy of some polymer surfaces showed differences for PS and PMMA. [99] At higher fluences, PMMA releases 80% of its oxygen content, and the carbon content decreases by a factor of 2, whereas PS shows only a small variation of its carbon content and oxidation is revealed by an appearance of oxygen peak. From their studies they concluded that PMMA dissociates easily under ion irradiation and PS tends to reticulate. PS is modified under radiation through oxidation and loss of hydrogen forming double bonds between carbon atoms (C=C) which results in reticulation of the polymer under irradiation by radical formation. It is probable that as a result of reticulation PS the formation of volatile recombination products with carbon is inhibited as shown by the small evolution in the RBS spectra.

SIMS analysis has been used together with X-Ray Photoelectron Spectroscopy (XPS) to monitor the damage on polymers. XPS results showed that PS loses its aromatic features as a result after an ion dose of  $10^{14}$  ions/cm<sup>2</sup> with 5 keV Ar<sup>+</sup> bombardment reflected in the  $\pi$ - $\pi^*$  shake-up satellite (Fig. I- 24). [101] In their study, Briggs and Wootten found similar effects after an ion dose of  $1.6 \times 10^{14}$  ions/cm<sup>2</sup> with 4 keV Ar<sup>+</sup>. [62] In a study for PMMA degradation by XPS, the carbonyl functionality was found to be sputtered preferentially at an ion dose of  $10^{16}$  ions/cm<sup>2</sup> with 2 keV Ar<sup>+</sup>. [102] For the same polymer, using SIMS analysis, Briggs suggested that beam damage effects were observed at an ion dose of  $10^{14}$  ions/cm<sup>2</sup> with Ne<sup>+</sup> bombardment [62] which suggests for detecting beam damage SIMS is more sensitive than XPS with a lower threshold. In a later, but more detailed study they found PMMA degrades at  $1-2 \times 10^{13}$  ions/cm<sup>2</sup> with 4 keV Xe<sup>+</sup> bombardment. [25] For PS, they found a lower value ( $1-5 \times 10^{13}$  ions/cm<sup>2</sup> with 4 keV Ar<sup>+</sup>) of ion dose at which the damage starts. [62]

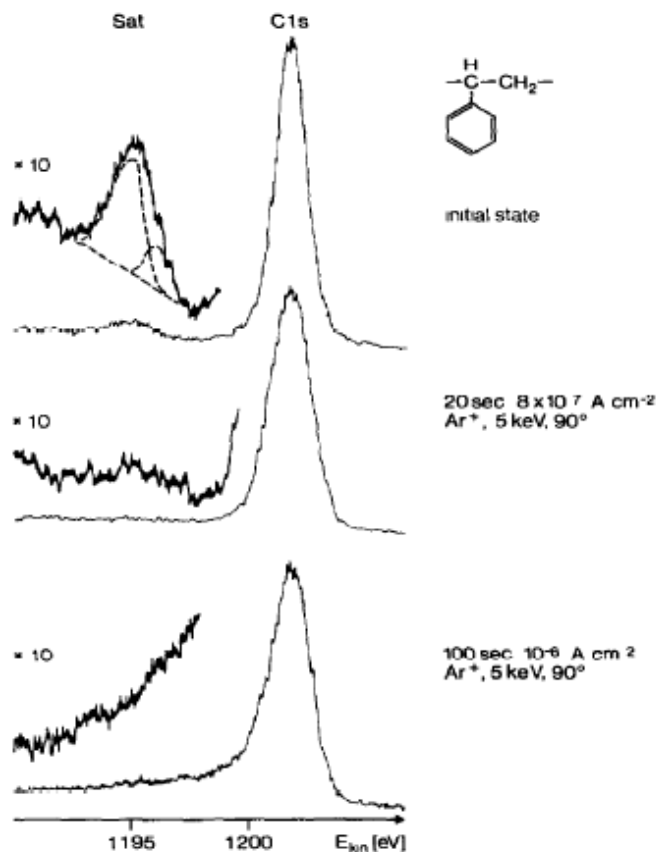


Fig. I- 24: Ion induced decomposition of polystyrene with 5 keV  $\text{Ar}^+$  [101]

The damage effects and fragmentation mechanism as a result of ion beam bombardment depend on the structure of the polymer. Ooij *et al.* studied some SIMS of aliphatic hydrocarbon polymers like Polyethylene (PE) and Polypropylene (PP) and their SIMS spectra in terms of molecular structure and fragmentation mechanisms, and they concluded branching and unsaturation effects.[103] Branching effects were observed through an increase in the  $\text{C}_8/\text{C}_2$  cluster ratio, an increase in  $\text{C}_3/\text{C}_2$  and  $\text{C}_4/\text{C}_2$  ratios due to short-range fragmentation effects of the pendant groups, whereas the decrease in the hydrogen content of  $\text{C}_2$  and  $\text{C}_5$  clusters compared to spectra of saturated polymers, the domination of the spectra with aromatic fragments unlike domination with aliphatic fragments in case of saturated polymers and the higher yields of  $\text{H}^+$  than for saturated polymers are the indications for unsaturation effects.[103]

The degradation of PP and variation of  $\text{C}_8$  cluster ion intensities with ion dose are described by Delcorte *et al.*[55] The curves follow such a trend that the degradation is greater for saturated fragments than the unsaturated ones and the degradation alternates from the most

saturated ion ( $C_8H_{17}^+$   $m/z=133$ ) to the least saturated one ( $C_8H_7^+$ ). This clearly shows the effect of dehydrogenation, as already mentioned in the section “fragmentation”.

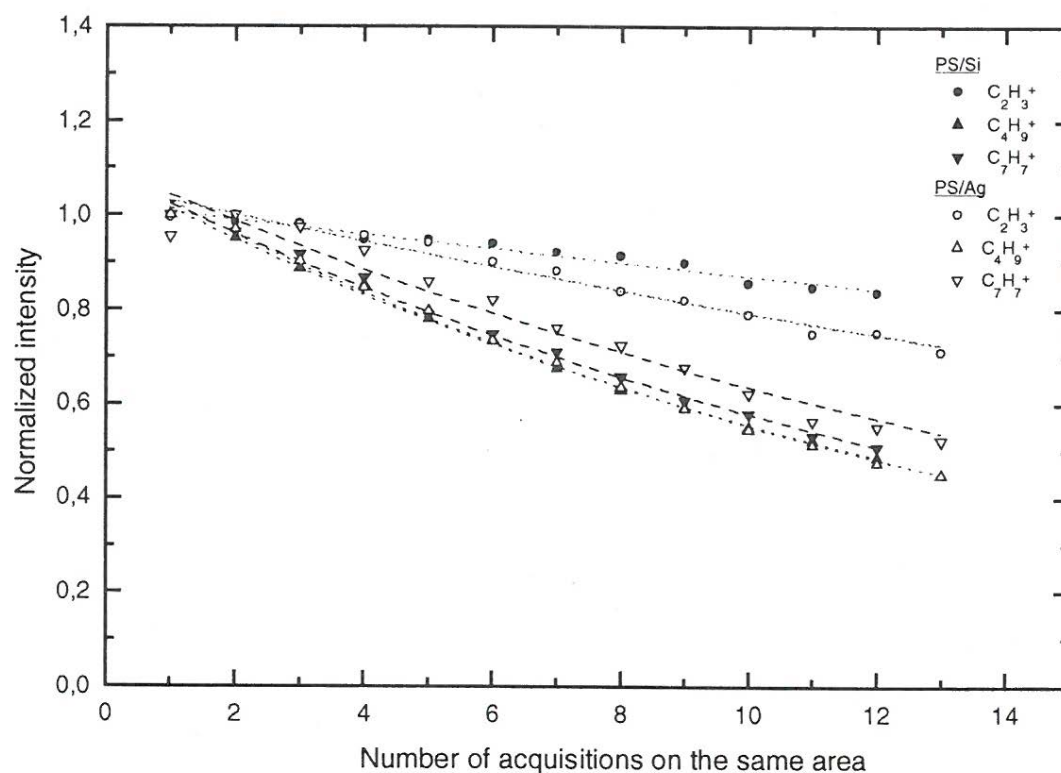


Fig. I-25: Degradation of several characteristic ions sputtered from PS spin-coated on Si and Ag.[38]

Degradation of various PS fragments with increasing primary ion fluence show different behaviour.  $C_4H_9^+$  ( $m/z=57$ , characteristic of the t-butyl endgroup), and  $C_7H_7^+$  ( $m/z=91$ , characteristic of the benzyl end group) are very sensitive to fluence, so surface degradation. The less characteristic  $C_2H_3^+$  fragments is less sensitive to surface damage, which suggests that this fragment could be formed as a result of degradation, whereas others originate from the unfragmented PS chains. The intensity of the latter decreases faster with fluence as a result of the damage created on the polymer film (Fig. I-25).

Leggett and Vickerman studied the effects of damage during SIMS analysis of PMMA and they observed a decrease in secondary ion intensities of all characteristic fragments with increasing primary ion dose due to damage being accumulated on the surface. Fig. I- 26 shows the change of intensity of most characteristic fragments ( $C_3H_5^+$  at  $m/z=41$ ,  $C_7H_7^+$  at  $m/z=91$ ,  $C_8H_9^+$  at  $m/z=105$ ,  $C_{10}H_{13}^+$  at  $m/z=133$ ,  $C_{10}H_8^+$  at  $m/z=128$ ) with time, so with increasing ion dose. First, the intensities of characteristic fragments increase, then they

decrease, followed by a sharper decrease for the most characteristic ions. In case of bombardment with atoms, they found much lower decay of intensities.

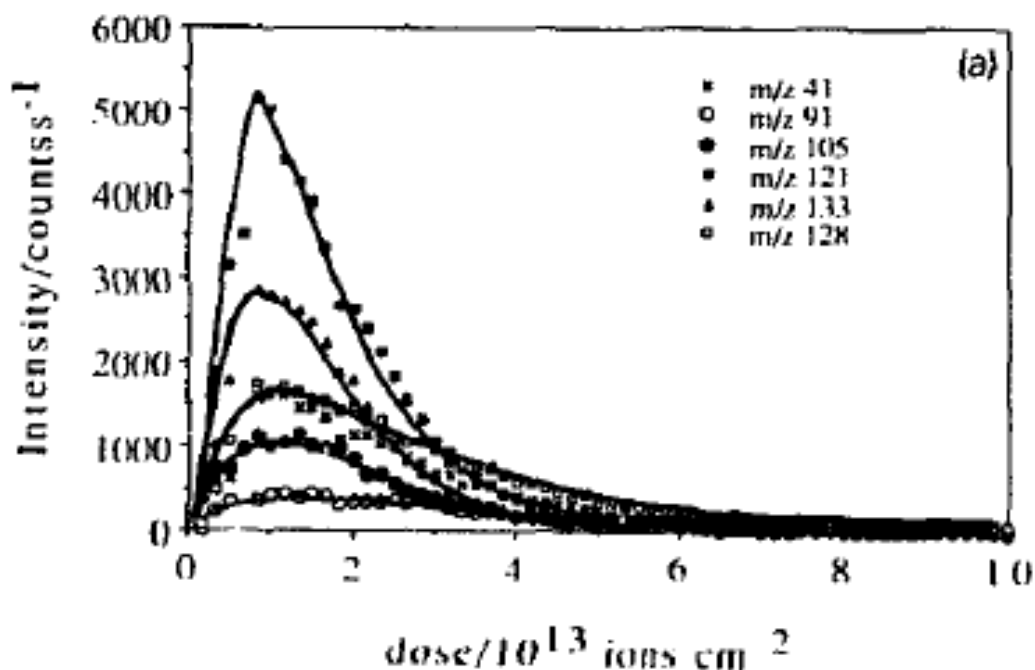


Fig. I- 26: Time dependent variation of intensities of characteristic ions of PMMA bombarded with 2 keV Ar ions.[63]

When PMMA was analysed at low doses, Briggs interpreted the spectra like in free-radical processes of polymers happening during thermal and radiation degradation of polymers. However, at higher ion doses, the spectra was much different as a result of primary ion damage, which was represented through formation of aromatic ions. [25]

Regarding the variation of some of the characteristic peaks with increasing ion doses, Briggs and Hearn define four different curve behaviour[25] (Fig. I- 27):

1. For  $m/z=185$  fragment, a small increase in intensity followed by a rapid decline which is characteristic of major fragments of PMMA.
2. For  $m/z=41$  a small intensity increase followed by a steady decline, characteristic of smaller fragments of the repeat unit
3. For  $m/z=133$  a significant increase followed by a steady decline attributed to backbone fragments
4. For  $m/z=91$  a major but slow increase followed by a slow decline which was attributed to cyclic tropylium ion  $C_7H_7^+$ .

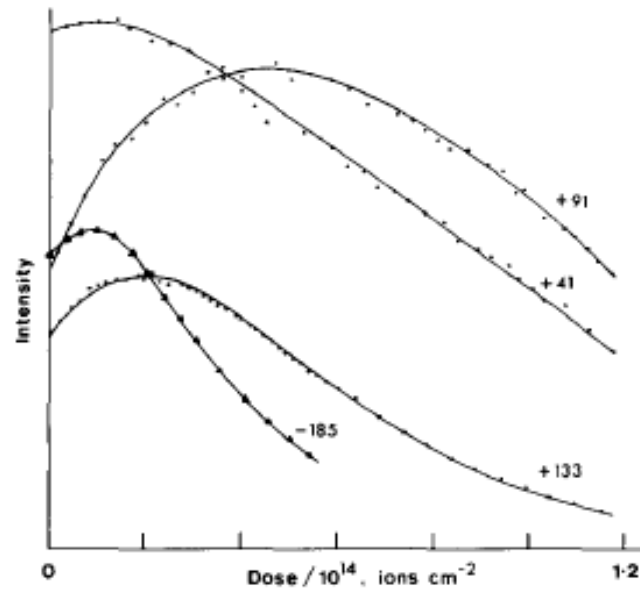


Fig. I- 27: Variation of intensities of characteristic PMMA fragments observed in the negative and positive SIMS spectra[25]

The statistical bond breaking model developed by Gilmore and Seah [65] explains the damage behaviour for polyethylene terephthalate (PET) and polytetrafluoroethylene (PTFE), however Briggs and Fletcher have argued that the model does not apply to PMMA, except for the fragment at  $m/z=185$ . [66] Their experimental data is inconsistent with the model. Following their experimental data (Fig. I- 28), they suggest[66]:

1. For formation of fragment at  $m/z=59$  can be formed by side chain scission which requires only one C-C bond to be broken, but it shows an initial increase.
2. Formation of fragment at  $m/z=69$  requires two C-C and one C-O bond to be broken, yet it shows a rapid decline.
3. For fragment at  $m/z=126$  three C-C bond should be broken, but it shows a steeper decline behaving in a similar way to the fragment at  $m/z=185$ , which requires two C-C bonds to be broken.

The model seems to be consistent with the model.[66] It is also demonstrated that PVC is more damage sensitive than PMMA due to easy elimination of HCl compared to ester side-chain loss.

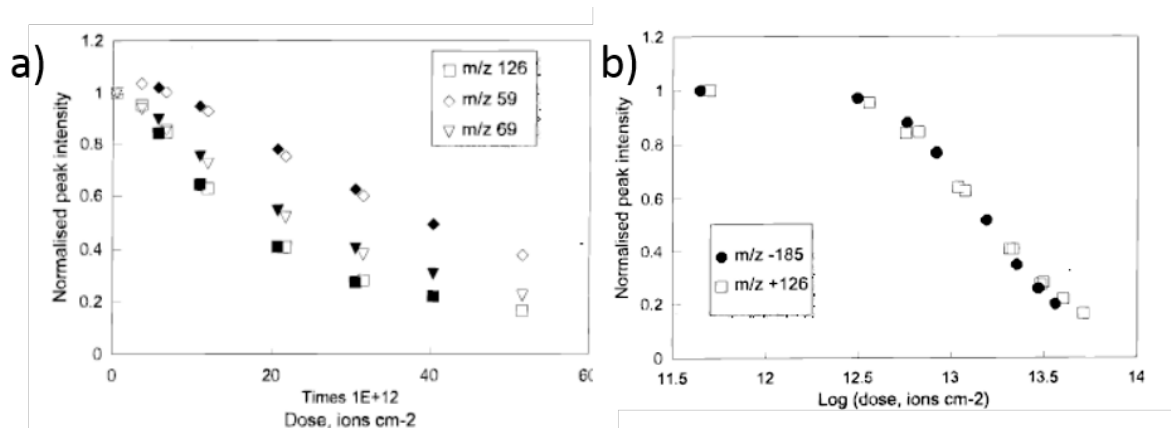


Fig. I- 28: Normalized intensity damage curves of positive secondary ions and superposition of damage curves of a) positive and b) negative secondary ions of PMMA[66]

## 4. Adsorption of organic molecules and fragments on surfaces

This section is aimed to give insights into the fundamental events during collection of matter onto the metallic collector during Storing Matter process. Here we deal with adsorption and sticking of hydrocarbon molecules of different sizes on the collector with lower energy impact, as well as that of fragments since most of the organic matter is assumed to fragment as a result of high energy bombardment during the sputtering part of the Storing Matter process. For this purpose, we review literature where MD simulations are used in order to have an understanding of hydrocarbon adsorption and sticking of small hydrocarbon fragments on surfaces, together with static electronic structure calculations (DFT calculations) to investigate adsorption energies and geometries.

### 4.1. MD Simulations of sticking of hydrocarbons on surfaces

The study of organic/metal interfaces is of paramount interest for many technological applications related to chemical or physical adsorption of polymers or macromolecules on solid surfaces: food packaging based on nanomaterials[104],[105],[106] polymer films as protective coatings for electronic devices and lubricants on solid surfaces and stabilization of colloidal suspensions[107], organic electronics[108] and surface modification of medical implants.[109] This requires a thorough understanding of chemical and physical interactions between the adsorbate and the substrate and up to now little is known about these interactions, especially between organic molecules and oxide[110]. This understanding is particularly important in plasma techniques which offer unique surface properties through efficient, non-polluting processes. However, it is difficult to study the interactions in the sub-monolayer regime due to fast deposition rates in plasmas, while it is crucial to understand



factors that govern the dynamics of molecular adsorption closer to the interface than the bulk since they can differ significantly.[107] Even though plasma treatments are widely used to improve surface properties, the interactions between species in plasma and surface are too complex to be studied by experimental methods only.[111] For an improved molecular-level understanding of polymer-metal interaction, it is helpful to complement experimental methods with atomistic level simulations. This also motivates theoretical developments.

#### 4.1.1. Sticking of hydrocarbon fragments on surfaces

For hydrocarbon sticking processes, unlike the case of atoms, there is no single universal value and no generally accepted definition for the sticking coefficient. The two extreme scenarios that might happen when a projectile hits the surface are that it is reflected or sticks completely. When a molecular projectile hits the surface, it might leave some of its constituents on the surface, or it might remove some atoms from the surface by physical or chemical sputtering. The hydrocarbons to be deposited could be both neutrals and ions with energies between 1-10 eV. The H/C ratio also can vary between 0.4 (hard films) - 1 (polymer-like films) and is mostly determined by the energy of the projectiles. It was also demonstrated that the sticking-cross section is strongly influence by the neighbourhood of an unsaturated carbon atom site and the angle of incidence for the incoming radicals.[112]

There does not exist much work in literature for MD simulation studies for adsorption and sticking of hydrocarbon radicals on metals. Most of MD simulation studies for sticking of hydrocarbon radicals on surfaces have been performed on carbon surfaces as plasma-facing materials for next-generation fusion devices. [113],[114]

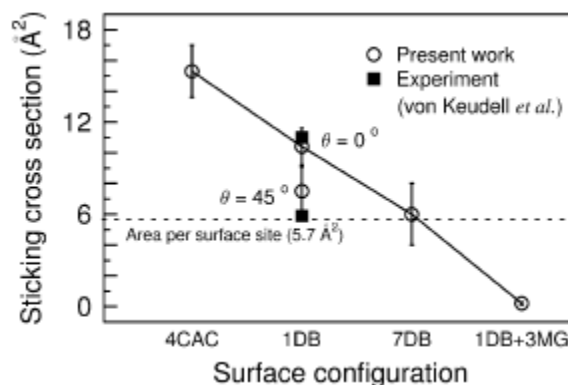


Fig. I-29: Sticking cross-sections obtained for different surface configurations, compared with the experimental values[112]

In their work for methyl radical chemisorptions on unsaturated carbon atom sites on diamond (111) surfaces with different surface configurations using Tight-binding MD simulations[115],[116], Traskelin *et al.* found that CH<sub>3</sub> radical chemisorption depends both on the angle of incidence of the incoming radicals and the local atomic neighbourhood of an unsaturated carbon atom site (Fig. I-29).

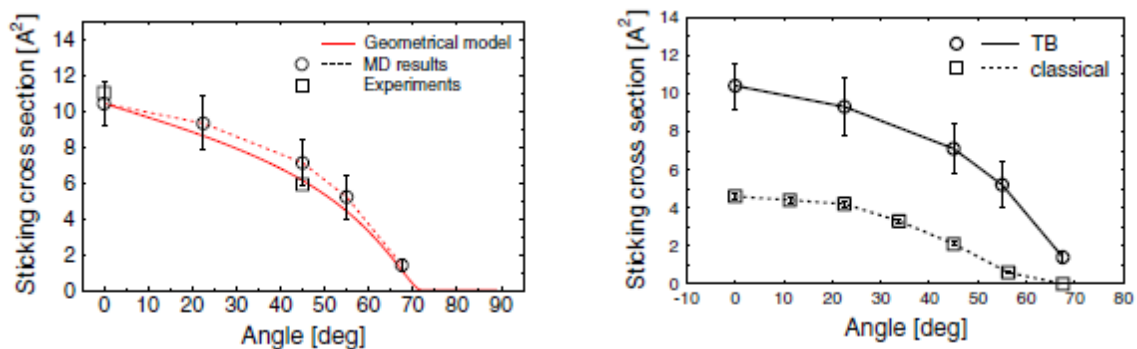


Fig. I-30: The dependence of sticking cross-sections on the angle of incidence of the incoming methyl radical compared to geometrical model and experimental data and by TB model and Brenner potential[117]

In another work, they compared the effect of using both tight-binding and empirical force[79] models on the sticking cross sections for CH<sub>3</sub> radical chemisorption on unsaturated sites of carbon surfaces. Fig. I-30 shows the dependence of sticking probabilities on the angle of incidence for the incoming methyl particles for their chemisorption on a single dangling bond on a diamond (111) surface. MD results well agree with experimental values for sticking cross sections and using TB is better suited for quantitative description of hydrocarbon reactions with surfaces giving 3 times higher cross sections. It was also suggested that the sticking probability is enhanced with increasing radical energy. [117]

The TB force model is able to describe well the chemistry in C-H systems. It uses quantum mechanical approach based on a second order expansion of Kohn-Sham total energy in DFT with respect to charge density fluctuations. Brenner potential also describes well C-H systems, however it is computationally less intensive while still describing bond formation and breaking correctly. The main difference between TB and Brenner methods lies in the way interatomic forces are obtained. The empirical potential energy is calculated from the analytical function of atom coordinates fitted to experimental data. In the TB method, the energy is obtained by solving Schrödinger equation for electrons in the field of cores of atoms.

Fig. I-31 shows that the sticking probability was observed to increase with radical temperature and decrease with the number of hydrogen atoms in the molecule. Fig. I-32 shows sticking profiles of hydrocarbons with different number of hydrogen atoms. They approach zero for impact points further away from the unsaturated carbon atom site. No sticking was observed for  $C_2H_6$  molecule.

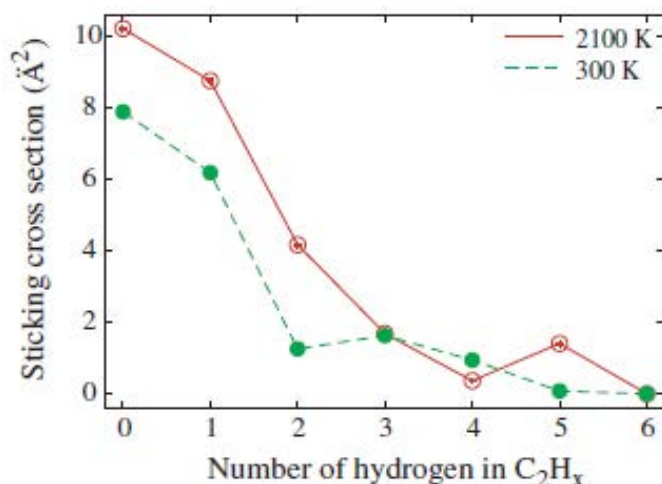


Fig. I-31: Variation of sticking cross-sections with number of hydrogen in the  $C_2H_x$  radical at 300 and 2100 K.[118]

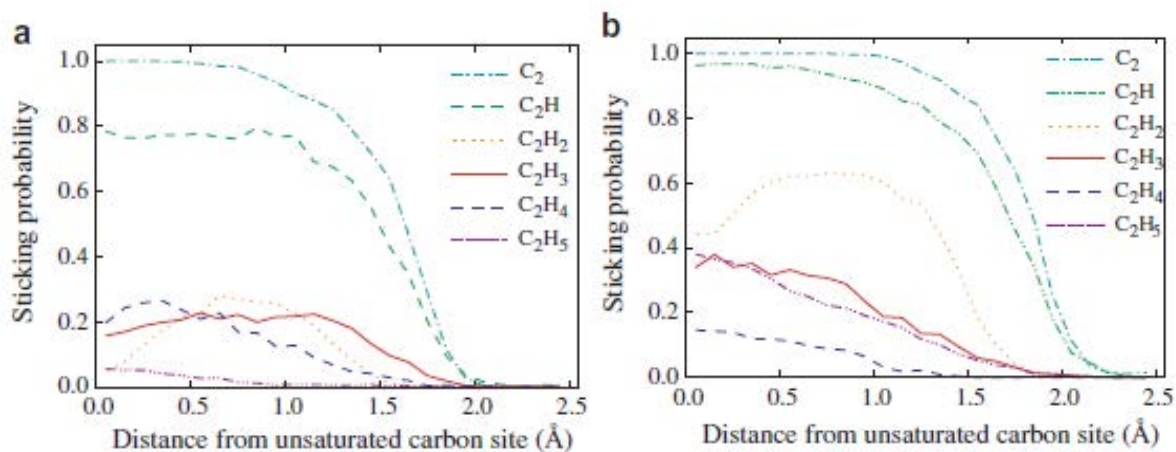


Fig. I-32: Variation of sticking probability of radicals with the distance from the unsaturated carbon site on the hydrogenated diamond (111) surface at a)300 and b)2100 K.[118]

The effect of energy on the sticking of on an amorphous hydrocarbon surface is better demonstrated by Sharma *et al.*(Fig. I-33) [119] For all the radicals represented in Fig. I-33, a decrease in reflection coefficients is observed, which is the complement of the sticking coefficient. This decrease is more pronounced for radicals with less number of hydrogen atoms.

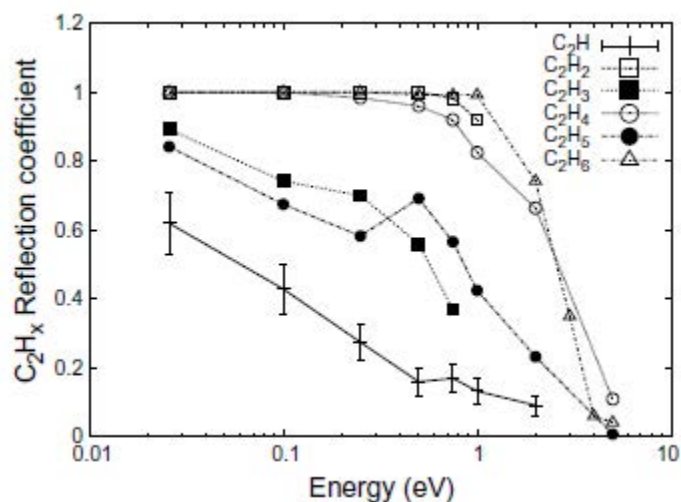


Fig. I-33: Variation of reflection coefficient for  $C_2H_x$  on amorphous hydrocarbon surface[119]

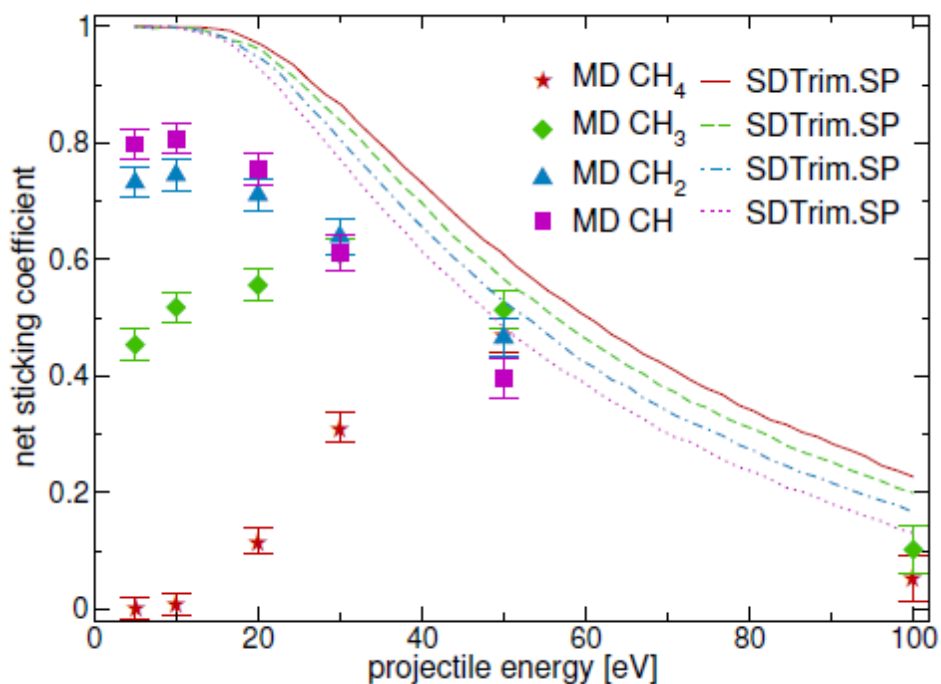


Fig. I-34: Sticking coefficients of various  $CH_x$  projectiles, incident at  $60^\circ$  to the surface normal. MD results are shown by symbols, SDTrim.SP by solid lines.[120]

Tichmann *et al.* studied the sticking coefficients of energetic (5-100 eV) hydrocarbon molecules on the amorphous hydrocarbon layers using MD simulations and BCA approach (SDTrim.SP). Fig. I-34 shows comparable values for both methods only at 50 eV. For energies lower than 50 eV, MD produces a better description for the sticking behaviours of radicals. The sticking coefficient for different molecules make a maximum at different

energies, but the general trend is that the sticking increases up to a certain energy and then for higher energies most carbon atoms are emitted as part of hydrocarbon chains.[120]

Dyson *et al.* studied the adsorption of the acetylene ( $C_2H_2$ ) and the methyl ( $CH_3$ ) radicals on the clean Si(001) surface with dimer reconstruction for the diamond thin-film growth experiments using extended Brenner (XB) empirical potential and accurate Hartree-Fock DFT [121] techniques in order to further characterize chemisorption.[122] Their MD simulations showed that both  $C_2H_2$  and  $CH_3$  bond to the clean Si surface with dimer reconstruction at different sites. Having the twice binding energy per carbon atom, the methyl radical is found to adsorb better on the surface. The other reason was that for coverages greater than one monolayer, the methyl radical found to have more flexibility binding to the second layer between dimer rows. XB potential is multi-particle interaction potential, mainly originating from the Tersoff potential, but differently taking into account the many body terms. The original Brenner potential was mainly first used for C-H systems[79] but has been extended to other systems like C-H-Si. [122]

#### 4.1.2. Sticking of alkane molecules

For the adsorption of alkane molecules on top of an alumina surface, not many simulation studies exist in literature. Kong *et al.* parameterized the non-bonded interaction terms for alumina and alkane interactions using both DFT calculations and MD simulations. In order to obtain a final parameter set, they used an iterative technique with an initial guess of interaction parameters.[123] Li *et al.* studied the effect of relaxed and unrelaxed alumina surfaces on the adsorption of normal alkane chains using MD simulations and found noticeable differences between them.[109] Claire *et al.* reported the adsorption of short hydrocarbon chains and the water penetration through this coated alumina surface. They found relatively low adsorption energy values since they did not consider relaxation of the alumina surface.[110]

The most precise technique to predict the structure and relaxation dynamics of metals oxides is *ab-initio* quantum methods like density functional theory (DFT)[109], yet they have the major disadvantage that they are too costly for studying large systems[109]. It is possible to model organic/metal interfaces with atomistic methods, i.e. molecular dynamics (MD), but it is first necessary to have reliable force fields[123]. The reactive force field developed by

Kieffer *et al.* incorporates Coulomb, three body and van der Waals interactions for non-bonded atoms in MD simulations and fulfils these conditions.[124],[125],[126],[127]

## **4.2. DFT Calculation studies for the interaction of hydrocarbon fragments with metallic surfaces**

### **4.2.1. DFT Calculations as a means to study metal/organic interfaces**

A fundamental understanding of nature of adsorption processes of organic molecules on metals is important for many applications, for instance, corrosion protection, lubrication, dye adhesion, heterogeneous catalysis, chemical sensors, coatings and organic electronics such as organic light-emitting diodes, organic photovoltaic cells, organic field effect transistors.[128],[129],[130],[131]. Such interfaces are of increasing attention since they can introduce new functionalities through combining best features of metals like electrical conductivity with highly tunable properties of organic molecules.[132] A better control of the functionality of these hybrid systems require an accurate description of the bonding. The nature of interactions can be qualitatively divided into two regimes: physisorption and chemisorption. Physisorption is assumed to be the result of long-range electrostatic interactions, whereas chemisorption includes covalent or charge transfer bonds.

Recently, experimental (LEED, HREELS, ARUPS, TPD, STM and work function measurements)[133] studies of organic molecule adsorption on metals have already been supported by state-of-the-art DFT calculations.[134] DFT calculations describe the equilibrium geometry and electronic structure, vibrational frequencies, total energy, and various total energy differences such as surface energies and linear and nonlinear responses to external static stimuli.[135] However, to describe organic/metal systems by DFT methods is still a challenge since these systems are comprised of a balance between covalent bonds, van der Waals (vdW) forces, hydrogen bonds, charge transfer, and Pauli repulsion.[132] DFT methods within the local density approximation (LDA) and generalized gradient approximation (GGA) have been successfully described chemisorption of organic species on metal surfaces since they can effectively treat short-range electron correlation including Pauli repulsion, covalent, ionic and strong hydrogen bonds.[136] However, GGA functional is considered much more appropriate than LDA for producing more accurate results.[134] On the other hand, the study of physisorbed organic species on metals is a challenge since these functionals fail to describe long-range vdW interactions.[132] Recently, there have been many attempts to include these weak interactions in DFT formalism.[137],[138],[132]

#### 4.2.2. Applications of DFT Calculations to adsorption of organic molecules on various metal surfaces

Most of the studies in adsorption of organic molecules on metal surfaces have been carried out using the simple aromatic benzene molecule on various metals and mostly on nickel for the catalysis purposes.[139]

Benzene molecule is weakly bonded to simple metals like Al(111) and this weak bonding is accounted by mutual polarization of the molecule and surface with no significant charge transfer from one to the other.[133] The molecule assumes a flat-lying geometry with minimal distortion from its gas-phase structure.

Bonding of benzene on ferromagnetic metals like Ni(111) is suggested to be of covalent nature, as a result of covalent combination of  $\pi$  orbitals from the molecule (two degenerate HOMOs and two degenerate LUMOs) with d orbitals from the metal.[140],[141]

Adsorption on coinage metals is characterized by a major contribution from sp electrons of metal since the d-band is relatively inert since it is below the Fermi level.[134] Adsorption of benzene ( $C_6H_6$ ) on coinage metal surfaces like Au(111), Cu(111) and Ag(111) is an example of physisorbed systems, which does not exhibit covalency, rather only weak overlap of electron orbitals.[142] Typical features of physisorbed systems are weak binding energy, large adsorption height, almost zero molecular distortion and flat potential-energy surface (PES) for sliding of adsorbed species parallel to the surface.[132] For these systems, mostly only vdW interactions bind the molecule to the surface. It can be seen in Fig. I-35 (a), including vdW forces by  $vdW^{surf}$  method within PBE-GGA functional brings the benzene molecule closer to the Au(111) surface. For physisorbed systems, adsorption height reduces and binding energy increases when vdW forces are included in DFT calculations.

Chemisorbed systems are strongly bound organic/metal systems and examples include benzene ( $C_6H_6$ ) on reactive transition metals like Pd(111), Pt(111), Rh(111) and Ir(111). These systems are characterized by short adsorption heights, bending of the molecule, elongation of the bonds and tilting of atoms. Fig. I-35 (b) shows a system where benzene is chemisorbed on Pt(111). Including vdW forces was found to increase the binding energy by 1.15 eV compared to standard PBE-GGA functional, however did not change the adsorption height significantly, which indicates that the adsorption height in chemisorbed systems is mainly determined by the chemical bonds.[132]

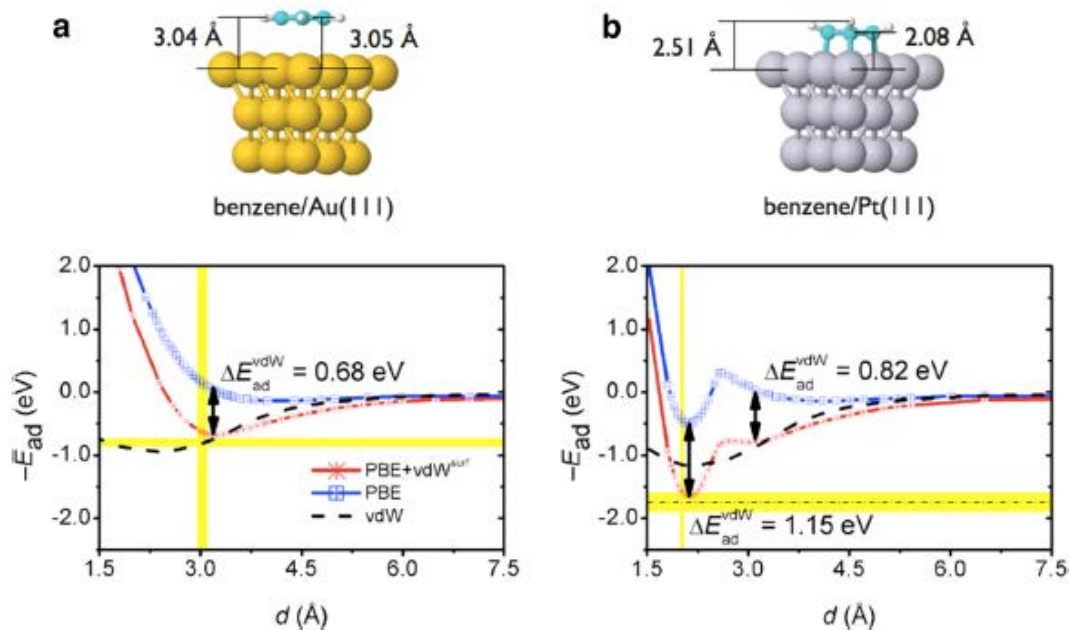


Fig. I-35: Adsorption structures of a) benzene/Au(111) and b) benzene/Pt(111). In the corresponding graphs, adsorption energies are given as a function of adsorption distance. Yellow lines represent experimental values.[132]

Comparing inclusion of vdW interactions in DFT calculations for physisorbed and chemisorbed systems, the role of vdW forces was found to be greater for chemisorbed systems, including benzene on many transition metals.[132] Hence, the stability of chemisorbed systems stems from a combination of covalent bonding and vdW interactions.

## 5. Storing Matter Technique

Secondary ion mass spectrometry (SIMS) is a powerful technique for surface analysis and the characterization of both inorganic and organic surfaces. It provides atomic and molecular information, however data interpretation and quantification is not straightforward since the ionization probability of the secondary species depends on the matrix it is sputtered from. In order to avoid this matrix effect in SIMS,[143] the Storing Matter (StoMat) technique was developed[144],[145],[146] at CRP Gabriel Lippmann based on an idea of G. Slodzian.[147] It decouples the analysis step from the sputtering of the specimen: in a first step the sputtered particles (ions, atoms, molecules, as well as neutrals) are deposited on a collector material in the sub-monolayer range, the collector with deposit is transferred to the analytical instrument under ultra-high vacuum (UHV) conditions using a dedicated suitcase[148] and in a second step the deposit is analysed with dynamic or static SIMS ( Fig. II-1). The technique enables depositing matter in the sub-monolayer range, so that the matter is surrounded mostly by the same matrix which is the collector material. The matrix effect encountered in SIMS is



reduced owing to the chosen chemical environment and quantification becomes possible for inorganic material analysis. Moreover, the collector material can be chosen so that the sensitivity of the technique is improved to optimize the analysis step of the Storing Matter.

For inorganic samples, previous studies show that StoMat has a quantitative potential while keeping the high sensitivity of SIMS.[149],[150],[151],[152] Recently, Kasel *et al.* showed for the first time that the SIMS matrix affect can be avoided when sputtering Ti from Ti, TiB<sub>2</sub>, TiC, TiN and TiO<sub>2</sub>. [152] The analytical potential of the technique for organic samples has also been assessed [153],[154],[155],[156],[157] showing that characteristic peaks can be found on the collector, both for polymers and organic molecules. The ionization probability can be increased by choosing noble metals as collector.[158] However, how the fragmentation of molecules during sputter deposition and the deposition of matter on the collector surface influences ToF-SIMS results has not been investigated up to now. This will be studied in this work.



# Chapter II: Materials and Methods

## 1. Introduction

This chapter describes all the experimental and simulation methods and materials used in this work which required a multi-characterization approach (Table I-2).

Table I-2: Summary of methods used in this work

Experimental methods		Simulation techniques
Ion beam sputter deposition (IBSD)	Characterization	
<ul style="list-style-type: none"><li>• Storing Matter (StoMat)</li></ul>	<ul style="list-style-type: none"><li>• ToF-SIMS</li></ul>	<ul style="list-style-type: none"><li>• MD Simulations</li></ul>
<ul style="list-style-type: none"><li>• In-situ XPS</li></ul>	<ul style="list-style-type: none"><li>• XPS</li></ul>	<ul style="list-style-type: none"><li>• DFT calculations</li></ul>

In the experimental part, first, a description of the instruments used for ion beam sputter deposition (Storing Matter and in-situ XPS) is given. Then, the sample preparation and experimental conditions for sputter deposition are detailed. Finally, instruments used for the characterization of sputter deposits (ToF-SIMS and XPS) are described together with analysis conditions.

In the simulations part, simulation methods used in this work, namely Molecular Dynamics (MD) and Density Functional Theory (DFT) methods are explained along with the simulated systems (adsorbents and substrates).

## 2. Experimental Methods

Experimental methods involve sputter deposition of Polystyrene (PS) and Poly (methyl methacrylate) (PMMA) on silver (Ag). First, we will give a description of the instruments used for this purpose followed by the instruments used for the sample characterization. The details for the sample preparation and materials will be given in the first part.

### 2.1. Sputter Deposition Techniques

Sputter deposition of polymers was done both in the Storing Matter instrument followed by ToF-SIMS analysis and in an XPS chamber followed by in-situ XPS analysis. The latter setup allowed to reduce the effect of impurities during analysis.

## 2.1.1. The Storing Matter Technique

### 2.1.1. a) Principles

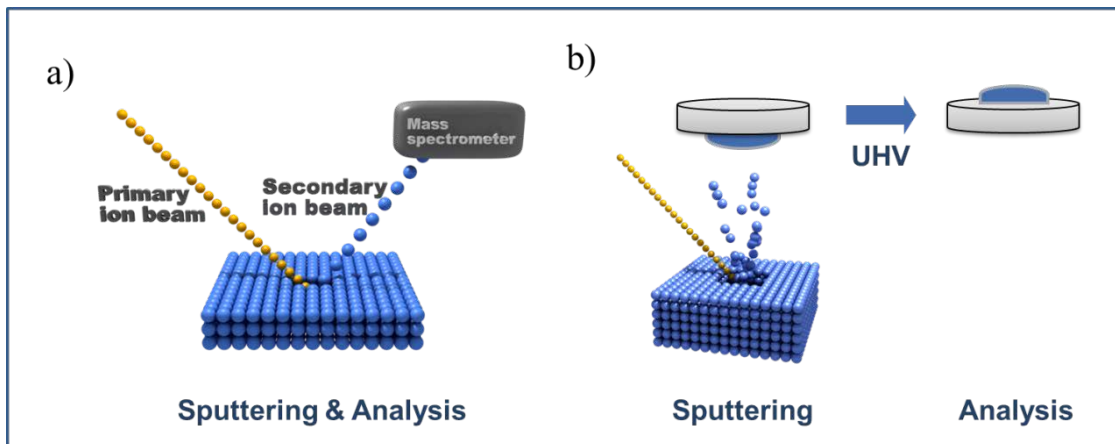


Fig. II-1: The difference of Storing Matter technique to conventional SIMS. a) in SIMS, the sample is sputtered and analysed consecutively b) in Storing Matter, first the sample is sputtered and collected and in a second step the collector with sputter-deposit analysed by SIMS (static or dynamic)

Unlike conventional SIMS, the Storing Matter technique decouples the analysis step from the sputtering of the specimen: in a first step the sputtered particles (ions, atoms, molecules, as well as neutrals) are deposited on a collector material in the sub-monolayer range, the collector with deposit is transferred to the analytical instrument under ultra-high vacuum (UHV) conditions using a dedicated suitcase[148] and in a second step the deposit is analysed with dynamic or static SIMS ( Fig. II-1).

### 2.1.1. b) Instrumentation

Fig. II-2 shows a picture of the prototype and the main parts of the instrument are shown in Fig. II-3. The main parts include  $\text{Ar}^+$  etching, collector coating and sputter-deposition chamber. They are all connected with 5 m long transfer and storage vacuum tube. There are two suitcase dockings for connecting portable suitcases. Ultra high vacuum (UHV) conditions in the different chambers and transfer tubes vary within  $10^{-8}$ - $10^{-10}$  mbar.

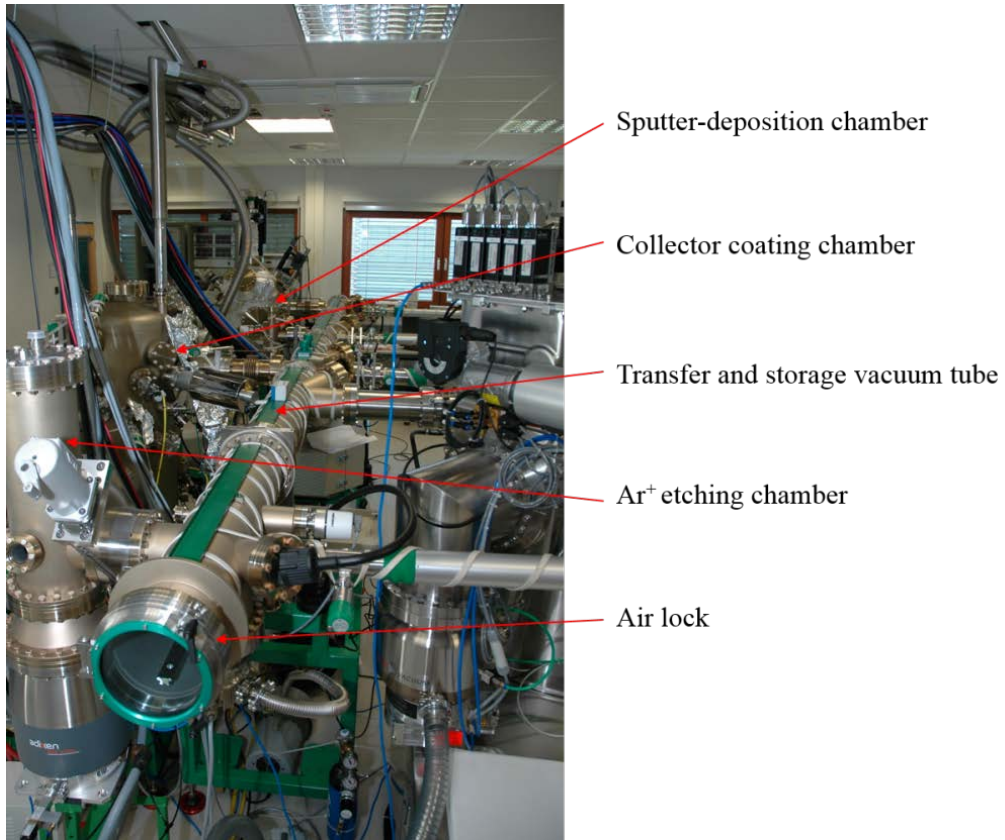


Fig. II-2: Detailed photo of the Storing Matter prototype at the LIST

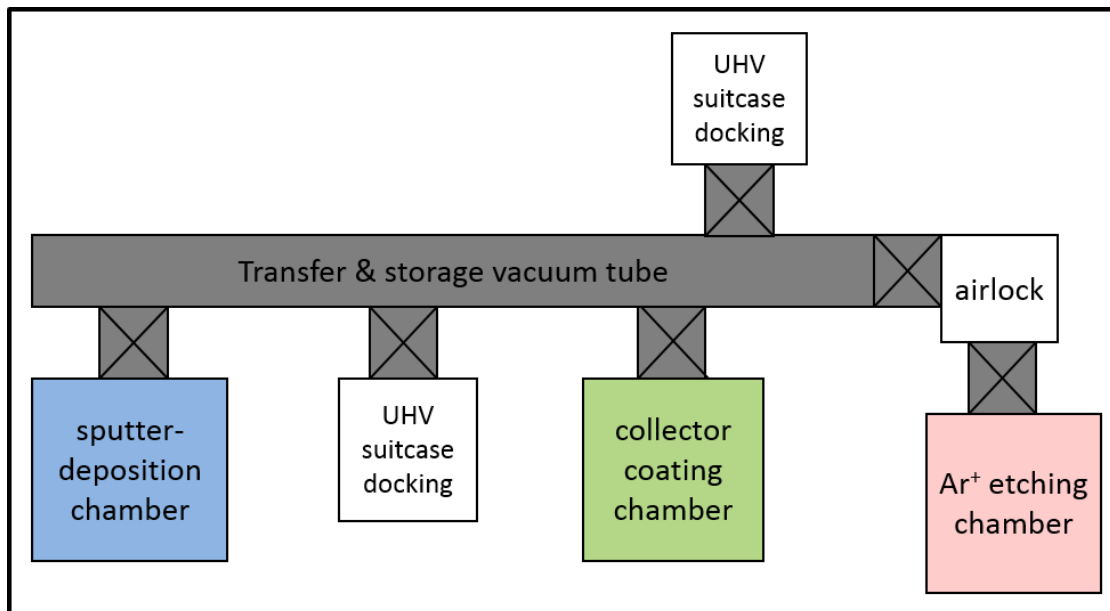


Fig. II-3: The schematic drawing of the Storing Matter instrument at LIST

In the next section, we will briefly describe the main parts of the Storing Matter technique.

**i. Ar<sup>+</sup> etching and collector coating chamber**

Collectors used for sputter deposition can be prepared using ion beam etching in the Ar<sup>+</sup> etching chamber and/or thermal evaporation in the collector coating chamber. In the Ar<sup>+</sup> etching chamber, the substrate is cleaned with an Ar<sup>+</sup> sputter gun (with beam current of 2 mA at 25 eV and 67 mA at 1200 eV) in order to avoid contaminations and increase accuracy and reproducibility of experiments. In the thermal evaporation chamber, the collector is coated with the appropriate metallic matrix by Molecular Beam Epitaxy (MBE). This chamber is equipped with 4 effusion cells, an electron beam evaporator, 2 quartz microbalances, Reflection High Energy Electron Diffraction (RHEED), and Residual Gas Analyser (RGA). The pressure in the MBE chamber is 10<sup>-10</sup> mbar.

**ii. Sputter-deposition chamber**

This is the most important part of the Storing Matter prototype where the sputter-deposition is done. The main elements of the sputter-deposition is a Floating low-energy ion gun (FLIG), secondary electron detector and 2 motorized high precision stages for the sample and the collector (Fig. II-4)

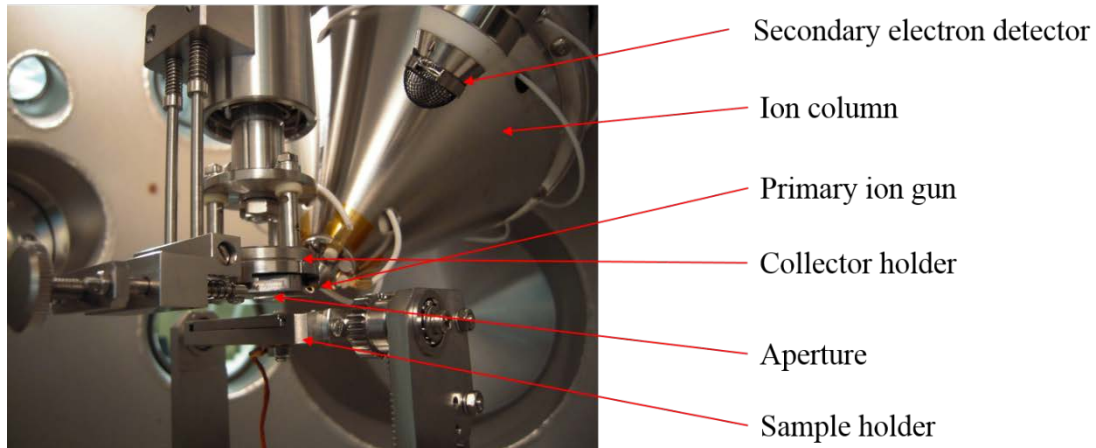


Fig. II-4: The main elements in the sputter-deposition chamber of the Storing Matter prototype

The FLIG can be operated with Xe<sup>+</sup> or Ar<sup>+</sup> ion beams which are produced by a duoplasmatron ion source and filtered by a Wien filter. A detailed description of the duoplasmatron source and the FLIG column can be found elsewhere. [159] It can deliver a focused ion beam with parameters specified in Table II-1.

Table II-1: Some specifications of the Ar<sup>+</sup> ion beam produced by the duoplasmatron ion source

Energy	200 eV – 10 keV
Current	Up to 50 nA
Spot diameter	15 μm
Raster scan area	1 mm x 1 mm

The target to be sputtered is placed on the sample holder and a collector fixed onto the collector holder is placed over it. Both, sample holder and collector stage can be moved in three dimensions (x, y and z) and can be rotated as well. An aperture is installed between them in order to limit the deposit area resulting from broad angular distributions of the sputtered matter for depth-to-lateral transformation in case of depth profiling. It also helps to avoid crater edge effects for a better dynamic range. In this work, no aperture is used since no depth information is studied and we would like to collect as much matter as possible. Secondary electron detector is used in order to visualize sputtering by the ion beam. The ion beam is rastered over the target by 4 deflector plates at voltage of up to 440 V, which corresponds to a raster area of 1.5 x 1.5 mm<sup>2</sup> at 10 keV energy. The rastering of the ion beam is synchronized with secondary electron/ion detection system which allows to visualize secondary electron images of calibration grids to have information about the approximate position and the spot size (μm range) of the ion beam, i.e. allow the tuning of the ion beam.

**iii. Transfer and storage vacuum tubes and UHV suitcase:**

Once the sputter-deposition is done in the sputter-deposition chamber, it is necessary to transfer the collectors with deposits within the prototype and also to the analytical instruments. The transfer and storage of the collectors in the prototype is made with the help of a specially designed cart shown in Fig. II-5.

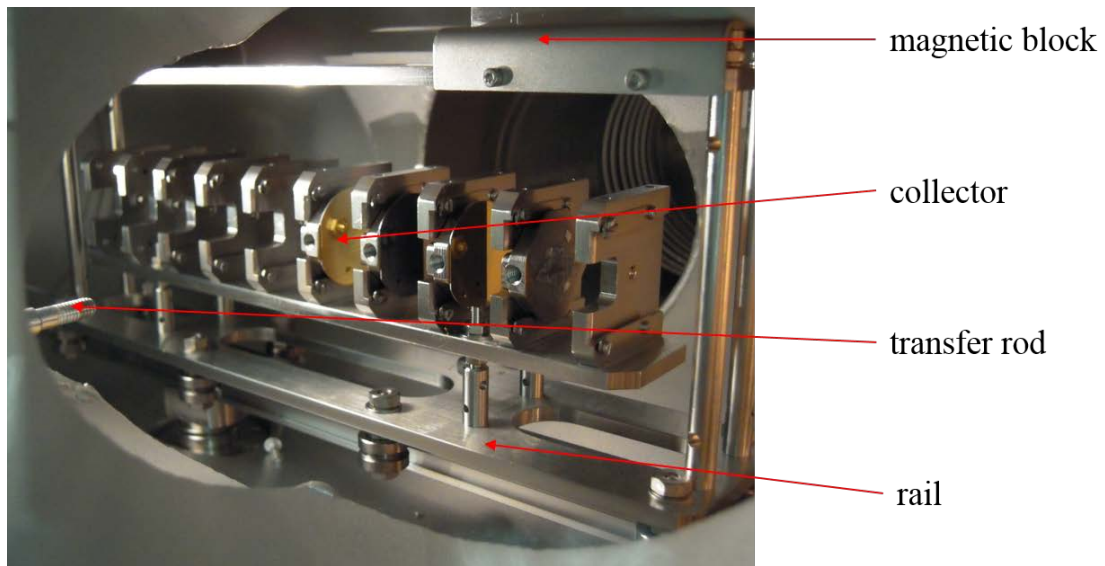


Fig. II-5: Cart for the transfer of collectors within the Storing Matter prototype

A dedicated portable UHV suitcase is used for the transfer of the collectors from the prototype to the analytical instruments (Fig. II-6) since it is important to keep the vacuum pressure as low as between  $10^{-8}$ - $10^{-10}$  mbar to minimize adsorption of air contaminants on the collector. This is of highest importance in case of organic matter deposition and analysis since it is more difficult to distinguish between the organics originating from deposit and contaminations.

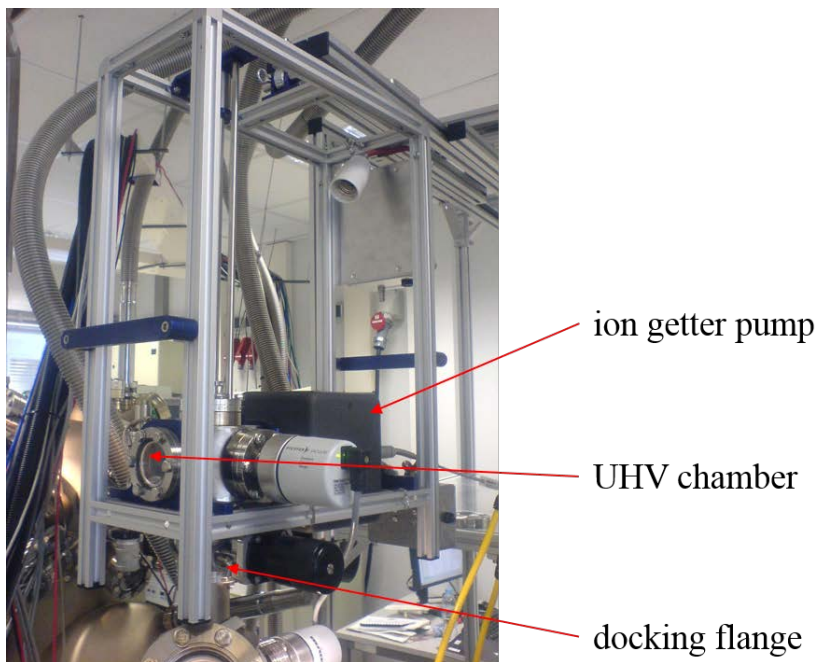


Fig. II-6: UHV suitcase for the transfer of collectors from the Storing Matter to the analytical instruments



### 2.1.1. c) Sample preparation

Sputter deposition in the StoMat prototype requires first the preparation of the collector material and the sputter target. The sputter-deposition process comes next (Fig. II-7).

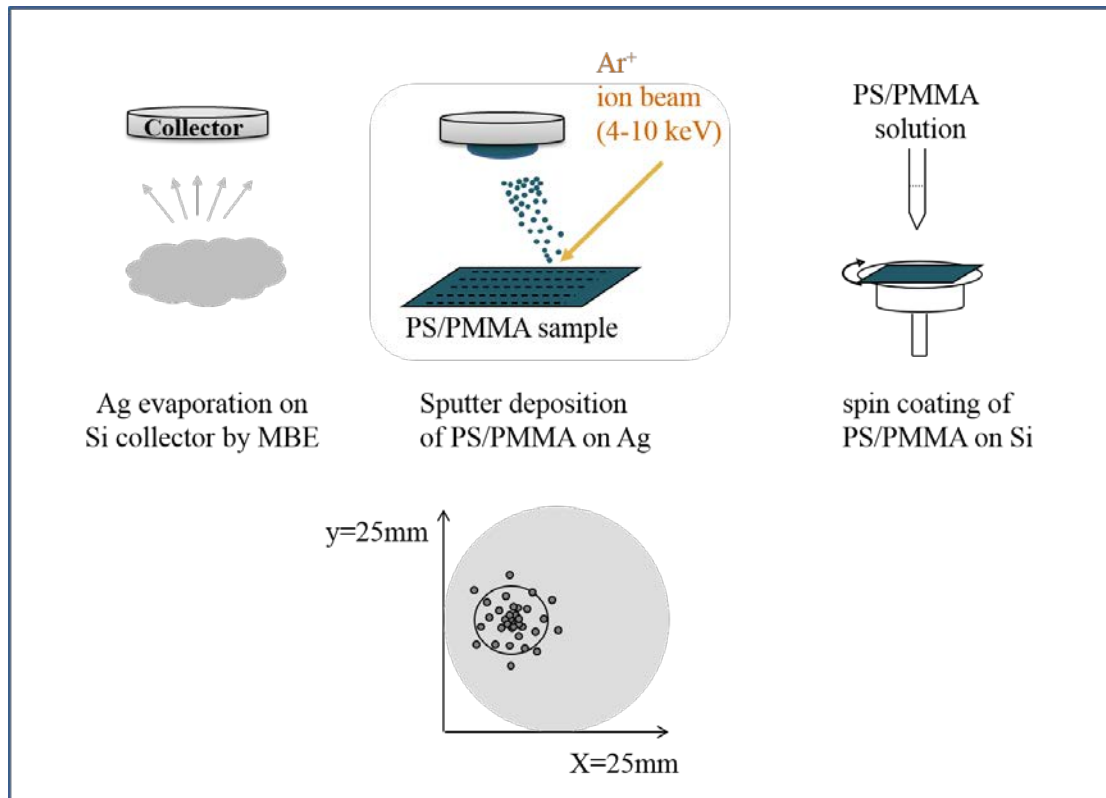


Fig. II-7: The process of sputter deposition by the Storing Matter technique

In order to obtain the collector material, silver (Ag) pellets were evaporated on cleaned 1 inch Si (111) wafers by electron beam evaporation. The film thickness was monitored by a pre-calibrated quartz microbalance. For a 30 nm film thickness, ToF-SIMS analysis showed that the silicon substrate was totally covered by silver. AFM (Atomic Force Microscopy) measurements revealed that the Ag collector surface is flat with a RMS (root-mean-squared) roughness of 3.4 nm calculated for an area of  $125 \times 125 \mu\text{m}^2$ . (Fig. II-8) XRD (X-ray diffraction) showed that the Ag film exhibits a polycrystalline cubic Ag phase with (111), (200), (220), and (311) orientations (Fig. II-9).

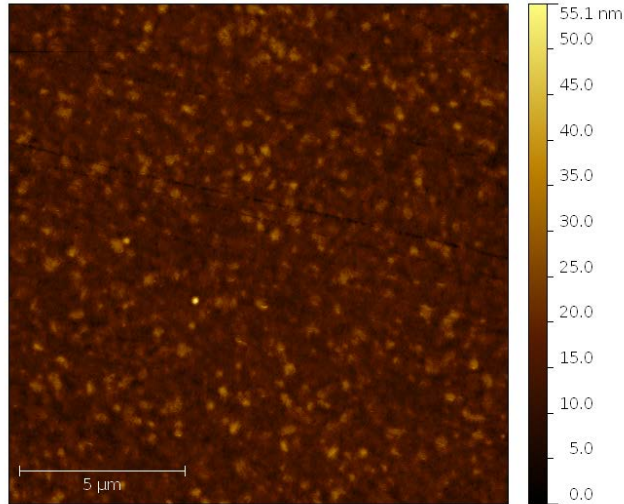


Fig. II-8: AFM image of the Ag collector surface. The two high intensity spots are probably due to dust particles

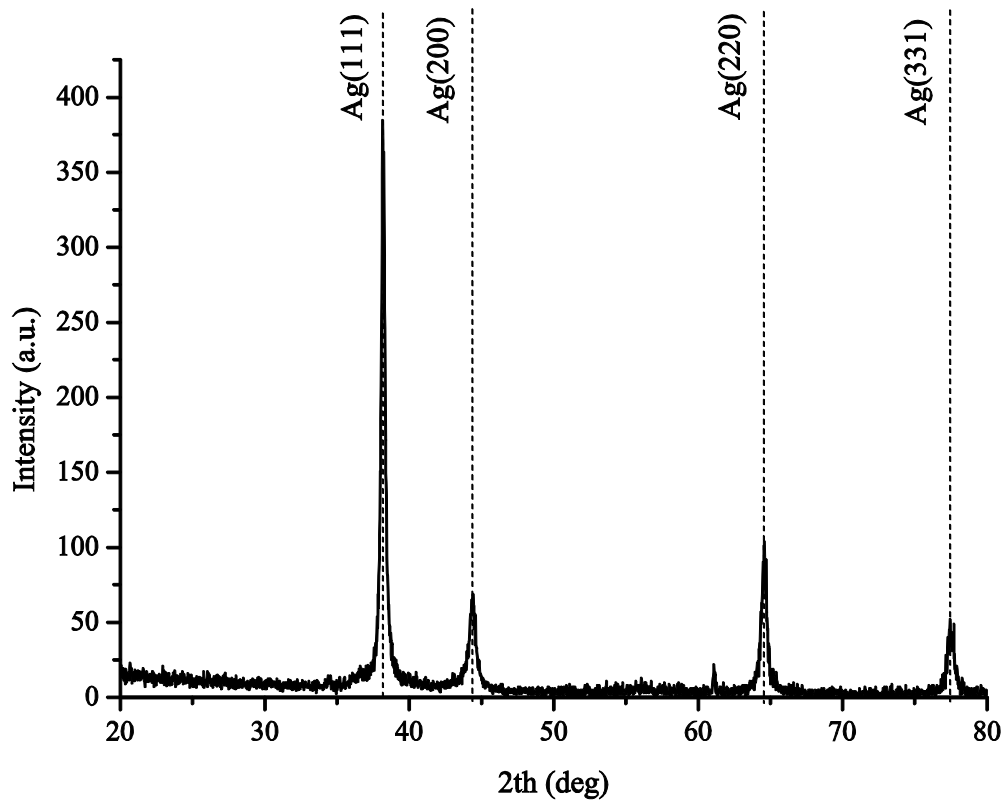
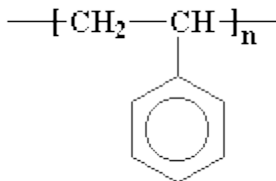
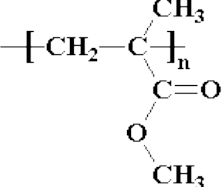


Fig. II-9: XRD Spectra of the Ag collector

Polymer thin films of Polystyrene (PS,  $M_w=2000$ , Sigma Aldrich) and Poly (methylmethacrylate) (PMMA,  $M_w=2000$ , Sigma Aldrich), to be used as sputter target, were prepared by spin-coating a PS or PMMA solution (2 wt % in toluene) on a silicon (100) wafer (Siltronix). The silicon wafers were cleaned in an ultrasonic bath of demineralised

water, acetone and ethanol (10 minutes each solvent). PS and PMMA film thicknesses were about 70 nm. The structure of sputter deposited polymers and some of their properties are shown in Table II-2.

Table II-2: Polymers used for sputter deposition in the Storing Matter prototype

Molecule	Polystyrene (PS)	Poly(methylmethacrylate)(PMMA)
Molecular formula	$(C_8H_8)_n$	$(C_5O_2H_8)_n$
Molecular weight ( $g\ mol^{-1}$ )	GPC 2000	GPC 2000
Structure		

For the sputter deposition, at first, experiments were carried out in the static regime, i.e. by keeping the local fluence below  $5.0 \times 10^{12}$  ions/cm<sup>2</sup>. The sputter-deposition was done in the storing matter instrument. A focused Ar<sup>+</sup> primary ion beam (10 keV impact energy, a beam focus diameter of 15 μm[32], a raster size of 1.5x1.5 mm<sup>2</sup> and a primary current of 2 nA) was raster-scanned over the PS/PPMA sputter target. (Fig. II-10a) The impact angle of the beam with respect to the surface normal was 45°. The distance between the sample and the collector was few millimeters.

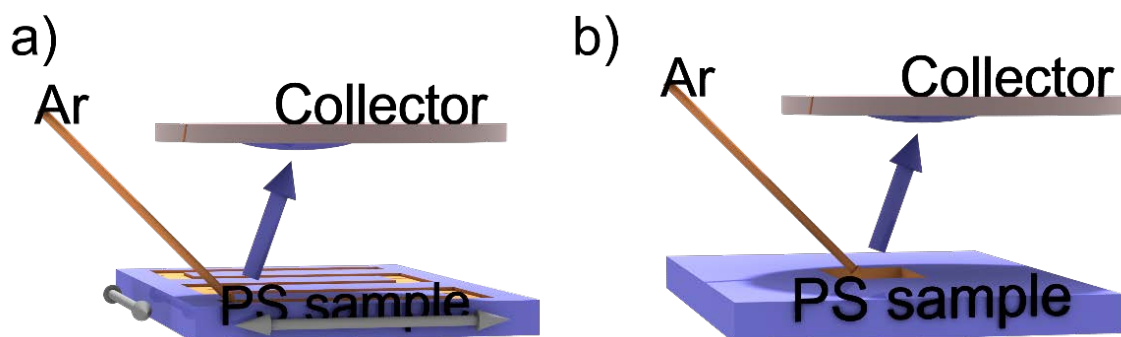


Fig. II-10: Ar<sup>+</sup> beam is raster scanned over PS sputter target for a) static regime where the sample is sputtered at a constant primary ion fluence by moving the sample below the ion beam in order to keep damage low; b) dynamic regime where the primary ion dose is accumulated on the sample by sputtering the sample at the same point of impact.

The coverage of the sputter deposited PS/PMMA on the Ag was varied by moving the sputter target below the primary ion beam with a constant speed of 0.15 mm/s while collecting emitted secondary particles on the collector. Collectors with varying coverage (obtained with total number of Ar<sup>+</sup> primary ions between 3.3x10<sup>12</sup>- 4.0x10<sup>13</sup>) were transferred to the ToF-SIMS instrument (ToF-SIMS V, ION-TOF, Münster, Germany) for analysis in UHV conditions using a dedicated suitcase.[148]

Secondly, the sputter depositions in the dynamic regime, i.e. by changing the primary ion fluence on the sputter target, were carried out both in the Storing Matter instrument and a modified XPS chamber. For the experiments in the StoMat, again using a focused Ar<sup>+</sup> primary ion beam (4 keV impact energy, a raster size of 1.5x1.5 mm<sup>2</sup> and a current of 2 nA), the primary ion fluence was varied between 6.6x10<sup>13</sup>- 4.0x10<sup>15</sup> ions/cm<sup>2</sup> corresponding to a total number of Ar<sup>+</sup> primary ions in the range 1.5x10<sup>12</sup>- 8.9x10<sup>13</sup>. The fluence was increased by increasing the sputtering and collection time while continuing to sputter the PS/PMMA sample in the same zone (Fig. II-10 b). The collectors with varying coverage of sputter-deposited PS were analysed by ToF-SIMS using the above-mentioned conditions.

### **2.1.2 In-situ XPS**

Ag collectors with deposit could still be analysed by ToF-SIMS after vacuum transfer, since SIMS is sensitive to sub-monolayers and the mass spectra contain molecular information. For XPS analysis, it was not possible to detect the deposit after vacuum transfer because contaminations accumulated on the surface quench the XPS signal. In order to avoid this problem, the sample holder of the XPS system (Surface Science SSx-100) was modified in order to do the sputter deposition and analysis in-situ. However, this was done only in the dynamic regime since moving the polymer target to stay locally in the static regime was not possible in the XPS chamber.

#### **2.1.2. a) Instrumentation**

The XPS chamber (Surface Science SSx-100 X-Ray Photoelectron Spectrometer) available at the Aalto University was modified in order to do sputter deposition and in-situ XPS analysis. The specifications of the system are given in Table II-3. The sample holder of the system was modified in a way that it was possible to tilt the surface at ±90 degrees and the sample could be rotated at 360 degrees (Fig. II-11). PMMA and PS films were placed at about 90 ° angles to the Silver (Ag) foil.

Table II-3: Specifications of the Surface Science SSx-100 X-Ray Photoelectron Spectrometer used for the analysis of sputter-deposited film

X-ray source	High throughput bent quartz crystal monochromated Al K $\alpha$
Detector	Hemispherical electron energy spectrometer
X-ray energy and current (keV- mA)	2.5 keV
X-ray analysis spot size ( $\mu\text{m}$ )	150, 300, 600, 1000
Binding energy (eV)	0-1000
Pass energies (eV)	25, 50, 100, 150
Energy resolution (eV)	<0.8 eV



Fig. II-11: Experimental setup showing the sample holder for the sputter deposition of PS/PMMA on Ag foil

The XPS used for the analysis was equipped with a differential ion gun for analysis. For sputtering, Ar<sup>+</sup> ion beam (4 keV impact energy, 4.7 nA primary ion beam current) was used so that the results could be comparable to that of Storing Matter technique. The highest possible impact energy for the mentioned XPS system was 4 keV. Thus, the StoMat sputter deposition in the dynamic regime was done at the same energy in order to be comparable with in-situ deposition in the XPS chamber. The PMMA and PS films were sputtered with Ar<sup>+</sup> ion beam at an angle of 30 ° with respect to the surface of the films and the sputtered material is collected on Ag foil. Sputtered material was deposited on Ag foil and Ag foil was analyzed with the Surface Science SSx-100 X-Ray Photoelectron Spectrometer.

Table II-4: varied ranges of emission current and ion beam energy of Ar<sup>+</sup> ions

Emission current (mA)	0.01-10
Ion beam energy (keV)	1-4

In order to be able to vary Ar<sup>+</sup> ion emission current and beam energy (in the ranges indicated in Table II-4), it was necessary to measure the sputtering current and correlate it with the emission current and beam energy. An external manipulator with a copper foil was introduced into the chamber and variation of sputtering current on the PS/PMMA sputter target as a function of Ar<sup>+</sup> ion emission current and beam energy was recorded. The sputtering current increases with both increasing emission current and beam energy. In order to see the effect of emission current on sputtering current, the beam energy was fixed at 4 keV and the emission current was varied in the range of 0.01 mA to 10 mA. The sputtering current increases with increasing emission current with different slopes within different regions (Fig. II-12). The effect of beam energy on the sputtering current was investigated for two different emission currents. The emission current was once fixed at 10 mA and once at 1 mA and for both cases an increase in sputtering current was observed for increasing beam energy, the increase rate not being the same for different currents and for different regions of the same current (Fig. II-13 and Fig. II-14).

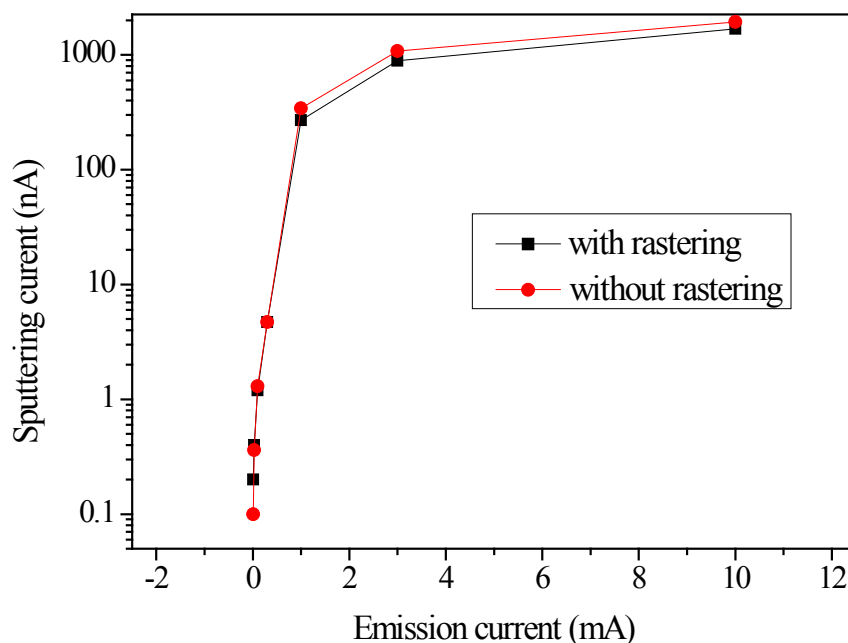


Fig. II-12: Variation of sputtering current with Ar<sup>+</sup> ion emission current at 4 keV beam energy

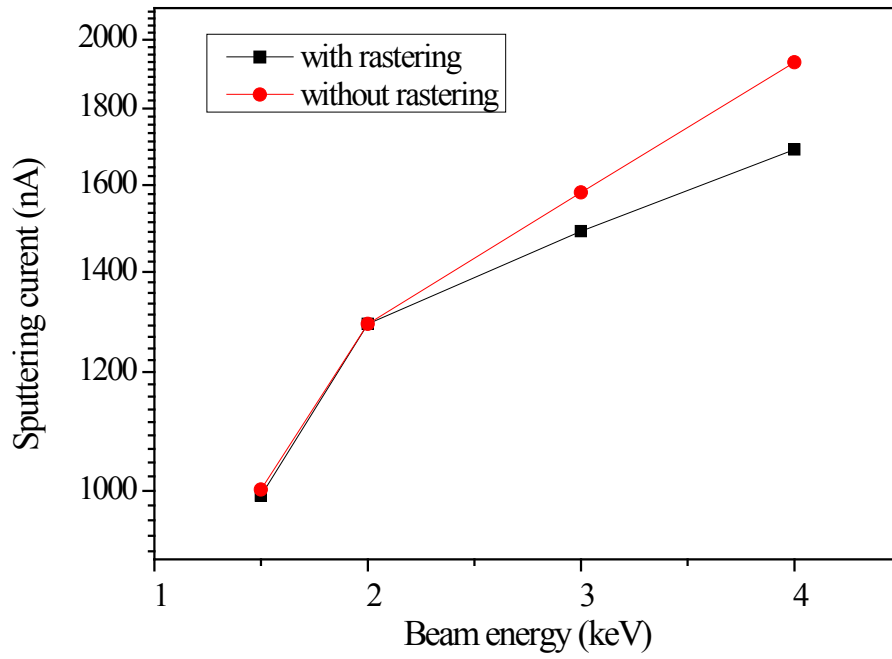


Fig. II-13: Variation of sputtering current with  $\text{Ar}^+$  ion beam energy at 10 mA emission current

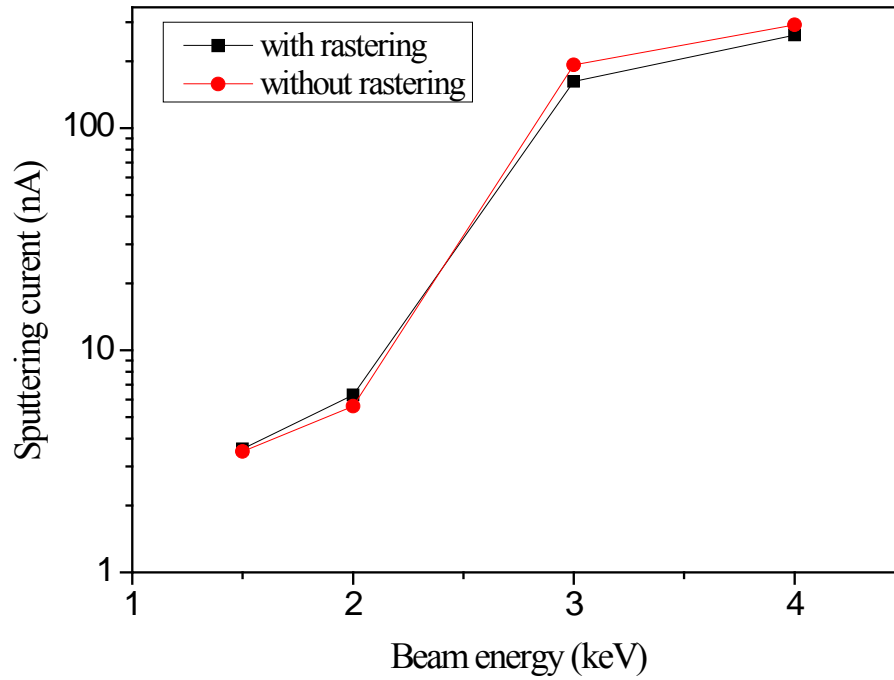


Fig. II-14: Variation of sputtering current with  $\text{Ar}^+$  ion beam energy at 1 mA emission current

### 2.1.2. b) Sample preparation

After being able to monitor sputtering current for varying emission current and beam energy, the beam energy and emission current was fixed at a certain value. The parameters used for sputter deposition of PMMA and PS films are given in Table II-5 . For the beam energy, the maximum of 4 keV was chosen since a decrease in intensity of both C1s and O1s peaks in XPS spectra was observed with decreasing beam energy. The emission current was kept at 0.3 mA in order to have low sputtering current which corresponds to 4nA and which is comparable to the current used for Storing matter deposition.

Table II-5: Parameters for sputter deposition in the XPS chamber

Initial pressure in the main chamber (mbar)	$2 \times 10^{-9}$
Pressure in the main chamber with Ar (mbar)	$1.5 \times 10^{-8}$
Emission current (mA)	0.3
Sputtering current (nA)	4
Ion beam energy (keV)	4

After optimization of parameters, it was necessary to check the rate with which impurities accumulate on the surface, since their interference with the XPS spectra could lead to misinterpretation of the results. For this, the following procedure was applied:

1. Initial Ag surface was analyzed with XPS.
2. The Ag surface was cleaned by sputtering with  $\text{Ar}^+$  ion beam for 5 min.
3. Cleaned Ag surface was analyzed with XPS.
4. The cleaned Ag foil was let in the XPS chamber under UHV for 1.5 hours.
5. The Ag surface was again analyzed with XPS.

As a result, less than 1% carbon accumulation was observed on the surface, which shows that the sputter deposition is made in reasonable time duration after the Ag surface is cleaned, and the impurities should not constitute any problem.



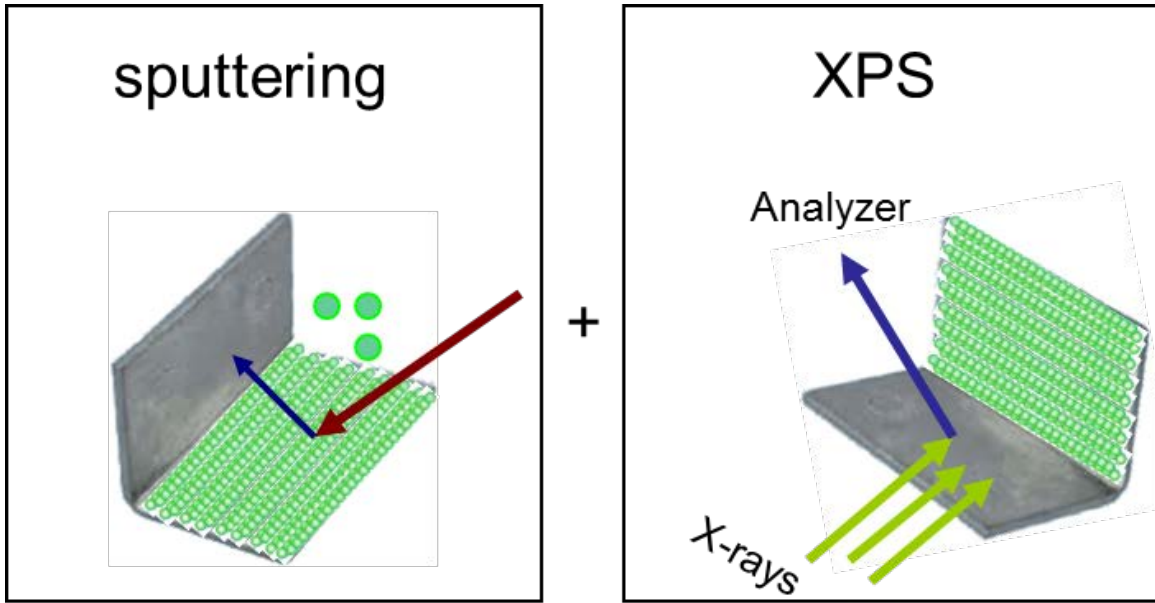


Fig. II-15: Sputter deposition of PS/PMMA on Ag and in-situ analysis process in the XPS chamber

Fig. II-15 shows a schematic for the sputtering and analysis process. Before each sputter deposition, the Ag foil was cleaned with Ar ion beam for 5 min. The same Ar<sup>+</sup> ion beam was used for the sputtering of the PS film and the emitted secondary particles were collected on a Ag foil which was placed at a 90° angle to the sputter target. XPS analyses were carried out both on the Ag surface with PS/PMMA deposit and PS/PMMA target after sputtering with fluences between  $8.3 \times 10^{12}$ -  $4 \times 10^{15}$  ions/cm<sup>2</sup>. In order to have a reference, an XPS analysis was made both on the clean Ag surface and the PS/PMMA film. The XPS spectra were fitted by Gaussian-Lorentzian shape lines and Shirley background type.

Table II-6 gives the set of values used to calculate the necessary primary ion fluence or, for a given primary ion fluence, to calculate the necessary parameters like area or duration of analysis for the sputter deposition in the Storing Matter, in-situ XPS and sputter depth profiling of PS/PMMA sputter target. The primary ion fluence or the dose density which is the number of impinging projectiles per surface area is defines as:

$$d = \frac{It}{eA} \quad (\text{II-1})$$

Where I is the primary ion current, t is the bombardment duration, e the elementary charge ( $e = 1.6 \times 10^{-19}$  C) and A the area of the bombarded surface.

Table II-6: Set of parameters used for obtaining required primary ion fluence

fluence (ions/cm <sup>2</sup> )	Storing Matter			In-situ XPS			Sputter depth profile		
	I (A)	t(s)	A(cm <sup>2</sup> )	I (A)	t(s)	A(cm <sup>2</sup> )	I (A)	t(s)	A(cm <sup>2</sup> )
8.3x10 <sup>12</sup>	2x10 <sup>-9</sup>	15	0.0225	4.7x10 <sup>-9</sup>	30	0.107	1.5x10 <sup>-7</sup>	2	0.27
3.3x10 <sup>13</sup>	2x10 <sup>-9</sup>	59	0.0225	4.7x10 <sup>-9</sup>	120	0.107	1.5x10 <sup>-7</sup>	10	0.27
6.6x10 <sup>13</sup>	2x10 <sup>-9</sup>	119	0.0225	4.7x10 <sup>-9</sup>	240	0.107	1.5x10 <sup>-7</sup>	19	0.27
1.2x10 <sup>14</sup>	2x10 <sup>-9</sup>	208	0.0225	4.7x10 <sup>-9</sup>	420	0.107	1.5x10 <sup>-7</sup>	33	0.27
2.5x10 <sup>14</sup>	2x10 <sup>-9</sup>	445	0.0225	2.6x10 <sup>-7</sup>	900	0.107	1.5x10 <sup>-7</sup>	71	0.27
5x10 <sup>14</sup>	2x10 <sup>-9</sup>	890	0.0225	2.6x10 <sup>-7</sup>	32	0.107	1.5x10 <sup>-7</sup>	142	0.27
1x10 <sup>15</sup>	2x10 <sup>-9</sup>	1779	0.0225	2.6x10 <sup>-7</sup>	65	0.107	1.5x10 <sup>-7</sup>	285	0.27
2x10 <sup>15</sup>	2x10 <sup>-9</sup>	3558	0.0225	2.6x10 <sup>-7</sup>	129	0.107	1.5x10 <sup>-7</sup>	569	0.27
4x10 <sup>15</sup>	2x10 <sup>-9</sup>	7116	0.0225	2.6x10 <sup>-7</sup>	258	0.107	1.5x10 <sup>-7</sup>	1139	0.27

## 2.2. Characterization of Deposits

### 2.2.1. ToF-SIMS

Fig. II-16 shows the schematic diagram of the Time of Flight Secondary Ion Mass Spectrometry (ToF-SIMS) instrument. It uses time of flight (ToF) for the determination of secondary ion masses. The time between a secondary ion leaving the sample surface and when it reaches the detector is referred to as time of flight. Since ions with the same energy but different masses reach the detector at different times (it takes longer for heavier ions) the mass of various ions can be distinguished and can be detected in parallel.

In this work, primary ions are emitted using the electrostatic field between the LMIS (Liquid metal ion source) source and the extractor, are accelerated and focused onto the sample by the objective lens. The beam is pulsed to a time slice of nanoseconds with the blanker and the sample is scanned by the beam deflector. An extraction voltage is applied to the sample

holder in order to extract secondary ions into the ToF analysis tube. Then, the secondary ions are guided to the micro-channel plate (MCP) detector by the secondary ion lens and the deflector.

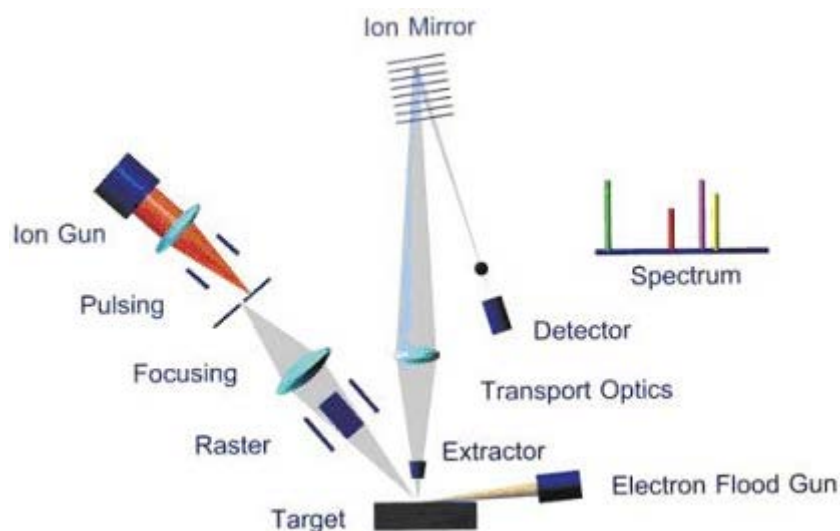


Fig. II-16: Schematic of the working principle of the ToF-SIMS instrument (ION-TOF GmbH)

The ToF-SIMS instrument (ToF-SIMS V, ION-TOF, Münster, Germany) used in this work is equipped with a cluster LMIG (liquid metal ion gun) with a cluster Bi LMIS, a dual source column with a C60 and a Cs source, and a flood gun for charge compensation. It is possible to heat and cool the stage between temperatures of  $-130$  to  $+600$  °C. There is a docking station for connecting the UHV suitcase for sample transfer and a sample holder specific to the collectors used in the Storing Matter instrument. The base pressure inside the analysis chamber is approximately  $5 \times 10^{-10}$  mbar. The mass resolution achieved by the TOF analyser is higher than 11 000 (FWHM) at  $m/z=29$  for  $\text{Bi}^+$  primary ions.

For this work,  $\text{Bi}^+$  and  $\text{Bi}_3^+$  primary ions with an impact energy of 25 keV, with a pulsed ion current of 1 pA for  $\text{Bi}^+$  and 0.3 pA for  $\text{Bi}_3^+$ , and a raster size of  $100 \times 100 \mu\text{m}^2$  were used. The pulse widths were bunched down to 100 ns. The impact angle of the ion guns was  $45^\circ$  and the secondary ions were extracted at  $90^\circ$  from the sample surface with a 2 keV extraction potential. The ion dose was calculated as  $1 \times 10^{12}$  ions/ $\text{cm}^2$ , which is under the static limit for analysis.

### 2.2.2. XPS

X-Ray photoelectron spectroscopy (XPS) is a surface-sensitive quantitative technique, which enables identification of surface elements using the energy distribution of the photoelectrons that are emitted from the surface, when irradiated by X-rays. The escape depth of photoelectrons is 5-10 nm.[160]

The kinetic energy (KE) spectrum gives information about the binding energy of the detected core electron. The electron binding energy of emitted electrons is determined by using the equation:

$$E_{binding} = E_{photon} - (E_{kinetic} + \emptyset) \quad (II-2)$$

where  $E_{binding}$  is the binding energy of the electron,  $E_{photon}$  is the energy of the X-ray photons,  $E_{kinetic}$  is the kinetic energy of electrons measured by the instrument and  $\emptyset$  is the work function depending on the spectrometer and the material.

The well-resolved kinetic energy distribution of the emitted photoelectrons gives information about the chemical environments of the emitting atoms. This enables detection of functional groups but not the identification of organic molecules, especially larger ones.

## 3. Simulation Methods

### 3.1. Deposition of Organic molecules by Molecular Dynamic (MD) Simulations

#### 3.1.1. MD Simulations

Molecular Dynamics (MD) is a computer simulation method used to study the motions of a system of atoms.[161] The starting configurations of different atoms are known and they are allowed to interact for a period of time, and their trajectories are determined by numerically solving Newton's equations of motion for a system of interacting particles. In order to determine new positions of atoms, different algorithms can be used. In the molecular dynamics code we used for this work, the 5<sup>th</sup> order Gear predictor-corrector algorithm is used, which is based on the Taylor expansion.

In general, a Taylor expansion of the position  $r$  of an atom around time  $t$  is given by

$$r(t + \Delta t) = r(t) + v(t)\Delta t + \frac{f(t)}{2m}\Delta t^2 + \frac{\Delta t^3}{3!}\ddot{r} + \mathcal{O}(\Delta t^4) \quad (\text{II-3})$$

$$r(t - \Delta t) = r(t) - v(t)\Delta t + \frac{f(t)}{2m}\Delta t^2 - \frac{\Delta t^3}{3!}\ddot{r} + \mathcal{O}(\Delta t^4) \quad (\text{II-4})$$

where  $\Delta t$  is the time step of the MD simulation,  $f$  the force acting on the atom,  $m$  the mass and  $v$  the velocity of the atom and  $\ddot{r}$  is defined by Newton's second law,  $\ddot{r} = a(t) = \frac{f(t)}{m}$

The sum of these two equations is

$$r(t + \Delta t) + r(t - \Delta t) = 2r(t) + \frac{f(t)}{m}\Delta t^2 + \mathcal{O}(\Delta t^4) \quad (\text{II-5})$$

The new position is estimated by

$$r(t + \Delta t) \approx 2r(t) - r(t - \Delta t) + \frac{f(t)}{m}\Delta t^2 \quad (\text{II-6})$$

$\Delta t^4$  defines the error and is assumed to be negligible, since the time step is often less than one femtosecond ( $10^{-15}$  s).

For the Gear predictor-corrector algorithm,

$$\begin{pmatrix} r_0^p(t + \delta t) \\ r_1^p(t + \delta t) \\ r_2^p(t + \delta t) \\ r_3^p(t + \delta t) \\ r_4^p(t + \delta t) \end{pmatrix} = \begin{pmatrix} 1 & 1 & 1 & 1 & 1 \\ 0 & 1 & 2 & 3 & 4 \\ 0 & 0 & 1 & 3 & 8 \\ 0 & 0 & 0 & 1 & 4 \\ 0 & 0 & 0 & 0 & 1 \end{pmatrix} \begin{pmatrix} r_0(t) \\ r_1(t) \\ r_2(t) \\ r_3(t) \\ r_4(t) \end{pmatrix} \quad (\text{II-7})$$

where index 0 to 4 refer to the derivatives and  $r_0$  is the position at  $t=0$ ,  $r_1 = \left(\frac{\partial r_0}{\partial t}\right)\delta t$ ,

$r_2 = \frac{1}{2}\left(\frac{\partial^2 r_0}{\partial t^2}\right)\delta t^2$ ,  $r_3 = \frac{1}{6}\left(\frac{\partial^3 r_0}{\partial t^3}\right)\delta t^3$ ,  $r_4 = \frac{1}{24}\left(\frac{\partial^4 r_0}{\partial t^4}\right)\delta t^4$  and superscript 'p' stands for

predicted. The final positions are given by:

$$\begin{pmatrix} r_0^c(t + \delta t) \\ r_1^c(t + \delta t) \\ r_2^c(t + \delta t) \\ r_3^c(t + \delta t) \\ r_4^c(t + \delta t) \end{pmatrix} = \begin{pmatrix} r_0^p(t + \delta t) \\ r_1^p(t + \delta t) \\ r_2^p(t + \delta t) \\ r_3^p(t + \delta t) \\ r_4^p(t + \delta t) \end{pmatrix} + \begin{pmatrix} c_0 \\ c_1 \\ c_2 \\ c_3 \\ c_4 \end{pmatrix} \delta r \quad (\text{II-8})$$

Where  $\delta r = r_2^c - r_2^p$  and superscript ‘c’ stands for corrected. The coefficients  $c_i$  values are taken from Table II-7 using the variable  $r_n(t)$ . These values of  $c_i$  are obtained from the FLX user manual guide.

Table II-7: Gear predictor-corrector algorithm coefficients for 4 orders of derivatives.

order	$c_0$	$c_1$	$c_2$	$c_3$	$c_4$
3	0	1	1		
4	1/6	5/6	1	1/3	
5	19/120	3/4	1	1/2	1/12
6	3/20	251/360	1	11/1	1/6

Since there exists a huge number of particles in a molecular system, MD uses numerical methods to circumvent this problem.

MD simulations can be performed under some ensembles like constant volume and energy (NVE), constant volume and temperature (NVT) or constant pressure and temperature (NPT), where N stands for constant number of particles, V for volume, E for energy, T for temperature and P for pressure. In this work, the constant volume and temperature (NVT) ensemble has been used for sample preparation and the constant volume and energy ensemble (NVE) for the deposition of molecules.

### 3.1.2. MD Simulations using a reactive force field: FLX

In this work, MD simulations were carried out using the reactive force field developed by Kieffer *et al* at the University of Michigan. It uses a Fortran program called FLX in order to simulate the behaviour of a system of atoms during a small period of time in order to deduce the positions of each particle. FLX uses a so-called reactive force field which allows bond

breaking and formation via an environment sensitive charge transfer and angular control routines. The force field includes Coulomb interactions, a Born-Mayer-Huggins repulsive term, Lennard-Jones potential, an attractive three-body term, a four-body torsion term.[124],[125],[126],[127],[162]

$$U_i = q_i \sum_{j \neq i}^N \frac{q_j}{4\pi\epsilon_0 r_{ij}} + \sum_{j=1}^{NC} C_{ij} e^{(\sigma_i + \sigma_j - r_{ij})\rho_{ij}} + \sum_{j \neq i}^N 4 \epsilon_{ij} \left[ \left( \frac{r_{ij}}{r_{ij}} \right)^{12} - \left( \frac{r_{ij}}{r_{ij}} \right)^6 \right] + \sum_{j=1}^{NC-1} \sum_{k=j+1}^{NC} (\varphi_{ij} + \varphi_{ik}) \Lambda_{ijk} + \sum_{i \in \{l,j,k,n\}} [B_1(1 + \cos \Phi_{ljk}) + B_2(1 - \cos 2\Phi_{ljk}) + B_3(1 + \cos 3\Phi_{ljk}) + B_4]. \quad (\text{II-9})$$

The different terms of the equation are described below briefly:

### 1. Coulomb term

This term describes the electrostatic interactions and is expressed as:

$$q_i \sum_{j \neq i}^N \frac{q_j}{4\pi\epsilon_0 r_{ij}} \quad (\text{II-10})$$

where  $q_i$  represents the charge of the particle  $i$ ,  $\epsilon_0$  the dielectric constant of vacuum and  $r_{ij}$  the interatomic distance.

### 2. Born-Mayer-Huggins repulsive term

The repulsive Born-Mayer-Huggins (BMH) term is given by

$$\sum_{j=1}^{NC} C_{ij} e^{(\sigma_i + \sigma_j - r_{ij})\rho_{ij}} \quad (7)$$

where  $r_{ij}$  is the interatomic distance,  $\sigma_i$  the atomic radius of atom  $i$ ,  $\rho_{ij}$  the hardness parameter and  $C_{ij} = A_{ij} \left( 1 + \frac{z_i}{n_i} + \frac{z_j}{n_j} \right)$ , where  $z_i$  is the valence and  $n_i$  is the number of electrons in the outer shell of atom  $i$ . [124]

### 3. Lennard-Jones potential

Interactions between nonbonded neutral atoms are described by the Lennard-Jones potential:

$$\sum_{j \neq i}^N 4 \epsilon_{ij} \left[ \left( \frac{\bar{r}_{ij}}{r_{ij}} \right)^{12} - \left( \frac{\bar{r}_{ij}}{r_{ij}} \right)^6 \right] \quad (8)$$

where  $\epsilon_{ij}$  is the well depth,  $\bar{r}_{ij}$  is the collision diameter and  $r_{ij}$  is the interatomic distance.

#### 4. Attractive three-body term

The first version of the three-body term proposed by Huang and Kieffer [124] is given by

$$\sum_{j=1}^{NC-1} \sum_{k=j+1}^{NC} (\varphi_{ij} + \varphi_{ik}) \Lambda_{ijk} \quad (9)$$

$\Lambda_{ijk} = e^{-\gamma_{ijk}(\bar{\theta} - \theta_{ijk})^2}$  depends on the angle formed by the three atoms  $\langle ijk \rangle$  and

$\varphi_{ij} = -C_{ij} \frac{\kappa_{ij}}{\eta_{ij}} \zeta_{ij} e^{(\lambda_{ij} - r_{ij})\eta_{ij}}$ , where  $r_{ij}$  is the interatomic distance and  $\zeta_{ij} = \left(1 + e^{b_c(r_{ij} - a_c)}\right)^{-1}$ , describes attractive forces between the atoms  $i$  and  $j$ . The positions of the atoms change during MD simulations, therefore the number of neighbours (coordination) of an atom is variable. Consequently, the three-body term should depend on the effective coordination number. In a second version by Huang and Kieffer, this fact is taken into account by replacing the angular part  $\Lambda_{ijk}$  by

$$\Lambda_{ijk} = \sum_{Z_0=3}^6 C_{Z_0} e^{-A_{Z_0}(Z_0 - Z_i)^2} e^{-\gamma_{Z_0}(\bar{\theta}_{Z_0} - \theta_{ijk})^2} \quad (10)$$

where  $Z_i$  is the effective coordination number of particle  $i$  (eq. 13),  $\bar{\theta}_{Z_0}$  is the equilibrium angle of  $i, j, k$  (for example  $\bar{\theta}_3 = 120^\circ$ ) and  $C_{Z_0}, A_{Z_0}, \gamma_{Z_0}$  are adjustable parameters.[125]

#### 5. Four body torsion term

This term describes the interaction between 4 atoms (eg.  $l, j, k, n$  in organic molecules and is expressed as[126]:

$$\sum_{i \in \{l, j, k, n\}} [B_1(1 + \cos \phi_{ljk n}) + B_2(1 - \cos 2\phi_{ljk n}) + B_3(1 + \cos 3\phi_{ljk n}) + B_4] \quad (11)$$



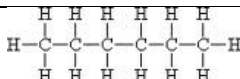
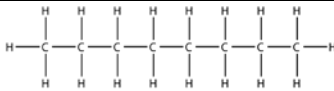
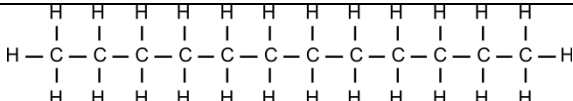
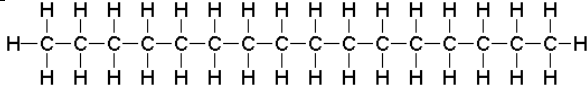
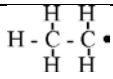
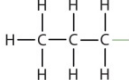
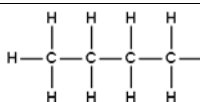
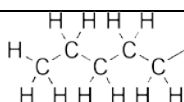
This term depends on the dihedral angle  $\phi$ , which is the angle between two planes  $P_1$  and  $P_2$  where  $\{l, j, k\} \subset P_1$  and  $\{j, k, n\} \subset P_2$

### 3.1.3. System preparation

The adsorption of alkane chains with lengths of 6 (n-hexane), 8, 12 and 16 backbone carbon atoms on an  $\alpha$ -alumina surface was studied using the reactive force field mentioned above. Other than this hydrocarbon radicals with 2, 3, 4, and 5 carbons were adsorbed on silicon. The latter part was carried out at the University of Helsinki.

## 1. Molecules

Table II-8: Physical properties and molecular structures of molecules and radicals used for MD simulations

Molecule	Molecular formula	Molecular weight (g mol <sup>-1</sup> )	Structure
n-hexane	C <sub>6</sub> H <sub>14</sub>	86.18	
octane	C <sub>8</sub> H <sub>18</sub>	114.23	
dodecane	C <sub>12</sub> H <sub>26</sub>	170.33	
hexadecane	C <sub>16</sub> H <sub>34</sub>	226.44	
Ethyl group	C <sub>2</sub> H <sub>5</sub>	28.05	
propyl	C <sub>3</sub> H <sub>7</sub>	60.1	
butyl	C <sub>4</sub> H <sub>9</sub>	57.11	
pentyl	C <sub>5</sub> H <sub>11</sub>	71.14	

N-hexane is a simple molecule and well suited for simulation studies, however its high vapour pressure (161.7 mbar or 16.17 kPa at 20 °C) makes it difficult to study its deposition under ultra-high vacuum conditions experimentally. For this reason, this simple alkane

molecule has been used as a starting point for MD simulations. Other than this, longer alkane chains ( $C_8H_{18}$ ,  $C_{12}H_{26}$ , and  $C_{16}H_{34}$ ) has been used in order to see the effect of chain length on adsorption of organics and hydrocarbon radicals ( $C_2H_5$ ,  $C_3H_7$ ,  $C_4H_9$ , and  $C_5H_{11}$ ) have been used for comparing hydrocarbon molecule vs. radical adsorption and sticking. Molecular weights and structures of different molecules and radicals are given in Table II-8.

## 2. Substrate

Since aluminium has always a native oxide layer, only an  $\alpha$ -alumina slab is modelled in MD simulations.  $\alpha$ -Alumina (corundum) is the most stable, well-characterized phase of alumina and is used in various sectors owing to its high hardness, resistance to corrosion and huge melting point combined with its relatively low electrical conductance.[163],[164]

The interaction parameters for the Al-O system were obtained by fitting simulation data to experimental infrared spectra, experimental density, radial distribution function and the elastic constants of  $\alpha$ - $Al_2O_3$  using the genetic algorithm reported elsewhere[165],[162],[166]. The optimized force field parameters are given in Table II-9. The different elastic constants for the relaxed  $\alpha$ - $Al_2O_3$  (0001) surface were calculated using the equations reported by Fast *et al.* for hexagonal systems.[167] The values obtained for the different elastic constants agree well with the experimental values (Table II-9). The unit cell dimensions of the relaxed surface are found to be  $a=4.759 \text{ \AA}$ ,  $b = 4.759 \text{ \AA}$  and  $c = 12.991 \text{ \AA}$ ,  $\alpha = 90^\circ$ ,  $\beta = 90^\circ$  and  $\gamma = 120^\circ$ . To further validate our model, the surface energy was calculated from the energy differences between the surface and bulk models. The modelled value ( $1.40\pm 0.05 \text{ J/m}^2$ ) is in good agreement with the values reported in literature ( $1.41\pm 0.09 \text{ J/m}^2$ )[109],[168]

Table II-9: Comparison of bulk modulus and elastic constants for  $\alpha$ -alumina between this and previous studies along with the experimentally reported values.[169]

Elastic constant (GPa)	This study	Other simulations	MD Experimental values
C11	553	523	498
C12	138	147	163
C13	103	129	117
C33	503	427	502
Bulk modulus	251	253	255

The alumina system for the adsorption simulations was constructed from the crystallographic unit cell of  $\alpha$ -alumina[170]. It is known that the non-polar aluminium terminated surface is the most stable[109],[171] hence the bulk structure was cleaved at the aluminium layer to obtain the unrelaxed (0001) surface of the  $\alpha$ -Al<sub>2</sub>O<sub>3</sub>. The system consisted of 3840 atoms in a (8×8×2) supercell with a surface area of 663.8 Å<sup>2</sup>. The relaxation of the alumina surface was carried out during 20 ps under NVT conditions (canonical ensemble) using global velocity rescaling for the temperature control. The topmost alumina layers tend to displace inwards during the relaxation process. This is well described by our model. The calculated displacements of the top four layers (-90%, -1.2%, -43% and 20%) in our model are very close to the previously reported values.

Previous simulations have shown that this force field can predict correctly the structural properties of inorganic and POSS systems. In the present work, we extended the parameter set to simulate the adsorption process and interface structure of the  $\alpha$ -alumina – organic interface. Parameters for C-C, C-H and H-H interactions were taken from a previous study.[126] The Lennard – Jones parameters for alkane –  $\alpha$ -Al<sub>2</sub>O<sub>3</sub> interactions presented in Table II-10 were obtained from the work reported by Sun.[172] However, it is important to note that the alkane chains are non-polar in their bulk state and the partial charges on the chains close to the alumina surface are also nearly negligible. Hence the charge transfers between alumina and alkane systems were ignored in our simulations. It was reported previously that this approach is good enough to calculate structural properties of alkane chain adsorption on top of alumina surfaces.[109]

Table II-10: Parameters for the Lennard – Jones potential.[172]

<b>Pairs</b>	$r_{ij}$ (nm)	$\epsilon_{ij}$ (kJ/mol)
Al-C	0.37	0.75
Al-H	0.33	0.40
O-C	0.36	0.50
O-H	0.35	0.25
C-C	0.35	0.27
C-H	0.30	0.12
H-H	0.20	0.10

The deposition process was simulated for  $C_6H_{14}$ ,  $C_8H_{18}$ ,  $C_{12}H_{26}$  and  $C_{16}H_{34}$  molecules. First, the molecules were relaxed at 300K for 20 ps. Next, deposition on the  $\alpha$ -alumina surface was simulated for deposition energies of 0.01, 0.1, 1.0, 5.0 and 10.0 eV and angles of  $0^\circ$ ,  $30^\circ$  and  $60^\circ$  with respect to the surface normal using a time step of 0.2 fs for a total duration of 20 to 100 ns. This is enough for most of the energy to be dissipated into the system, although the molecules might be still diffusing on the alumina surface due to the low binding energies between alkane chains and substrate. For each condition, the deposition on 20 randomly selected sites was simulated. The deposition process is also carried out at 300K.

## **3.2. Deposition of PS and PMMA fragments by DFT Calculations**

### **3.2.1. DFT Calculations**

Properties of materials are determined by their electronic structure (i.e. the interactions of electrons with nuclei) and these interactions are dealt with quantum mechanics. Density functional theory (DFT) is a computational quantum mechanical modelling method used for investigating electronic structure, mainly ground states of many-body systems. One way to predict the ground state properties of an atom is to solve the N-electron Schrodinger equation for the N-electron ground-state wave function. This approach is potentially accurate, however computationally inefficient for large systems.

In DFT approach, it is assumed that ground state properties of a system are determined by the total ground state electron density, to say instead of determining the N-electron wave function, N one-electron wave functions are determined. Each one electron wave function is evaluated iteratively and the total electron density is obtained as a sum of all electrostatic and exchange-correlation energies. Being a simple independent-particle theory, Kohn-Sham DFT is in principle able to describe exact density and exact total energy of any interaction, correlated electronic system. Yet, its complexity lies in the exchange-correlation functional term it uses to approximate ground states. Exchange is a result of antisymmetry due to the Pauli Exclusion Principle and the correlation accounts for many body effects. Simple approximations like local density approximation (LDA), generalized gradient approximation (GGA), meta-GGA and hybrids have performed well for a wide range of problems in chemistry and physics.

While DFT approach is able to describe ground state properties, it is not able to describe electronically excited states. It tends to underestimate the gap between occupied and unoccupied states in non-metallic systems.

LDA exchange-correlation functional is likely to produce poor results for molecules, however GGA is considered to be more appropriate. [134]

### 3.2.2. System Preparation

In order to adsorb characteristic fragments of PS and PMMA on various substrates, first the fragments and substrates were prepared and relaxed. The details are given below.

#### 1. Molecules

Some specific fragments for PS ( $C_3H_3^+$ ,  $C_3H_5^+$ ,  $C_6H_5^+$ ,  $C_7H_7^+$ ,  $C_8H_9^+$  and  $C_9H_7^+$ ) and PMMA ( $C_2H_3O_2^+$ ,  $C_4H_5O^+$ ,  $C_6H_{11}O_2^+$ ), which were also observed in the positive ToF-SIMS spectra of PS and PMMA deposits, were chosen. In order to obtain fragments, one hydrogen was removed from the radical carbon after creating neutral molecules using Avogadro software.[173] Resultant PS and PMMA fragments with their corresponding radical atoms are shown by Leeson *et al.* [174] and Fig. II- 18:. They were let to relax until self-consistent forces were lower than  $1 \times 10^{-6}$  eV/Å using DFT calculations with parameters mentioned above.

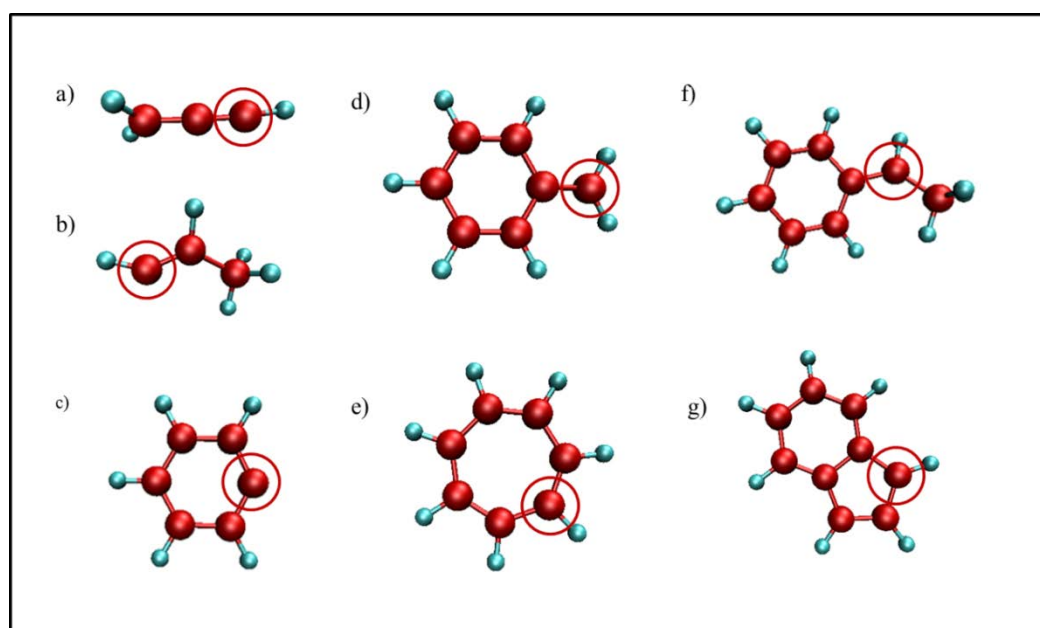


Fig. II- 17: Structures of PS fragments adsorbed on Ag(111), Ag(100),  $Al_2O_3(0001)$ , Pt(111) and Si(111) surfaces for a)  $C_3H_3$ , b)  $C_3H_5$ , c)  $C_6H_5$ , d)  $C_7H_7$  (benzylum), e)  $C_7H_7$  (tropylium) f)  $C_8H_9$  g)  $C_9H_7$ . Red spheres represent C and cyan H atoms. Radical C atoms are indicated by red circle.

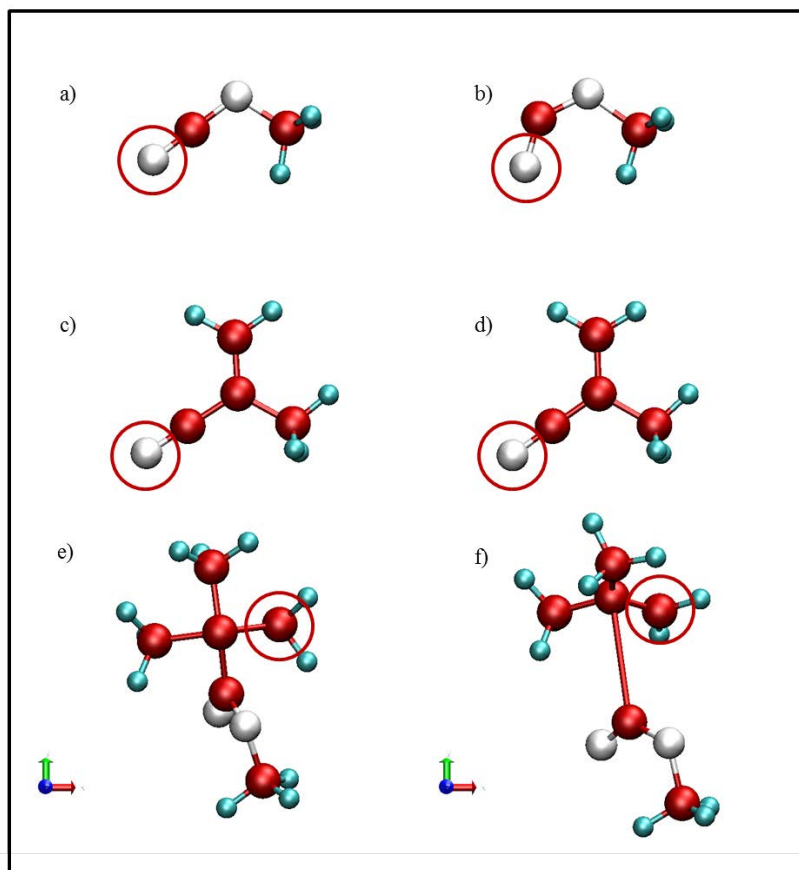


Fig. II- 18: Structures of PMMA fragments adsorbed on Ag(111), Ag(100), Al<sub>2</sub>O<sub>3</sub>(0001), Pt(111) and Si(111) surfaces for a) C<sub>2</sub>H<sub>3</sub>O<sub>2</sub> before relaxation, b) C<sub>2</sub>H<sub>3</sub>O<sub>2</sub> after relaxation, c) C<sub>4</sub>H<sub>5</sub>O before relaxation, d) C<sub>4</sub>H<sub>5</sub>O after relaxation, e) C<sub>6</sub>H<sub>11</sub>O<sub>2</sub> before relaxation, and f) C<sub>6</sub>H<sub>11</sub>O<sub>2</sub> after relaxation. Red spheres represent C, cyan H, and white O atoms. Radical C atoms are indicated by red circle.

## 2. Substrates

Ag(100) fcc, Ag(111) fcc, Al<sub>2</sub>O<sub>3</sub> (0001) hexagonal, Pt(111) fcc and Si(111) unit cells were created by VESTA software[175] and the thickness of the slab was increased using GDIS software[176]. The surface energy was calculated for varying thicknesses of the slab and the thickness of the surface was optimized with respect to the surface energy; ie. the thickness corresponding to the minimum surface energy was taken. Lattice parameters, cut-off energy and k-point spacing were optimized with respect to the total energy of the system. Final optimized slabs, with periodic boundary conditions consisting of different number of layers and different size of supercells are shown in Fig. II-19, Fig. II- 20:, Fig. II- 21:, Fig. II- 22:, and Fig. II- 23. The periodic repetitions were separated by 15 Å of vacuum. All parameters used (atomic layer slabs, size of supercell) for building the surface and optimization parameters (cut-off energy, k-point mesh) are shown in Table II- 11. In the calculations, few bottom layers were kept fixed for all the surfaces and the rest of the atoms were all relaxed until self-consistent forces were lower than  $5 \times 10^{-4}$  eV/Å.

Table II- 11: Parameters used for building different surfaces

	Ag(100)	Ag(111)	Al <sub>2</sub> O <sub>3</sub> (0001)	Pt(111)	Si(111)
slab thickness (layers)	5	5	7	5	5
vacuum (Å)	15	15	15	15	15
Cut-off energy (eV)	500	500	450	400	400
k-point sampling	3x3x1	2x2x1	1x1x1	2x2x1	2x2x1
supercell	3x3	2x2	3x3	4x4	3x3

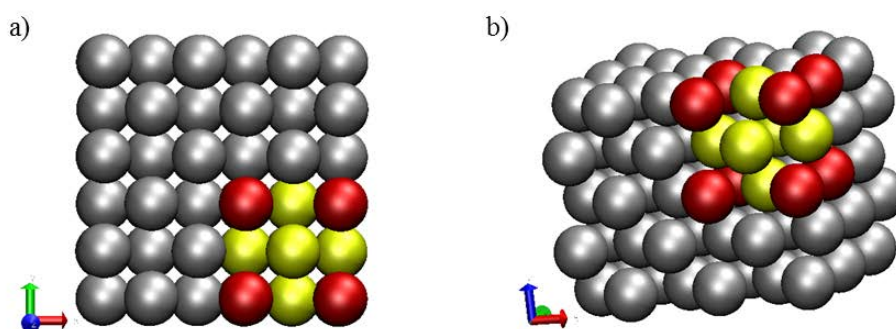


Fig. II-19: a) top and b) side view of the Ag (100) slab. Red spheres represent the corner and yellow the face atoms involved in the unit cell

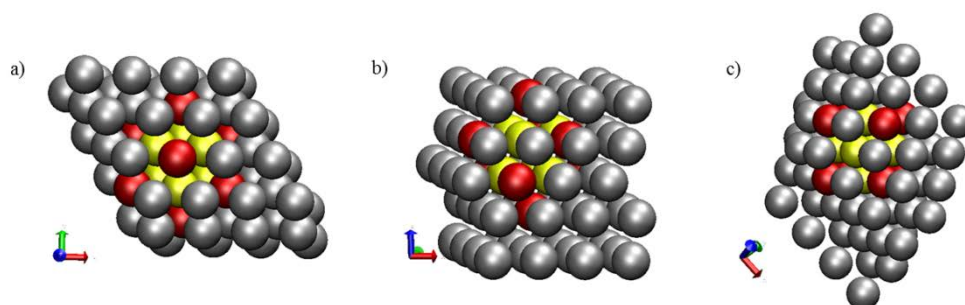


Fig. II- 20: a) top and b) side and c) (100) plane of the Ag(111) slab. Silver atoms are shown in grey. Red spheres represent the corner and yellow the face atoms involved in the unit cell.



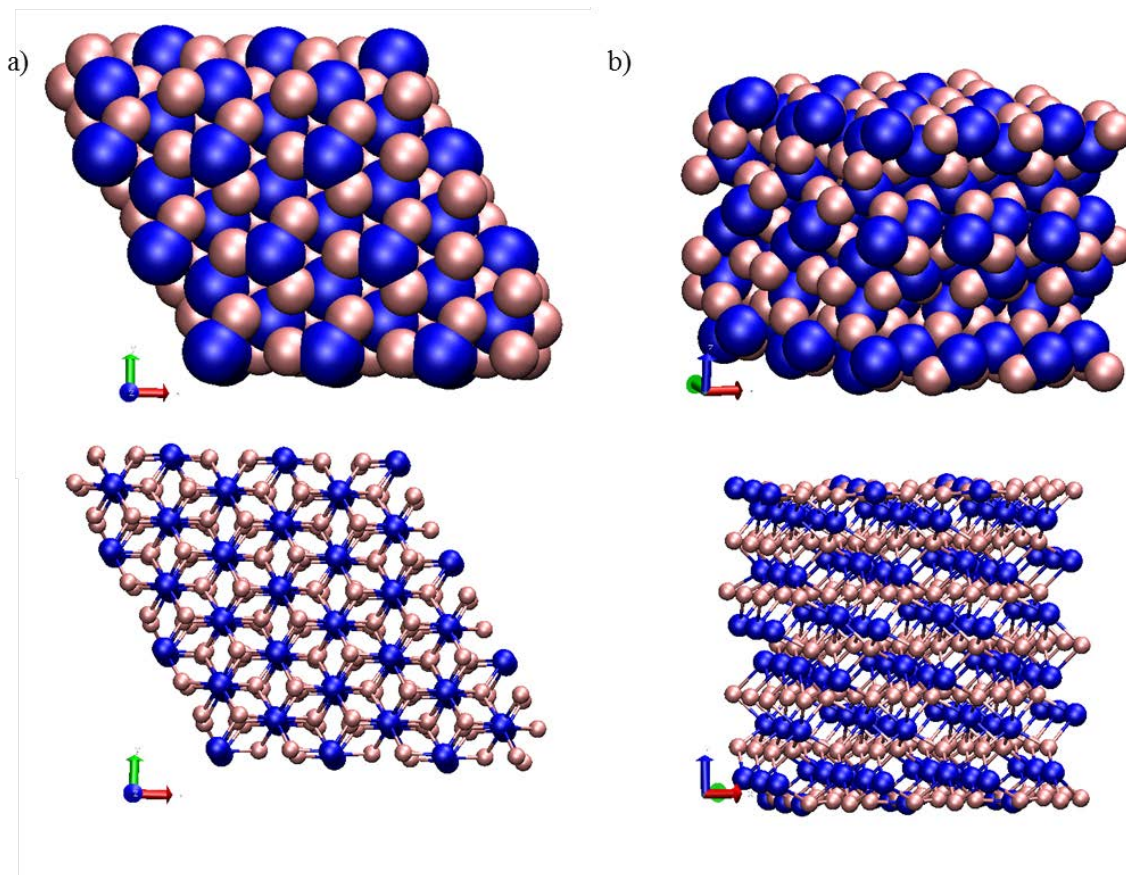


Fig. II- 21: a) top and b) side views of the  $\text{Al}_2\text{O}_3$  (0001) slab. Aluminium atoms are shown in blue and oxygen atoms in pink.

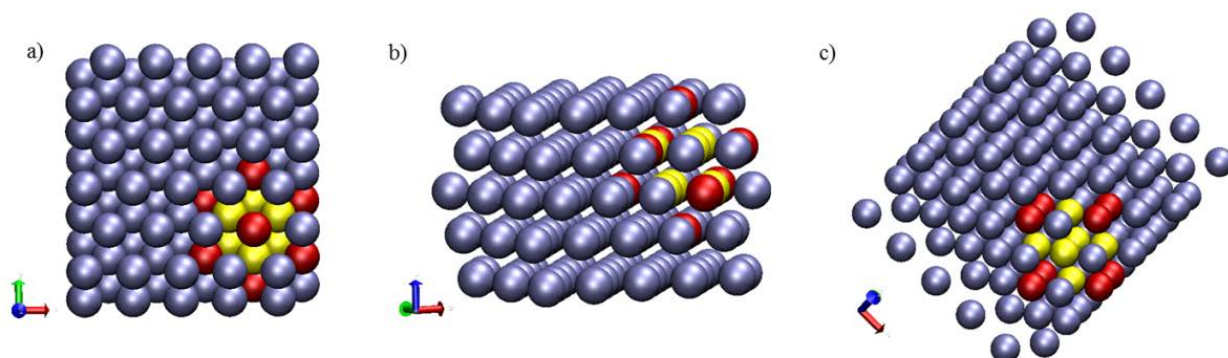


Fig. II- 22: a) top and b) side and c) (100) plane of the Pt(111) slab. Red spheres represent the corner and yellow the face atoms involved in the unit cell. Platinum atoms are represented in ice blue.



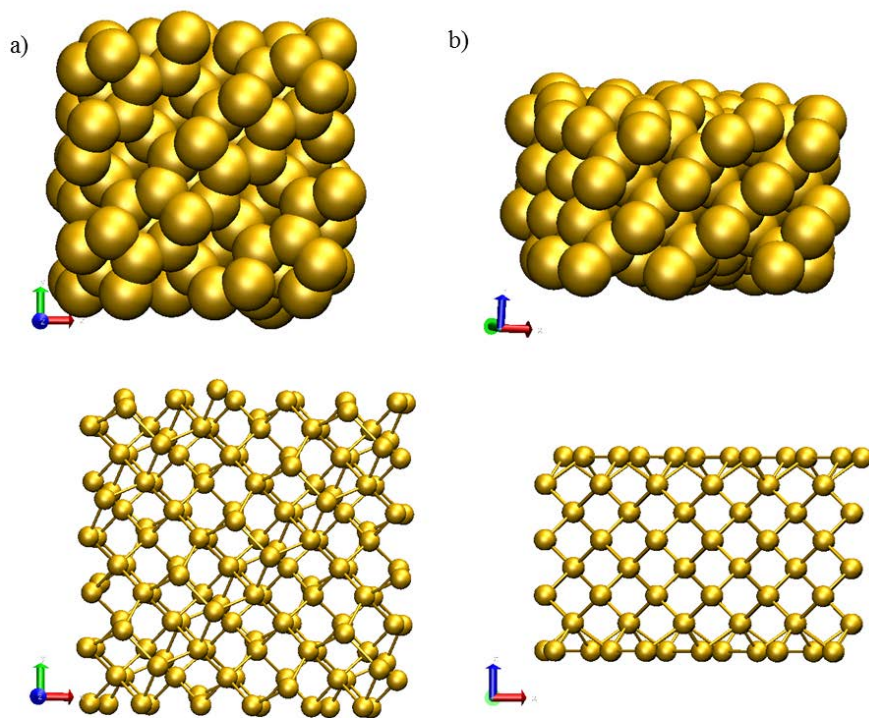


Fig. II- 23 a) top and b) side views of the Si (111) slab. Silicon atoms are represented in yellow.

### 3. Adsorption of molecules on the substrates

Characteristic PS and PMMA fragments were adsorbed on Ag(111), Ag(100), Al<sub>2</sub>O<sub>3</sub> (0001), Pt(111) and Si(111) using DFT calculations. Periodic DFT calculations were carried out using the Vienna ab-initio simulation package (VASP)[177],[178],[179],[180] using the Perdew-Wang generalised gradient approximation (GGA-PW91)[181],[182] and the projector augmented wave (PAW) method for the silver,  $\alpha$ -alumina, platinum, silicon, carbon, hydrogen, and oxygen pseudopotentials.[183],[184] The electronic one-particle wave functions were expanded to a plane-wave energy cut-off of 400-500 eV. The fragments were positioned on three different binding sites on the surface (only for Ag) and simultaneous relaxation of the fragment and two top layers of the substrate were continued until the self-consistent forces were lower than 0.01 eV/Å. The adsorption energy of the fragments on all surfaces was calculated for each case. As the interaction of molecular fragments with the metal surface lead to chemisorption, Lennard-Jones interactions were not considered. The adsorption energy was defined as[185]:  $E_{ad}=E_{tot}-(E_{surf}+E_{mol})$  where  $E_{tot}$ ,  $E_{surf}$ , and  $E_{mol}$  are the total energy of the relaxed adsorption complex, the energy of the clean surface and the energy of the isolated molecule.



# **Chapter III:**

## **Adsorption of alkane fragments and chains on the silicon and $\alpha$ -alumina surface by MD simulations**

### **1. Introduction**

This chapter is aimed to be a preliminary work for the following chapters and gives the results of MD simulations on the adsorption of molecules and fragments of hexane and longer alkane chains on silicon and  $\alpha$ -alumina surfaces. Simulations with hexane fragments were carried out at the University of Helsinki, while the ones with hexane and longer alkane chains were carried out at CRP Gabriel Lippmann, both with the aim of planning experimental work. The results of sticking are important for the choice of substrates for the Storing Matter Technique in relation to collection part of the technique which is mainly governed by sticking of the matter on the collector substrate. First experimental trials showed that the hexane molecule is not a good choice for the Storing Matter experiments, mainly because of its relatively high vapour pressure and the difficulty to distinguish it from impurities. Moreover, the use of this simple molecule and its fragments gives an idea about the sticking of intact molecules vs. fragments. Longer alkane chains have also been used in order to see the effect of some parameters like energy, angle of incidence and the chain length on adsorption.

### **2. Adsorption of hexane fragments on silicon (University of Helsinki)**

No sticking of hexane on silicon at room temperature was observed by MD simulations. However, for radicals the sticking probability increases dramatically (Fig. III-1). For  $C_5H_{11}$  at 300 K, impacting on the surface at 2.5 eV, about 80% of the radicals stick with the fragment deposited at normal incidence. Up to an incidence angle of about  $40^\circ$  with respect to the surface normal, the sticking probability does not change significantly. For more grazing incidence the probability decreases. At  $80^\circ$  incidence, about 40% of the fragments stick on the surface. For smaller fragments, the probability is even higher (e.g. about 90% for  $C_2H_5$ ).

These results were confirmed by ab-initio DFT calculations. The global trend can be explained by the dangling bond in the radicals which can react with one silicon atom of the reconstructed dimers. At the same time, the bond energy between the carbon radical and the substrate atoms increases for shorter chain lengths. For example,  $\text{CH}_3$  has an adsorption energy of 1.53 eV on Ag, and  $\text{C}_5\text{H}_{11}$  an adsorption energy of 1.03 eV calculated by ab-initio DFT calculations. The energy changes systematically with the number of backbone carbon atoms. For  $\text{Al}_2\text{O}_3$ , the energies for the same radicals change to 0.36 eV and 0.15 eV, respectively. On the oxygen terminated  $\text{Al}_2\text{O}_3$ , no dangling bonds are available which explains the weaker adsorption energies. At the same time, this results in reduced sticking probabilities for eV hexane fragment deposition.

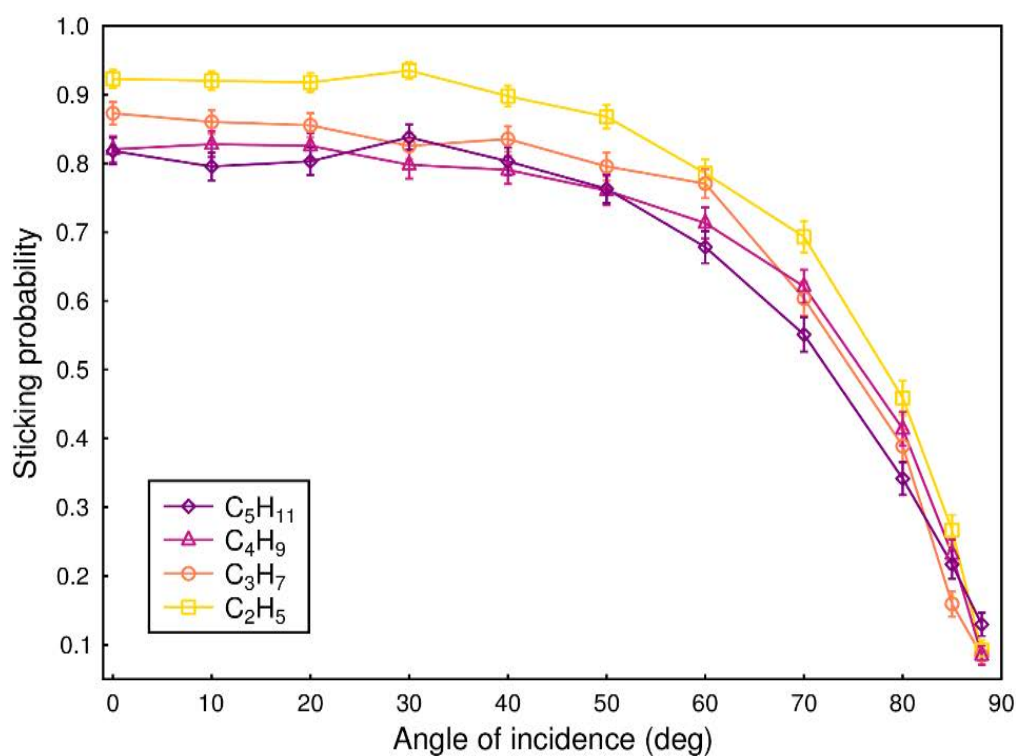


Fig. III-1-: Sticking probability of 2.5 eV fragments deposited at 300 K on a Si(100) surface by ab-initio MD simulations

### 3. Adsorption of alkane chains of different lengths on $\alpha$ -alumina (LIST)

For the adsorption of intact molecules, the interactions are mainly controlled by van der Waals forces. For hexane ( $\text{C}_6\text{H}_{14}$ ), they are too weak to observe adsorption at room temperature. DFT calculations give adsorption energies between 0.2 and 0.3 eV for hexane adsorption on alumina depending on the orientation of the molecule. For metal surfaces like

silver, the bonds are even weaker (0.01 – 0.02 eV depending on orientation). The situation changes for longer alkane molecules. C<sub>8</sub>H<sub>18</sub> and C<sub>12</sub>H<sub>26</sub> stick on the alumina surface for deposition energies of 0.1 eV or lower and C<sub>16</sub>H<sub>34</sub> sticks for deposition energies of 1 eV or lower. Not surprisingly, an increased chain length results in larger van der Waals and a higher probability of sticking. In order to shed further light on hydrocarbon sticking on alumina, we have studied the sticking process of alkane chains with lengths varying between 6 and 16 backbone carbon atoms on an  $\alpha$ -alumina surface by means of the reactive force field developed by Kieffer *et al.* For each number of carbon atoms, the deposition energy was varied between 0.01-10.0 eV and the incidence angle between 0-60 °. Sticking coefficients have been calculated for each case, and the effect of carbon chain length, deposition energy and incidence angle on adsorption were examined.

Table III-1: Adsorption probability of alkane molecules on the  $\alpha$ -Al<sub>2</sub>O<sub>3</sub> with respect to changing chain size, deposition energy and incidence angle. The colour scale shows the adsorption probability, white representing 100 % and black 0 % adsorption. No landing on the surface is observed for the dark red region.

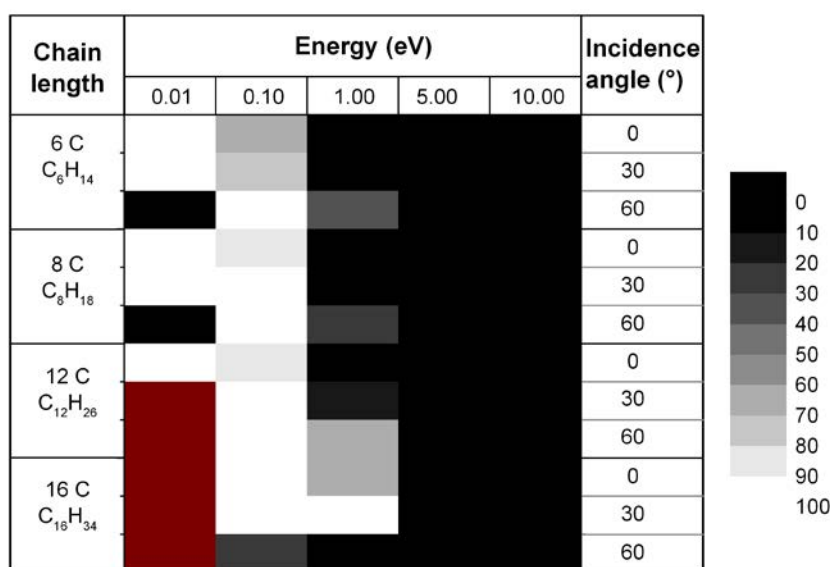


Table III-1 shows the information about adsorption of various lengths of single molecule of alkanes on the  $\alpha$ -Al<sub>2</sub>O<sub>3</sub> surface for various energies and incidence angles. Three different cases are observed for the adsorption of alkane molecules, so three different regions are defined. In region I (dark grey), which corresponds to higher deposition energies used in this study, no sticking of the molecules is observed. The molecule is backscattered once it lands on the alumina surface. In the region II (white to light grey), which is characterized by lower to medium adsorption energies depending on the chain lengths and in some cases incidence angle, the molecule stays on the surface with or without bouncing once. At this point it

should be noted that for constant energy, the velocities decrease with increasing molecule size, which explains the higher adsorption probabilities for larger molecules. Region III is specified by the lowest energy and the largest alkane chains. In this region, the thermal energy of the molecule is large compare to the deposition energy, so that the downward motion of the molecule is lost after some time. However, if the molecules would arrive on the surface, adsorption is expected.

The most common mechanism for the incoming alkane molecule was either to stay on the surface or to be repelled. In case of region II, adsorption of the molecule on the surface can only be confirmed for the time scales invested in this study as the molecule is still diffusing after landing on the surface. In this study, the ratio of chain length to deposition energy defines whether adsorption is observed or not, which is related to the relatively weak van der Waals interactions. For shorter chains, adsorption is only possible if a radical is in the alkane chain. This has been observed for the deposition of alkane radicals on a hydrogenated diamond surface with a dangling bond site, where sticking is expected to be much more frequent compared to neutral and nonpolar alkane molecules, Träskelin *et al.* found that the highest sticking probability resulted when the molecule was impinging on the surface at a distance of 0.7 Å from the dangling bond site[117]. Over a distance of 1.7 Å, almost no sticking was observed. The difference between our work and the one by Träskelin *et al.* is physisorption in our case and chemisorption in the latter. The final equilibrium distance between alkane molecules and alumina substrate of 3 Å is simply a result of the balance between repulsive and attractive van der Waals forces experienced by all the atoms of the alkane chain.

In Table III-1, within regions I and II, different grey colour scales correspond to different adsorption probabilities of alkane molecules on alumina, white for a full adsorption and black for zero adsorption. It can be seen that the most important parameters for adsorption are the length of the molecule and the deposition energy. The incidence angle plays only a minor role. At 1 eV, this effect can be seen clearly for C<sub>6</sub>H<sub>14</sub>, C<sub>8</sub>H<sub>18</sub> and C<sub>12</sub>H<sub>26</sub>. At this energy, the probability of adsorption increases with increasing angle of incidence. The effect of the energy and chain length can be observed in a wider range of parameters. Region II consists of higher energy and lower chain length compared to region III and lower energy and higher chain length compared to region I. Starting with the energy of of 1 eV or higher, the molecule is backscattered from the surface with the exception of higher incidence angles and some of

the longer chains. For adsorption at higher energies, much longer chains would be required. When the molecule approaches the surface with energies of 1 eV or higher, the adsorption energy resulting from the van der Waals interactions is small compared to the kinetic energy and adsorption is impossible. For the case of 12 or 16 C deposited at 1 eV depending on the angle of incidence, the forces acting per atom decreases because of the increased length of the chain and this gives to the molecule more possibility to interact with the surface without being backscattered immediately. The deposition energy, the chain length and to some extent the incidence angle, limit the adsorption of molecules in region I.

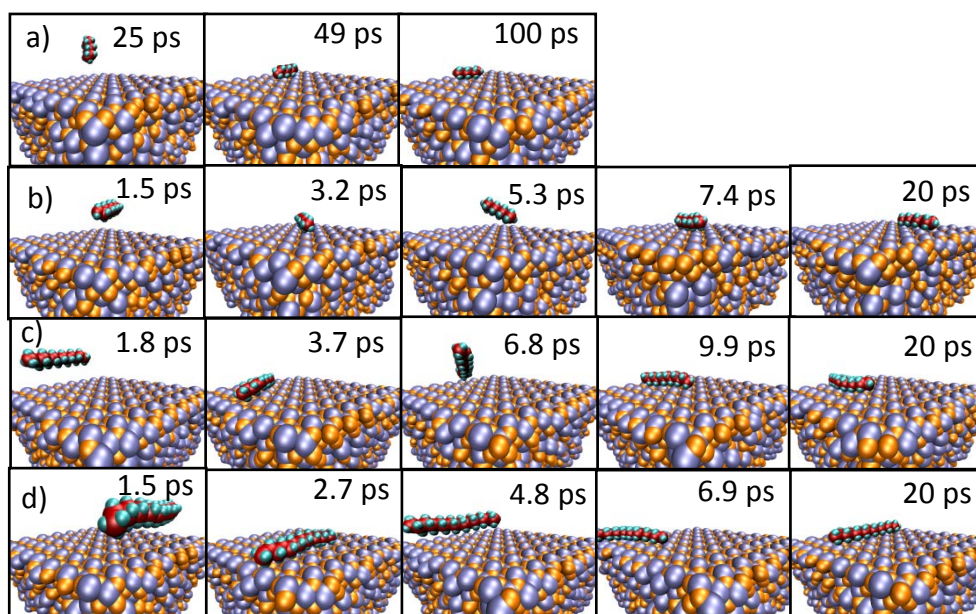


Fig. III-2: Adsorption and diffusion of alkane molecules of different length on the  $\alpha$ -Al<sub>2</sub>O<sub>3</sub> at indicated time scales and energies: a) 6 C, 0.01 eV b) 8 C, 0.1 eV, c) 12 C, 0.1 eV d) 16 C, 1.0 eV. Red spheres represent carbon atoms, cyan hydrogen, orange oxygen and blue aluminium.

Fig. III-2 shows the geometries and time scales of adsorption for various alkane molecule sizes at different energies. All the cases are taken from region II where the molecule stays on the surface until the end of the simulation. The time to arrive on the alumina surface depends on the ratio of energy to molecular mass. It is obvious that it takes much longer (49 ps) for the C<sub>6</sub>H<sub>14</sub> molecule to land on the surface in case of 0.01 eV than for the longer chains and the considered energies (Fig. 1a). With increasing energy and longer chain size, it takes a much shorter time for the molecule to land on the surface: 3.2 ps for C<sub>8</sub>H<sub>18</sub> at 0.1 eV, 3.7 ps for C<sub>12</sub>H<sub>26</sub> at 0.1 eV and 2.7 ps for C<sub>16</sub>H<sub>34</sub> at 1.0 eV (Fig. 1b, c, d). Considering they are being deposited at similar energies, the small time difference between 8 C and 12 C is due to the increased chain length. For 16 C it takes the shortest time to reach the surface which is

due to higher deposition energy. For energies of 0.1 eV and higher, the molecule bounces once after coming into contact with the alumina surface. After landing on the surface a second time, it stays and diffuses over the surface for the remaining time: 7.4-20 ps for 8 C, 9.9-20 ps for 12 C and 6.9-20 ps for 16 C. For all the cases the molecule prefers to orient parallel to the surface rather than perpendicular, since the van der Waals interactions between surface and alkane chain are the only forces acting on the molecule. For a dense alkane layer on  $\alpha$ -Al<sub>2</sub>O<sub>3</sub>, Claire *et al.* found that molecules adsorb perpendicular to the surface mainly because of interactions between neighbouring chains.[110]

## 4. Conclusion

For the adsorption of hexane molecule and fragments on silicon, no sticking was observed for the intact molecule on silicon at room temperature studied by MD simulations. However, for the fragments the sticking was frequent, increasing with the decreasing radical size and decreasing angle of incidence. The results were also confirmed by ab-initio DFT calculations.

For the adsorption of hexane and longer alkane chains on  $\alpha$ -alumina, an  $\alpha$ -Al<sub>2</sub>O<sub>3</sub> (0001) surface and single chain alkane models were constructed and validated successfully. MD simulations using a reactive force field predict that the adsorption of alkane chains on the alumina surface is only observed in a well-defined region depending on the ratio of molecule size to deposition energy. For chains with 12 carbon atoms, adsorption occurs at energies below 1 eV. In case of shorter chains, i.e. 6 and 8 carbon atoms, the molecule adsorbs only at lower energies of 0.01 and 0.1 eV. Hence, the simulations reveal that the deposition and adsorption of molecules are highly influenced by the deposition energy and chain length rather than the incidence angle.

Comparing the adsorption of hydrocarbon radicals to that of intact molecules of various lengths, sticking is more often observed in case of radicals including different conditions of impact energy and angle. Since, use of intact molecules would require a thorough selection of these parameters, we stick to the adsorption of fragments in the next chapters. However, since the adsorption of hexane molecule and thus its fragments is not viable experimentally for Storing Matter deposition, fragments of polystyrene and poly (methyl methacrylate) polymers were chosen for the rest of this work.



# Chapter IV:

## Sputter deposition of Polystyrene (PS)

### 1. Introduction

In this chapter, both experimental and simulation results of the sputter deposition of Polystyrene (PS) in the sub-monolayer are presented. Experimental methods involve ion beam sputtering (Storing matter and sputter deposition in the XPS chamber) for deposition and ToF-SIMS and in-situ XPS for analysis, whereas numerical methods include DFT calculations for adsorption energies and geometries.

First, ToF-SIMS analyses of bulk PS samples using different primary ion projectiles are discussed. Then, the possibilities of sputter deposition of PS in the Storing Matter instrument are assessed. The detection of the deposit and the effect of different primary ion projectiles (for analysis) on the fragmentation are addressed.

For the analysis of organics, the critical primary ion fluence, which is often defined at or below  $1.0 \times 10^{13}$  ions/cm<sup>2</sup>, is an important factor since high fluences increase the fragmentation of organic matter and limit the secondary ion yield. In order to distinguish between two different regions (below and above static limit), investigations of PS sputter deposition were made both in static (below the static limit) and dynamic (above the static limit) regime.

For the static part, the coverage was varied while keeping the primary ion fluence constant and moving the sample under the ion beam. The effect of changing coverage on the fragmentation is observed and ToF-SIMS results are presented. For the dynamic part, the effect of primary ion fluence on the extent of fragmentation was investigated. ToF-SIMS and in-situ XPS results are presented in this section.

The last part concerns the numerical studies which are complementary to experimental studies mentioned in the first three sections.

## 2. ToF-SIMS analysis of bulk Polystyrene samples

In this section, analysis of bulk polystyrene was done by using  $\text{Ar}^+$  and  $\text{Bi}_1^+$  monoatomic and  $\text{Bi}_3^+$  polyatomic primary ions. This enabled us not only to see the effect of different monoatomic projectiles, but also the results of using either monoatomic or polyatomic projectiles on the fragmentation of polystyrene. This data allows us to discuss how the Storing Matter results of this work compare to previous results obtained by the same technique and to compare it to mass spectra obtained on bulk polymer samples. First, secondary ion mass spectra by using different projectiles are shown, and then a comparison of these three different projectiles is made with a discussion of their possible effects on fragmentation. Reference data exists already in literature, but the new data is used as internal reference.

### 2.1. ToF-SIMS spectra of PS analysed by different primary ions

Fig. IV-1 shows ToF-SIMS spectra of PS2000 sample spin-coated on Si substrate. The analysis was done using  $\text{Bi}_1^+$  and  $\text{Bi}_3^+$  primary ions. The most intense peaks observed are  $\text{C}_7\text{H}_7^+$  ( $m/z=91$ ),  $\text{C}_8\text{H}_9^+$  ( $m/z=105$ ),  $\text{C}_9\text{H}_7^+$  ( $m/z=115$ ),  $\text{C}_9\text{H}_9^+$  ( $m/z=117$ ). The same major fragments were observed in a work on the fragmentation of polystyrene by Kawashima *et al.*, where the analysis was made using  $\text{Bi}_3^+$  clusters. [186] In the spectra of PS analysed by  $\text{Bi}_1^+$  ions, there is one order of magnitude of decrease in peak intensities although the primary ion fluences are comparable. (Fig. IV-2). However, the most intense peaks observed are similar. Fig. IV-3 shows the prominent peaks in the fingerprint mass spectra of PS when analysed with  $\text{Ar}^+$  primary ions. [187] In addition to those observed when analysed with  $\text{Bi}_1^+$  and  $\text{Bi}_3^+$  primary ions, peaks at  $m/z=39$  ( $\text{C}_3\text{H}_3^+$ ),  $m/z=51$  ( $\text{C}_4\text{H}_3^+$ ), and some others at low mass region of the spectra are observed. In earlier analysis of polymers using quadrupole analyser recording flight times of ions and using  $\text{Ar}^+$  as analysis beam, the mass spectra of PS showed similar fragments in the lower mass region, like  $\text{C}_3\text{H}_3^+$  ( $m/z=39$ ),  $\text{C}_4\text{H}_3^+$  ( $m/z=51$ ),  $\text{C}_6\text{H}_5^+$  ( $m/z=77$ ),  $\text{C}_7\text{H}_7^+$  ( $m/z=91$ ) and  $\text{C}_9\text{H}_7^+$  ( $m/z=115$ ). [62],[25]. More recently, when analysed with time of flight analysers using  $\text{Ar}^+$ , similar hydrocarbon fragments have been observed in the mass spectra of PS. [93],[188] In general, the intensity of fragments in the lower mass region of the spectra is higher relative to those in the higher mass region (like  $\text{C}^+$ ,  $\text{CH}^+$ ,  $\text{C}_3\text{H}_3^+$  and  $\text{C}_4\text{H}_3^+$ ) in case of  $\text{Ar}^+$ . Hence, our data for the analysis of bulk PS films is comparable to the one in literature, which is a good starting point for the Storing Matter experiments.

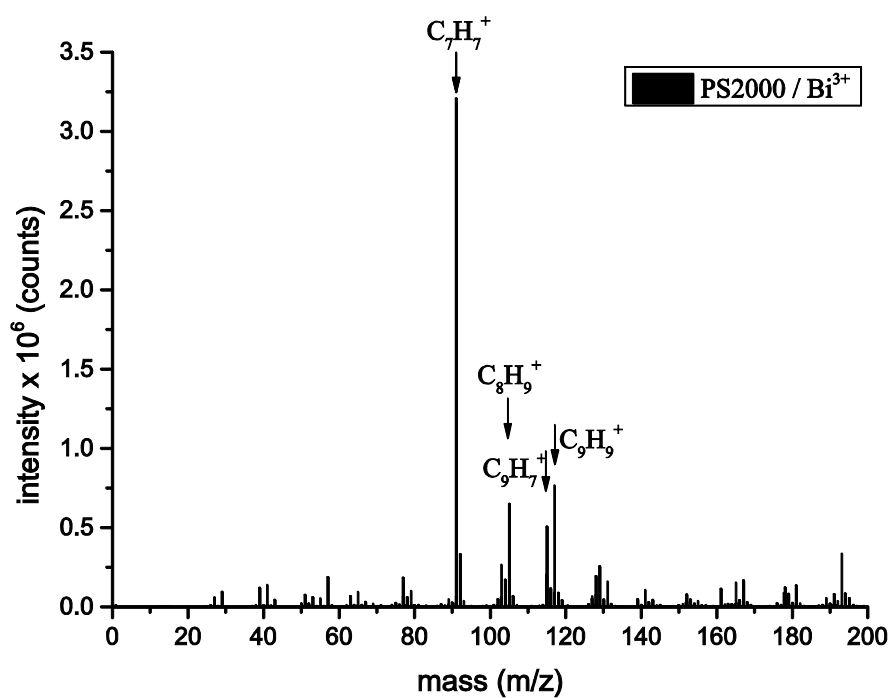


Fig. IV-1: Positive mass spectra of the PS2000 sample spin-coated on Si substrate analysed by Bi<sub>3</sub><sup>+</sup> (primary ion energy: 25 keV, primary ion fluence: 1.2x10<sup>12</sup> ions/cm<sup>2</sup>)

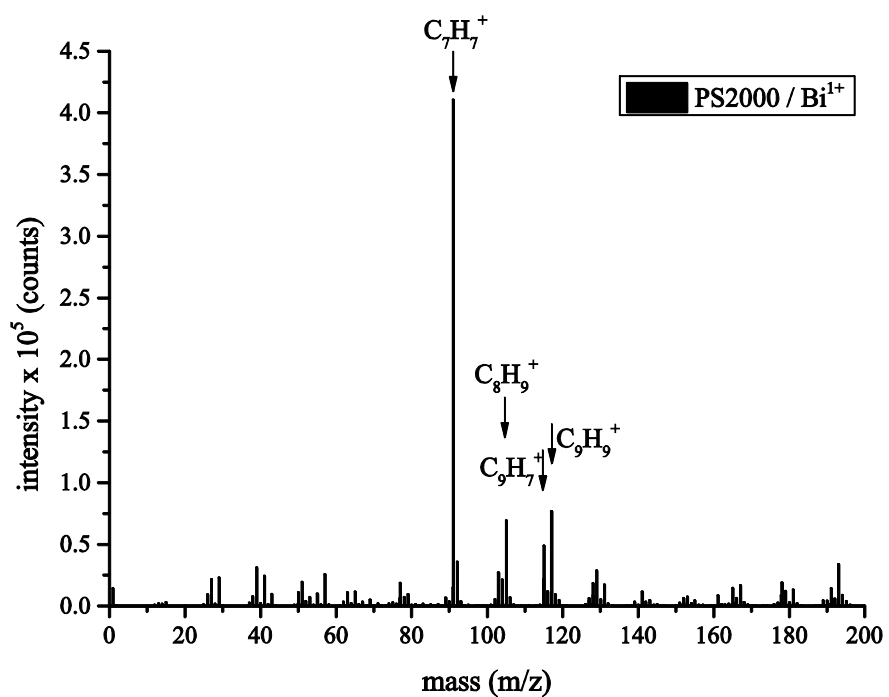


Fig. IV-2: Positive mass spectra of the PS2000 sample spin-coated on Si substrate analysed by Bi<sup>1+</sup> (primary ion energy: 25 keV, primary ion fluence: 3.8x10<sup>12</sup> ions/cm<sup>2</sup>)

Since the analyses by different primary ions are carried out on different instruments (ToF-V for  $\text{Bi}_1^+$  and  $\text{Bi}_3^+$  and ToF-III for  $\text{Ar}^+$ ), and the primary ion energies are also different (25 keV for  $\text{Bi}_1^+$  and  $\text{Bi}_3^+$  and 10 keV  $\text{Ar}^+$ ), absolute ToF-SIMS intensities cannot be compared directly. For this reason, in the next section we look at the high/low peak intensity ratios for three different primary ions and discuss about their effect on the fragmentation of PS.

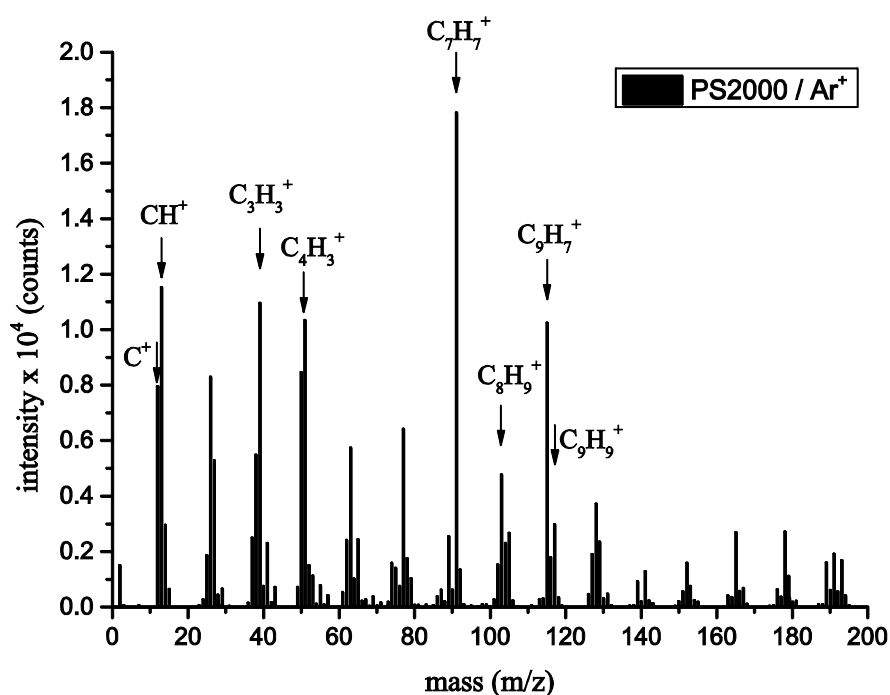


Fig. IV-3: Positive mass spectra of the PS2000 sample spin-coated on Si substrate analysed by  $\text{Ar}^+$  (primary ion energy: 10 keV, primary ion fluence:  $5.6 \times 10^{12}$  ions/cm<sup>2</sup>)

## 2.2. Comparison of effects of $\text{Ar}^+$ and $\text{Bi}_1^+$ and $\text{Bi}_3^+$ projectiles on fragmentation of PS

Table IV-1 contains peak ratios obtained for bulk PS analysis by  $\text{Ar}^+$ ,  $\text{Bi}_1^+$  and  $\text{Bi}_3^+$  primary ions. The results show that the least fragmentation is obtained when the surface is analysed by  $\text{Bi}_3^+$  ions. This is expected since high sputter yields and low penetration depths reduce the damage accumulation on the surface induced by the ion beam in case of the polyatomic bombardment of organic samples.[53] It is also known that significantly higher secondary ion yields are rather obtained for bulk organic samples than for thin layers.[189],[190] Most fragmentation in case of  $\text{Ar}^+$  ions can be explained by the monoatomic character of the projectile, and the lower secondary ion yields caused by the small mass of the projectile ion and, hence, small nuclear stopping power. It is widely accepted that there is considerable

increase in secondary ion yields with the advent of using polyatomic projectiles such as  $C_{60}^+$ ,  $Au_3^+$ ,  $SF_5^+$  and  $Bi_3^+$  as compared to monoatomic projectiles like  $Ar^+$ ,  $Cs^+$ , or  $Ga^+$ . [36] Polyatomic projectiles also cause surface-localized damage which reduces the fragmentation in case of polymer analysis. Thus, it is expected that  $Bi_3^+$  will result in the least fragmentation within the primary ions used in this work. Then, for comparing  $Ar^+$  and  $Bi^+$  projectiles, it is shown by Heile *et al.* that  $Bi^+$  has higher stopping power compared to  $Ar^+$  for the analysis of various organic samples with metallized overlayers. [189] Since the damage created on the analysed surface is correlated with stopping power and with the primary ion energy deposited near the surface, so it is also not surprising that there is less fragmentation in case of analysis with  $Bi_1^+$  compared to  $Ar^+$ , which has a lower stopping power.

Table IV-1: Peak ratios in the mass spectra obtained on the PS reference analysed with  $Bi_1^+$ ,  $Bi_3^+$ , and  $Ar^+$  primary ions. PS reference analysis (no Storing Matter preparation involved).

Peak ratio	$Ar^+$	$Bi_1^+$	$Bi_3^+$
$C_7H_7^+ / CH_3^+$	27.85	126.49	1198.00
$C_7H_7^+ / C_3H_3^+$	1.63	13.24	26.93
$C_7H_7^+ / C_3H_5^+$	7.75	17.03	22.90
$C_8H_9^+ / CH_3^+$	4.18	21.33	242.85
$C_8H_9^+ / C_3H_3^+$	0.24	2.23	5.46
$C_8H_9^+ / C_3H_5^+$	1.16	2.87	4.64
$C_9H_7^+ / CH_3^+$	16.00	15.03	188.16
$C_9H_7^+ / C_3H_3^+$	0.93	1.57	4.23
$C_9H_7^+ / C_3H_5^+$	4.45	2.02	3.60

For the remaining of the chapter, same fragments as in Table IV-1 have been used.

### 3. Development of protocols for ToF-SIMS analysis of PS storing matter deposits

#### 3.1. Detection and localization of the PS StoMat deposit

The Ag collectors with PS fragments from the sputter-deposition process were analysed by ToF-SIMS. The deposits were localized with a stage scan of the collector. Fig. IV-4 shows the secondary ion images of the positive ions that are specific and non-specific to polystyrene. For the fragments that are specific to PS such as  $C_7H_7^+$ ,  $C_8H_9^+$ , and  $C_9H_7^+$ , there is an increase in the intensity in the region where the deposit is located. This distinguishes PS specific fragments from the others, which might not be necessarily resulting from the fragmentation of PS, but rather from carbohydrate impurities. Then, a series of spectra were taken along several diameters of the collector until finding the maximum intensity of specific PS fragments in vertical and horizontal directions. After finding the centre of the deposit, a series of spectra were taken through the centre of the deposit (Fig. IV-4).

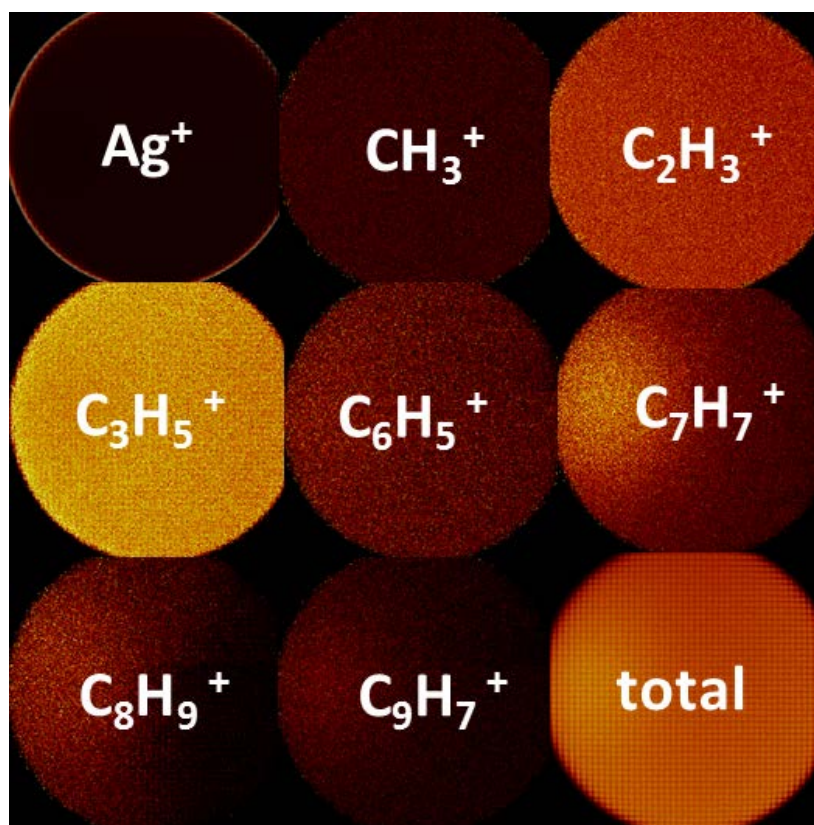


Fig. IV-4: Secondary ion images of positive ions observed in the positive secondary ion mass spectra of the Ag collector with PS deposit obtained by a stage scan of the collector (deposits prepared with constant primary ion fluence at  $5.6 \times 10^{12}$  ions/cm<sup>2</sup> for a total number of primary ions of  $2.66 \times 10^{13}$ ) / intensities normalized to Ag intensity

Fig. IV-5 shows the secondary ion images of the PMMA fragments for a given counts of secondary ions. Here, in addition to the increase of intensities of specific fragments, a slight increase in Ag intensity can be observed enhanced by the presence of the deposit. For this reason, Ag intensity is not used for normalizing ToF-SIMS data.

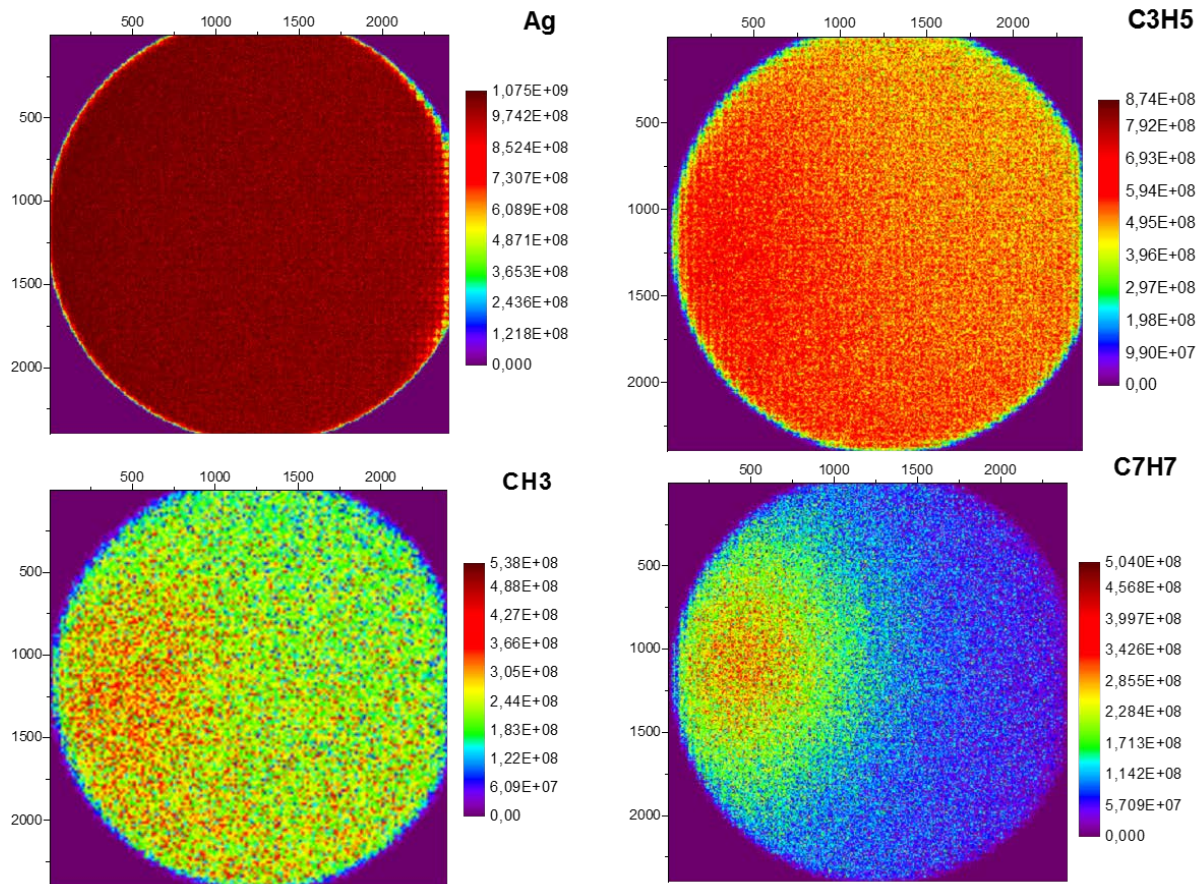


Fig. IV-5: Secondary ion images of positive ions observed in the positive secondary ion mass spectra of the Ag collector with PS deposit obtained by a stage scan of the collector (8x8 pixel binning) (deposits prepared with constant primary ion fluence at  $5.6 \times 10^{12}$  ions/cm<sup>2</sup> for a total number of primary ions of  $2.66 \times 10^{13}$ ) / absolute intensities for a total secondary ion counts of  $1.12 \times 10^8$

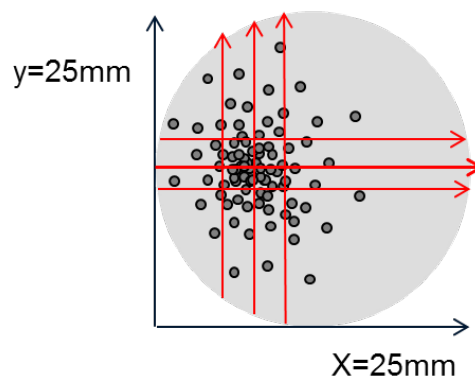


Fig. IV-6: Several linescans taken along diameter of the collector in order to localize the centre of the deposit.

Fig. IV-7 shows spectra taken on the pristine Ag collector, in the centre of the collector with sputter-deposited PS (for  $1.3 \times 10^{13}$   $\text{Ar}^+$  primary ions) and on a thin film of PS spin-coated on silicon. On both the pristine collector and the collector with deposit, hydrocarbon contaminations can be observed in the low-mass range of the spectra. Impurities are mostly of hydrocarbon type and they might be stemming from the many steps during the StoMat deposit preparation: preparation of collectors, preparation of deposits in the StoMat deposition chamber, and transfer of deposits within the StoMat prototype or to the analytical instrument for analysis. The interference of impurities with the ToF-SIMS spectra cannot be completely avoided, but can be reduced to a significant extent by a careful handling of the samples and regular maintenance and cleaning of the vacuum transfer suitcase and of the chambers used for collector preparation and deposition. Even in case of impurities, our results will not be affected qualitatively since these impurities will increase the background signal. However, since they remain low and we are mainly concerned about ratios of fragments as will be shown in the following paragraph, they will not have a huge impact on our results.

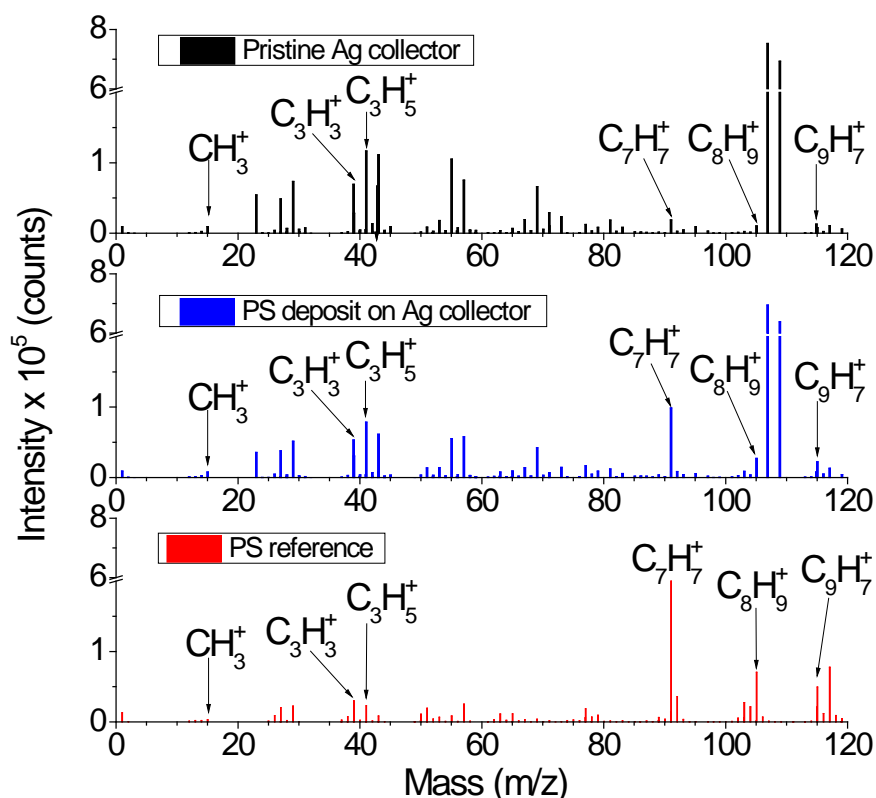


Fig. IV-7: Positive ToF-SIMS Spectra of the Ag collector, PS StoMat deposit (deposits prepared with constant primary ion fluence at  $5.6 \times 10^{12}$  ions/cm<sup>2</sup> for a total number of primary ions of  $2.66 \times 10^{13}$ ) and PS reference film



The spectra of the deposit shows also the addition PS characteristic peaks ( $C_7H_7^+$ , ( $m/z=91$ ),  $C_8H_9^+$  ( $m/z=105$ ),  $C_9H_7^+$  ( $m/z=115$ ), which can be observed with high intensity, yet lower than those in the reference PS spectra.

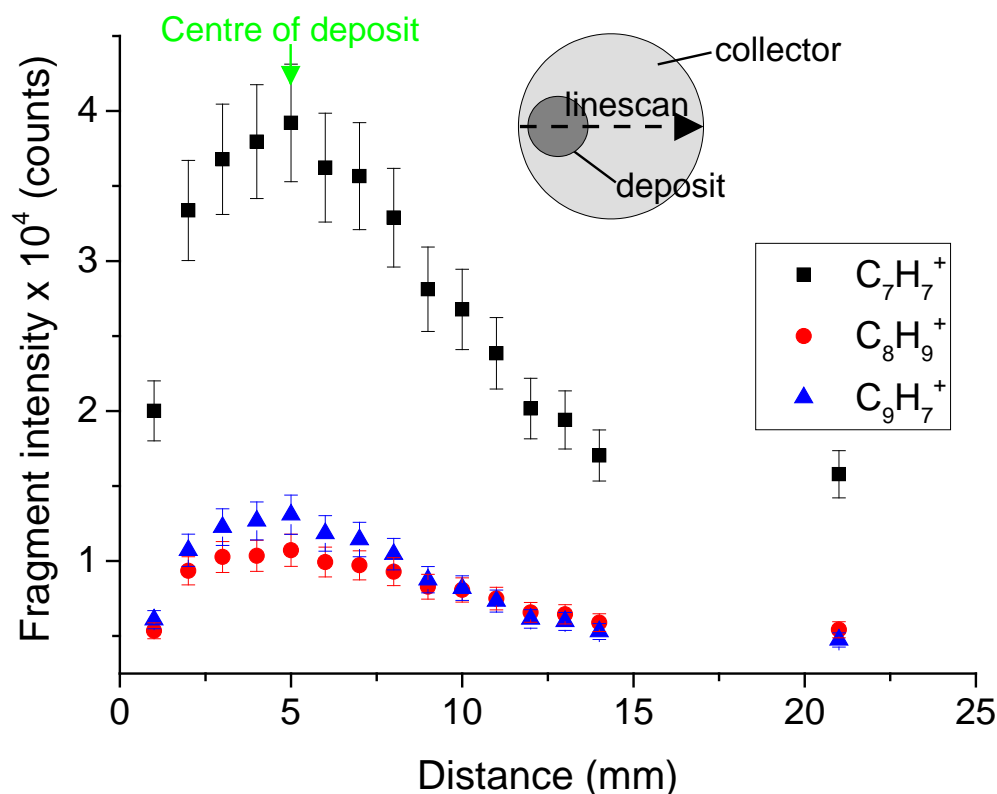


Fig. IV-8: Distribution of PS fragment intensities, along the diameter obtained by ToF-SIMS

Fig. IV-8 shows the intensity distributions of some PS fragments with the highest intensities along the diameter of the collector with the deposit prepared by  $4.0 \times 10^{13} \text{ Ar}^+$  ions. The centre of the deposit is located close to one border of the 2" collector because the experimental setup does not allow for a different position of the collector with respect to the primary beam during the deposition process. Although the deposit is symmetric, all the data points cannot be shown in Fig. IV-8, due to above-mentioned geometrical constraint during the preparation of the deposit. Assuming a symmetric deposit, the data was fitted to a Lorentz curve for deposition of titanium on silicon[191]. This follows the assumption that the angular distribution of sputtered matter follows a cosine law and the projection of the angular distribution on a plane above the surface corresponds to a Lorentz function. Although the angular distribution of sputtered matter in case of organics does not necessarily follow the cosine law, the symmetry of the data can be extrapolated from the existing data. Similar distributions can be observed for the other fragments. For the presentation of the results,

instead of absolute intensities, intensity ratios (larger specific PS fragments to smaller ones, namely  $C_7H_7^+/CH_3^+$ ,  $C_7H_7^+/C_3H_3^+$ ,  $C_7H_7^+/C_3H_5^+$ ,  $C_8H_9^+/CH_3^+$ ,  $C_8H_9^+/C_3H_3^+$ ,  $C_8H_9^+/C_3H_5^+$ ,  $C_9H_7^+/CH_3^+$ ,  $C_9H_7^+/C_3H_3^+$ ,  $C_9H_7^+/C_3H_5^+$ ) will be used. Absolute intensity values of different collectors are not always comparable due to the instability in the bismuth emission current leading to changing secondary ion intensities for the fragments of interest. The use of intensity ratios allows correcting for that issue.

### **3.2. Comparison of effects of $Ar^+$ and $Bi_1^+$ and $Bi_3^+$ projectiles on fragmentation of PS in case of storing matter deposits**

Comparing Table IV-1 and Table IV-2, a considerable amount of decrease in high/low mass peak ratios can be seen when the samples are prepared by Storing Matter. This shows that a lot of the fragmentation occurs during the sputter deposition. The degree of fragmentation during the Storing Matter deposition can be explained by the different mechanisms to form fragments from bulk polymer samples[39], and the sticking factor of the secondary particles on the collector. The important parameters for secondary ion formation during the analysis of the collector surface are the secondary ion yields of the sputtered matter and fragments and the sticking efficiency of the different fragments on the collector surface. All these will obviously effect the high/low mass peak ratios. Another important factor which might affect these ratios is hydrocarbon contaminations which are more probable for the StoMat sample preparation than for bulk polymer samples which do not involve any sputter deposition. Contaminations will mostly increase the intensity of fragments in the low mass range, resulting in a decrease in the high/low mass peak ratios. The influence of the primary ion beam during the ToF-SIMS analysis of the collector surface is shown by the large-to-small fragment ratios which are higher for the  $Ar^+$  than for the  $Bi_3^+$  beam (Table IV-2). This is opposite to what was observed for the analysis of bulk PS samples (Table IV-1), where  $Bi_3^+$  resulted in higher high/low mass peak ratios. For the case of StoMat deposits, using  $Ar^+$  primary ions seems more advantageous. This difference can be explained by the fact that yield enhancements with polyatomic projectiles are rather observed for the analysis of bulk polymer samples than for thin layers.[190],[189] Since StoMat deposits are in the sub-monolayer range, using polyatomic projectiles does not result in less fragmentation of the polymer.

Table IV-2: Peak ratios in the mass spectra obtained on the PS storing matter deposits analysed with  $\text{Bi}_1^+$ ,  $\text{Bi}_3^+$ , and  $\text{Ar}^+$  primary ions

	<b>Analysis of Storing Matter deposits (<math>6.7 \times 10^{12}</math> ions for deposit preparation)</b>	
<b>Peak ratio</b>	<b><math>\text{Ar}^+</math></b>	<b><math>\text{Bi}_3^+</math></b>
$\text{C}_7\text{H}_7^+ / \text{CH}_3^+$	2.68	2.61
$\text{C}_7\text{H}_7^+ / \text{C}_3\text{H}_3^+$	1.13	0.43
$\text{C}_7\text{H}_7^+ / \text{C}_3\text{H}_5^+$	0.28	0.11
$\text{C}_8\text{H}_9^+ / \text{CH}_3^+$	1.28	0.95
$\text{C}_8\text{H}_9^+ / \text{C}_3\text{H}_3^+$	0.54	0.16
$\text{C}_8\text{H}_9^+ / \text{C}_3\text{H}_5^+$	0.13	0.04
$\text{C}_9\text{H}_7^+ / \text{CH}_3^+$	0.61	0.71
$\text{C}_9\text{H}_7^+ / \text{C}_3\text{H}_3^+$	0.26	0.12
$\text{C}_9\text{H}_7^+ / \text{C}_3\text{H}_5^+$	0.06	0.03

#### **4. Study of the effect of coverage and primary ion fluence on fragmentation of PS**

This section discusses the results of experiments for sputter deposition of PS both in the static and dynamic regime in order to see the effect of varying coverage and primary ion fluence on its fragmentation. For the static regime, the local primary ion fluence was kept constant at  $5.6 \times 10^{12}$  ions/cm<sup>2</sup> and a focused  $\text{Ar}^+$  primary ion beam (10 keV impact energy, a beam focus diameter of 15  $\mu\text{m}$ [192], a raster size of  $1.5 \times 1.5$  mm<sup>2</sup> and a primary current of 2 nA) was raster-scanned over the PS sputter target. The coverage of the sputter deposited PS on the Ag was varied moving the sputter target below the primary ion beam while collecting emitted secondary particles on the collector (Fig. IV-9a).

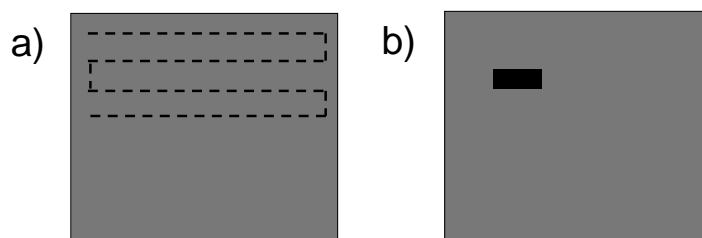


Fig. IV-9: Ar<sup>+</sup> ion beam raster scanning over PS sputter target for a) static regime b) dynamic regime sputter deposition

For the experiments in the dynamic regime, the fluence was increased by increasing the sputtering and collection time while continuing to sputter the PS sample in the same zone (Fig. IV-9b).

## 4.1. Constant primary ion fluence

### 4.1.1. ToF-SIMS analysis of collectors with varying coverage

The sputter deposition experiments were carried out in the static regime in order to see the effect of varying coverage on the fragmentation of PS and the mass spectra. First, the distribution of peak ratios on the collector and ToF-SIMS spectra for the highest ratios will be shown for three different coverages. After sputter-depositing PS fragments on Ag collectors and localizing the deposit with a stage scan of the collector, a series of ToF-SIMS spectra were taken along the diameter of the collector passing through the centre of the deposit. Positive mass spectra obtained in the centre of the deposit with highest PS fragment intensities, for three different coverages are shown in Fig. IV-10. ToF-SIMS spectra of the Storing Matter deposit of PS on Ag show specific PS fragments which are also observed in reference PS spectra. In Fig. IV-11, the intensity ratios of larger specific PS fragments to smaller ones (namely  $C_7H_7^+/CH_3^+$ ,  $C_7H_7^+/C_3H_3^+$ ,  $C_7H_7^+/C_3H_5^+$ ,  $C_8H_9^+/CH_3^+$ ,  $C_8H_9^+/C_3H_3^+$ ,  $C_8H_9^+/C_3H_5^+$ ,  $C_9H_7^+/CH_3^+$ ,  $C_9H_7^+/C_3H_3^+$ ,  $C_9H_7^+/C_3H_5^+$ ) are plotted for the three coverages along the diameter of the collector.

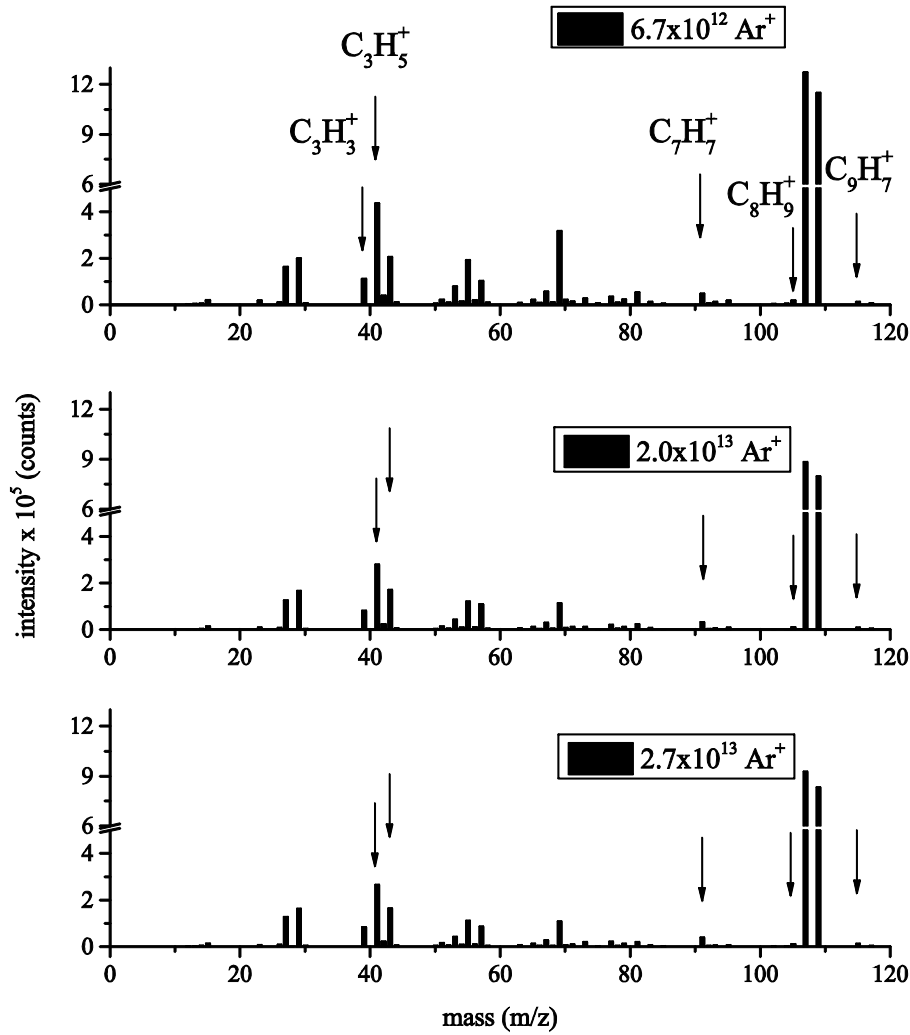


Fig. IV-10: ToF-SIMS Spectra of the PS StoMat deposit prepared at three different coverages corresponding to  $6.7 \times 10^{12}$ ,  $2.0 \times 10^{13}$  and  $2.7 \times 10^{13}$  Ar<sup>+</sup> primary ions (deposits prepared with constant primary ion fluence at  $5.6 \times 10^{12}$  ions/cm<sup>2</sup>)

Fig. IV-11 a-c shows the evolution of the ratios of C<sub>7</sub>H<sub>7</sub><sup>+</sup> intensities to the three small fragment intensities (CH<sub>3</sub><sup>+</sup>, C<sub>3</sub>H<sub>3</sub><sup>+</sup>, and C<sub>3</sub>H<sub>5</sub><sup>+</sup>) at coverages corresponding to  $6.7 \times 10^{12}$ ,  $2.0 \times 10^{13}$  and  $2.7 \times 10^{13}$  Ar<sup>+</sup> primary ions impinging on the PS sample during the sputter-deposition process. In all figures, similar distributions for the peak ratios are observed and there is a clear maximum at the centre of the deposit where the proportion of characteristic fragments is highest. When comparing the different curves, highest peak ratios are observed for C<sub>7</sub>H<sub>7</sub><sup>+</sup>/CH<sub>3</sub><sup>+</sup>. They decrease for C<sub>7</sub>H<sub>7</sub><sup>+</sup>/C<sub>3</sub>H<sub>3</sub><sup>+</sup> and C<sub>7</sub>H<sub>7</sub><sup>+</sup>/C<sub>3</sub>H<sub>5</sub><sup>+</sup> subsequently. Since the C<sub>7</sub>H<sub>7</sub><sup>+</sup> distribution is fixed for a given collector, it is concluded that C<sub>3</sub>H<sub>5</sub><sup>+</sup> and C<sub>3</sub>H<sub>3</sub><sup>+</sup> are more present on the collector surface than CH<sub>3</sub><sup>+</sup>, i.e. they show lower peak ratios. With increasing coverage, the C<sub>7</sub>H<sub>7</sub><sup>+</sup>/CH<sub>3</sub><sup>+</sup>, C<sub>7</sub>H<sub>7</sub><sup>+</sup>/C<sub>3</sub>H<sub>3</sub><sup>+</sup> and C<sub>7</sub>H<sub>7</sub><sup>+</sup>/C<sub>3</sub>H<sub>5</sub><sup>+</sup> ratios increase slightly.

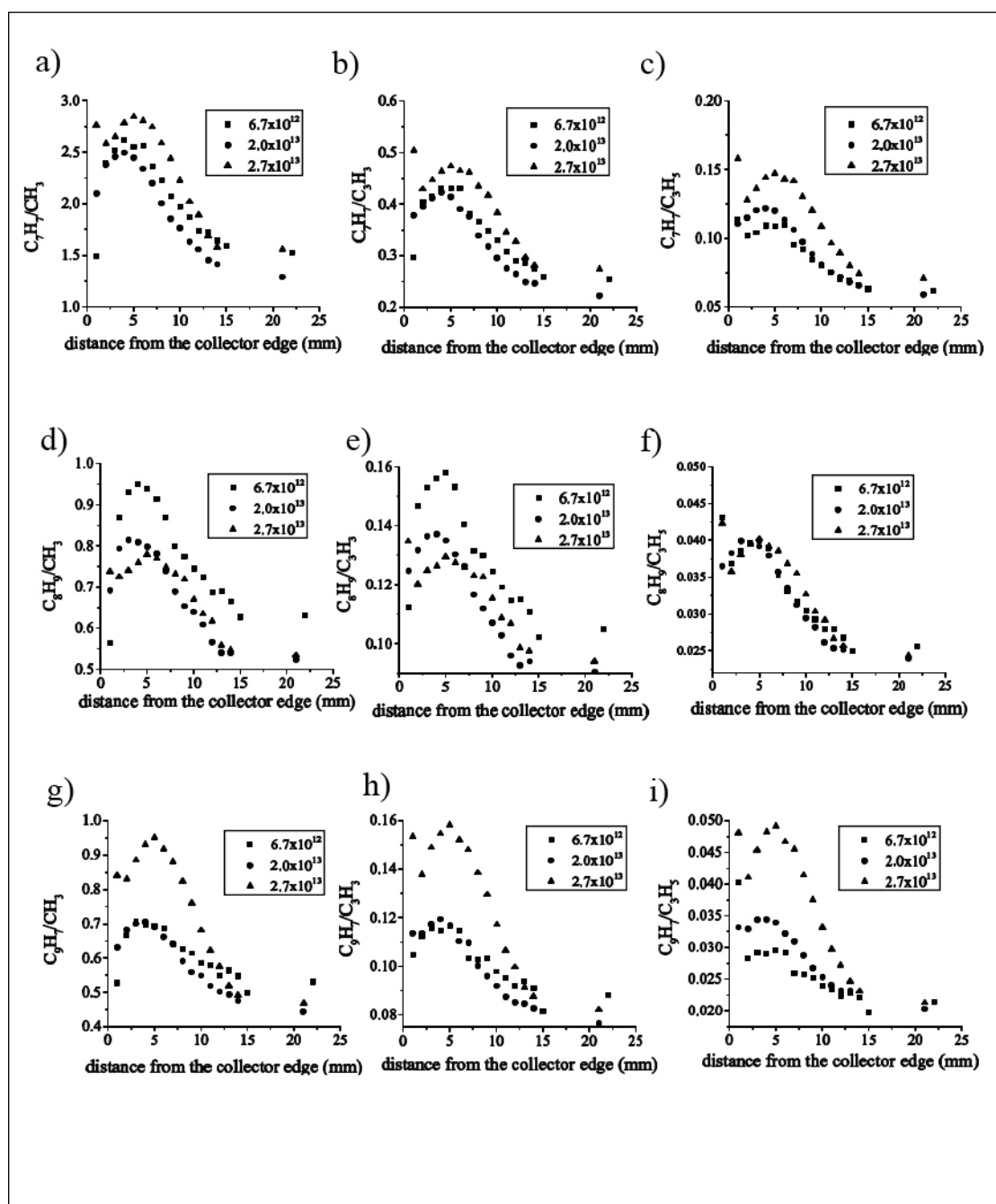


Fig. IV-11: Large-to-small peak ratios vs. distance for several PS fragments at three different coverages corresponding to  $6.7 \times 10^{12}$ ,  $2.0 \times 10^{13}$  and  $2.7 \times 10^{13}$   $\text{Ar}^+$  primary ions at a constant primary ion fluence at  $5.6 \times 10^{12}$  ions/cm<sup>2</sup>, a)  $\text{C}_7\text{H}_7^+/\text{CH}_3^+$ , b)  $\text{C}_7\text{H}_7^+/\text{C}_3\text{H}_3^+$ , c)  $\text{C}_7\text{H}_7^+/\text{C}_3\text{H}_5^+$ , d)  $\text{C}_8\text{H}_9^+/\text{CH}_3^+$ , e)  $\text{C}_8\text{H}_9^+/\text{C}_3\text{H}_3^+$ , f)  $\text{C}_8\text{H}_9^+/\text{C}_3\text{H}_5^+$ , g)  $\text{C}_9\text{H}_7^+/\text{CH}_3^+$ , h)  $\text{C}_9\text{H}_7^+/\text{C}_3\text{H}_3^+$ , i)  $\text{C}_9\text{H}_7^+/\text{C}_3\text{H}_5^+$ .

The same kind of behaviour is observed for the  $\text{C}_9\text{H}_7^+$  fragment (Fig. IV-11g-i). However, the situation is different for the  $\text{C}_8\text{H}_9^+$  fragment (Fig. IV-11d-f): the  $\text{C}_8\text{H}_9^+/\text{CH}_3^+$  and  $\text{C}_8\text{H}_9^+/\text{C}_3\text{H}_3^+$  peak ratios decrease with increasing coverage and the  $\text{C}_8\text{H}_9^+/\text{C}_3\text{H}_5^+$  ratio stays constant. A possible hydrocarbon contamination resulting in an increase of the smaller fragments cannot be the reason for the decrease in the proportion of larger fragments in the case of  $\text{C}_8\text{H}_9^+$  since

this would be the case for  $C_7H_7^+$  and  $C_9H_7^+$  too, where the opposite trend is observed. Indeed, for a same coverage the data is coming from a same collector. The ratios with  $CH_3^+$  and  $C_3H_3^+$  stay more or less constant for changing coverage. The same is true for the  $C_8H_9^+/C_3H_5^+$ . The different behaviour of  $C_8H_9^+$  can be explained by the different type of fragments classified by Vanden Eynde *et al.*[193] and the different pathways via which the fragments can form: C-C bond breaking, a hydrogen capture mechanism, or multiple bond scissions.[39] In bulk PS,  $C_7H_7^+$  and  $C_9H_7^+$  are formed via H capture, H exchange reactions and multiple bond scissions. For  $C_8H_9^+$ , the hydrogen capture mechanism is less important. On the collector surface, fragmentation and recombination reactions are different from bulk polymer samples and might change with increasing coverage. For  $C_8H_9^+$  fragments adsorbed on the collector surface, hydrogen atoms of the alkyl group might be lost easier than for  $C_7H_7^+$  which is another type III fragment. These hydrogen atoms might serve as hydrogen source for the formation of other fragments. This mechanism would become more probable with increasing coverage and would explain the difference between  $C_8H_9^+$  and the  $C_7H_7^+$  and  $C_9H_7^+$  fragments. For  $C_7H_7^+$  and  $C_9H_7^+$ , the hydrogen loss could be less probable because of the shorter alkyl group of  $C_7H_7^+$  and the polycyclic structure of  $C_9H_7^+$ .

After seeing the distributions of peak ratios over the collector, the maximum peak intensities in the centre of the deposit were taken in order to see their change with coverage. Fig. IV-12a-c shows the variation of peak ratios (larger PS fragments,  $C_7H_7^+$ ,  $C_8H_9^+$ ,  $C_9H_7^+$  to smaller ones,  $CH_3^+$ ,  $C_3H_3^+$ , and  $C_3H_5^+$ ) with coverage which is changed by varying the number of  $Ar^+$  primary ions between  $3.3 \times 10^{12}$ -  $4.0 \times 10^{13}$  during the StoMat deposition process. For each deposit, the maximum peak intensities in the centre of the deposit were taken (cf. Fig. IV-8 for deposit prepared with  $4.0 \times 10^{13}$   $Ar^+$  ions). In Fig. IV-12a-c highest peak ratios are observed for  $C_7H_7^+/CH_3^+$ ,  $C_7H_7^+/C_3H_3^+$ ,  $C_7H_7^+/C_3H_5^+$  ratios (Fig. IV-12a-c), and then they decrease for the  $C_8H_9^+/CH_3^+$ ,  $C_8H_9^+/C_3H_3^+$ ,  $C_8H_9^+/C_3H_5^+$  (Fig. IV-12a-c) and the  $C_9H_7^+/CH_3^+$ ,  $C_9H_7^+/C_3H_3^+$ ,  $C_9H_7^+/C_3H_5^+$  ratios (Fig. IV-12c) which indicates that  $C_7H_7^+$  is more abundant on the collector surface compared to  $C_8H_9^+$  and  $C_9H_7^+$ . The overall increase in  $C_7H_7^+/C_3H_5^+$  and  $C_9H_7^+/C_3H_5^+$  peak ratios with increasing coverage can be originating either from a preferential sticking of the larger fragments compared to the smaller ones, or a recombination of smaller fragments to form larger ones. Otherwise a similar ratio would be observed for all samples. During the sputter deposition, the only parameter changing is the number of  $Ar^+$  impacting on the surface, and, hence the amount of sputtered matter. All other parameters are kept unchanged, including fluence, impact energy and beam raster size.

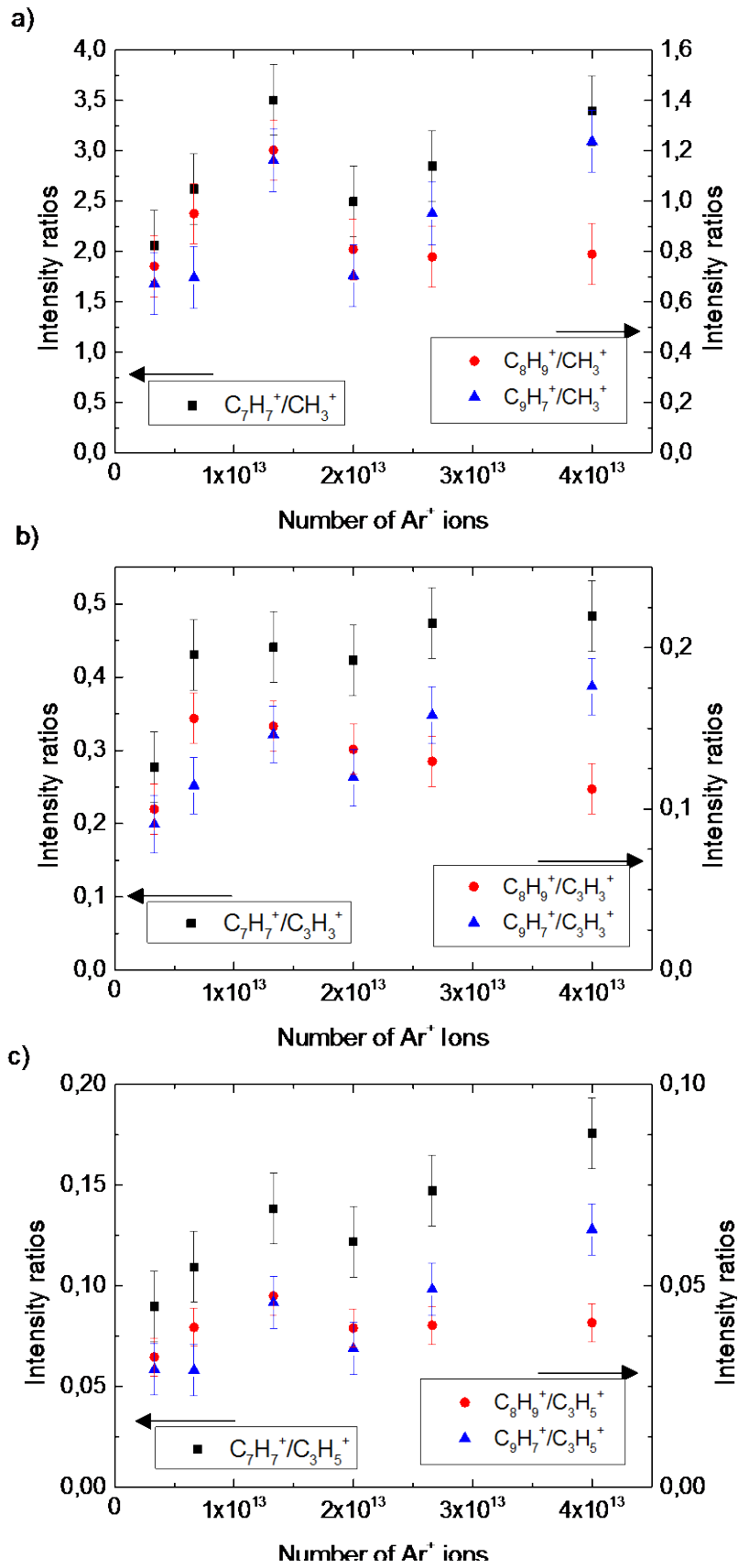


Fig. IV-12: Variation of large-to small peak ratios with increasing number of  $\text{Ar}^+$  ions used during the sputter deposition process, i.e. with increasing coverage at a constant primary ion fluence at  $5.6 \times 10^{12}$  ions/cm<sup>2</sup>: ratios of  $\text{C}_7\text{H}_7^+$ ,  $\text{C}_8\text{H}_9^+$ ,  $\text{C}_9\text{H}_7^+$  to a)  $\text{CH}_3^+$  b)  $\text{C}_3\text{H}_3^+$  c)  $\text{C}_3\text{H}_5^+$



For SIMS analysis, it was observed by Chatterjee *et al.* that the desorption mechanisms of organic molecules on metal strongly depends on the coverage of organic layers.[59] Muddiman *et al.* also studied the effect of surface coverage on secondary ion yields and found that secondary ion yields increase with surface coverage up to a fraction of 0.43 and then decreases until full coverage (i.e. a fraction of 1.0).[194] The effect of coverage on SIMS analysis has already been discussed in Chapter I, section 3.2.4.1. Since StoMat deposits are expected to be in the sub-monolayer coverage, no significant decrease in peak ratios is observed (Fig. IV-12a-c). Thus, the increase could be due to changing sticking probabilities for the different fragments on the collector with increasing coverage or, to the recombination of the fragments on the collector surface. During the sputter-deposition or the analysis process, the increasing coverage combined with surface diffusion would increase the probability of two fragments to interact and to form larger ones. If this is true, the increase of the ratios should be even more pronounced when changing the primary ion fluence during the deposition process, i.e. when increasing the PS fragmentation.

## **4.2. Varying primary ion fluence**

### **4.2.1. ToF-SIMS analysis of collectors with varying primary ion fluence**

In the second part, PS sputter-deposition experiments were repeated in the dynamic regime, i.e. by changing the Ar<sup>+</sup> fluence, in order to see how increasing fragmentation influences the Storing Matter process, and, hence to get more information on the mechanisms occurring on the collector surface. The impact energy during the sputter deposition process was reduced to 4 keV in order to be comparable to the experiments done in the equipment with the XPS, as this had an upper energy limit of 4 keV. Although this will influence ion-induced fragmentation pathways compared to experiments with constant fluence, the general trends for the large-to-small peak ratios will be not influenced. The Ar<sup>+</sup> primary ion fluence was varied within a range of  $6.6 \times 10^{13}$  -  $4.0 \times 10^{15}$  ions/cm<sup>2</sup> (corresponding to a total number of Ar<sup>+</sup> primary ions in the range  $1.5 \times 10^{12}$  -  $8.9 \times 10^{13}$ ). Since the number of Ar<sup>+</sup> primary ions is comparable to those in the static regime experiments, and the deposits have still sub-monolayer thickness, no matrix effects are expected.

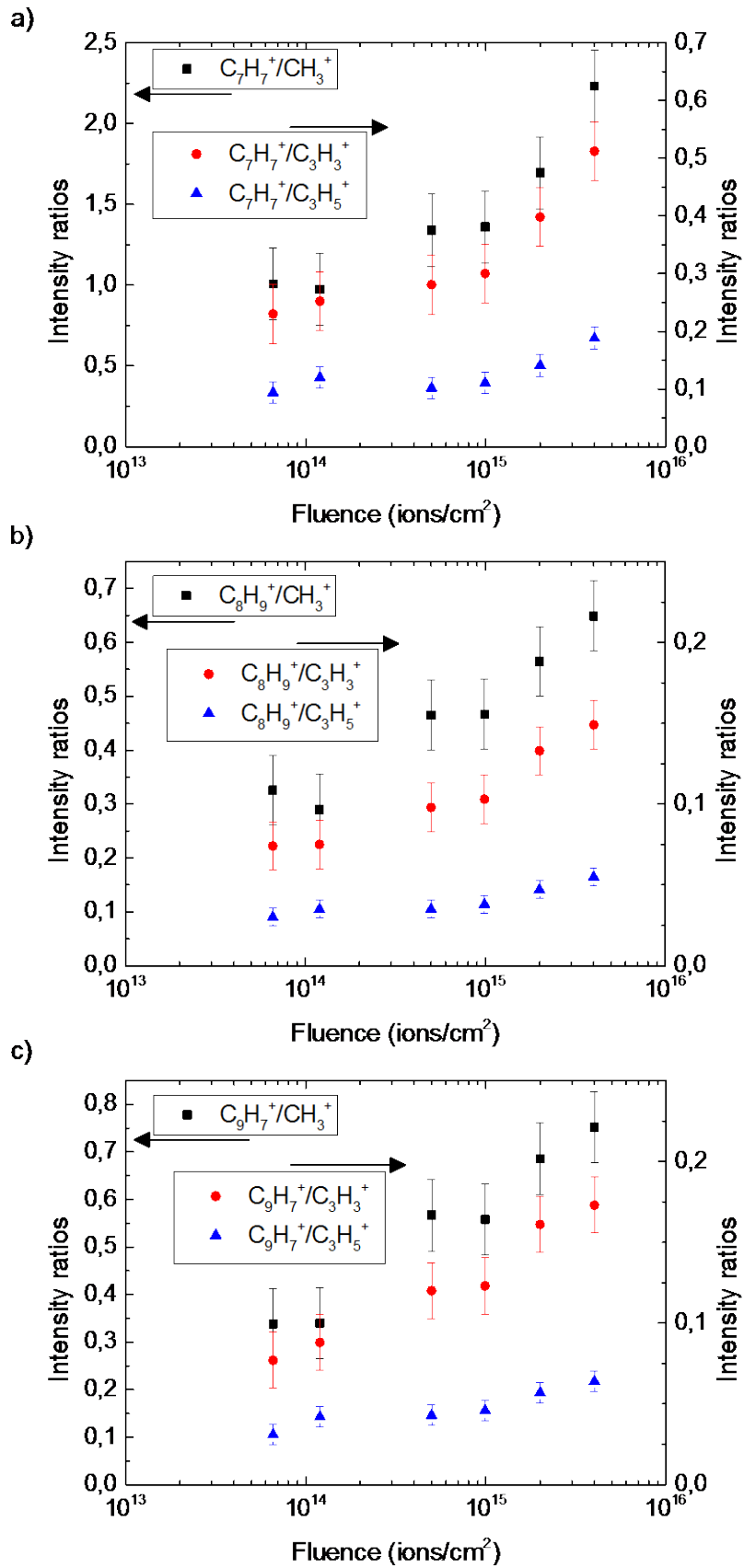


Fig. IV-13: Variation of large-to small peak ratios with increasing Ar<sup>+</sup> fluence, i.e. increasing coverage for a total number of Ar<sup>+</sup> primary ions in the range 1.5x10<sup>12</sup> - 8.9x10<sup>13</sup>: ratios of a) C<sub>7</sub>H<sub>7</sub><sup>+</sup>, b) C<sub>8</sub>H<sub>9</sub><sup>+</sup>, c) C<sub>9</sub>H<sub>7</sub><sup>+</sup> to CH<sub>3</sub><sup>+</sup>, C<sub>3</sub>H<sub>3</sub><sup>+</sup> and C<sub>3</sub>H<sub>5</sub><sup>+</sup>

The variation of peak ratios with increasing fluence is shown in Fig. IV-13a-c. A significant increase by a factor two is observed for all ratios, namely  $C_7H_7^+/X$ ,  $C_8H_9^+/X$  and  $C_9H_7^+/X$  (where X refers to  $CH_3^+$ ,  $C_3H_3^+$  or  $C_3H_5^+$ ). However, the ratios are expected to decrease with increasing fluence since the ion bombardment increases the fragmentation for fluences above the static regime, as already discussed in Chapter I. Delcorte *et al.* observed that characteristic fragment intensities in the fingerprint SIMS spectra showed a monotonic decay with increasing fluence.[55] Moreover, they developed a kinetic model showing that the decay of saturated fragments with higher numbers of hydrogen gives rise to the production of less saturated fragments with lower H content, which is explained by dehydrogenation as a result of polymer degradation. The degradation is found to be faster in case of the most characteristic fragments.

Hence, the increasing intensities of the larger characteristic fragments must be explained by mechanisms leading to a preferential sticking of the large fragments or a recombination of the smaller fragments to form larger ones. For the collectors prepared by changing fluence, this becomes even more apparent than for the first series of experiments at constant fluence. Next, XPS analyses are carried out to give quantitative and structural information about the deposit and to help to explain the mechanisms involved.

#### **4.2.2. XPS analysis of craters in bulk PS and of collectors with varying primary ion fluence**

ToF-SIMS characterization of the PS sputter-deposit gives an idea about the change in fragmentation for various coverage and fluences, however, it does not provide any structural information. The irradiation-induced chemical changes both on the sputtered PS film and the deposit on the Ag collector are investigated using in-situ XPS characterization.

First, the changes in the XPS spectra of the crater formed after  $Ar^+$  bombardment of the PS film at increasing ion fluences were analysed. An XPS peak fit of the bulk PS C1s core level reveals two peaks of aliphatic (24%) and aromatic (73%) character and a shake-up (3%) with a stoichiometric ratio expected from PS (Fig. IV-14a).[195] Fig. IV-14b shows the evolution of the C1s core level components as a function of the fluence. With increasing ion fluence the percentage for the aliphatic compound increases whereas that for the aromatic decreases. The decrease in the intensity of the shake-up satellite with fluence is even more pronounced. At an ion fluence of  $2.5 \times 10^{14}$  ions/cm<sup>2</sup>, the  $\pi-\pi^*$  shake-up transition is completely eliminated. Zekonyte *et al.* reported that the satellite peak disappears for an ion dose of  $10^{15}$  ions/cm<sup>2</sup> at 1

keV. [20] For  $10^{14}$   $\text{Ar}^+$  ions/ $\text{cm}^2$  at 5 keV, it was shown by Briggs *et al.* that the aromaticity of PS is destroyed.[62] Damage rates with 4 keV  $\text{Ar}^+$  ions are expected to be higher than at 1 keV and lower than at 5 keV ions. So, our data agrees well with the results of Zekonyte and Briggs. It is known that the aromatic character of PS gives stability to the polymer against chemical changes by ion irradiation.[25] However, at such high ion fluence, a broader carbon peak suggests loss of the aromaticity within the XPS attenuation depth of a few nm due to ring opening and saturated carbon bonding environment on the PS surface. [20] Since PS is a crosslinking polymer, the chemical changes are due to chain scissions, creation of new bonds and even formation of other functional groups.[52] A small fraction of scissions is still present in PS, but it is almost negligible. A close correlation between the crosslink density and shake-up probability was reported by Wanxi *et al.*: they found that the shake-up probability (ratio of shake-up peak intensity to main peak intensity) decreased by increasing crosslink density through reduction of the  $\pi$ -electron conjugation in the cross-linked polystyrene.[196] In Fig. IV-14b, it can be seen that the shake-up probability decreases indicating an increasing crosslink density with increasing fluence. After a fluence of  $5.0 \times 10^{14}$  ions/ $\text{cm}^2$ , a saturation behaviour is observed; i.e. the aliphatic compound reaches a maximum intensity while the aromatic compound and shake-up almost completely disappear. The crosslink density of PS was reported to increase linearly until a certain fluence ( $10^{14}$  ions/ $\text{cm}^2$ ) and a saturation behaviour was observed with further increasing fluence.[52]

Next, the XPS spectra of the PS deposit on the silver collector with different  $\text{Ar}^+$  ion fluences were recorded. Again, changes in the C1s core level are studied. A peak fit of the C1s core level of the PS deposit is shown in Fig. IV-15a. Compared to the XPS fit of the PS film, new components with oxygen are observed in addition to aliphatic and aromatic compounds.[20] We suggest that the carbon-oxygen components are due to the interaction with residual CO in the UHV chamber. The shake-up characteristic for PS does not appear in these spectra, which is an indication for damage in the aromatic rings. At least, the remaining amount of intact rings on the collector surface is too small to be detected by XPS. For the analysis of bulk PS, Calcagno *et al.* found that after an ion fluence of  $3.0 \times 10^{15}$  ions/ $\text{cm}^2$  trigonal ( $\text{sp}^2$ ) carbon is transformed into tetrahedral configuration ( $\text{sp}^3$ ).[52] Fig. IV-15b shows the evolution of the percentages of all components in the C1s fit of the XPS spectra. For all fluences, the aliphatic carbon content is the highest (between 60-80 %). The aromatic carbon content varies between 0-10 %. The percentage of other components changes between 0-15 percent. As opposed to the trend observed for the analysis of the PS film, a slight decrease in the aliphatic component

and a slight increase in the aromatic compound is observed with increasing fluence. For the rest of the components, there is no significant and regular change in intensities. The XPS results of the deposit on the silver surface depend not only on the ion beam conditions, but also on the sticking probabilities of the PS fragments on the silver and a possible recombination of fragments. Thus, it is more complicated to interpret XPS data for the PS deposit than for the PS film. It should also be taken into account that the PS deposit has sub-monolayer coverage and the PS bulk sample is thick if compared within the information depth of XPS.

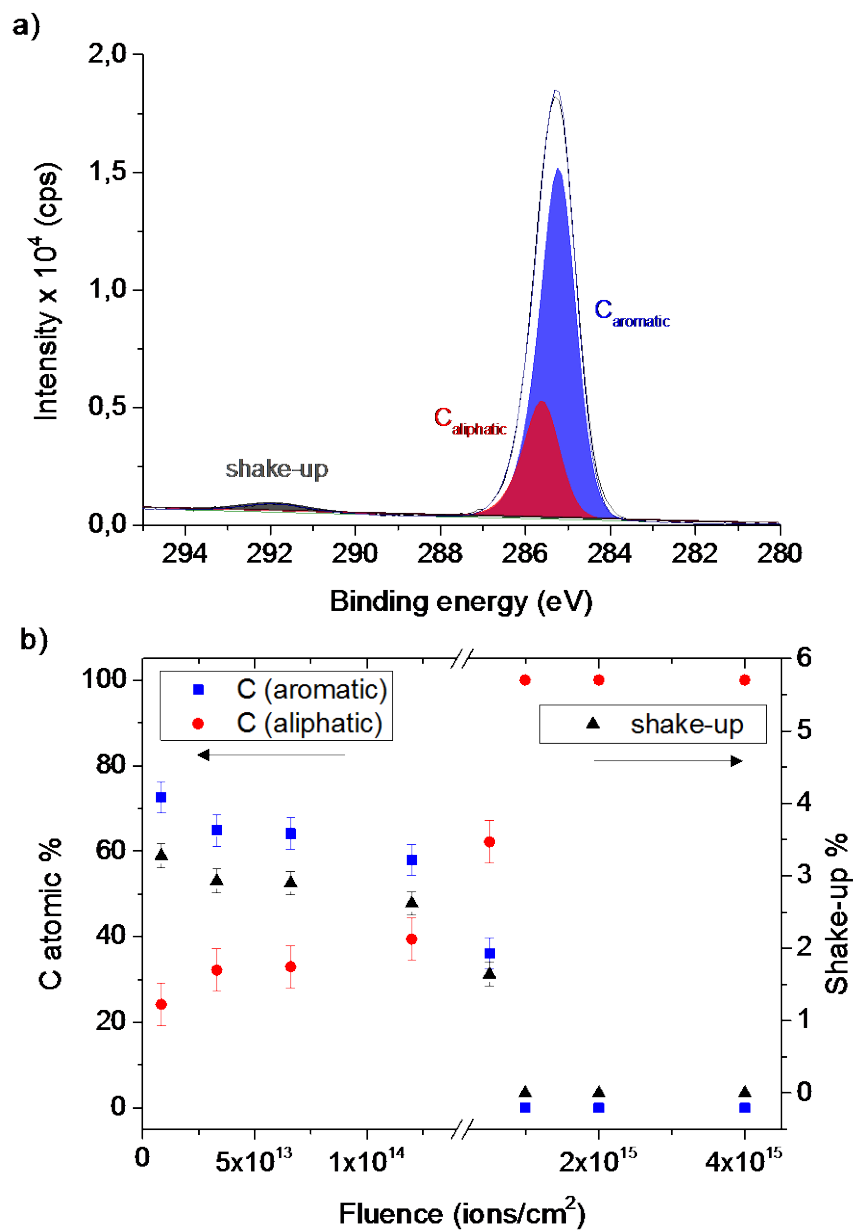


Fig. IV-14: a) XPS peak fit of the C1s core level of bulk PS, b) Evolution of percentage values of C1s core level of bulk PS as a function of the primary ion fluence for a total number of Ar<sup>+</sup> primary ions in the range 1.5x10<sup>12</sup>-8.9x10<sup>13</sup>.

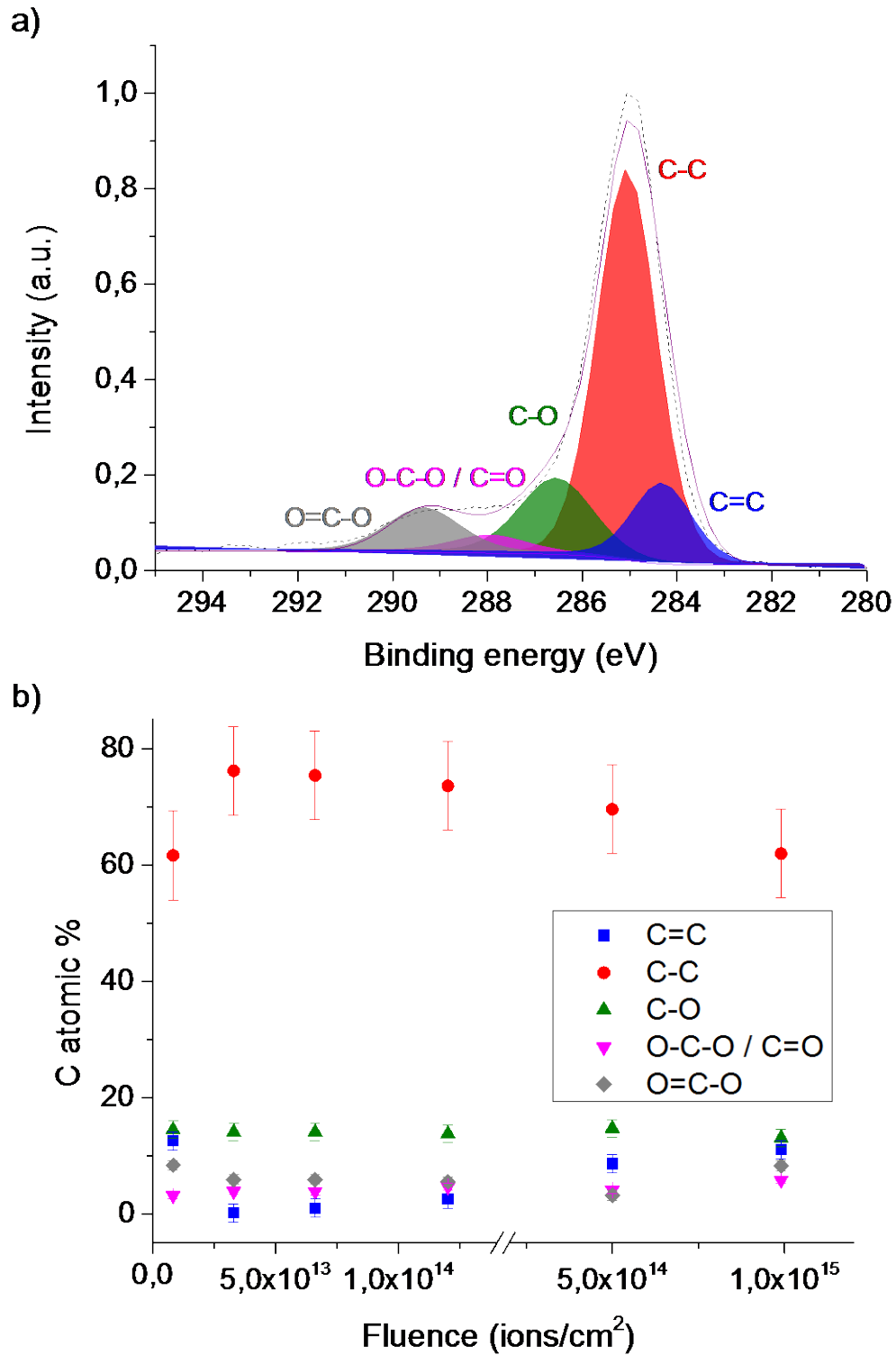


Fig. IV-15: a) XPS peak fit of the C1s core level of the PS deposit, b) evolution of percentage values of C1s core level of PS deposit as a function of PI fluence a total number of Ar<sup>+</sup> primary ions in the range  $1.5 \times 10^{12}$ - $8.9 \times 10^{13}$ .

### 4.2.3. DFT calculations of adsorption of PS fragments on Ag

ToF-SIMS and XPS experiments are not able to provide some information on the sticking probability of large fragments compared to small ones. The DFT method is not able to provide directly sticking probabilities, but it has been used as a means to calculate the adsorption energies and geometries of PS fragments on the Ag collector, and which gives some indication about the adsorption probabilities of the different fragments. For this purpose, different sizes of characteristic PS fragments, which have been observed in the ToF-SIMS spectra, were adsorbed on 3 different adsorption sites on Ag(100) and Ag(111) surfaces. For each of the  $C_3H_3$ ,  $C_3H_5$ ,  $C_6H_5$ ,  $C_7H_7$ ,  $C_8H_9$  and  $C_9H_7$  fragments, the radical carbon atom (structures of the fragments and adsorbing radicals are shown in Fig. IV-16) was positioned at atop (on top of an Ag atom), bridge (on top of two Ag atoms) and threefold and fourfold-hollow (in between three Ag atoms for Ag(111) and between four for Ag(100) ) sites. It should be noted that adsorption of these fragments by DFT is not directly comparable with the real-world deposition process, since only static calculations are carried out and only non-charged fragments are studied. However, this is in line with the fact that most of the sputtered matter is neutral.[153] At the same time, adsorption energies give valuable information on sticking probabilities and possible diffusion mechanisms.

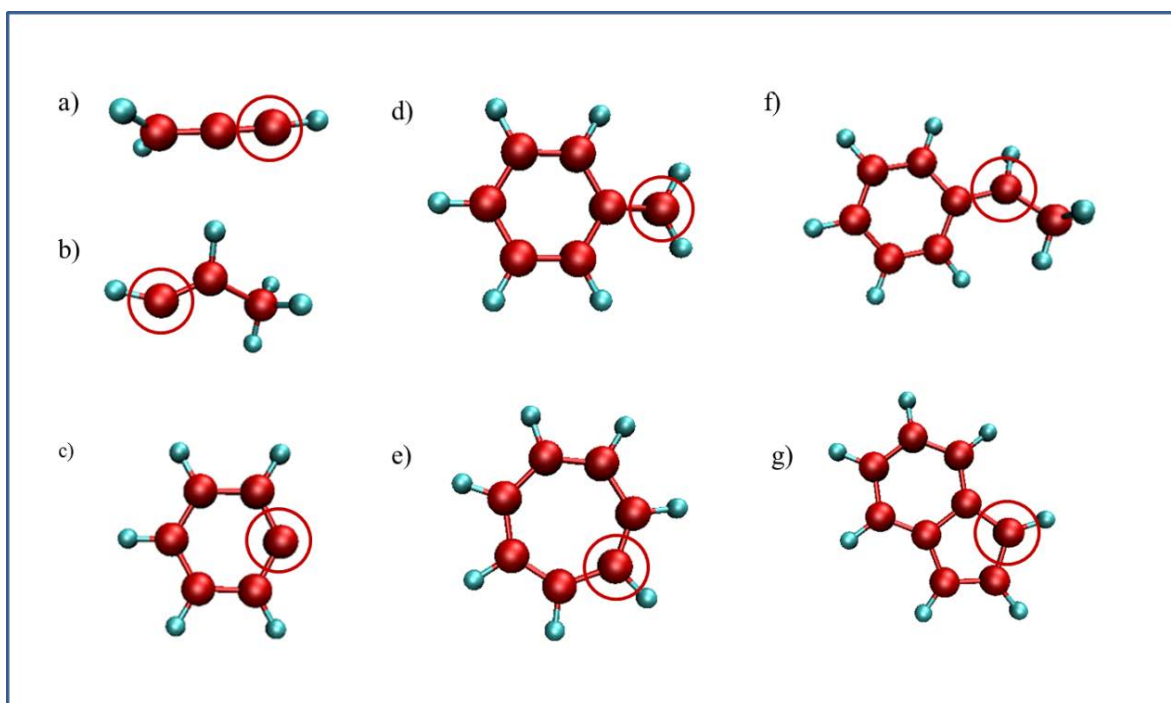


Fig. IV-16: Structures of PS fragments adsorbed on Ag(111) and Ag(100) surfaces for a)  $C_3H_3$ , b)  $C_3H_5$ , c)  $C_6H_5$ , d)  $C_7H_7$  (benzylum), e)  $C_7H_7$  (tropylium) f)  $C_8H_9$  g)  $C_9H_7$ . Radical C atoms are indicated by red circle.

Adsorption energies have been calculated for each case and they have been compared with respect to the Ag surface orientation, different binding sites and different size and structure of adsorbed fragments. The precision is of 0.01 eV.

Table IV-3: Calculated adsorption energies (eV) of PS fragments on Ag(111)

	<b>C<sub>3</sub>H<sub>3</sub></b>	<b>C<sub>3</sub>H<sub>5</sub></b>	<b>C<sub>6</sub>H<sub>5</sub></b>	<b>C<sub>7</sub>H<sub>7</sub></b>	<b>C<sub>7</sub>H<sub>7</sub></b>	<b>C<sub>8</sub>H<sub>9</sub></b>	<b>C<sub>9</sub>H<sub>7</sub></b>
atop	-1.46	-1.73	-1.61	-0.60	-0.29	-0.50	-0.61
bridge	-1.31	-1.85	-1.61	-0.53	-0.22	-0.30	-0.48
fourfold-hollow	-1.49	-1.85	-1.61	-0.46	-0.20	-0.47	-0.47

Table IV-4: Calculated adsorption energies (eV) of PS fragments on Ag(100)

	<b>C<sub>3</sub>H<sub>3</sub></b>	<b>C<sub>3</sub>H<sub>5</sub></b>	<b>C<sub>6</sub>H<sub>5</sub></b>	<b>C<sub>7</sub>H<sub>7</sub></b>	<b>C<sub>7</sub>H<sub>7</sub></b>	<b>C<sub>8</sub>H<sub>9</sub></b>	<b>C<sub>9</sub>H<sub>7</sub></b>
atop	-1.72	-2.02	-1.70	-0.74	-0.35	-0.68	-0.98
bridge	-1.72	-2.01	-1.74	-0.71	-0.55	-0.57	-0.80
threefold-hollow	-1.72	-2.00	-1.66	-0.67	-0.36	-0.50	-0.88

Table IV-3 and Table IV-4 show calculated adsorption energies for all abovementioned conditions. The calculations reveal that the adsorption energies vary considerably with surface orientation. On average they are about 20% higher on Ag(100) than on Ag(111) which indicates that the interactions between the adsorbents and Ag(100) are much stronger than on Ag(111). In Table IV-3 and Table IV-4 it can also be observed that the preferred adsorption site depends on the size and structure of the molecule, with atop and bridge sites being slightly more favourable for most fragments, though the differences should not affect the adsorption process. The largest adsorption energies (-1.72 eV for C<sub>3</sub>H<sub>3</sub> and -2.02 eV for C<sub>3</sub>H<sub>5</sub>) were found for smaller fragments which do not have any cyclic character. The difference between the two configurations is due to the number of C atoms involved in



bonding: for  $C_3H_3$  there are two C atoms and for  $C_3H_5$  there is only one C atom which interacts with the surface. Moreover, for these smaller fragments there are no significant energy variations for different adsorption sites. For the other fragments with cyclic character ( $C_7H_7$ ,  $C_8H_9$  and  $C_9H_7$ ), except  $C_6H_5$ , adsorption energies are considerably smaller.  $C_6H_5$  is adsorbed vertically on Ag (Fig. IV-17) with a maximum adsorption energy of -1.74 eV on the bridge site, with less than 0.1 eV difference for the two other bonding sites. Two different possible structures for  $C_7H_7$  have been adsorbed[197]: benzylium and tropylium (Fig. IV-17). Tropylium was found to have the smallest adsorption energy of all fragments. Its flat adsorption on the Ag surface gives the largest number of atoms and delocalised electrons the possibility to interact with the surface, but the structure in general seems to be less favourable, decreasing the adsorption energy. The adsorption energy for benzylium is almost twice as high. The fragment adsorbs with an angle between the Ag surface and the phenyl ring. A similar adsorption structure was observed for  $C_8H_9$ , with a higher adsorption angle compared to benzylium. Out of all cyclic fragments, (except  $C_6H_5$ ),  $C_9H_7$  has the highest adsorption energy (-0.978 eV when atop of Ag) possibly due to its polycyclic structure. It adsorbs parallel to the surface, like tropylium, giving all C atoms the possibility to interact with Ag atoms. However, the adsorption energy is increased instead of decreased. Adsorption geometries of all fragments are shown in Fig. IV-17.

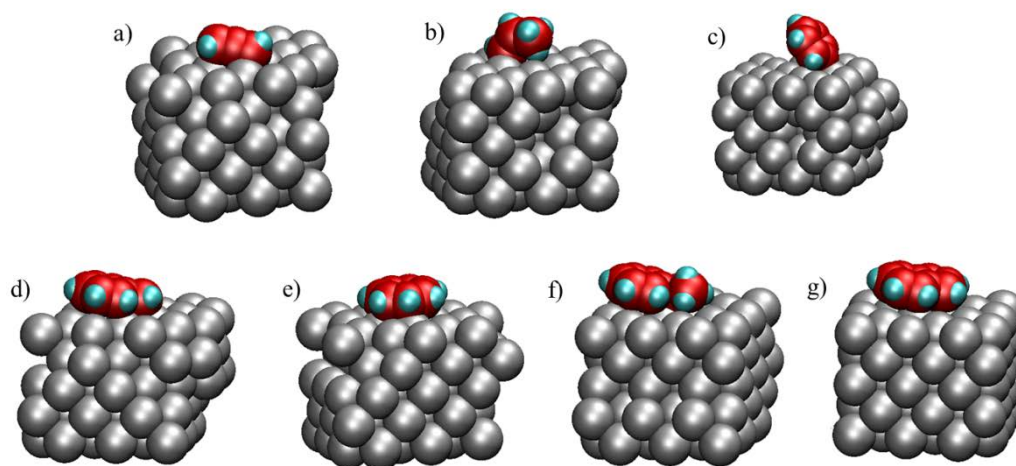


Fig. IV-17: Adsorption geometry for several fragments on Ag(100) surface: a)  $C_3H_3$ , b)  $C_3H_5$ , c)  $C_6H_5$ , d)  $C_7H_7$  (benzylium), e)  $C_7H_7$  (tropylium) f)  $C_8H_9$  g)  $C_9H_7$

For the small fragments, different initial starting configurations all yield identical adsorption structures and energies. For the other fragments with cyclic character, adsorption energies

vary with fragment size and initial adsorption site. The phenyl ring limits the angle between the Ag and fragment depending on its structure.

The DFT results suggest that small, aliphatic PS fragments adsorb easier, and with higher adsorption energies, on the Ag surface. This finding seems to be in contradiction with the ToF-SIMS results of the PS deposits (both in the static and dynamic range) where the proportion of larger fragments increases with increasing coverage and fluence. However, ToF-SIMS analyses inform only about the mass of the fragments sputtered from the surface, but they do not give information about the structure of the deposit and the pathways through which these fragments have been formed. XPS analysis, as a complementary technique, indicates that the deposit is mostly of aliphatic character, with a small percentage of cyclic component involvement. At this point, DFT calculations suggest that aliphatic small fragments should adsorb better on the Ag surface than the cyclic ones. This result, combined with a larger proportion of larger fragments in ToF-SIMS, implies that at least a part of the larger fragments detected in ToF-SIMS is being formed by recombination of smaller fragments on the collector surface. At this point it cannot be clearly identified if this recombination occurs during the deposition process by diffusion on the silver surface and/or during the ion bombardment in ToF-SIMS analyses.

## **5. Conclusion**

A multi-technique approach was used to characterise and understand how fragmentation during the sputter deposition process affects the Storing Matter results. In particular, the effects of increasing coverage and fluence on the deposition of fragmented polystyrene molecules on a silver collector, and hence on the ToF-SIMS mass spectra, were studied. The study showed that, as expected, the polymer chains get damaged during the sputter deposition process. In addition, most of the aromatic character is lost for the matter sputtered onto the collector surface. For the sputter deposition with changing fluence, fragmentation of the chains is also expected to increase with fluence. However, the proportion of larger fragments increases when increasing the fluence up to  $4.0 \times 10^{15}$  ions/cm<sup>2</sup> during deposit preparation, and the ratios of large to small fragments on the collector increase by about a factor two. This is opposite to what was expected. At the same time, DFT calculations predict that small aliphatic fragments adsorb best. Comparison of experimental with DFT data indicates that the fragments sputtered during the deposition process must recombine on the collector surface. Hence, the methodology used in this study is well suited to identify surface reactions similar

to those occurring during sputter deposition and similar to those during plasma-based surface treatments. At the same time, these results show that the study of organic samples by the Storing Matter technique is complicated, since fragments detected by ToF-SIMS on the collector surface are not necessarily present in the initial sample used for sputter deposition, but may have formed by recombination on the collector surface. For the further development it is important to work with the lowest possible coverage in order to minimise the recombination reactions between different fragments. This is especially important when several compounds are present in the sample. In addition, the use of massive  $\text{Ar}_n^+$  cluster ions beams instead of monatomic  $\text{Ar}^+$  ions may help to circumvent this issue by largely reducing the fragmentation during the sputter deposition.



# Chapter V:

## Sputter deposition of Poly (methyl methacrylate) (PMMA)

### 1. Introduction

After PS analysis in the previous chapter, this chapter deals with the analysis of bulk PMMA polymer, as well as of Storing Matter PMMA deposits. Compared to PS, PMMA is a non-cross-linking polymer and contains oxygen, which might affect the results considerably.

For the analysis of bulk PMMA, we show ToF-SIMS and XPS results for changing primary ion fluence and compare them to studies in literature.

For Storing Matter PMMA deposits, ToF-SIMS analyses were carried out both in the static (constant primary ion fluence for deposition) and dynamic range (varying primary ion fluence for deposition). XPS analyses were used in addition to obtain more detailed information on the fragmentation and damage induced on the PMMA film. Similarly, the StoMat deposits were prepared both in the static and dynamic regime and analysed by ToF-SIMS and XPS to see how these parameters affect the PMMA Storing Matter deposits.

### 2. Analysis of bulk Poly(methyl methacrylate) films

To start with, thin PMMA(2000) films were characterized by ToF-SIMS and XPS. The effect of  $\text{Ar}^+$  ion bombardment on PMMA as a function of primary ion fluence was studied. Molecular and structural changes in the PMMA film after 4 keV  $\text{Ar}^+$  bombardment were investigated with increasing primary ion fluence.

SIMS depth profiling of organic materials has been subject of many studies and has rapidly advanced.[53] The most common developed techniques use cluster ions or the dual-beam technique where the sample is etched by a low-energy sputter ion beam and analysed with high-energy ions. Since we are limited to  $\text{Ar}^+$  primary ions as sputter beam for sputtering of polymers for Storing Matter technique, we have only studied its effect on degradation of the polymer by using both ToF-SIMS and XPS for analysis.

## 2.1. Study of the effect of primary ion fluence on fragmentation of PMMA

### 2.1.1. ToF-SIMS analysis of bulk Poly (methyl methacrylate) films

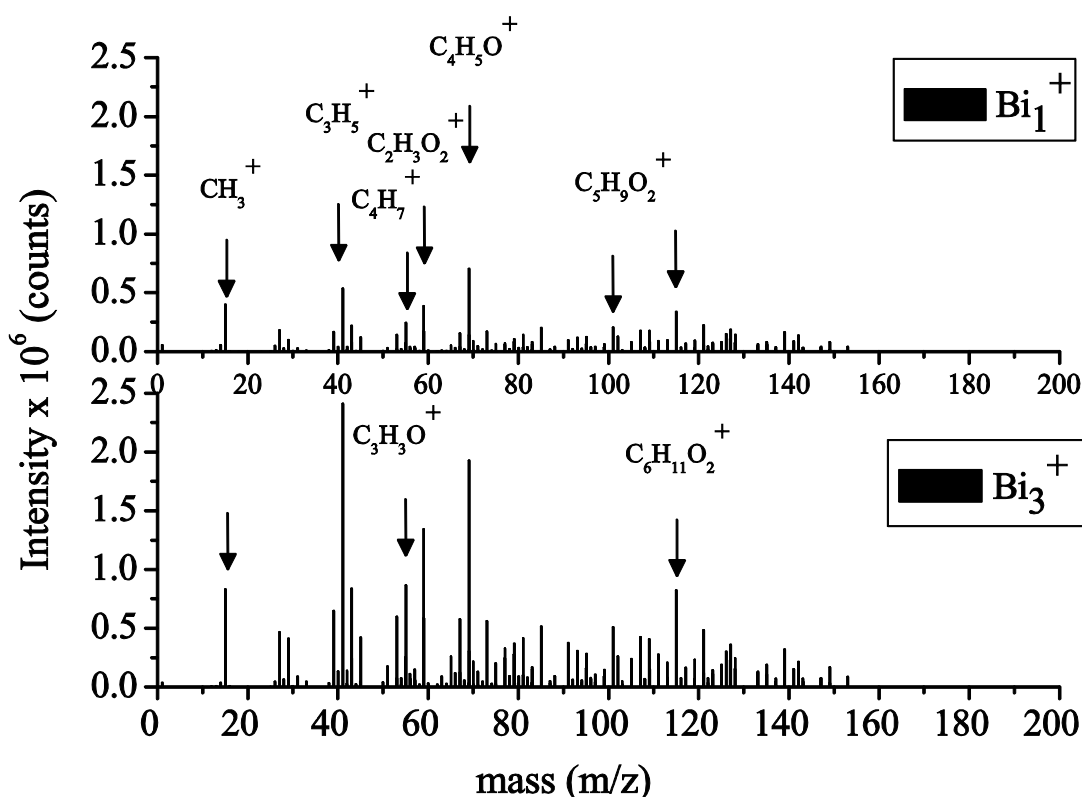


Fig. V-1: Positive ToF-SIMS spectra of bulk PMMA using 25 keV  $\text{Bi}_1^+$  and  $\text{Bi}_3^+$  ions. Primary ion dose during spectral acquisition was  $1 \times 10^{12}$  ions/cm<sup>2</sup>.

Fig. V-1 shows the positive mass spectra of the PMMA film prepared by spin-coating on a silicon wafer. Both spectra contains hydrocarbon peaks that are characteristic of PMMA like  $\text{CH}_3^+$  ( $m/z = 15$ ),  $\text{C}_3\text{H}_5^+$  ( $m/z = 41$ ),  $\text{C}_4\text{H}_7^+$  ( $m/z = 55$ ) which reflect the backbone structure and more specific oxygenated fragments like  $\text{C}_3\text{H}_3\text{O}^+$  ( $m/z = 55$ ),  $\text{C}_2\text{H}_3\text{O}_2^+$  ( $m/z = 59$ ),  $\text{C}_4\text{H}_5\text{O}^+$  ( $m/z = 69$ ),  $\text{C}_5\text{H}_9\text{O}_2^+$  ( $m/z = 101$ ) and  $\text{C}_6\text{H}_{11}\text{O}_2^+$  ( $m/z = 101$ ). It is possible to detect many characteristic peaks in the negative mass spectra of PMMA although it is mostly dominated by  $\text{O}^-$  and  $\text{CH}^-$  peaks. Since negative PMMA spectra of the Storing Matter deposits did not provide any valuable information (the intensities of specific fragments were hardly higher than the background signal)[187], the negative spectra are not shown for PMMA films or for Storing Matter spectra in the following sections.

When analysed by  $\text{Bi}_3^+$  ions, there is a significant increase in both background signal and intensity of specific fragments compared to analysis with  $\text{Bi}_1^+$  (Fig. V-1). This is not

surprising since cluster ion bombardment increases sputter yields and decreases damage on the surface compared to analysis with monoatomic ion bombardment.

### 2.1.1. a) Varying fluence

Before evaluating Storing Matter deposits, in order to see the damage effect of  $\text{Ar}^+$  ion bombardment on sputtering of PMMA and to get some additional reference data to compare to Storing Matter mass spectra, a thin PMMA film was sputtered with various primary ion fluences above the static limit ( $1 \times 10^{12}$  ions/cm<sup>2</sup>) and the resulting craters on the film were analysed by ToF-SIMS.

Fig. V-2 and Fig. V-3 show the change in intensity of secondary ions in the fingerprint spectra of PMMA film after sputtering with  $\text{Ar}^+$  ion fluences between  $3.3 \times 10^{13}$  -  $2 \times 10^{15}$  ions/cm<sup>2</sup>. Each point refers to a crater obtained after sputtering the PMMA film with  $\text{Ar}^+$  primary ion which is rastered over an area of about  $1.5 \times 1.5$  mm<sup>2</sup>.

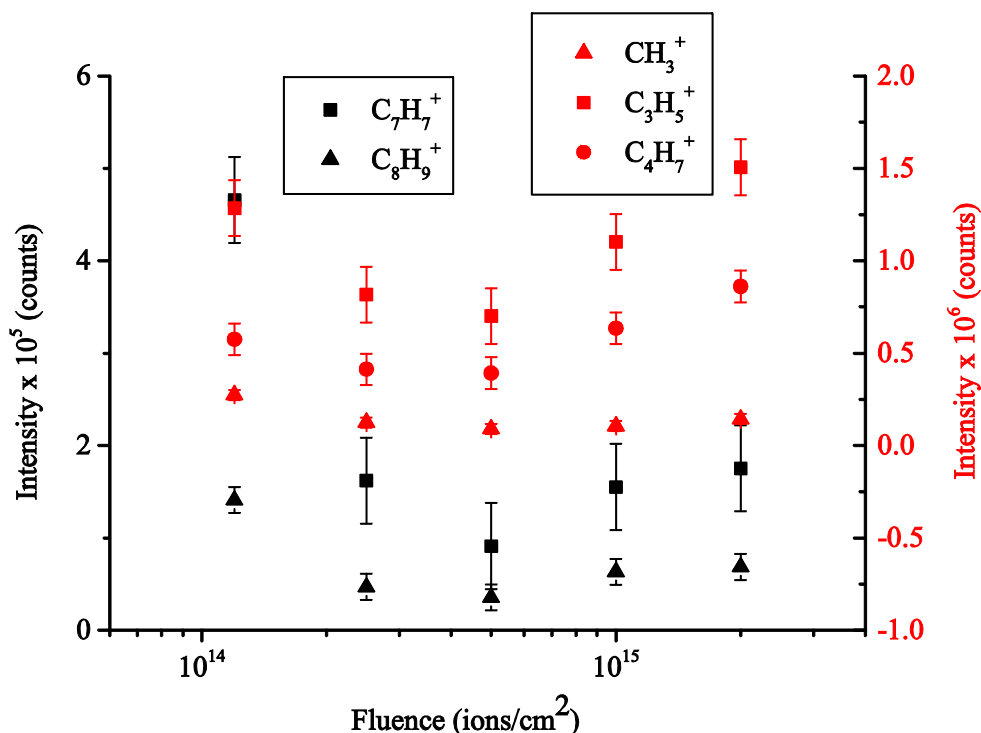


Fig. V-2: Variation of non-characteristic and characteristic ion intensities on the PMMA crater with incident fluence. Etching was carried out using 4 keV  $\text{Ar}^+$  monoatomic ions and for analysis  $\text{Bi}_3^+$  cluster ions were used.

Fig. V-2 shows the change in intensities of some specific fragments like  $\text{CH}_3^+$ ,  $\text{C}_3\text{H}_5^+$  and  $\text{C}_4\text{H}_7^+$  and non-specific hydrocarbons peaks like  $\text{C}_7\text{H}_7^+$  and  $\text{C}_8\text{H}_9^+$ . Fig. V-3 shows the change for oxygenated specific fragments like  $\text{C}_3\text{H}_3\text{O}^+$ ,  $\text{C}_2\text{H}_3\text{O}_2^+$ ,  $\text{C}_4\text{H}_5\text{O}^+$ , and  $\text{C}_6\text{H}_{11}\text{O}_2^+$ . The trend

is that the intensities of all fragments decrease with increasing fluence until a fluence of  $4 \times 10^{14}$  ions/cm<sup>2</sup>. Ninomiya *et al.* achieved depth profiling of some polymers including PMMA using large Ar clusters.[54] They observed first an initial decrease in the intensity of the characteristic PMMA fragment ion  $C_4H_5O^+$  ( $m/z = 69$ ) until a fluence of  $5 \times 10^{13}$  ions/cm<sup>2</sup> (which is well known in SIMS experiments due to damage accumulation and saturation from the primary beam irradiation) and then a steady state was observed until a fluence of  $3 \times 10^{14}$  ions/cm<sup>2</sup> which was followed by a sudden decrease in its intensity. In case of 5.5 keV Ar monomer ion probe, there was a rapid decrease in  $C_4H_5O^+$  intensity with increasing fluence; no steady state was observed.[54] Using 4 keV  $Ar^+$  primary ions for sputtering, we first observed a decrease in intensity within the same fluence range (up to  $3 \times 10^{14}$  ions/cm<sup>2</sup>) as Ninomiya *et al.* without steady state. Differently, at higher fluences (up to  $5 \times 10^{15}$  ions/cm<sup>2</sup>), an increase in most of the fragment intensities was observed. However, Ninomiya *et al.* did not consider an as high fluence as  $5 \times 10^{15}$  ions/cm<sup>2</sup>. Davenas *et al.* observed changes on the PMMA irradiated at ion doses from below  $1 \times 10^{15}$  ions/cm<sup>2</sup> up to above  $1 \times 10^{16}$  ions/cm<sup>2</sup> by Infrared Spectroscopy. [99] For fluences up to  $1 \times 10^{15}$  ions/cm<sup>2</sup>, regular disappearance of  $CH_2$ ,  $CH_3$ ,  $CH_3-O$ ,  $C-C-O$  and ester group is observed. For fluences between  $1 \times 10^{15}$  ions/cm<sup>2</sup> and  $1 \times 10^{16}$  ions/cm<sup>2</sup> the ester group shows better stability, however there is scission of the valence bond  $-C-CH_3$  of the quaternary carbon. Above a fluence of  $1 \times 10^{16}$  ions/cm<sup>2</sup>, PMMA is degraded by scission of the valence of  $-C-CH_3$  mainly and shows good stability for the ester group.

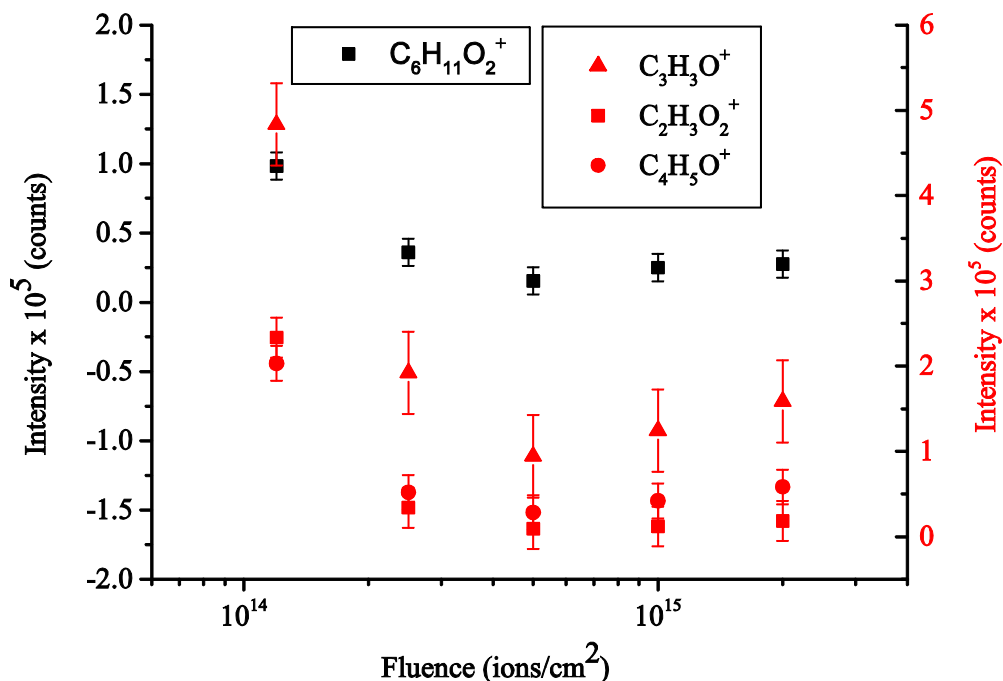




Fig. V-3: Variation of oxygenated characteristic ion intensities on the PMMA crater with incident fluence. Etching was carried out using 4 keV Ar<sup>+</sup> monoatomic ions and for analysis Bi<sub>3</sub><sup>+</sup> cluster ions were used.

Considering only the decreasing part of intensity with fluence for many specific PMMA fragments and combining this with increasing Si<sup>+</sup> signal, there seems to be a removal of PMMA layer by Ar<sup>+</sup> monoatomic ion beam sputtering. Up to a certain fluence, there is damage accumulation on the sputtered PMMA and the film is transformed into a carbon-rich material through preferential sputtering of oxygen. At very high fluences, since the polymer does not keep its original structure, other dynamics must be taking over. It is possible that as a result of sputtering of an already formed carbon-rich layer, fragments with high internal energies may be formed and they might undergo rearrangement owing to this high internal energy. In the work of Davenas *et al.*, they have done radiolytically evolved gas analysis of the ion beam irradiated polymers, and suggested that the observation of a rise of pressure in the implantation chamber might result from the breaking of molecular bonds in the polymer at the instant of particle-matter interaction.[98] As a result, the initial bonds may be restored or new molecules may be formed.

Increase of low mass range hydrocarbon intensities can be explained by already mentioned rearrangement of the sputtered species. However, this cannot explain the increase in the intensities of oxygen containing fragments. Davenas *et al.* studied the variation of carbon and oxygen profile with increasing fluences for polystyrene, poly(methyl methacrylate) and polyimide. The RBS spectra showed for PMMA 80% of the initial oxygen was lost after a fluence of  $2 \times 10^{14} \text{ a/cm}^2$ , and C peak decreases by a factor of 2 for the same fluence.[99]

The information we could obtain from Fig. V-2 and Fig. V-3 is that by increasing the fluence of the ion beam, the characteristic and also non-characteristic peak intensities tend to decrease until a certain fluence, and above a critical fluence, they might reform as a result of bond scissions and rearrangement of radicals. Assuming that the rate of disappearance of oxygen is faster than carbon with increasing fluence, the increase in intensities of fragments with oxygen might be due to exposing samples to air during the sample transfer from the Storing Matter chamber to the ToF-SIMS instrument. It should be also taken into account that the degradation rate of PMMA decreases with increasing fluence[99] which can be correlated with its decreasing sputter rate with fluence[54] which facilitates the formation of new molecules.

### 2.1.2. XPS analysis of bulk Poly(methyl methacrylate) films

Since ToF-SIMS only gives information about fragments sputtered from the topmost surface, XPS was used in addition to provide information about structural changes and surface damage on the PMMA sample, as well as on elemental/molecular composition of the sample. The damage depth could be evaluated more accurately using two surface analysis methods with different surface sensitivities. This section provides a reference for the study of Storing Matter deposits prepared with changing primary ion fluences. A thin PMMA film was bombarded with  $\text{Ar}^+$  primary ions at ion fluences between  $8.3 \times 10^{12} - 4.0 \times 10^{15}$ , which is similar to the range used for ToF-SIMS analysis. The change in carbon and oxygen content, as well as in the content of molecules forming these carbon and oxygen moieties are investigated.

#### 2.1.2. a) Varying fluence

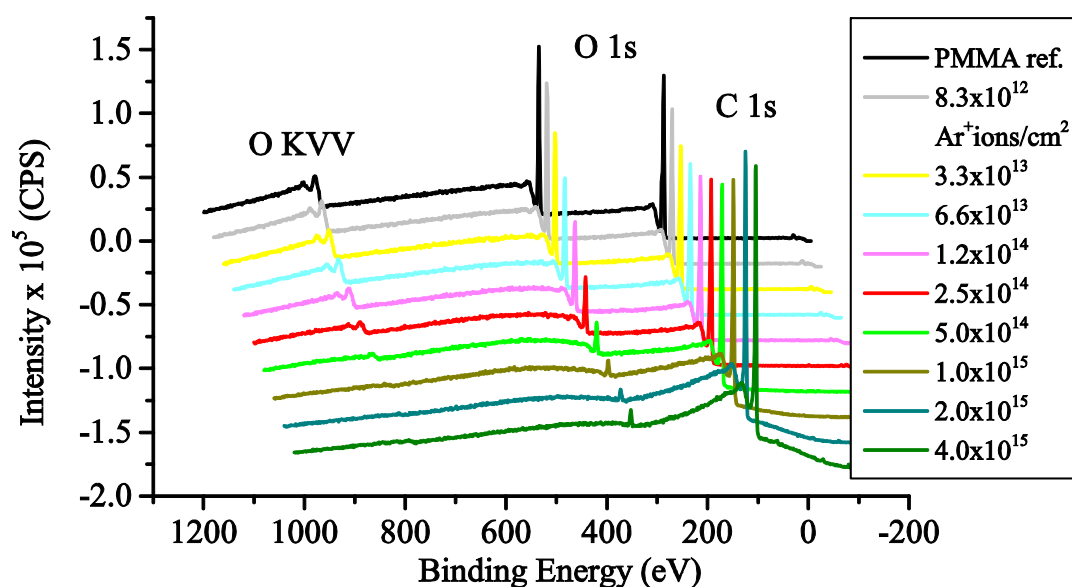


Fig. V-4: Variation of C1s and O1s peaks of the XPS Survey spectra of PMMA crater sputtered with  $\text{Ar}^+$  primary ions for fluences between  $8.3 \times 10^{12} - 4.0 \times 10^{15}$  ions.

Fig. V-4 shows the survey spectra of PMMA before (black peak) and after bombarding the surface by  $\text{Ar}^+$  ions with various fluences. In the survey spectra 3 main peaks can be observed: C1s at energies between 282-293 eV, O1s between 530-540 eV and O KVV at 984 eV. The XPS spectrum of the reference PMMA before  $\text{Ar}^+$  bombardment reveals 75 atomic percent of carbon and 25 atomic percent of O, which agrees with theoretical atomic

percentages in PMMA molecule (71.4 % C, 28.6 % O excluding H since XPS cannot detect H).

With increasing fluence, there is a continuous increase in the C1s peak and a continuous decrease in the O1s peak. The change in their intensities can be seen in Fig. V-5. There is already a significant loss of oxygen (50%) at a fluence of  $1 \times 10^{14}$  ions/cm<sup>2</sup>. PMMA completely degrades at a fluence of  $1 \times 10^{15}$  ions/cm<sup>2</sup>. When bombarded with ion beams PMMA dissociates faster than PS. Briggs *et al.* reported for a similar primary ion dose of  $1 \times 10^{14}$  ions/cm<sup>2</sup>, the relative damage on PS was much less than on PMMA.[25] Unlike PMMA, PS contains no electronegative elements and is highly aromatic. It is well known that the aromatic moieties increase the stability against radiation. In case of PMMA, electronegative elements (e.g. oxygen) are preferentially sputtered, leading to faster dissociation and changes by ion impact.

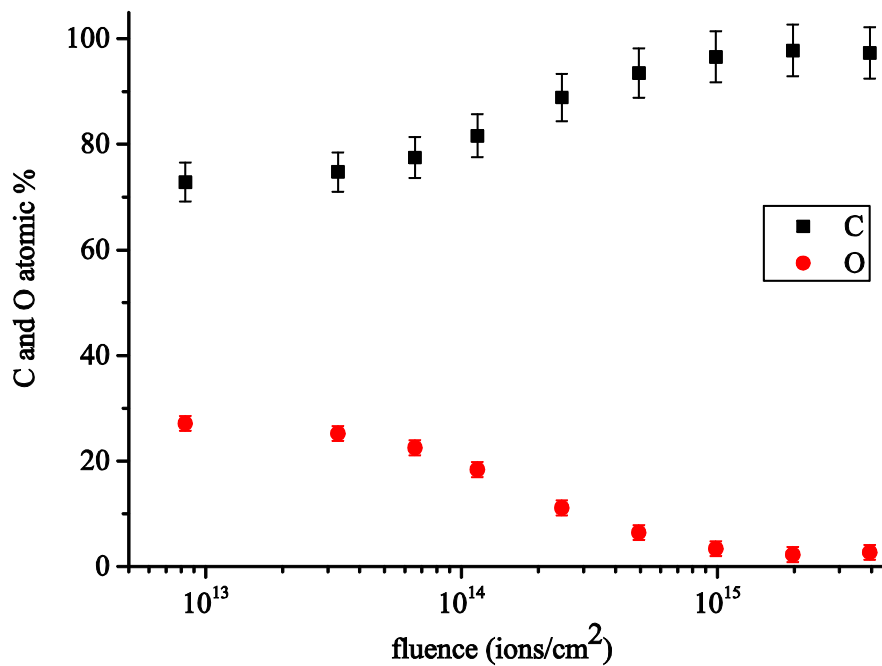


Fig. V-5: Variation of atomic percentages of carbon and oxygen contents of PMMA crater sputtered with Ar<sup>+</sup> primary ions for fluences between  $8.3 \times 10^{12}$  –  $4.0 \times 10^{15}$  ions.

Fig. V-5 not only shows the loss of oxygen through preferential sputtering, but also the increase in carbon content as a result of decrease in O:C atomic ratio. After a fluence of  $1 \times 10^{15}$  ions/cm<sup>2</sup>, most of the surface is covered with carbon-rich layer through preferential loss of oxygen-containing pendant groups. This is in contradiction with ToF-SIMS results from the previous section, since an eventual increase in intensities of oxygen-containing

characteristic fragments was observed. This difference is most probably due to different information depths for SIMS and XPS techniques. In ToF-SIMS secondary ions escape from a depth down to 1 nm[198] whereas the escape up to a maximum depth of photoelectrons is 5-10 nm in case of XPS. [199] In case of XPS, oxygen is only present in a small fraction of the analysed volume, while it is present in the whole volume for SIMS. The other reason is the oxidation of the crater during sample transfer before ToF-SIMS analysis. For the crater analysis, transfer of samples under UHV conditions was not possible as in the case of Storing Matter deposits since the transfer suitcase allows only the transfer of collectors due to geometrical constraints. The craters formed with different primary ion fluences have different degrees of irradiation induced damage which leads to different degrees of oxidation at the sample surface. This might explain the increasing oxygen content for the analysis of samples with ToF-SIMS.

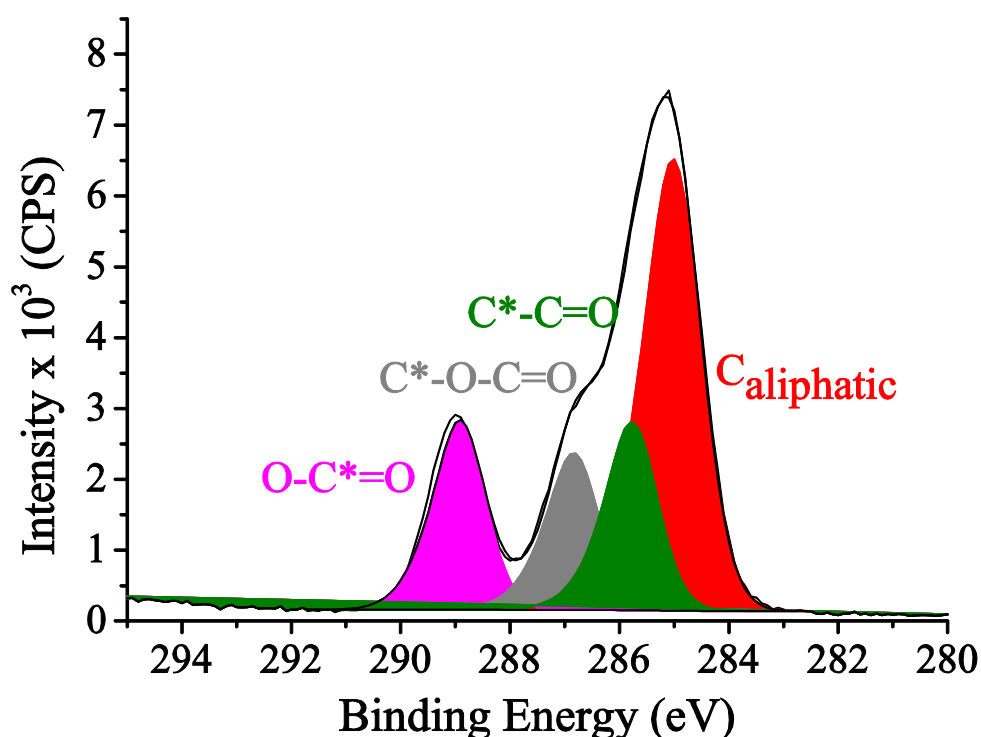


Fig. V-6: C1s core level spectrum and peak fit of bulk PMMA showing contributions from the four different types of C atom.

The C1s is generally deconvoluted into four components.[25],[200],[201],[202] The C1s spectra with these four components is shown in Fig. V-6. The components are  $\underline{\text{C}}\text{-CH}_3$ ,  $\underline{\text{C}}\text{-C(=O)-R}$ ,  $\underline{\text{C}}\text{-O-C=O}$  and  $\text{O-}\underline{\text{C}}\text{=O}$ . The binding energies used for fitting peaks of different

components are shown in Table V-1. The positions of the peaks are not exactly same as in literature, but the differences between the peak positions are similar.

Table V-1: Binding energies of different components in the C1s core level shift of the PMMA spectra

C 1s Component	Binding energy (eV)	Binding energy (eV)[200]
$\underline{\text{C}}\text{-CH}_3$	284.10	285
$\underline{\text{C}}\text{-C(=O)-R}$	284.79	285.72
$\underline{\text{C}}\text{-O-C=O}$	286.10	286.79
C-OR/C-OH	286.21	286.90
O- $\underline{\text{C}}\text{=O}$	288.10	289.03

The deconvolution of the the C1s peak was made for the various  $\text{Ar}^+$  ion fluences. The change in atomic percentages of deconvoluted components can be seen in Fig. V-7. There is a continuous increase in aliphatic carbon percentage, whereas the percentage of the other components decreases. This is not surprising since pendent groups of PMMA contain oxygen and as a result of preferential sputtering of oxygen, these groups diminish after a certain fluence giving rise to formation of other radicals.

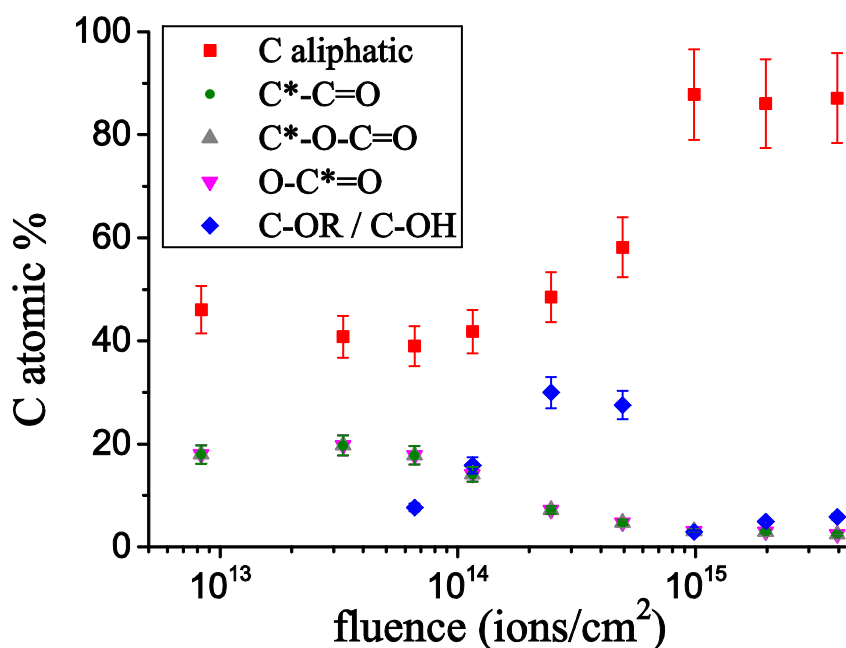


Fig. V-7: Variation of atomic percentages of carbon components of PMMA crater sputtered with Ar<sup>+</sup> primary ions for fluences between  $8.3 \times 10^{12} - 4.0 \times 10^{15}$  ions.

For the first fluences, it was possible to fit the spectra with four components, however after a fluence of  $3 \times 10^{13}$  ions/cm<sup>2</sup>, the C1s spectra changed significantly and it was not possible to fit it using four components, but a fifth was needed. Briggs *et al.* did the fitting of C1s spectra with four components for changing fluences and like in our case they observed an increase in aliphatic carbon atomic percentage and a decrease in other component atomic percentages.[25] However, they have not presented a justification for using four components at different ion doses. Since there is a structural change even after an ion dose of  $3 \times 10^{13}$  ions/cm<sup>2</sup>, and the spectra looks different (Fig. V-8 and Fig. V-9) than the PMMA reference spectra (Fig. V-6), we have used five components for fitting C1s spectra at higher fluences. The new component appearing at higher fluences can be attributed to C-OR/ C-OH. [36]

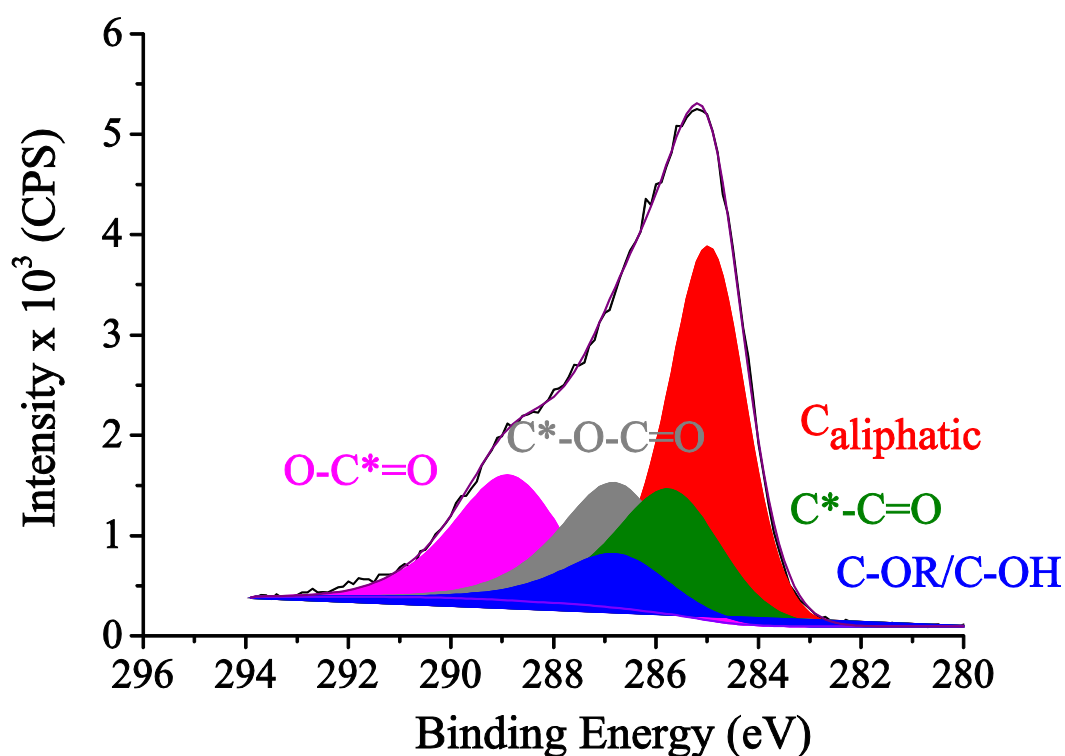


Fig. V-8: C1s core level spectrum and peak fit of PMMA crater showing contributions from the four different types of C atom after bombardment with  $6.6 \times 10^{13}$  Ar<sup>+</sup> ions/cm<sup>2</sup>

It is not very common in literature to deconvolute the O1s peak into its components. The deconvoluted spectra shows almost equal percentages (50%) of C-O-C and C=O components (Fig. V-10).

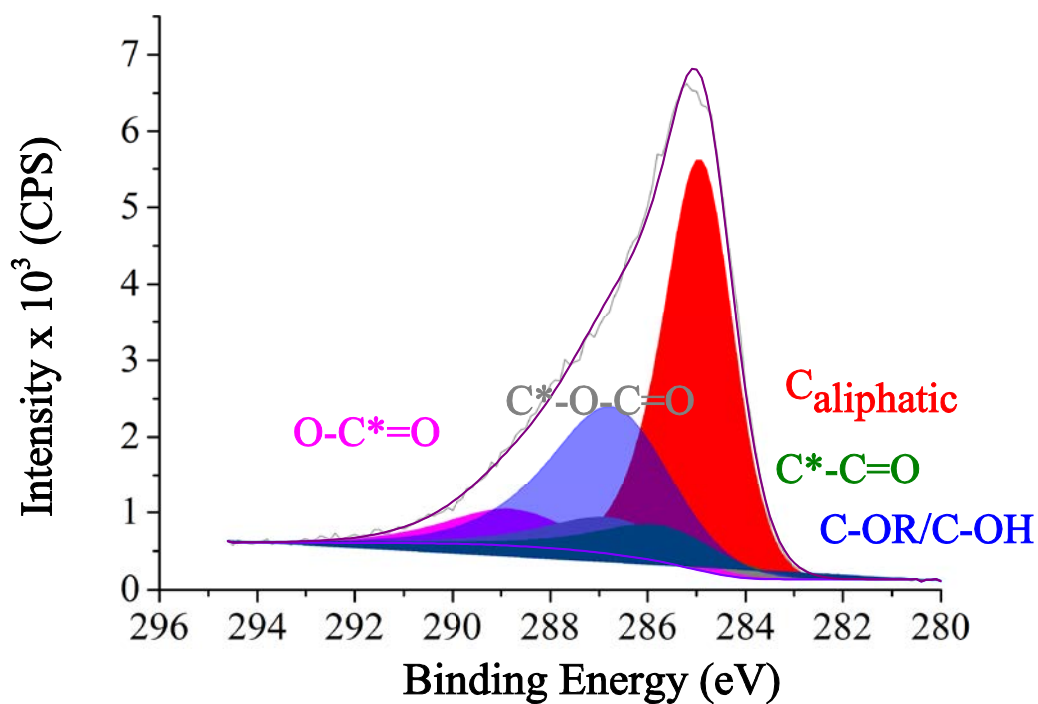


Fig. V-9: C1s core level spectrum and peak fit of PMMA crater showing contributions from four different types of C atom after bombardment with  $2.5 \times 10^{14}$  Ar<sup>+</sup> ions/cm<sup>2</sup>.

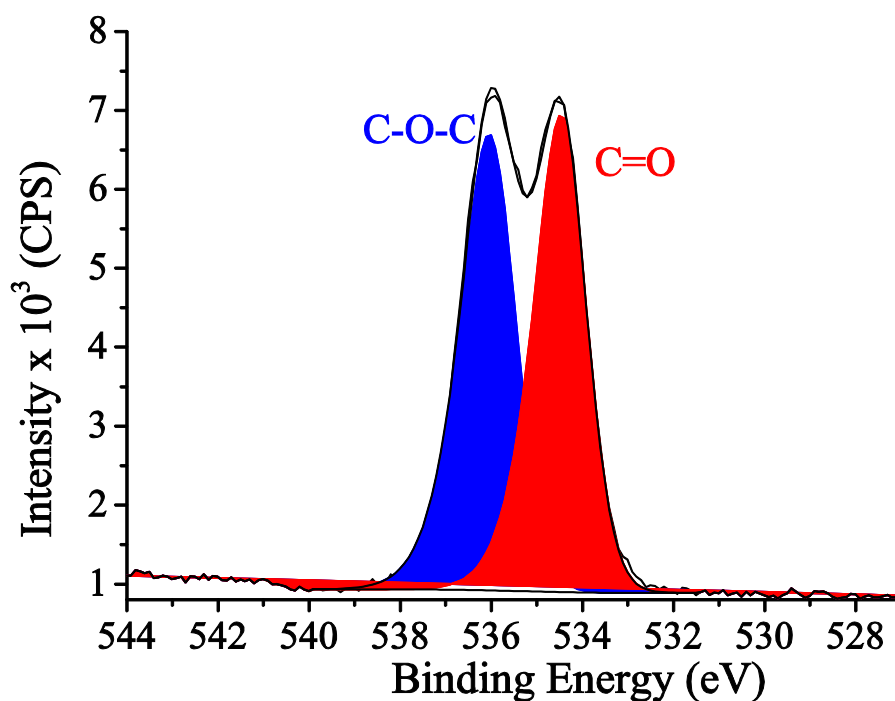


Fig. V-10: O1s core level spectrum and peak fit of PMMA crater showing contributions from two different types of O atom after bombardment with  $2.5 \times 10^{14}$  Ar<sup>+</sup> ions/cm<sup>2</sup>.

Fig. V-11 shows the variation of percentages of two components with increasing fluence. The fitting of the O1s spectra was possible until a fluence of  $10^{15}$  ions/cm<sup>2</sup>. For the last data points, the O1s spectra was too noisy and not possible to fit. If we only consider data until the fluence of  $10^{15}$  ions/cm<sup>2</sup>, it is expected that C=O percentage decreases and C-O-C percentage increases. With increasing fluence, double bonds are broken more easily and the new radicals form new components, mostly without oxygen.

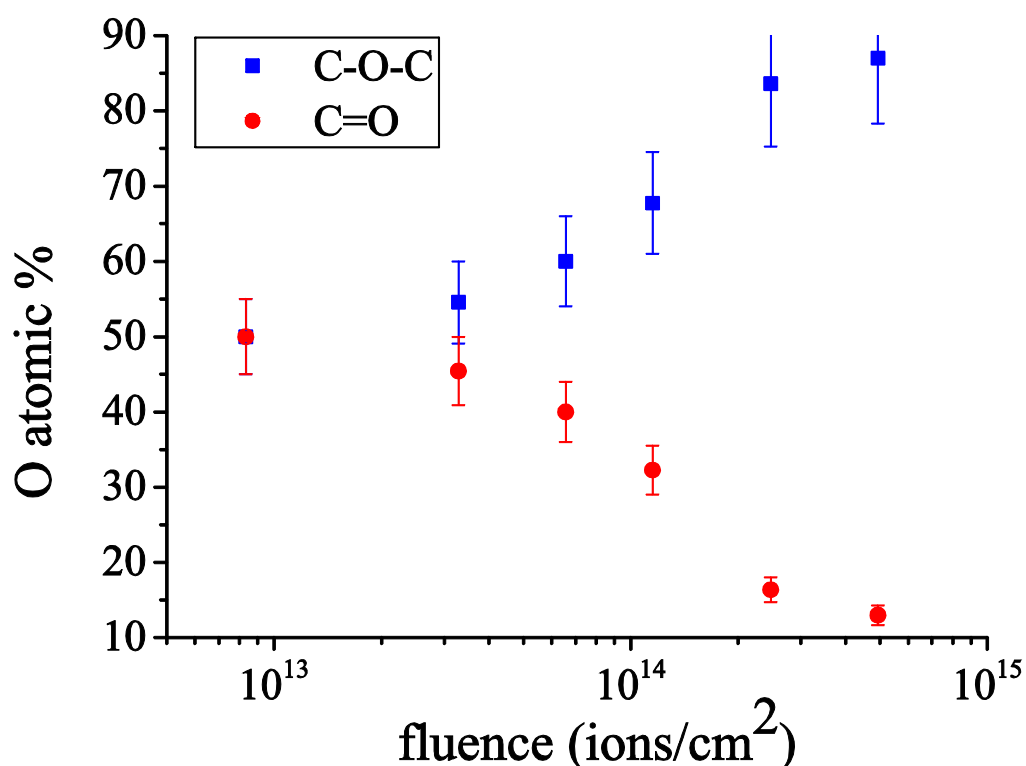


Fig. V-11: Variation of atomic percentages of oxygen components of PMMA crater sputtered with Ar<sup>+</sup> primary ions for fluences between  $8.3 \times 10^{12}$  –  $4.0 \times 10^{15}$  ions/cm<sup>2</sup>.

Yamamoto *et al.* evaluated the damage effect of polyatomic and monoatomic ions on sputtering of PMMA with 5 and 20 keV Ar clusters and 20 keV Ar monatomic bombardment. In the XPS spectra of PMMA film before sputtering and after sputtering with an ion fluence of  $1 \times 10^{14}$  ions/cm<sup>2</sup> Ar polyatomic and monoatomic ions, there were significant differences. The XPS peak at about 288 eV attributed to the O-C=O component disappeared after Ar monatomic bombardment, however was retained after Ar polyatomic bombardment. The binding energy in the molecule is 4 eV and 20 keV Ar monatomic bombardment was enough to break the bonds.[203] In case of cluster bombardment, each atom in the cluster has incident energies of 2.5 or 10 eV/atom for 5 and 20 keV Ar ion beam respectively. C and O



elemental percentages stayed unchanged compared to XPS analysis of reference PMMA surface in case of 5 keV Ar cluster ion bombardment which was achieved by keeping the energy per atom value below binding energy of the molecule. In case of Ar monoatomic primary ion bombardment, the carbon ratio increased. A carbon-rich layer was formed on the surface by damage accumulation as oxygen is preferentially sputtered. [203]

### **3. Analysis of PMMA Storing Matter deposits**

#### **3.1. Detection and localization of the PMMA Storing Matter deposit**

Similar to PS storing matter deposits, Ag collectors with PMMA fragments from the sputter-deposition process were analysed by ToF-SIMS. The deposits were localized with a stage scan of the collector. Like in the case of localization of PS deposit, the region on the collector with maximum intensity was found through taking a series of spectra along several diameters of the collector until finding the maximum intensity of specific PS fragments and then a series of spectra were taken through the centre of the deposit.

Secondary ion images of the specific and non-specific PMMA fragments are shown in Fig. V-12 (with a higher number of pixel binning). For example for some specific PMMA fragments like  $\text{CH}_3^+$ ,  $\text{C}_2\text{H}_3\text{O}_2^+$ ,  $\text{C}_6\text{H}_{11}\text{O}_2^+$  secondary ion images, an increase in intensity is observed at the region where the deposit is expected. The increasing intensity is represented by a colour contrast ratio. For other specific fragments like  $\text{CH}_3\text{O}^+$ ,  $\text{C}_4\text{H}_5\text{O}^+$  and  $\text{C}_5\text{H}_9\text{O}_2^+$ , it is difficult to see the contrast since the amount of matter collected is too small to make a contrast. For the specific hydrocarbon fragments like  $\text{C}_3\text{H}_5^+$ ,  $\text{C}_4\text{H}_7^+$  it is difficult to distinguish the deposit from the hydrocarbon impurities on the collector although the intensity of peaks are high enough to create a contrast.

Fig. V-13 shows the secondary ion images of the PMMA fragments for a given counts of secondary ions. Here, in addition to the increase of intensities of specific fragments, a slight increase in Ag intensity can be observed enhanced by the presence of the deposit.

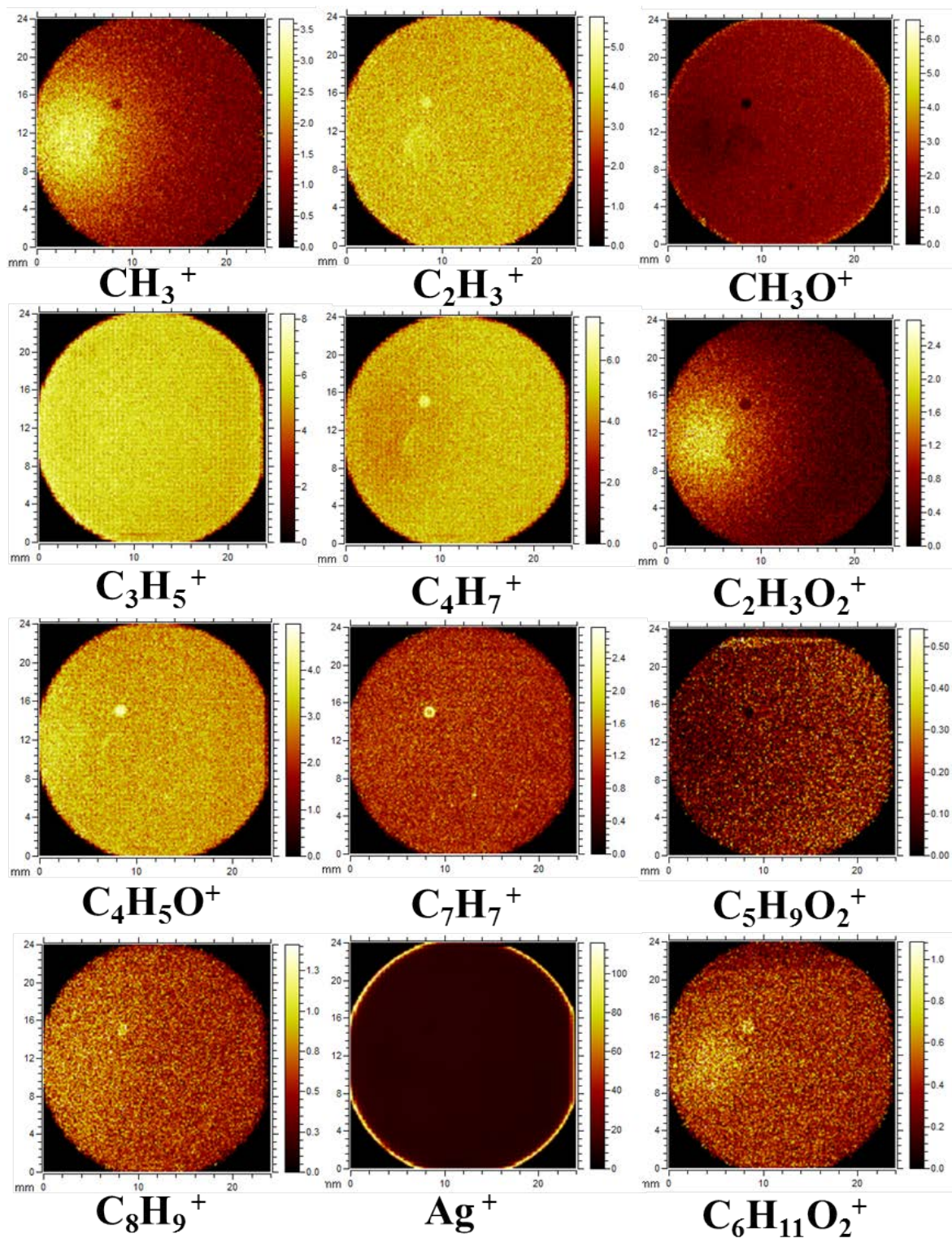


Fig. V-12: Secondary ion images of positive ions observed in the positive secondary ion mass spectra of the Ag collector with PMMA deposit obtained by a stage scan of the collector (16x16 pixel binning) (deposits prepared with constant primary ion fluence at  $5.6 \times 10^{12}$  ions/cm<sup>2</sup> for a total number of primary ions of  $4.0 \times 10^{13}$ ) / intensities normalized to Ag intensity



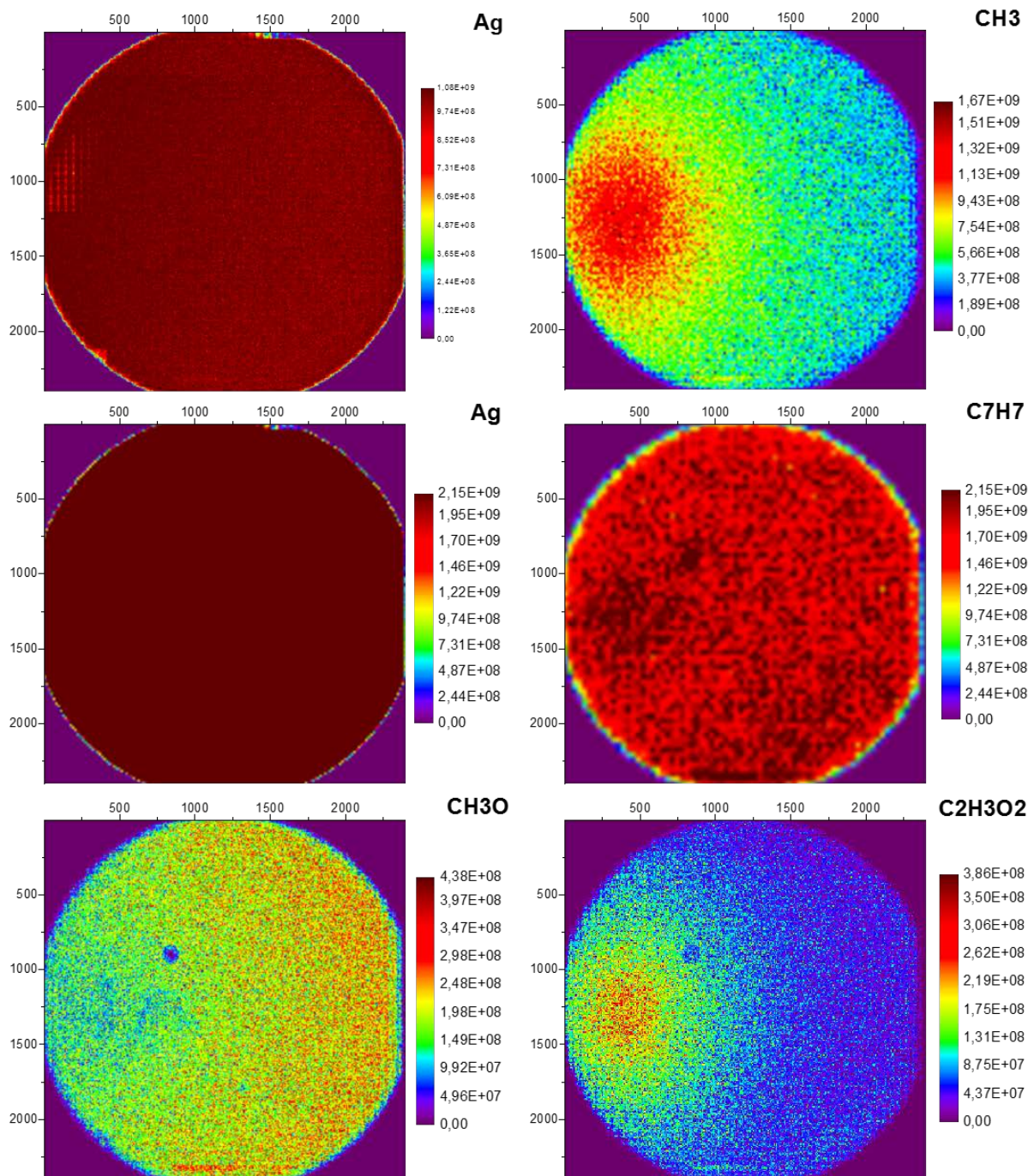


Fig. V-13: Secondary ion images of positive ions observed in the positive secondary ion mass spectra of the Ag collector with PMMA deposit obtained by a stage scan of the collector (8x8 pixel binning for first Ag, CH<sub>3</sub>, CH<sub>3</sub>O and C<sub>2</sub>H<sub>3</sub>O<sub>2</sub> and 16x16 pixel binning for second Ag and C<sub>7</sub>H<sub>7</sub>) (deposits prepared with constant primary ion fluence at  $5.6 \times 10^{12}$  ions/cm<sup>2</sup> for a total number of primary ions of  $4.0 \times 10^{13}$ ) / absolute intensities for a total secondary ion counts of  $1.4 \times 10^8$

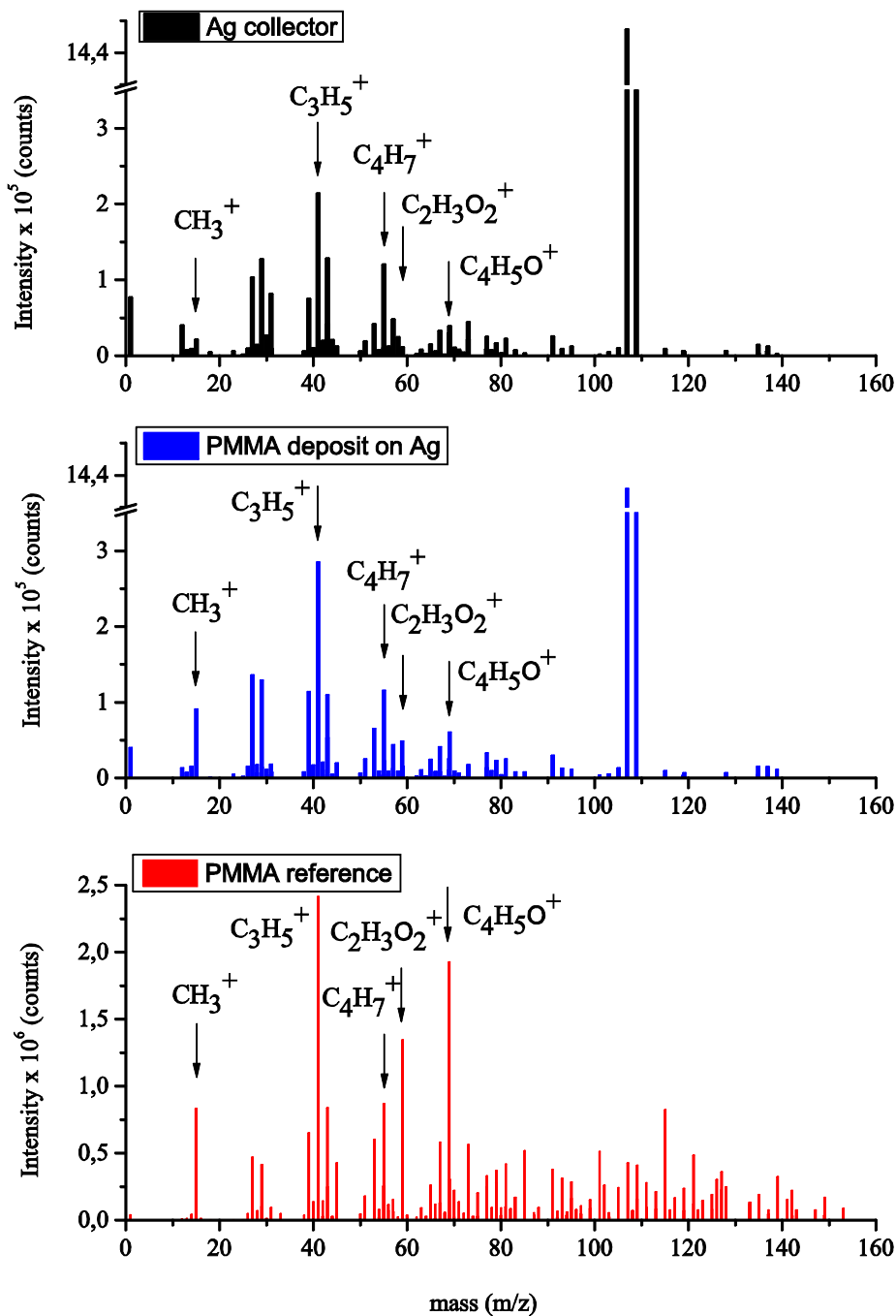


Fig. V-14: ToF-SIMS Spectra of the Ag collector, PMMA StoMat deposit (prepared with constant primary ion fluence at  $5.6 \times 10^{12}$  ions/cm<sup>2</sup> for a total number of primary ions of  $4.0 \times 10^{13}$ ) and PMMA reference.

Fig. V-14 shows the positive mass spectra of the pristine Ag collector, of the collector with deposit and finally of the PMMA reference film. The most dominant peaks in the spectra of PMMA reference are at 15 (CH<sub>3</sub><sup>+</sup>), 41 (C<sub>3</sub>H<sub>5</sub><sup>+</sup>), 55 (C<sub>4</sub>H<sub>7</sub><sup>+</sup>), 59 (C<sub>2</sub>H<sub>3</sub>O<sub>2</sub><sup>+</sup>) and 69 (C<sub>4</sub>H<sub>5</sub>O<sup>+</sup>). Most of the hydrocarbon fragments are already present on the silver collector without deposit which makes it difficult to notice the difference between the spectra of the pristine Ag collector and of the collector with deposit. However, there is a clear difference for the major

peaks that are also observed in the reference PMMA spectra. For hydrocarbon peaks like  $C_3H_5^+$ ,  $C_4H_7^+$  the high intensity on the spectra of silver collector helps to explain the fact that no contrast is observed for the stage scan of the collector with the deposit in Fig. V-12. The high contrast in the stage scan for the  $CH_3^+$  fragment can be justified by the bigger difference in its intensity on the pristine silver and the silver with deposit. For oxygenated specific PMMA fragments like  $C_2H_3O_2^+$  and  $C_4H_5O^+$  it is more difficult to see the difference in intensity compared to hydrocarbon fragments although  $C_2H_3O_2^+$  fragment is one of the easiest to observe in the stage scan of the deposit.

### **3.2. Study of the effect of coverage and primary ion fluence on fragmentation of PMMA during Storing Matter deposition**

#### **3.2.1. Constant fluence**

Like in the case of PS, we first studied the effect of changing deposit coverage on the fragmentation of PMMA polymer keeping the  $Ar^+$  primary ion fluence constant at  $1 \times 10^{12}$  ions/cm<sup>2</sup>. Fig. V-15 shows the positive ToF-SIMS spectra in the centre of the deposit with the highest PMMA specific fragment intensities for different coverages of the deposit. Some hydrocarbon and oxygenated PMMA specific fragments which are also observed in the reference PMMA spectra are highlighted here. The red arrows highlight fragments at masses of 15 ( $CH_3^+$ ), 59 ( $C_2H_3O_2^+$ ) and 69 ( $C_4H_5O^+$ ) while black arrows highlight masses of 41 ( $C_3H_5^+$ ) and 55 ( $C_4H_7^+$ ). What can be noticed quickly is an increase in intensity for the first group of fragments and no trend for the second group of fragments with increasing deposit coverage. For the first group of fragments ( $CH_3^+$  and  $C_2H_3O_2^+$ ), it should also be noted that their stage scan showed contrast for the stage scan of collectors, whereas no contrast was observed for the second group of fragments ( $C_3H_5^+$  and  $C_4H_7^+$ ).

Next, in order to see the distribution of these fragments along the diameter of the collector, the variation of their intensities was plotted for all five deposit coverages. Unlike in the case of PS, for representation of results we did not use fragment intensity ratios since the primary ion current during ToF-SIMS analysis was stable.

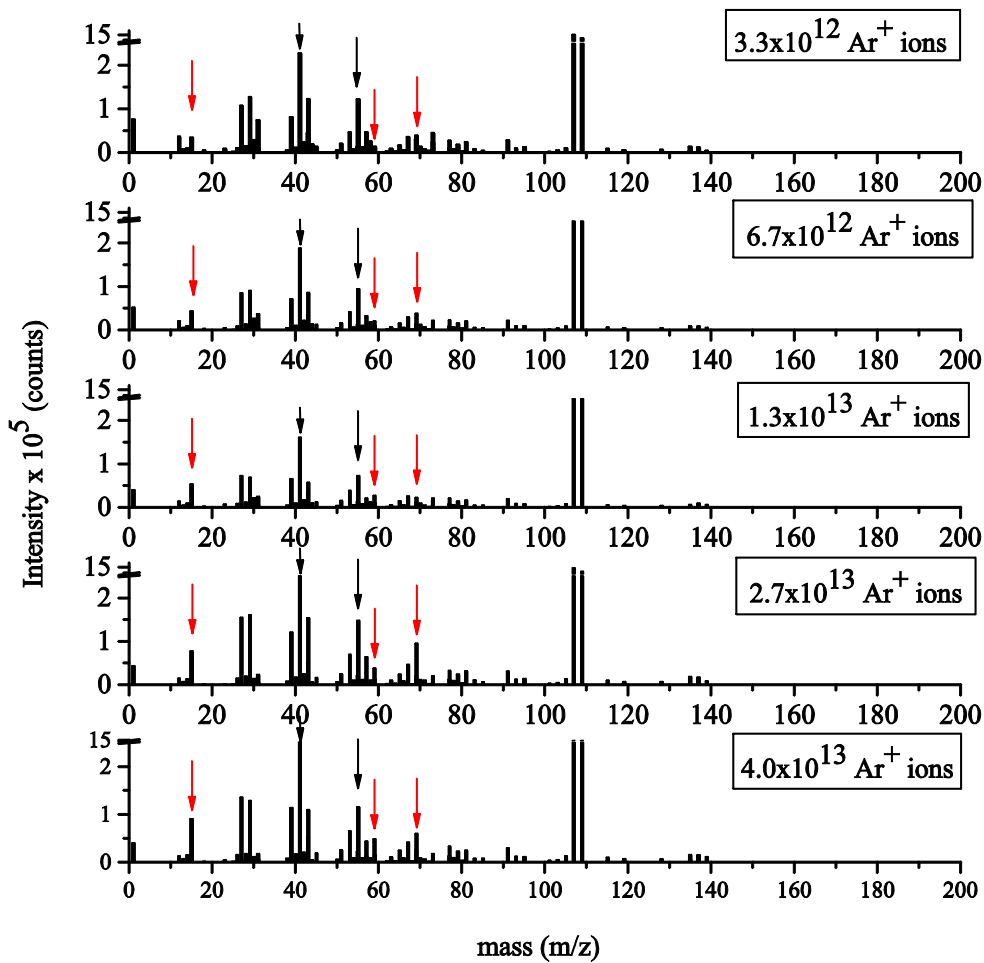


Fig. V-15: ToF-SIMS Spectra of the PMMA StoMat deposit prepared at five different coverages with incoming  $3.3 \times 10^{12}$ ,  $6.7 \times 10^{12}$ ,  $1.3 \times 10^{13}$ ,  $2.7 \times 10^{13}$  and  $4.0 \times 10^{13}$   $\text{Ar}^+$  ions at a constant primary ion fluence of  $5.6 \times 10^{12}$  ions/cm<sup>2</sup>

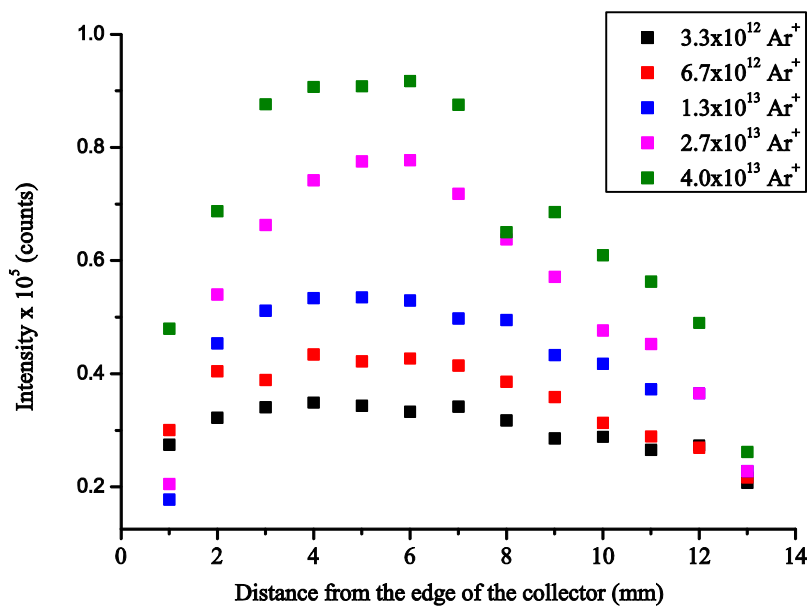


Fig. V-16: Variation of  $\text{CH}_3^+$  fragment intensities with varying coverage along the diameter of the collector (deposits are prepared by sputtering PMMA film with different incoming number of  $\text{Ar}^+$  primary ions at a constant primary ion fluence of  $5.6 \times 10^{12}$  ions/cm<sup>2</sup>)

Fig. V-16, Fig. V-17 and Fig. V-18 show the distribution for the first group of fragments ( $\text{CH}_3^+$ ,  $\text{C}_2\text{H}_3\text{O}_2^+$  and  $\text{C}_6\text{H}_{11}\text{O}_2^+$ ), with a maximum intensity at the centre of the deposit. The intensity distributions follow a similar pattern for all three fragments with an increase in intensity with increasing deposit coverage. These graphs just give an idea about how the distribution of specific fragments looks like. More detailed information about the change of intensities with coverage will be given later in this section.

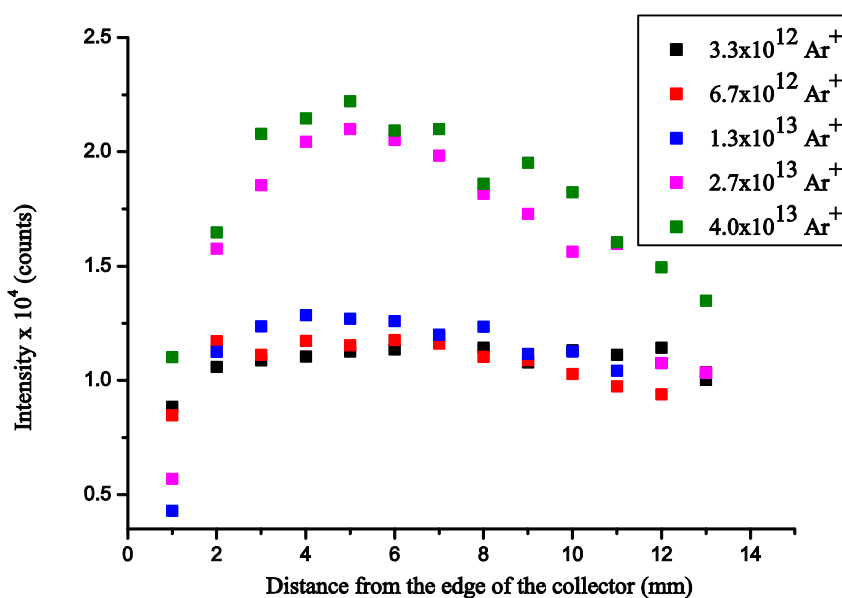


Fig. V-17: Variation of  $\text{C}_2\text{H}_3\text{O}_2^+$  fragment intensities with varying coverage along the diameter of the collector (deposits are prepared by sputtering PMMA film with different incoming number of  $\text{Ar}^+$  primary ions at a constant primary ion fluence of  $5.6 \times 10^{12}$  ions/cm<sup>2</sup>)

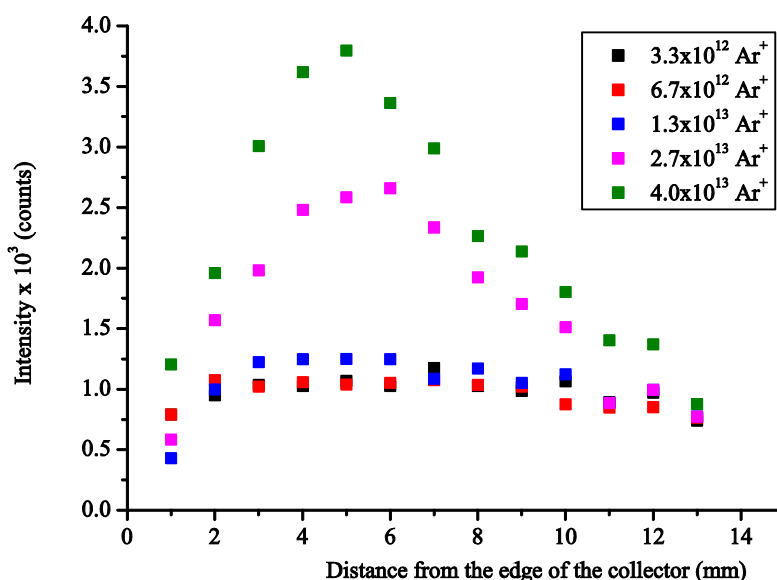


Fig. V-18: Variation of  $\text{C}_6\text{H}_{11}\text{O}_2^+$  fragment intensities with varying coverage along the diameter of the collector (deposits are prepared by sputtering PMMA film with different incoming number of  $\text{Ar}^+$  primary ions at a constant primary ion fluence of  $5.6 \times 10^{12}$  ions/cm<sup>2</sup>)

For the second group of fragments ( $C_3H_5^+$  and  $C_4H_7^+$ ) a different distribution of intensities along the collector is observed than for the oxygenated specific fragments. In Fig. V-19 and Fig. V-20 the distribution of intensities for  $C_3H_5^+$  and  $C_4H_7^+$  are shown at different coverages. There is not an increasing trend of intensities with increasing coverage like in the case of first group of fragments. The two different behaviours of these two different groups of fragments back to Fig. V-15. The first group of fragments for which intensity distributions tend to increase with coverage correspond to the ones indicated by a red arrow in the ToF-SIMS spectra. The second group of fragments which do not show a regular trend corresponds to the one highlighted by a black arrow. Still, both groups of fragments are characteristic for the PMMA structure. Since the fragments which are represented by a black arrow ( $C_3H_5^+$  and  $C_4H_7^+$ ) do already exist on the pristine collector, it is difficult to see intensity variations with increasing coverage. Moreover, as seen in Fig. V-19 and Fig. V-20, the different levels of intensities for different coverages should be an indication of the level of contaminations on the collector surface. The highest levels of intensities are observed for deposits obtained with  $2.7 \times 10^{13}$  and  $4.0 \times 10^{13}$   $Ar^+$  ions respectively and the lowest with  $1.3 \times 10^{13}$   $Ar^+$  ions. Although we expect the highest intensity levels with  $4.0 \times 10^{13}$  and lowest with  $3.3 \times 10^{12}$   $Ar^+$  ions, this is not the case. Moreover, the intensity distributions of  $C_3H_5^+$  and  $C_4H_7^+$  are quite similar to those of  $C_7H_7^+$  and  $C_8H_9^+$  (Fig. V-21 and Fig. V-22) which are not characteristic for PMMA. This also shows that the contamination levels on different collectors are not the same and makes it difficult to see the intensity variations for the specific hydrocarbon fragments.

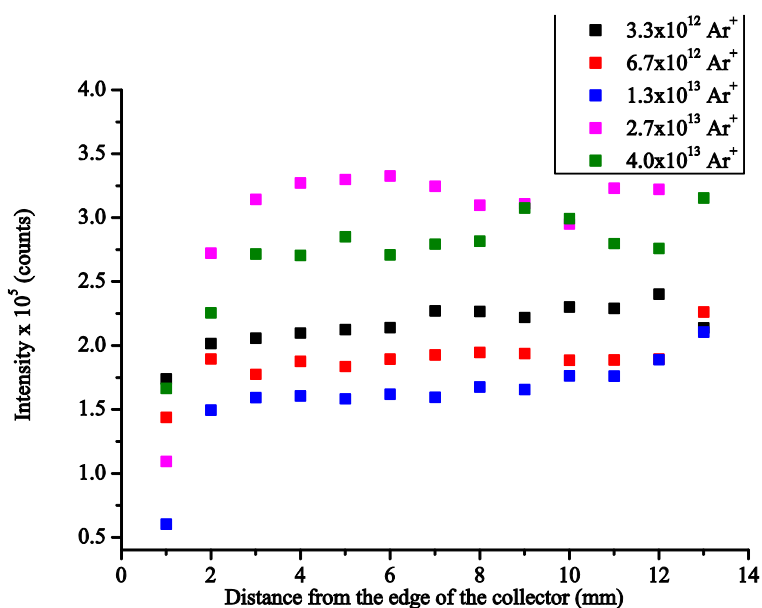


Fig. V-19: Variation of  $C_3H_5^+$  fragment intensities with varying coverage along the diameter of the collector (deposits are prepared by sputtering PMMA film with different incoming number of  $Ar^+$  primary ions at a constant primary ion fluence of  $5.6 \times 10^{12}$  ions/cm<sup>2</sup>)



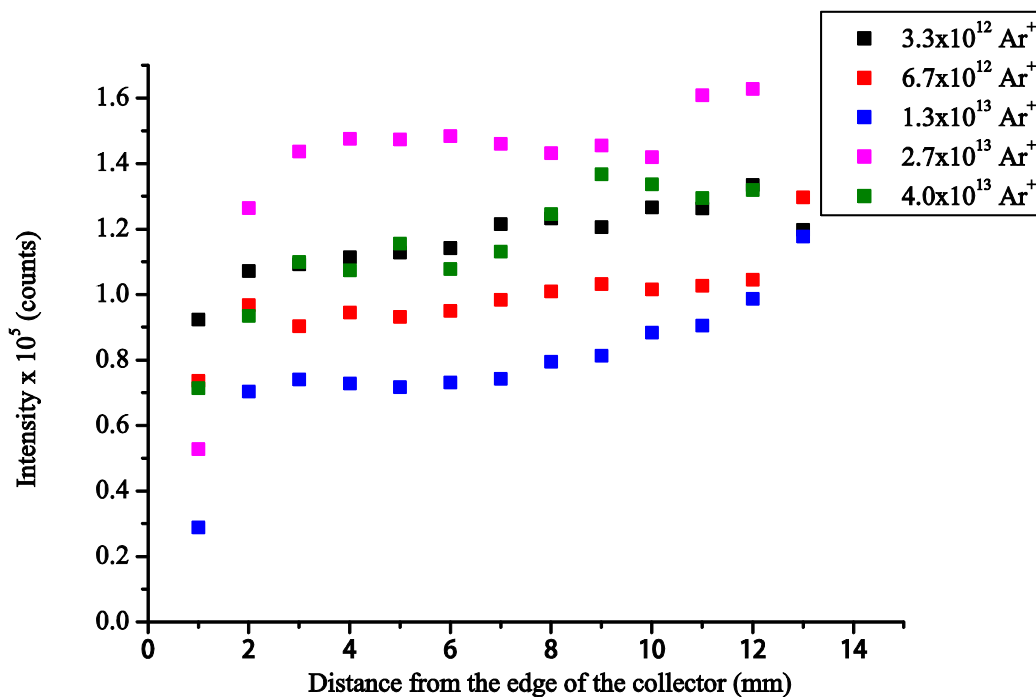


Fig. V-20: Variation of  $C_4H_7^+$  fragment intensities with varying coverage along the diameter of the collector (deposits are prepared by sputtering PMMA film with different incoming number of  $Ar^+$  primary ions at a constant primary ion fluence of  $5.6 \times 10^{12}$  ions/cm<sup>2</sup>)

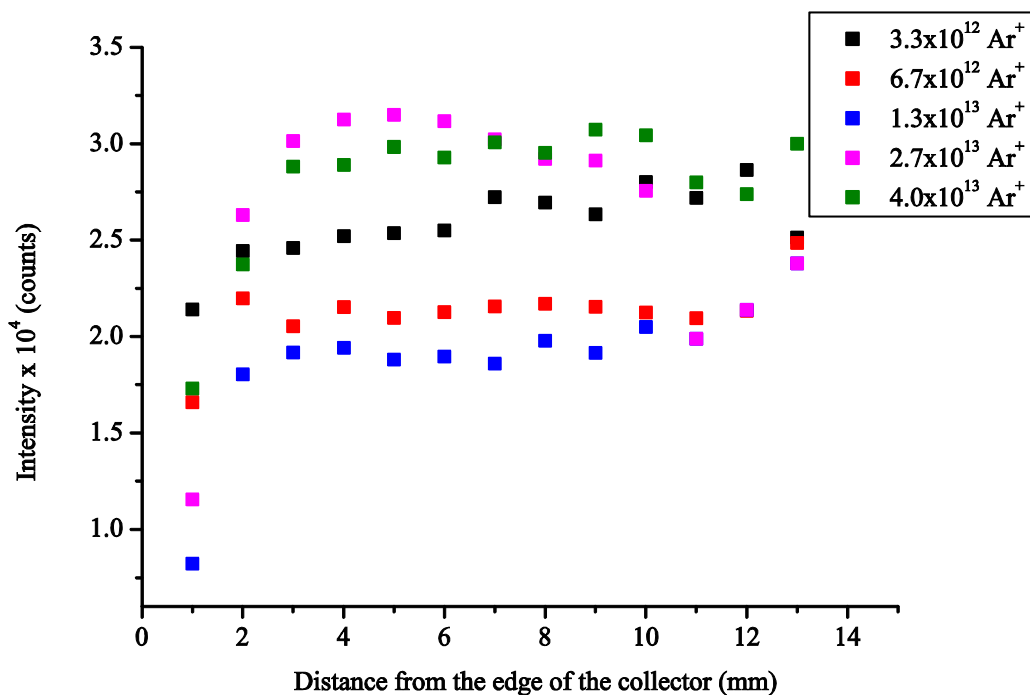


Fig. V-21: Variation of  $C_7H_7^+$  fragment intensities with varying coverage along the diameter of the collector (deposits are prepared by sputtering PMMA film with different incoming number of  $Ar^+$  primary ions at a constant primary ion fluence of  $5.6 \times 10^{12}$  ions/cm<sup>2</sup>)

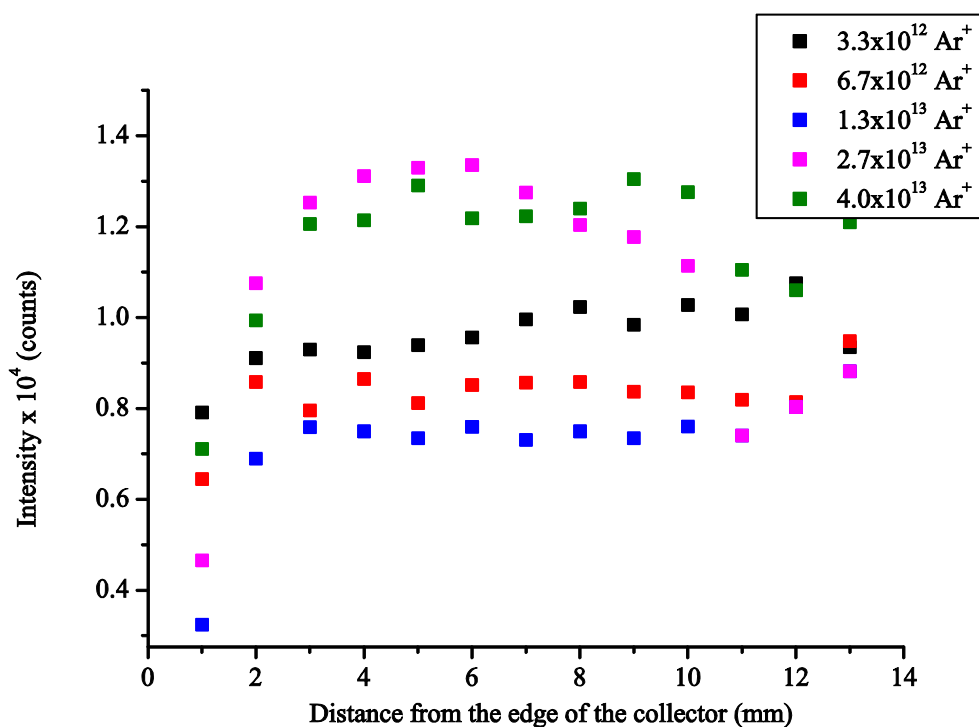


Fig. V-22: Variation of  $C_8H_9^+$  fragment intensities with varying coverage along the diameter of the collector (deposits are prepared by sputtering PMMA film with different incoming number of  $Ar^+$  primary ions at a constant primary ion fluence of  $5.6 \times 10^{12}$  ions/cm<sup>2</sup>)

Fig. V-23 and Fig. V-24 show the variation of intensities for hydrocarbon peaks and for oxygenated peaks with increasing number of  $Ar^+$  ions, i.e. with increasing coverage. In Fig. V-23 it can be seen that there is no clear trend for the change of intensities of hydrocarbon peaks except of  $CH_3^+$ . It can be observed that for  $3.3 \times 10^{12}$   $Ar^+$  ions there is a drop in intensity for all hydrocarbon fragments (including PMMA specific ones) except for  $CH_3^+$ , which could be attributed to different contamination levels of the collectors. Previously,  $CH_3^+$  has been grouped with oxygenated fragments since it shows similar behaviour to them. Here, for the ease of representation, it has been show together with other hydrocarbon fragments. Absolute intensities for hydrocarbon fragments including  $CH_3^+$  are at least one order of magnitude higher than those of oxygenated fragments. The different behaviour of  $CH_3^+$  can be explained by the process of secondary ion formation through loss of small functional groups.[47] The other two methods are protonation and de-protonation as well as formation of molecular radicals and cationization. Cationization does not seem to be a possible secondary ion formation process since in the mass spectra of the PMMA deposit, no Ag cationized components can be observed. This is due to the  $Bi_3^+$  primary ions. In case of analysis with  $Ar^+$ , it was observed that  $Ar^+$  enhances cationization, which facilitates molecular ion ejection.[158] Here, the only possible secondary ion formation processes would be the loss of

small functional groups and protonation and de-protonation. For PMMA polymer, it is easier to lose a side chain methyl group by breaking only one C-C or C-O bond than forming any of the  $C_xH_y^+$  fragments shown in Fig. V-23. This explains the increase with increasing coverage.

Unlike  $C_xH_y^+$  fragments, we see the effect of increasing coverage on the oxygenated fragments. The absolute intensities of these fragments all increase with increasing coverage. (Fig. V-24) The high mass resolution spectra of PMMA showed mostly fragments of  $C_xH_yO_z^+$  type rather than  $C_xH_y^+$ . [66] Since the primary ion fluence for both deposition and analysis was kept at  $1 \times 10^{12}$  ions/cm<sup>2</sup>, we do not expect high damage on the polymer and no significant bond-scission and rearrangement of fragments, at least during ToF-SIMS analysis. What could affect all the process, would be sticking factors of fragments on the collector surface and their rearrangement on the surface. Since we assume that the deposit has less than monolayer coverage, sputtered matter would land on silver substrate reducing the possibility of interactions between different fragments. The increase in intensities of  $C_xH_yO_z^+$  fragments are line with the study of Muddiman *et al.*, suggesting that secondary ion yields increase with surface coverage up to a fraction of 0.43 and then decreases until full coverage (i.e. a fraction of 1.0)[194] The regular increase of intensities of fragments sputter-deposited with up to  $4.0 \times 10^{13}$  Ar<sup>+</sup> ions is probably due to secondary ion yield increase in earlier stages of coverage. In order to see the effects of even higher coverages (monolayer and more), the sputtered area of the thin polymer film should be increased, which would be too time consuming for the StoMat process.

Chatterjee *et al.* also showed that the secondary ion yields of benzene deposited on silver increased up from a sub-monolayer coverage to monolayer coverage, however decreased with further increasing coverage.[59] At low coverage, the subsurface is more Ag like and as the coverage increases it changes more to carbon-like environment. At very high exposures of benzene, the collision cascade develops rather in the benzene layers than the silver crystal. The decrease in intensities over monolayer coverage is due to the difference in ejection yields from silver and carbon substrate: ejection yield from a carbon substrate is much less than the one from a heavier metal.

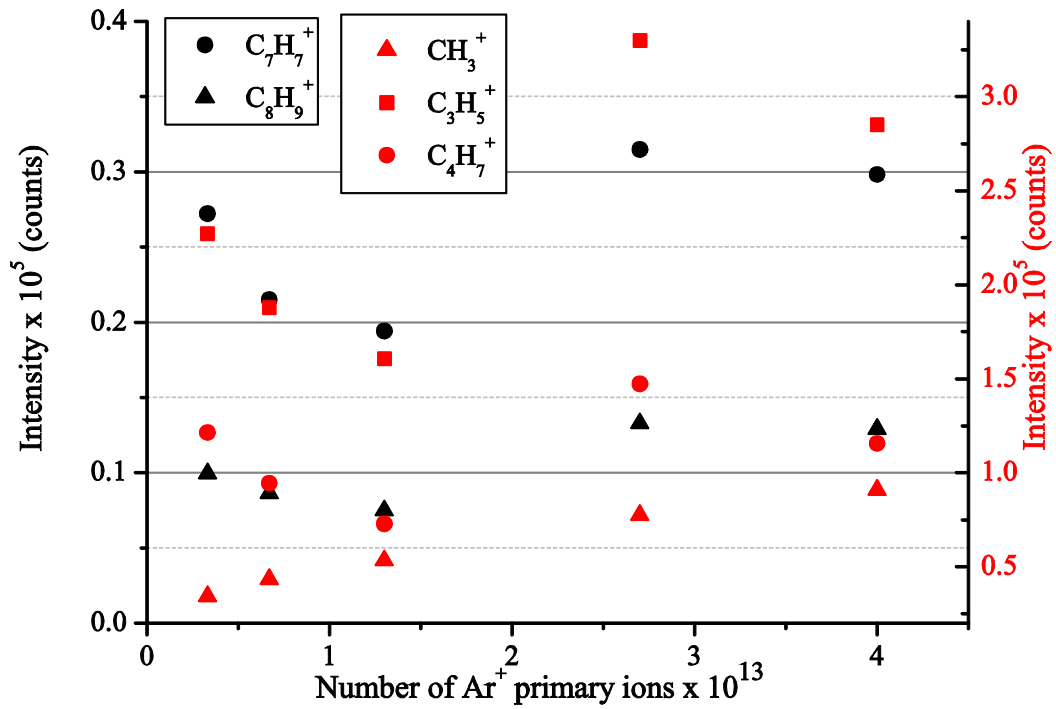


Fig. V-23: Variation of intensities of  $\text{CH}_3^+$ ,  $\text{C}_3\text{H}_5^+$ ,  $\text{C}_4\text{H}_7^+$ ,  $\text{C}_7\text{H}_7^+$  and  $\text{C}_8\text{H}_9^+$  of the PMMA deposit prepared by sputtering the PMMA sample with increasing number of  $\text{Ar}^+$  primary ions at a constant fluence of  $5.6 \times 10^{12}$  ions/cm<sup>2</sup> analysed with ToF-SIMS

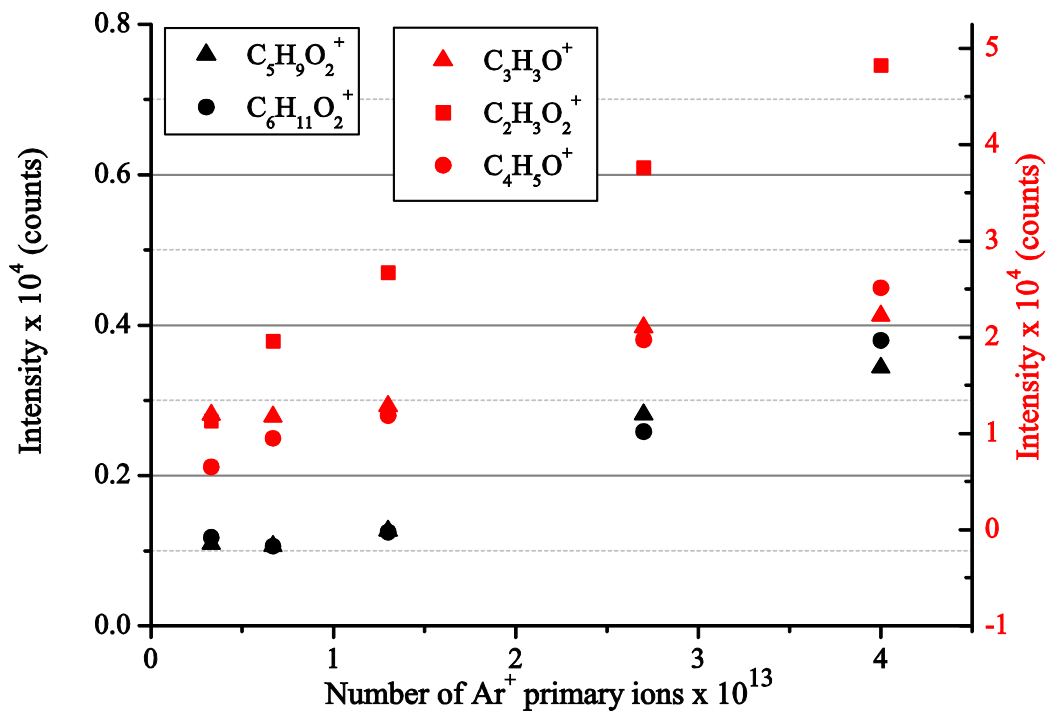


Fig. V-24: Variation of intensities of  $\text{C}_3\text{H}_3\text{O}^+$ ,  $\text{C}_2\text{H}_3\text{O}_2^+$ ,  $\text{C}_4\text{H}_5\text{O}^+$ ,  $\text{C}_5\text{H}_9\text{O}_2^+$ , and  $\text{C}_6\text{H}_{11}\text{O}_2^+$  of the PMMA deposit prepared by sputtering the PMMA sample with increasing number of  $\text{Ar}^+$  primary ions at a constant fluence of  $5.6 \times 10^{12}$  ions/cm<sup>2</sup> analysed with ToF-SIMS

### 3.2.2. Varying fluence

As for PS, in the second part of the chapter, the effect of increasing fluence on the damage of PMMA thin film, and also on the StoMat deposit were investigated.

### 3.2.3. a) ToF-SIMS analysis

For preparation of PMMA StoMat deposits for ToF-SIMS analysis, the  $\text{Ar}^+$  primary ion fluence was varied within a range of  $3.3 \times 10^{13}$ -  $2.0 \times 10^{15}$  ions/cm<sup>2</sup> (corresponding to a total number of  $\text{Ar}^+$  primary ions in the range  $3 \times 10^{12}$ -  $4.5 \times 10^{13}$ ). Since the number of  $\text{Ar}^+$  primary ions is comparable to those in the static regime experiments, the deposits are assumed to be of sub-monolayer thickness.

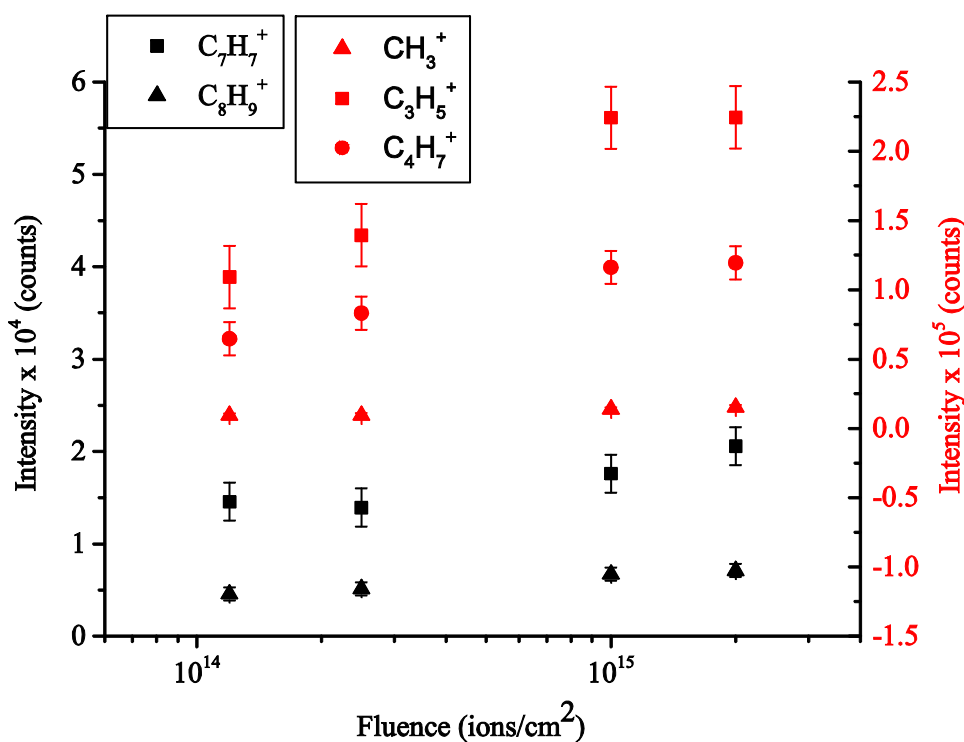


Fig. V-25: Variation of intensities of  $\text{CH}_3^+$ ,  $\text{C}_3\text{H}_5^+$ ,  $\text{C}_4\text{H}_7^+$ ,  $\text{C}_7\text{H}_7^+$  and  $\text{C}_8\text{H}_9^+$  of the PMMA deposit prepared by sputtering the PMMA sample with increasing  $\text{Ar}^+$  primary ion fluence analysed with ToF-SIMS

Fig. V-25 and Fig. V-26 show a change in absolute intensities of  $\text{C}_x\text{H}_y^+$  and  $\text{C}_x\text{H}_y\text{Oz}^+$  type fragments on the collector during ToF-SIMS analysis. In both cases, an increase in intensities with increasing fluence is observed, which is more significant for the PMMA characteristic fragments. As already discussed in Chapter I, it is known that the intensity of characteristic PMMA fragments decrease with increasing ion fluence. In the previous chapter, for the case of PS, the intensity increase for the characteristic fragments was explained by possible

recombination reactions on the collector surface. For PMMA, the scenario might be different since it is a non-cross-linking polymer and different from PS contains oxygen. For  $C_xH_y^+$  fragments, the increase in intensity is more pronounced for the PMMA characteristic fragments except of  $CH_3^+$  (Fig. V-25). The increase of intensity for the non-specific fragments is not continuous, furthermore a small decrease is observed for lower fluences. Although  $CH_3^+$  fragment showed similar behaviour to  $C_xH_yO_z^+$  type fragments with increasing coverage, here with increasing fluence, it shows a different behaviour. Its intensity decreases with fluence, whereas the intensities of oxygenated fragments increases, but at different rates (Fig. V-26). This might be an indication that small fragments are formed in a larger amount than with constant fluence and the probability of recombining on the collector surface is increased. For the oxygenated fragments, the variation in intensity increases with increasing fragment size. Their variation is also larger compared to specific hydrocarbon fragments ( $C_3H_5^+$  and  $C_4H_7^+$ ). This might result from the preferential sputtering of oxygen in the early stages of increasing fluence. As the fluence increases, less of PMMA specific fragments are sputtered from the PMMA sample. However, it is possible that, since some specific fragments already adsorb on the collector at low fluences, they might combine with non-specific fragments sputtered at higher fluences and lead to an increase in their intensity. This might be also supported by the increase in the intensity of  $CH_3^+$  fragment with increasing fluence. For the  $C_xH_y^+$  type fragments, the conclusions of ToF-SIMS analysis are not as obvious since it is known that a carbon rich layer is formed on the PMMA sample after a certain fluence which might directly affect the sputtering of these fragments after this certain fluence, and hence their adsorption on the collector. Correlated with the ToF-SIMS analysis of the craters formed in bulk PMMA sample,  $C_xH_yO_z^+$  type fragments help to explain the dynamics between the sputtering from the polymer surface and adsorption of the sputtered fragments on the collector. The Intensity of these fragments seemed to decrease in the craters with increasing fluence in the initial stages of sputtering due to the preferential sputtering of oxygen. Most of these sputtered oxygenated fragments adsorb and stay on the collector surface shown by the increase in their intensities with increasing fluence in Fig. V-26. The difference between the analysis of collectors and craters formed on PMMA sample is that the former were transferred to ToF-SIMS under UHV and the latter not, which might seriously affect the results with analysis of oxygenated fragments.

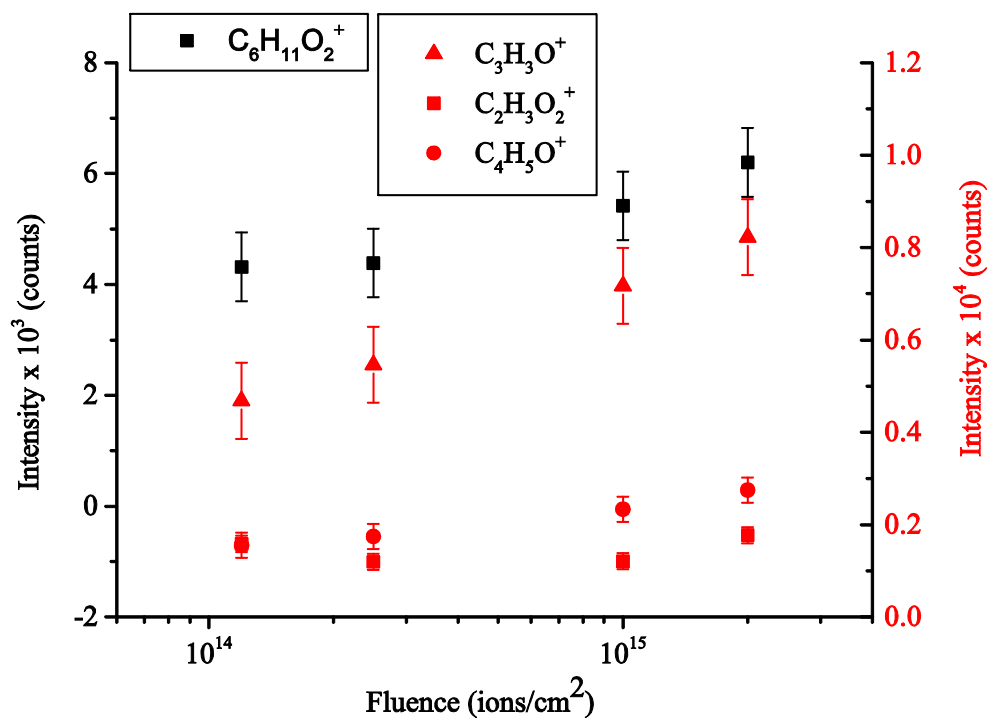


Fig. V-26: Variation of intensities of  $C_3H_3O^+$ ,  $C_2H_3O_2^+$ ,  $C_4H_5O^+$ ,  $C_5H_9O_2^+$ , and  $C_6H_{11}O_2^+$  of the PMMA deposit prepared by sputtering the PMMA sample with increasing  $Ar^+$  primary ion fluence analysed with ToF-SIMS

Although providing useful information about the variation of molecules with increasing fluence on the collector, ToF-SIMS analysis cannot say much about the nature of these fragments and their chemical environments. Thus, in the following section, XPS analysis is used in order to further elucidate the sputter deposition of PMMA.

### 3.2.3. b) XPS analysis

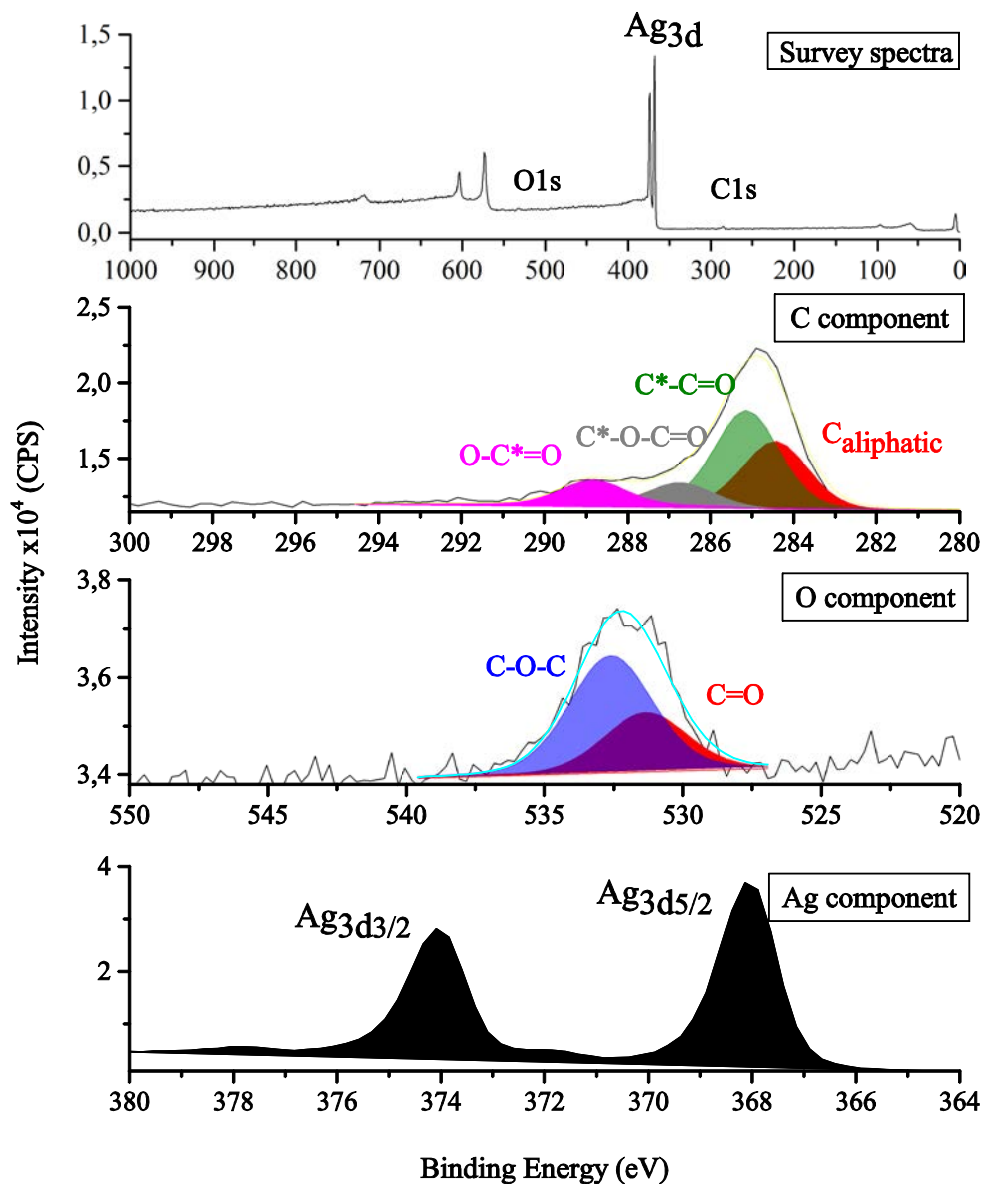


Fig. V-27: Survey, C1s, O1s, and Ag3d XPS Spectra of PMMA StoMat deposit on silver prepared by sputtering the PMMA sample at primary ion fluence of  $2.5 \times 10^{14}$  ions/cm<sup>2</sup>

Fig. V-27 shows the survey spectra, and carbon, oxygen and silver components for the XPS analysis of PMMA sputter deposit prepared using an Ar<sup>+</sup> ion fluence of  $2.5 \times 10^{14}$  ions/cm<sup>2</sup>. We have obtained these spectra for fluences between  $8.3 \times 10^{12}$  -  $1.0 \times 10^{15}$  and following we discuss their evolution with fluence.



Fig. V-28 shows change in atomic percentage of these components with increasing fluence. Although there is not a clear trend, the carbon content seems to increase slightly, while the oxygen content seems to decrease. Next, these spectral components are deconvoluted in order to have more structural information about the environments of carbon and oxygen.

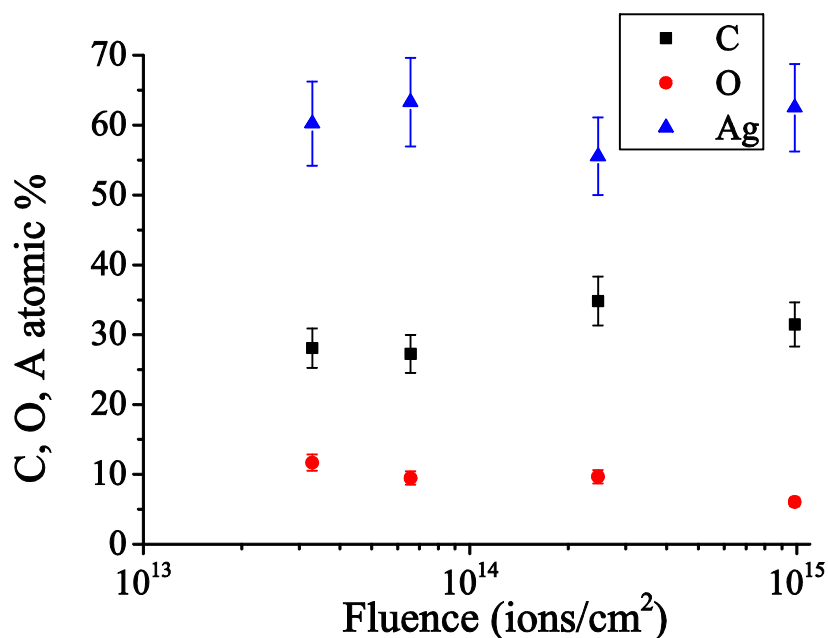


Fig. V-28: Variation of atomic percentages of carbon, silver and oxygen contents of PMMA deposit as a function of PI fluence for a total number of Ar<sup>+</sup> primary ions in the range  $2.6 \times 10^{12}$  -  $2.2 \times 10^{13}$

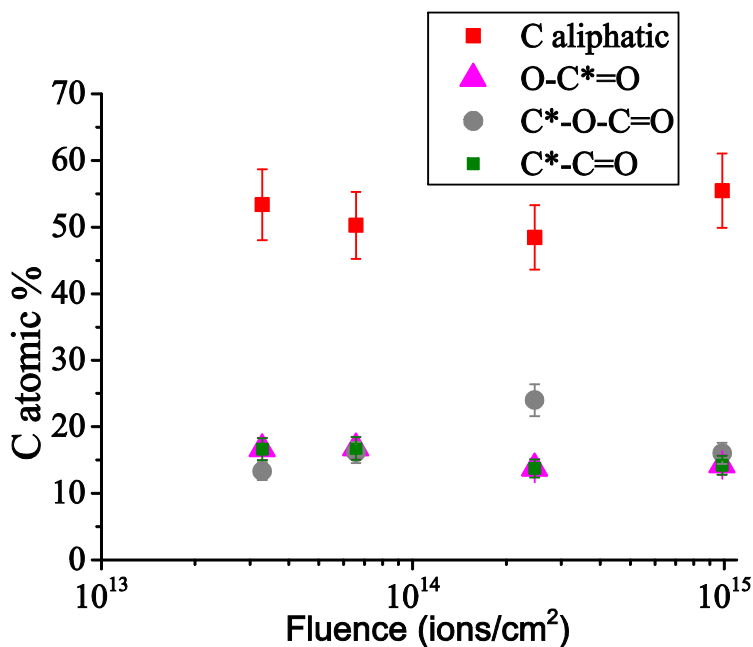


Fig. V-29: Variation of atomic percentages of carbon components in the C1s spectra of PMMA deposit as a function of PI fluence for a total number of Ar<sup>+</sup> primary ions in the range  $2.6 \times 10^{12}$  -  $2.2 \times 10^{13}$

Atomic percentages of components in the C1s spectra change with fluence as shown in Fig. V-29. For fitting of the spectra, components observed in the spectra of XPS analysis of bulk PMMA polymer were used. Opposite to the analysis of bulk polymer, the aliphatic compound tends to decrease until a certain fluence, while the other components with oxygen either increase or do not change significantly. However, the percentage of oxygen components is lower and that of aliphatic component is higher for all the fluences compared to bulk PMMA. This is expected since with increasing fluence, less oxygen containing fragments are supposed to get sputtered from the PMMA sample and thus more of  $C_xH_y^+$  type fragments should arrive on the collector.

The variation of the oxygen component is given in Fig. V-30. The trend is that C-O-C component decreases while C=O component increases. This is the opposite trend of what is observed for the bulk PMMA. As the fluence increases, for the bulk polymer, more C=O bonds are broken, some being converted into C-O bonds, resulting in increase of C-O-C component. An increase in the C=O and a decrease in the C-O-C component for the PMMA desposits support the possibility of more fragments combining on the collector surface, and also forming C=O bonds.

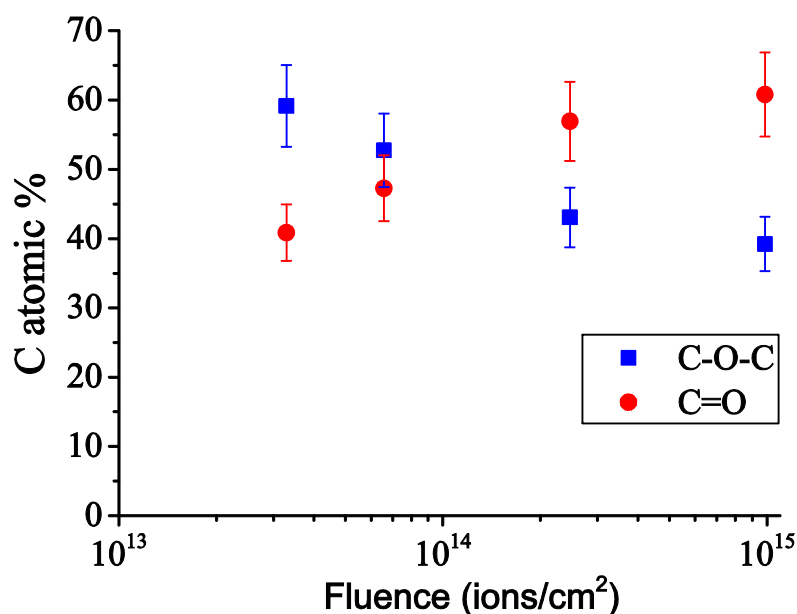


Fig. V-30: Variation of atomic percentages of oxygen components in the O1s spectra of PMMA deposit as a function of PI fluence for a total number of  $Ar^+$  primary ions in the range  $2.6 \times 10^{12}$ -  $2.2 \times 10^{13}$

## 4. Adsorption of PMMA fragments on silver using DFT calculations

Table V-2: Calculated adsorption energies (eV) of PMMA fragments on Ag(100)

E <sub>ads</sub> (eV)			d <sub>ads</sub> (Å)		
C <sub>2</sub> H <sub>3</sub> O <sub>2</sub>	C <sub>4</sub> H <sub>5</sub> O	C <sub>6</sub> H <sub>11</sub> O <sub>2</sub>	C <sub>2</sub> H <sub>3</sub> O <sub>2</sub>	C <sub>4</sub> H <sub>5</sub> O	C <sub>6</sub> H <sub>11</sub> O <sub>2</sub>
-1.99	-0.75	-0.88	2.19	2.30	2.24

Table V-2 shows calculated adsorption energies for C<sub>2</sub>H<sub>3</sub>O<sub>2</sub>, C<sub>4</sub>H<sub>5</sub>O and C<sub>6</sub>H<sub>11</sub>O<sub>2</sub> fragments on Ag(100) using DFT calculations. The adsorption energy is highest for the C<sub>2</sub>H<sub>3</sub>O<sub>2</sub> fragment: -1.99 eV. The adsorption energy decreases by more than a factor two for the larger fragments (C<sub>4</sub>H<sub>5</sub>O and C<sub>6</sub>H<sub>11</sub>O<sub>2</sub>). For all the fragments, bonds form between the silver surface and a carbon atom. (Fig. V-31). For the C<sub>2</sub>H<sub>3</sub>O<sub>2</sub> fragment, the bond between the carbon atom which is in interaction with the silver atom and the oxygen of the fragment seem to break, which explains higher calculated adsorption energy. As the fragments become larger, the adsorption energy decreases, which suggest the van der Waals interactions become more significant. In general, the trend is the same than for PS fragments and supports the recombination of fragments on the collector surface.

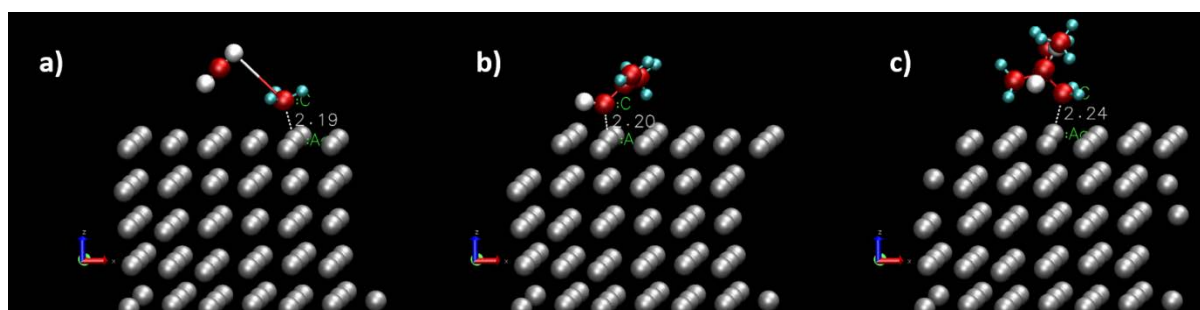


Fig. V-31: Adsorption configurations of PMMA fragments on the Ag(100) surface: a) C<sub>2</sub>H<sub>3</sub>O<sub>2</sub>, b) C<sub>4</sub>H<sub>5</sub>O c) C<sub>6</sub>H<sub>11</sub>O<sub>2</sub>. Red represents carbon, cyan hydrogen, and grey represents silver atoms.

## 5. Conclusion

For the sputtering and analysis of bulk PMMA samples, ToF-SIMS results show that after a certain fluence, the polymer does not keep the memory of its original structure.

For the analysis of PMMA Storing Matter deposits, both the effect of varying coverage and primary ion fluence have been studied. The results show that the absolute intensities of molecular fragments that are specific to PMMA increase with primary ion fluence. For the

increasing coverage, the intensity increase is visible only for the oxygenated fragments. This is in agreement with XPS results, which suggest that the oxygen content decreases to less than 10 % as the fluence increases. However, when the fluence is not changing, which is the case of increasing coverage, fragments with oxygen continue to sputter from the PMMA surface and adsorb on the collector. The increase of fragment intensities with increasing fluence, especially  $C_3H_3O$  cannot be explained similarly. As the fluence increases, less oxygenated fragments should sputter from the sample. So, the increase can be explained with recombination reactions occurring on the collector.

DFT calculation results show that the highest adsorption energies are obtained for  $C_2H_3O_2$ , which is in line with the results of ToF-SIMS and XPS analysis, showing a higher rate of increase of this fragment compared to  $C_4H_5O$  and  $C_6H_{11}O_2$  fragments, which is more significant for the case of increasing coverage.

Although DFT calculations suggest that  $C_2H_3O_2$  fragment should adsorb easier on the surface, the bond breaking observed increases the possibility that fragments could recombine on the collector surface, to form larger fragments including the oxygenated fragments like  $C_2H_3O_2$ ,  $C_4H_5O$  and  $C_6H_{11}O_2$ .

# Chapter VI:

## Adsorption of Polystyrene and Poly(methyl methacrylate) fragments by DFT Calculations

### 1. Introduction

In this chapter, results of DFT calculations on the adsorption of PS and PMMA fragments are presented. This helps to understand their adsorption characteristics on different substrates during the collection step of the Storing Matter process. We have chosen DFT calculations to study the effect of different substrates on sticking of molecules and molecular fragments since experimentally information like adsorption energy and geometry for different fragments could not be obtained at all. It should be noted that adsorption of these fragments by DFT is not directly comparable with the real-world deposition process, since only static calculations are carried out and only non-charged radicals are studied. The latter is justified by most of the sputtered fragments being neutral. Although MD simulations would provide valuable insight into the dynamics of adsorption and diffusion of molecules, we are more concerned with their static adsorption properties, giving information about the nature of interactions between molecules or molecular fragments and different metallic substrates, and the electronic structure and bonding at surface. DFT calculations provide us with important ground state properties like equilibrium geometry, electronic structure, total energy, various total energy differences such as surface energies and adsorption energies[135]. At the same time, adsorption energies give valuable information on sticking probabilities and possible diffusion mechanisms.

The main disadvantage of DFT calculations is that they are computationally demanding, limiting the size of the system and the time scale of the simulations. For this reason, we have limited the size of the molecules and of the substrate. The fragments that are specific to PS ( $C_3H_3^+$ ,  $C_3H_5^+$ ,  $C_6H_5^+$ ,  $C_7H_7^+$ ,  $C_8H_9^+$  and  $C_9H_7^+$ ) and PMMA ( $C_2H_3O_2^+$ ,  $C_4H_5O^+$ ,  $C_6H_{11}O_2^+$ ) were chosen from the ToF-SIMS spectra. Their molecular structure is given in Chapter II. In

order to obtain fragments, one hydrogen atom that is bonded to the radical carbon atom was removed in case of PS. For PMMA the carbon or oxygen atom was the radical atom. Four different substrates were used for simulations: Ag(100), Ag(111), Al<sub>2</sub>O<sub>3</sub> (0001), Pt(111) and Si(111). Although oxide surfaces are primarily of interest and they produce more realistic results for comparing to experiments, for Ag and Si, we have chosen to study simpler surfaces except of  $\alpha$ -alumina since it is a theoretically well-studied material. More details on the substrates studied are given in Chapter II.

DFT calculations are not able to easily handle dispersion interactions, i.e. van der Waals (vdW) forces. However, accounting the fact that in this work only the adsorption of molecular fragments is studied, which results in much higher adsorption energies compared to molecule adsorption, we assume that the effect of vdW forces can be neglected.

The PS and PMMA fragments were adsorbed on abovementioned substrates using the Vienna ab initio simulation package (VASP) [177],[178],[179],[180] with the Perdew-Wang generalised gradient approximation (GGA-PW91) [181],[182] and the projector augmented wave (PAW) method for the silver,  $\alpha$ -alumina, platinum, silicon, carbon, hydrogen and oxygen pseudopotentials.[183],[184]

In this chapter, first, the adsorption energies and geometries on various substrates are presented. Also, the effect of initial molecular orientation and different adsorption sites on the adsorption characteristics are discussed. Finally, the effect of different substrates on the adsorption behaviour of molecular fragments is compared in terms of electronic structure and density of states.

## **2. Adsorption of PS fragments on Ag (111) and Ag(100)**

The fragments were positioned on three different binding sites on the surface and simultaneous relaxation of the molecule and two top layers of the substrate were continued until the self-consistent forces were lower than 0.01 eV/Å.

### **2.1. Adsorption sites**

Different sizes of characteristic PS fragments, which have been observed in the ToF-SIMS spectra, were adsorbed on 3 different adsorption sites on Ag(100) and Ag(111) surfaces (Fig. VI-1). For each of the C<sub>3</sub>H<sub>3</sub>, C<sub>3</sub>H<sub>5</sub>, C<sub>6</sub>H<sub>5</sub>, C<sub>7</sub>H<sub>7</sub>, C<sub>8</sub>H<sub>9</sub> and C<sub>9</sub>H<sub>7</sub> fragments, the radical carbon

atom was positioned at atop (on top of an Ag atom), bridge (on top of two Ag atoms) and threefold and fourfold-hollow (in between three Ag atoms for Ag(111) and between four Ag(100)) sites. It should be noted that in literature these adsorption sites usually refer to the position of the whole molecule with respect to the surface defined by many authors.[204],[134] Since we deal with the adsorption of fragments where one hydrogen is missing, the position of the radical atom with respect to the surface is taken into account. Given enough flexibility, the radical atom is mostly the atom involved in bonding with the surface. Moreover, we studied fragments of different character, i.e. small linear, aromatic, polycyclic, symmetric and non-symmetric ones.

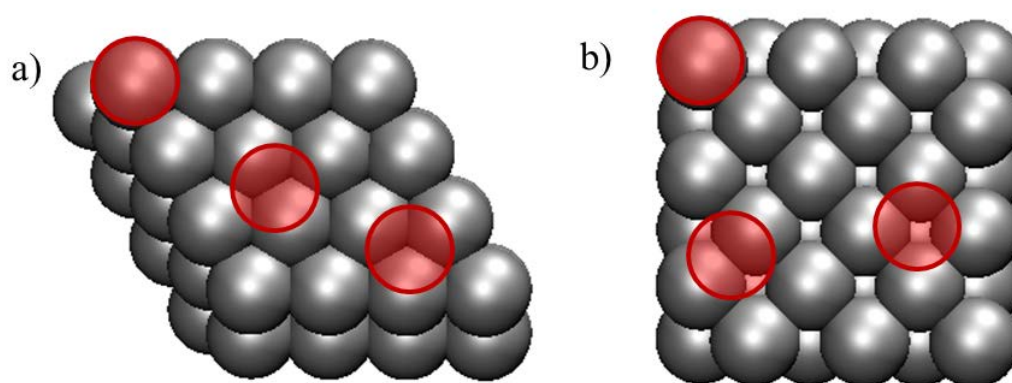


Fig. VI-1: Adsorption sites on a) Ag (111) and b) Ag (100) surfaces where the radical carbon atoms were placed on top of the substrates

## 2.2. Adsorption Geometries

Fig. VI-2 shows the adsorption structures of PS fragments on Ag (111) surfaces. To start with, PS fragments are placed almost flat with respect to the surface. After convergence of energies, it can be seen that the adsorption structure of the fragments depends on the structure, size and flexibility of the adsorbate. Since  $C_3H_3$  and  $C_3H_5$  are linear fragments and differ from the rest of the fragments which are cyclic, they undergo the highest angular tilt upon adsorption. For the other fragments, which have cyclic character, the adsorption configuration depends on the position of the radical atom with respect to the whole fragment. Two different possible structures for  $C_7H_7$  have been adsorbed[197]: benzylium and tropylium. Benzylium has some flexibility around the radical atom whereas tropylium not and assumes a flat-lying geometry. Benzylium adsorbs with an angle between the Ag surface and the phenyl ring. A similar adsorption structure was observed for  $C_8H_9$ , with a higher tilt angle between the phenyl ring and the surface.

Flat adsorption of tropylium on the Ag surface gives all atoms and delocalized electrons the possibility to interact with the surface, but the structure in general seems to be less favourable possibly due to not being aromatic which makes the fragment less stable. C<sub>9</sub>H<sub>7</sub> fragment adsorbs parallel to the surface, like tropylium, giving all C atoms the possibility to interact with Ag atoms.

Recently there have been studies for adsorption of benzene molecule on coinage metals like copper (Cu), gold (Au) and also silver (Ag). Since it is the simplest aromatic molecule, it has been the subject of many DFT studies, thus there exists many literature studies on its adsorption. Although our work concerns adsorption of fragments, we will refer to the case of benzene for comparison, which is the simplest and closest molecule to PS fragments. Lorente *et al.* studied the adsorption of benzene (C<sub>6</sub>H<sub>6</sub>), phenyl (C<sub>6</sub>H<sub>5</sub>) and benzyne (C<sub>6</sub>H<sub>4</sub>) on Cu (100), which is a coinage metal with an electronic configuration to similar to silver.[205] They found that benzene chemisorbs flat on the hollow site on the Cu surface with a distance of 2.23 Å between the adsorbate carbon atom and the uppermost Cu atoms. The phenyl radical was found to chemisorb with an angle with the unpaired C bonding onto the top site and the benzyne almost stood up on the hollow site. Similar to the adsorption of phenyl radical in Lorente's work, our results show that the C<sub>6</sub>H<sub>5</sub> fragment adsorb with a tilt angle on Ag, and which was the highest of all adsorbed PS fragments. In a recent study by Chwee *et al.* on the adsorption of benzene on coinage metals (Cu, Au and Ag), the adsorbate was found to lie almost flat at a distance  $d_{\text{ben-metal}}$  above the metal surface, which agrees with results of Lorente *et al* for the adsorption of benzene.[206]



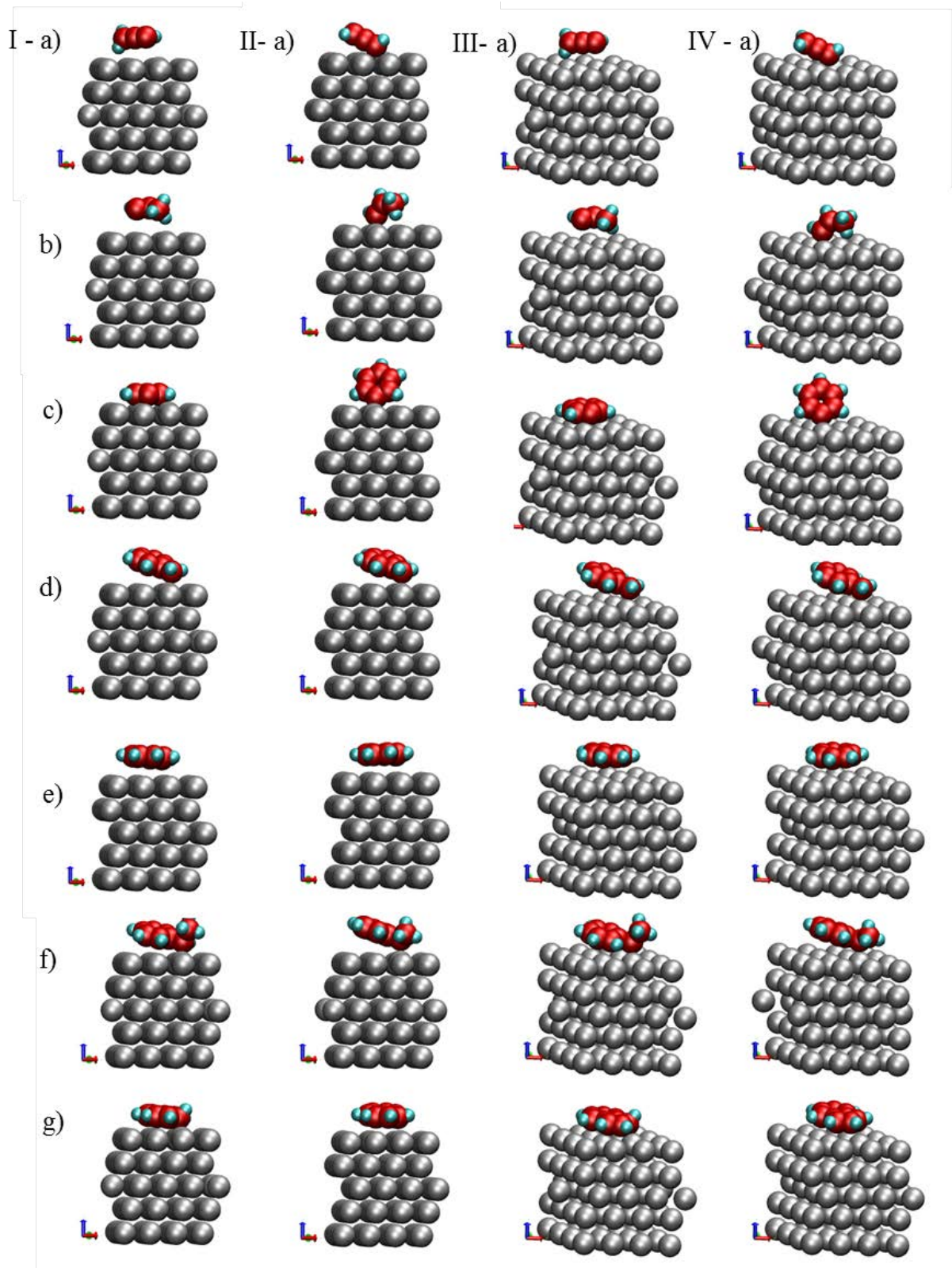


Fig. VI-2: Adsorption geometry for several PS fragments on Ag(111) surface: a)  $C_3H_3$ , b)  $C_3H_5$ , c)  $C_6H_5$ , d)  $C_7H_7$  (benzylum), e)  $C_7H_7$  (tropylium) f)  $C_8H_9$  g)  $C_9H_7$ . I and III shows initial configurations and II and IV final configurations after adsorption.

### 2.3. Adsorption Energies:

The adsorption energy of the fragments on both Ag(111) and Ag(100) surfaces were calculated. The adsorption energy was defined as:  $E_{ad}=E_{tot}-(E_{surf}+E_{mol})$ [185]

where  $E_{tot}$ ,  $E_{surf}$ , and  $E_{mol}$  are the total energy of the relaxed adsorption complex, the energy of the clean surface and the energy of the isolated molecule.

Adsorption energies have been calculated for each case and they have been compared with respect to the Ag surface orientation, different binding sites and different size and structure of adsorbed fragments. Table VI-1 and Table VI-2 show calculated adsorption energies for all abovementioned conditions.

Table VI-1: Calculated adsorption energies (eV) of PS fragments on Ag(111)

	<b>C<sub>3</sub>H<sub>3</sub></b>	<b>C<sub>3</sub>H<sub>5</sub></b>	<b>C<sub>6</sub>H<sub>5</sub></b>	<b>C<sub>7</sub>H<sub>7</sub></b> <b>(benzylum)</b>	<b>C<sub>7</sub>H<sub>7</sub></b> <b>(tropylium)</b>	<b>C<sub>8</sub>H<sub>9</sub></b>	<b>C<sub>9</sub>H<sub>7</sub></b>
atop	-1.46	-1.73	-1.61	-0.60	-0.29	-0.50	-0.61
bridge	-1.31	-1.85	-1.61	-0.53	-0.23	-0.30	-0.48
fourfold-hollow	-1.49	-1.85	-1.61	-0.46	-0.20	-0.47	-0.47

Table VI-2: Calculated adsorption energies (eV) of PS fragments on Ag(100)

	<b>C<sub>3</sub>H<sub>3</sub></b>	<b>C<sub>3</sub>H<sub>5</sub></b>	<b>C<sub>6</sub>H<sub>5</sub></b>	<b>C<sub>7</sub>H<sub>7</sub></b> <b>(benzylum)</b>	<b>C<sub>7</sub>H<sub>7</sub></b> <b>(tropylium)</b>	<b>C<sub>8</sub>H<sub>9</sub></b>	<b>C<sub>9</sub>H<sub>7</sub></b>
atop	-1.72	-2.02	-1.70	-0.74	-0.35	-0.68	-0.98
bridge	-1.72	-2.02	-1.74	-0.71	-0.55	-0.58	-0.80
threefold-hollow	-1.72	-1.99	-1.66	-0.67	-0.36	-0.50	-0.88

In Table VI-1 and Table VI-2, it can be observed that the preferred adsorption site depends on the size and structure of the molecule, with atop and bridge sites being most favourable for most of cyclic fragments. Since substrate-adsorbate bonding mainly occurs through the  $\sigma$  or  $\pi$  orbitals of the dehydrogenated carbon atom, the bonding between the fragment and the substrate are chemisorption. The largest adsorption energies (-1.72 eV for C<sub>3</sub>H<sub>3</sub> and -2.02 eV for C<sub>3</sub>H<sub>5</sub>) were found for smaller fragments which do not have any cyclic character. The difference between the two configurations is due to the number of C atoms involved in bonding: for C<sub>3</sub>H<sub>3</sub> there are two C atoms and for C<sub>3</sub>H<sub>5</sub> there is only one C atom with a free

electron. Moreover, for these smaller fragments there are no significant energy variations for different adsorption sites. For the other fragments with cyclic character ( $C_7H_7$ ,  $C_8H_9$  and  $C_9H_7$ ), except  $C_6H_5$ , adsorption energies are considerably smaller.  $C_6H_5$  is adsorbed vertically on Ag (Fig. VI-2) with a maximum adsorption energy of -1.74 eV on the bridge site, which is less than 0.1 eV difference for the two other bonding sites. Tropylium was found to have the smallest adsorption energy of all fragments. The non-aromatic character of this fragment renders it less stable decreasing the adsorption energy, although it is expected that its flat adsorption should give all the delocalized electrons the possibility to interact with the surface. The adsorption energy for benzylium is almost twice as high. Since it adsorbs with an angle between the Ag surface and the phenyl ring, the radical carbon atom with a free electron has more chances of getting closer to the surface. A similar adsorption structure was observed for  $C_8H_9$ , with a higher adsorption angle, but a smaller adsorption energy compared to benzylium. Out of all cyclic fragments, (except  $C_6H_5$ ),  $C_9H_7$  has the highest adsorption energy (-0.98 eV when atop of Ag), possibly due to its polycyclic structure. It adsorbs parallel to the surface, like tropylium, giving all C atoms the possibility to interact with Ag atoms. However, the adsorption energy is increased instead of decreased since it is more stable with two aromatic rings.

Since there exists no study for adsorption of PS fragments by DFT in literature, it is not possible to compare our results with literature for all the fragments we study. For adsorptions on silver, we make comparison to the other coinage metals. Olsson *et al.* studied adsorption of acetylene series ( $C_2H_2$ ,  $C_2H$  and  $C_2$ ) on Cu(001) and found their adsorption energies shows a strong variation for this sequence: 1.31 eV, 4.22 eV and 6.57 eV for  $C_2H_2$ ,  $C_2H$  and  $C_2$  respectively.[207] This is not surprising since an increasing number of free electrons with a decreasing number of hydrogen atoms bonded to the carbon atom, dramatically increases the adsorption energy. The same is expected for in our case for the adsorption of  $C_3H_3$  and  $C_3H_5$  on Ag(111) and Ag(100). However, we see an increase in adsorption energy with increasing number of hydrogen atoms. This is possibly due to the two double bonds  $C_3H_3$  has: it makes the molecule less flexible around the radical carbon atom. The free carbon atom of  $C_3H_5$  can interact more strongly with the surface.

In their studies for adsorption of benzene ( $C_6H_6$ ), phenyl ( $C_6H_5$ ) and benzyne ( $C_6H_4$ ) on Cu (100), Lorente *et al.* calculated adsorption energies of 0.68 eV, 2.59 eV and 3.52 eV for  $C_6H_6$ ,  $C_6H_5$  and  $C_6H_4$  respectively.[205] Like in the study of Olsson *et al.*, it can be seen that

the adsorption energy increases with decreasing number of hydrogen atoms bonded to carbon atoms. However adsorption energy of 2.59 eV of C<sub>6</sub>H<sub>5</sub> is larger than what we calculate (1.74 eV) for the adsorption on bridge site on Ag (100). However, it should be taken into account that calculated adsorption energies on copper and silver vary considerably although they have similar electronic configuration. In a very recent study, Reckien *et al.* calculated adsorption energies for adsorption of benzene on three coinage metals: Ag, Au and Cu.[208] The binding between benzene and copper was the largest with  $E_{\text{ads}} = 1.22$  eV. For benzene-gold it was 0.91 eV and then the lowest value was calculated for silver with  $E_{\text{ads}} = 0.79$  eV. This is in line with the adsorption energy for C<sub>6</sub>H<sub>5</sub> on copper by Lorente *et al.* being larger than the adsorption energy in case of silver for our calculations.

Moreover, Reckien *et al.* found that the adsorption energies calculated on a given metal were almost independent of the surface type with a variation of 0.03 eV within different surface orientations. However, our calculations reveal that the adsorption energies vary considerably with surface orientation. On average they are about 20% higher on Ag(100) than on Ag(111) which indicates that the interactions between the adsorbents and Ag(100) are much stronger than on Ag(111). This difference is probably due to using a fragment with a radical atom rather than a molecule, which was benzene for the study of Reckien *et al.* This probably also has to do with the symmetry of the fragment or molecule. Using a different orientation of silver might not have a big effect on the adsorption energy of symmetric benzene molecule, while the non-symmetric C<sub>6</sub>H<sub>5</sub> fragment might have better chances of interacting with more silver atoms with changing orientation of the substrate atoms.

It can be seen in literature that there is a large variation in calculated adsorption energies for a given molecule on similar surfaces. Chen *et al.* calculated much higher adsorption energy than Lorente *et al.* for the adsorption of benzene on Cu (100).[209] They reported adsorption energies within the range 1.95 – 2.28 eV with an adsorption distance of 2.00 – 2.06 Å. This adsorption energy is considerably higher than 0.68 eV (for adsorption distance of 2.23 Å) reported by Lorente *et al.* The difference might be due to the use of different functionals for DFT calculations. Chen *et al.* used LDA functional which is much less reliable than the GGA approach. Our results are comparable to the results obtained by Lorente *et al.* since we used the same functional. For the adsorption of C<sub>6</sub>H<sub>5</sub> fragment  $E_{\text{ads}} = 1.74$  eV and  $d_{\text{ads}} = 2.22$  Å are calculated.

Much lower binding of benzene on coinage metals have been reported by Bilic *et al.* [204] They reported 0.03 eV, 0.05 eV and 0.08 eV on Cu (111), Ag (111) and Au (111) surfaces respectively. They point out that long range interactions are not captured within DFT calculations and they also demonstrate that there is a lack of chemisorptive bonding by assuming that the adsorption is mainly dominated by physisorption. Within the last decades many attempts have been made in order to include vdW interactions within the DFT calculations[210],[211],[212],[138],[213],[214] however this is beyond the scope of this thesis. We are more interested in trends in adsorption energy for various PS and PMMA fragments and somehow the missing vdW interactions are compensated by the use of GGA which overestimates the covalent bonding.[134]

## 2.4. Adsorption distances

Final adsorption distances of fragments are shown in Table VI-3.

For the fragments with cyclic character, adsorption distances are inversely proportional to adsorption energies. For the non-cyclic fragments there is not such a trend: adsorption distances are directly proportional to calculated adsorption energies. For  $C_3H_3$  and  $C_3H_5$ , higher adsorption distances correspond to larger calculated adsorption energies. Within the cyclic fragments, the  $C_6H_5$  fragment has the highest adsorption energy of -1.61 eV on Ag(111) with the smallest adsorption distance of 2.21 Å between the radical carbon atom and the silver atom to which it is bonded. For benzene adsorption on Cu(100), Lorente *et al.* found an adsorption distance of 2.23 Å between the adsorbate carbon atom and the uppermost Cu atoms.[205] Our results are in agreement with their results with an adsorption distance of 2.21 Å for  $C_6H_5$  or 2.27 Å for benzylium. However, Chen *et al.* reported a distance of 2.00 – 2.06 Å for flat-lying benzene on the hollow site.[209] This smaller distance corresponds to a higher adsorption energy which might be a result of overestimation of covalent contribution to the organic-metal binding calculated by LDA functional. Reckien *et al.* found a much larger distance of 3.17 Å between benzene and the topmost layer of Ag(111)[208]. The larger adsorption distance in their case is due to the PBE functional used in combination with D3 dispersion corrections with repulsive three-center term. For a similar adsorption on Cu(111), they found a distance of 2.86 Å which indicates the differences between two metals for the adsorption of same molecule. This is in agreement with the fact that benzene has a higher adsorption energy (1.01 eV) on Cu(111) than on Ag(111) which is 0.75 eV.

Table VI-3: Calculated adsorption distances (Å) of PS fragments on Ag (111)

	<b>C<sub>3</sub>H<sub>3</sub></b>	<b>C<sub>3</sub>H<sub>5</sub></b>	<b>C<sub>6</sub>H<sub>5</sub></b>	<b>C<sub>7</sub>H<sub>7</sub></b> <b>(benzylum)</b>	<b>C<sub>7</sub>H<sub>7</sub></b> <b>(tropylium)</b>	<b>C<sub>8</sub>H<sub>9</sub></b>	<b>C<sub>9</sub>H<sub>7</sub></b>
atop	2.30	2.15	2.25	2.27	2.61	2.34	2.47
bridge	2.24	2.31	2.21	2.27	2.91	2.34	3.20
fourfold-hollow	2.31	2.31	2.24	2.37	3.16	2.77	2.95

Regarding different adsorption sites, for smaller non-cyclic fragments there is not much difference between final adsorption distances. It can be seen in Fig. VI-3 that regardless of the initial adsorption site, the radical carbon atom of the C<sub>3</sub>H<sub>3</sub> fragment shares its electrons with two silver atoms on the top layer of the silver slab. Since it is smaller compared to the cyclic fragments, it has more flexibility on the surface and can move more freely. For the atop position as an adsorption site, initially the radical carbon atom is 2.22 Å and 3.17 Å away from the first and second silver atom involved (Fig. VI-3 I-a). After adsorption, it gets away from the first silver atom by 0.08 Å and gets closer to the second one by 0.69 Å with final adsorption distances of 2.30 and 2.48 Å. For the two other adsorption sites, the final distances to two silver atoms are 2.24 and 2.51 Å and 2.31 and 2.41 Å for the bridge and threefold-hollow sites respectively. Since the radical carbon atom chemisorbs to two silver atoms, we can talk about an average adsorption distance. It is 2.39, 2.38 and 2.36 Å for the atop, bridge and hollow sites respectively, which shows a smaller spread than the smallest adsorption distances (2.30, 2.24 and 2.31 Å for the atop, bridge and hollow sites respectively).

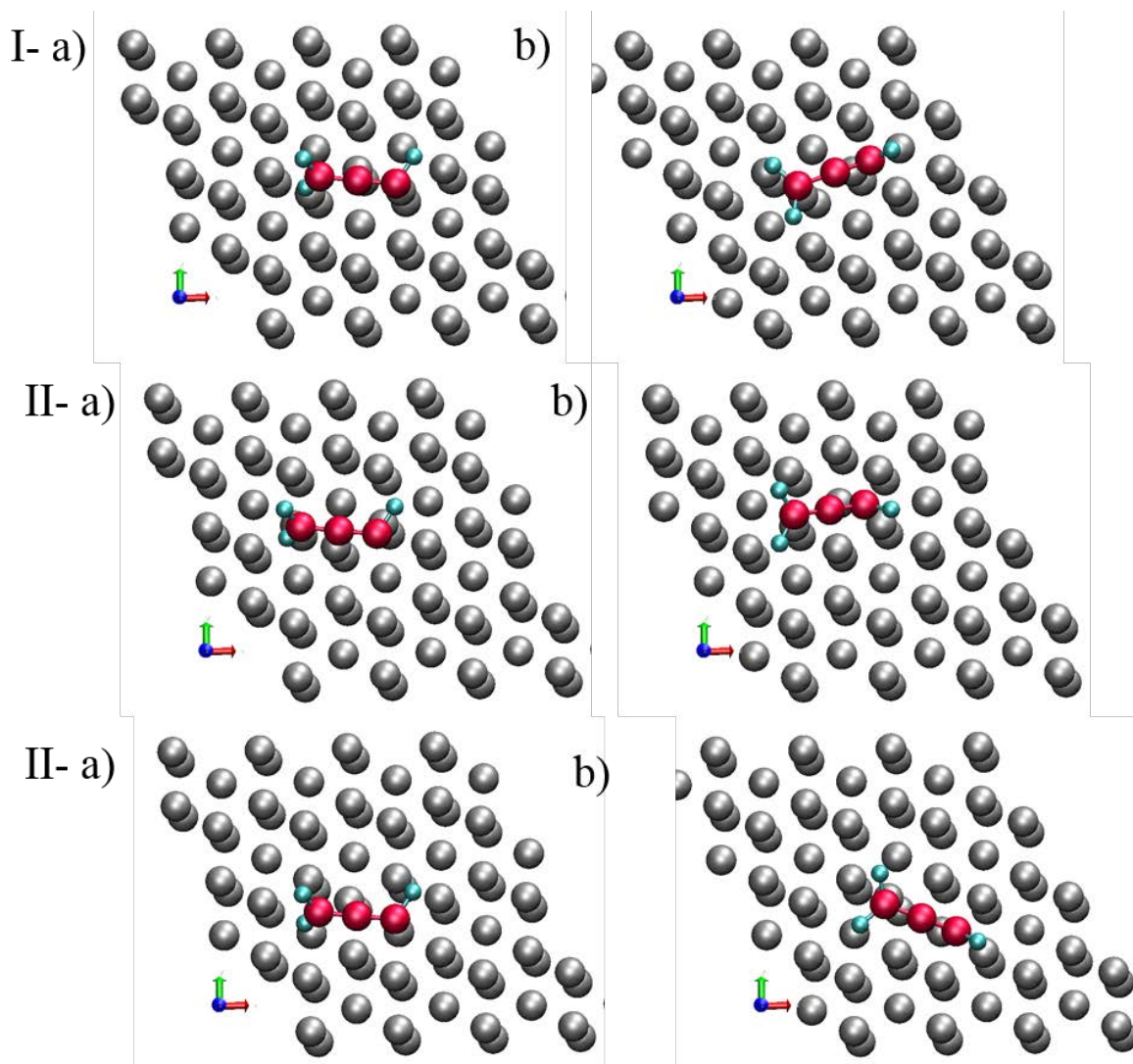


Fig. VI-3: Adsorption configurations for  $C_3H_3$  fragment on Ag(111) surface for: I) atop II) bridge III) three-fold hollow site. (a) represents some intermediate configuration and (b) the final adsorption configuration. Silver color represent Ag, red C and cyan hydrogen atoms.

As the fragments become larger (like in the case of  $C_3H_5$ ) (Fig. VI-4) or of cyclic character (like in the cases of  $C_6H_5$ ,  $C_7H_7$ ,  $C_8H_9$  and  $C_9H_7$ ) (Fig. VI-5) the molecule has less flexibility to move on the surface and there is mainly one silver atom involved in the chemisorption (except tropylium and  $C_9H_7$  fragments which adsorb flat on the surface and all the carbon atoms can interact with different silver atoms). Bonding to only one silver atom is more pronounced for  $C_6H_5$ , benzylum and  $C_8H_9$  fragments which adsorb with a tilt angle to the surface.



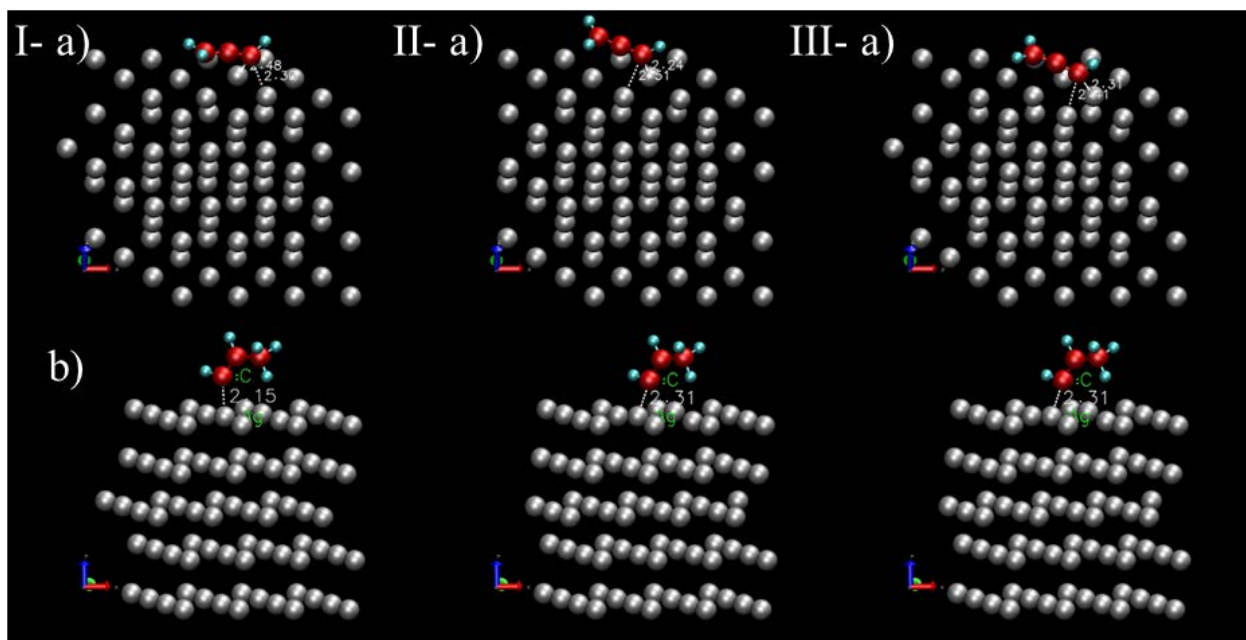


Fig. VI-4: Final adsorption configurations and distances for non-cyclic PS fragments on Ag(111) surface: a)  $C_3H_3$ , b)  $C_3H_5$ . I, II, and III corresponds to atop, bridge and threefold-hollow adsorption sites respectively. Red represents carbon, cyan hydrogen, and grey represents silver atoms.



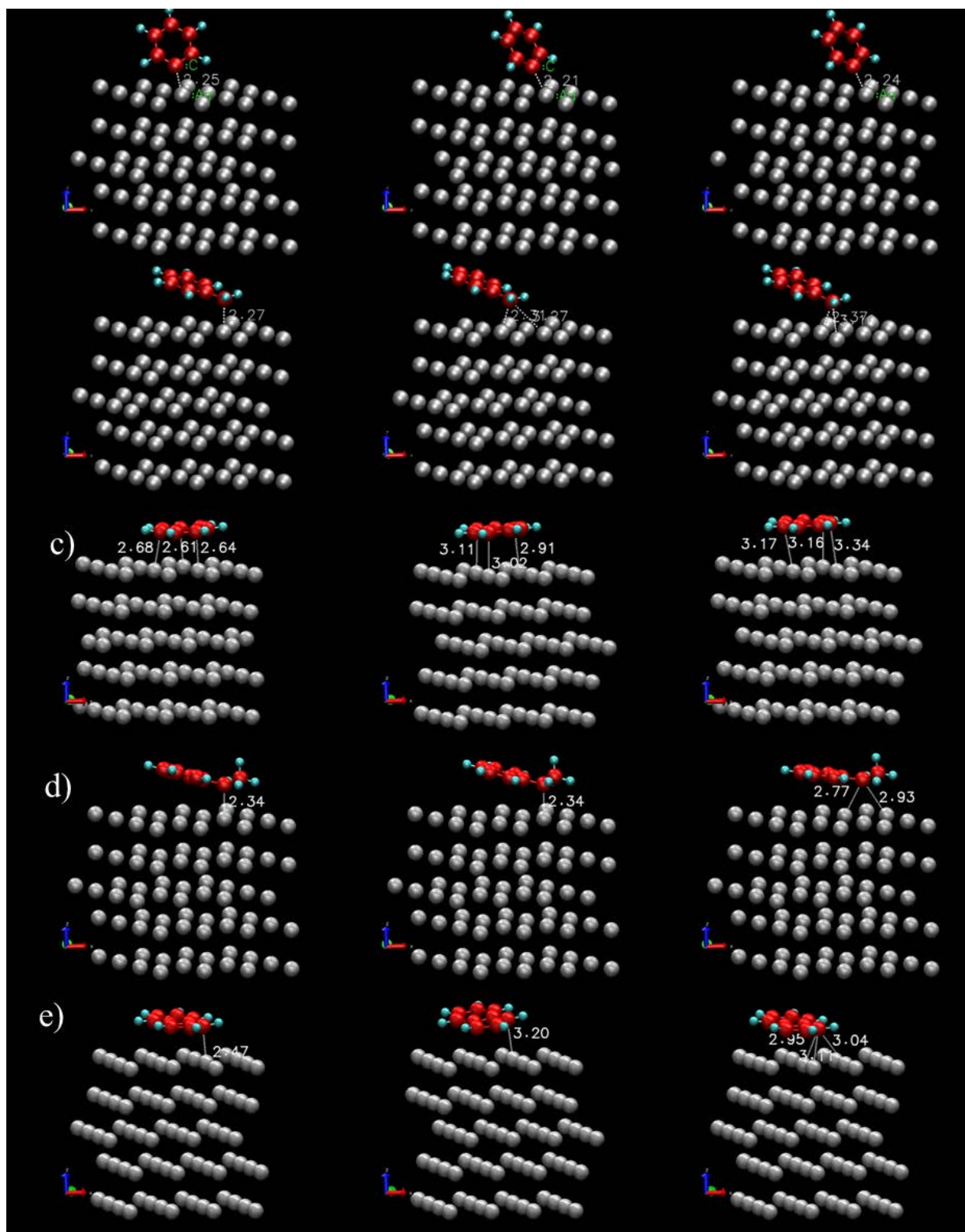


Fig. VI-5: Final adsorption configurations and distances for cyclic PS fragments on Ag(111) surface: a)  $C_6H_5$ , b)  $C_7H_7$  (benzylum), c)  $C_7H_7$  (tropylium) d)  $C_8H_9$  e)  $C_9H_7$  I, II, and III corresponds to atop, bridge and threefold-hollow adsorption sites respectively. Red represents carbon, cyan hydrogen, grey represents silver atoms.

On the Ag(100) surface, adsorption distances are smaller than on Ag(111) (Table VI-4). This is in agreement with larger adsorption energies of fragments on the Ag(100) surface. Similar

to Ag(111) surface, there is not much difference between final adsorption energies for small non-cyclic fragments; they assume similar final adsorption sites. The differences are larger for the cyclic fragments depending on their initial adsorption site, yet smaller than that on the Ag(111) surface.

Table VI-4: Calculated adsorption distances of PS fragments on Ag (100)

	$C_3H_3$	$C_3H_5$	$C_6H_5$	$C_7H_7$ (benzylum)	$C_7H_7$ (tropylium)	$C_8H_9$	$C_9H_7$
atop	2.31	2.26	2.17	2.27	2.46	2.32	2.47
bridge	2.28	2.28	2.21	2.30	2.48	2.45	2.79
fourfold-hollow	2.27	2.27	2.18	2.27	2.51	2.71	2.93

Adsorption configurations of non-cyclic and cyclic PS fragments on Ag(100) surface are given in Fig. VI-6 and Fig. VI-7. On Ag(100), it can be observed that the tilt angle of  $C_6H_5$ , benzylum and  $C_8H_9$  fragments are smaller compared to that on Ag(111). As the radical carbon atom gets closer to the surface, which is the case on Ag(100), the carbon atoms in the cyclic ring experience more attraction towards the surface than on Ag(111). This might be reducing the tilt angle of the fragment on the surface for Ag(100).

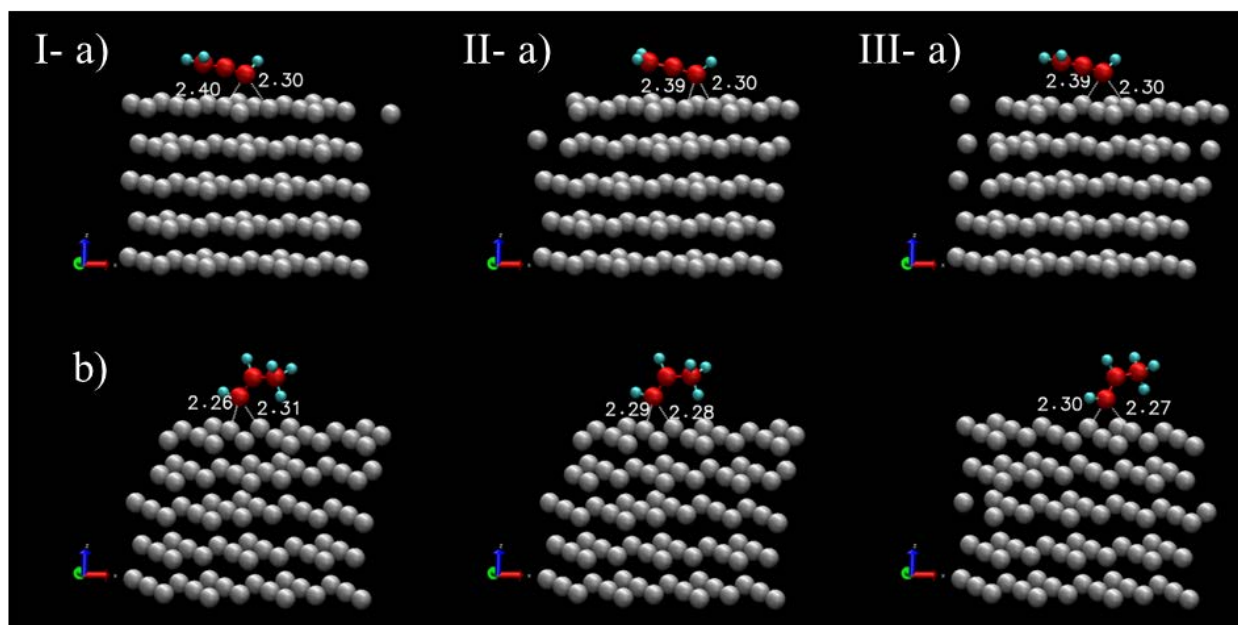


Fig. VI-6: Final adsorption configurations and distances for several PS fragments on Ag(100) surface: a)  $C_3H_3$ , b)  $C_3H_5$ . I, II, and III corresponds to atop, bridge and threefold-hollow adsorption sites respectively. Red represents carbon, cyan hydrogen, and grey represents silver atoms.

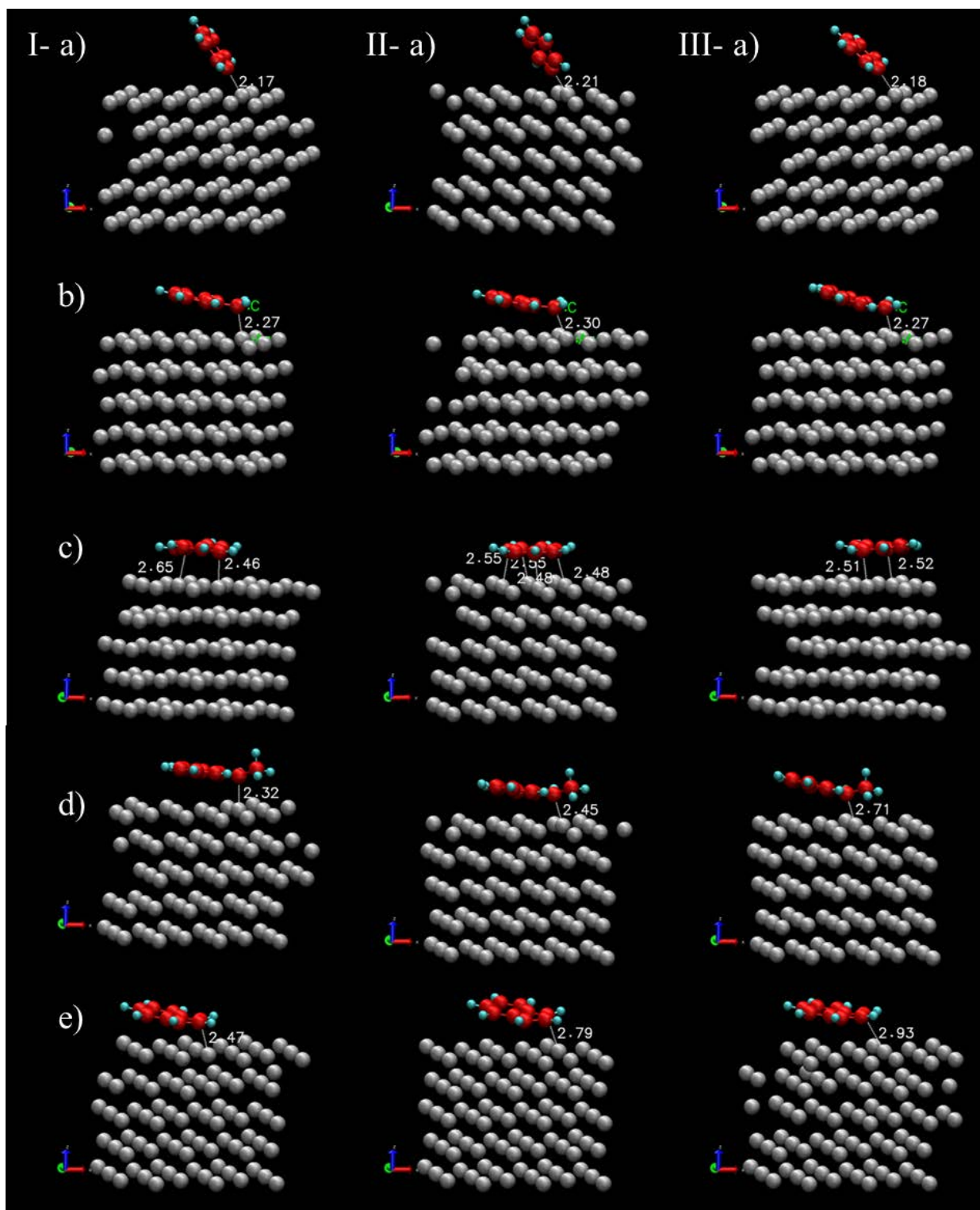


Fig. VI-7: Final adsorption configurations and distances for several PS fragments on Ag(100) surface: a)  $C_6H_5$ , b)  $C_7H_7$  (benzylum), c)  $C_7H_7$  (tropylium) d)  $C_8H_9$  e)  $C_9H_7$ . I, II, and III corresponds to atop, bridge and threefold-hollow adsorption sites respectively. Red represents carbon, cyan hydrogen, and grey represents silver atoms.

For the tropylium fragment there is a larger difference in adsorption distances for Ag(100) and Ag(111) surfaces. The adsorption distances are 2.46, 2.48 and 2.51 for Ag(100) and 2.61, 2.91 and 3.16 for Ag(111) on atop, bridge and hollow sites respectively. Depending on the initial adsorption site, the tropylium fragment on the Ag(100) can adjust itself in such a way that the carbon atoms directly fall on a silver atom which increases the attraction and reduces the distance between the carbon and silver atom. (Fig. VI-8). On the Ag(111) when carbon atoms do not directly fall on a silver atom, it can be seen that the adsorption distances get larger than 3 Å. (Fig. VI-8 III-b)

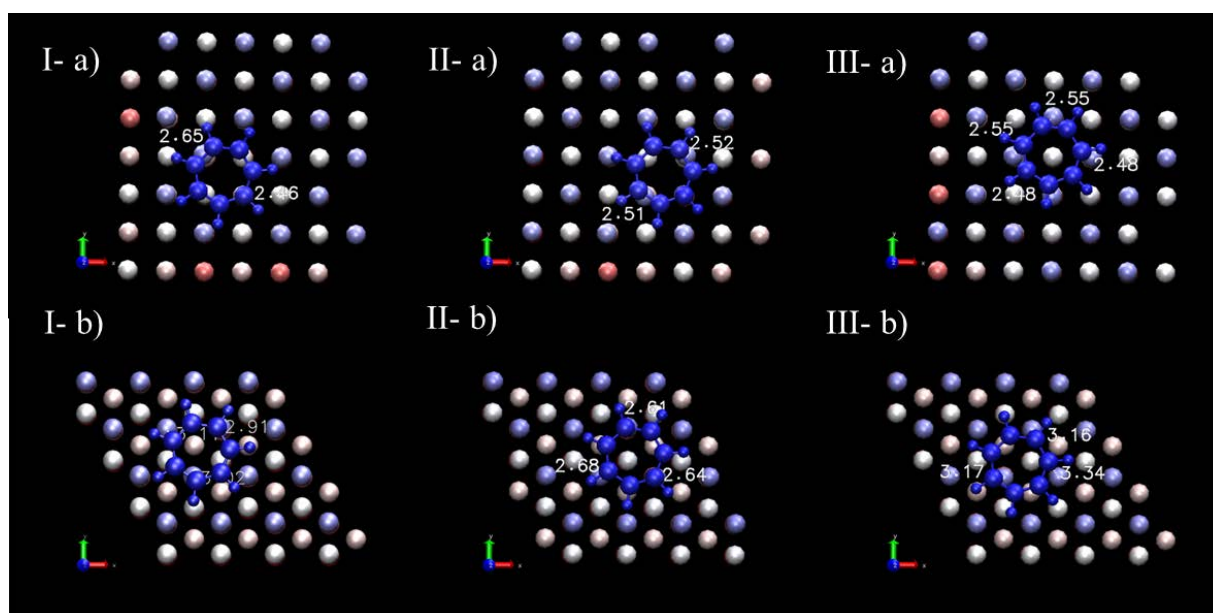


Fig. VI-8: Adsorption configurations and distances for tropylium on a) Ag(100) and b) Ag(111) surfaces for: I) atop b) bridge c) three-fold hollow site. Dark blue represents the fragment. Light blue represents first, grey second and pink and red lower layers of the silver slab.

For the small fragments, different initial starting configurations all yield identical adsorption structures and energies. For the other fragments with cyclic character, adsorption energies vary with fragment size and adsorption site. The phenyl ring limits the angle between the Ag and fragment depending on the structure of the fragment.

### 3. Adsorption of PMMA fragments on Ag(100)

#### 3.1. Adsorption sites

Three different PMMA fragments ( $C_2H_3O_2$ ,  $C_4H_5O$ ,  $C_6H_{11}O_2$ ), which have been observed in the ToF-SIMS spectra, were adsorbed on Ag (100). As higher adsorption energies for PS



fragments were observed on Ag(100) than on Ag(111), DFT calculations were done only on the Ag (100) surface. The fragments were placed randomly on the silver surface as shown in Fig. VI-9 since the radical atom for adsorption was not known for sure. Highlighted atoms in Chapter II were reported to be radical atoms with +1 charge.[174] However, in the following sections we will see the atom through which the fragment binds to the surface depends on the substrate.

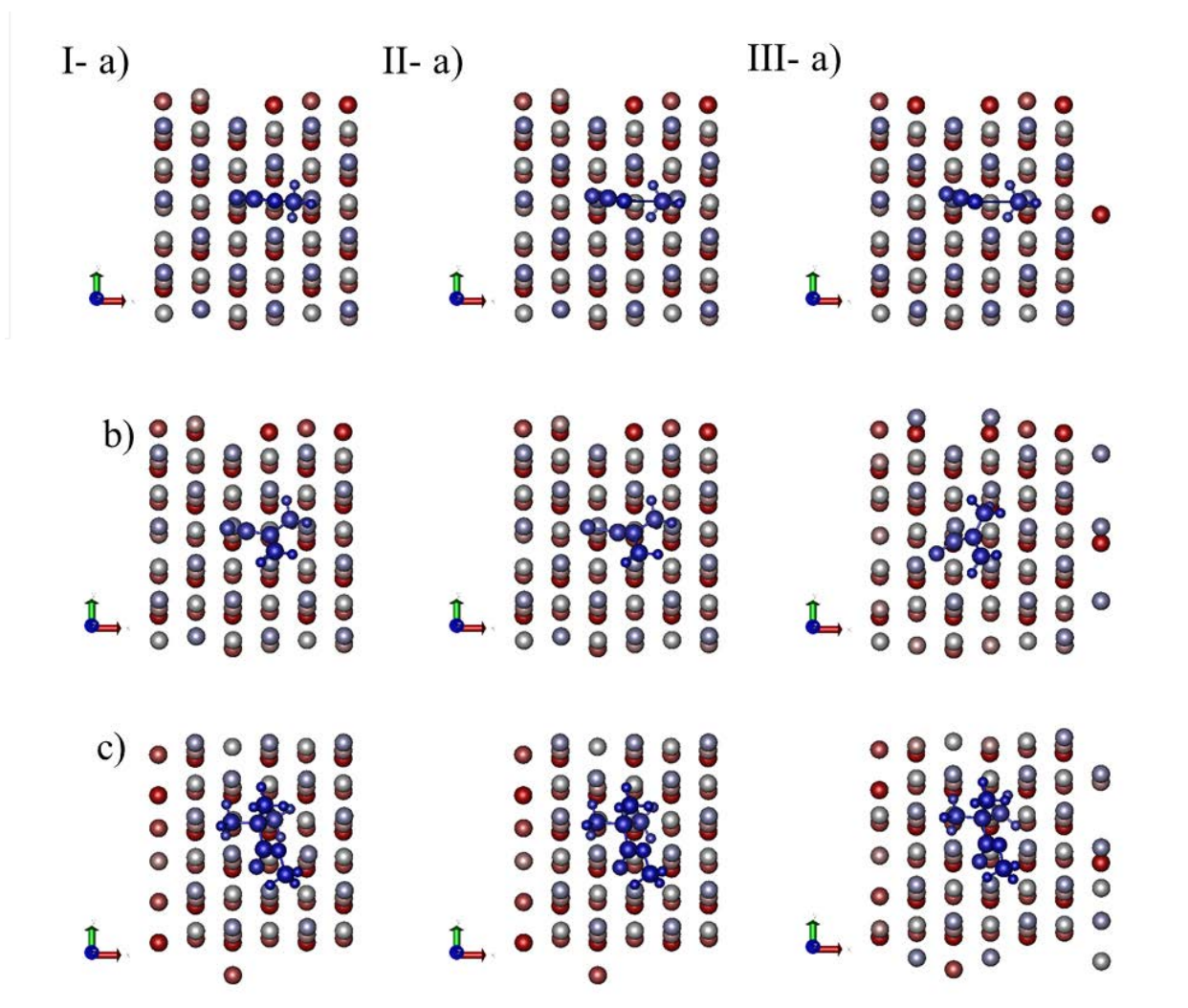


Fig. VI-9: Top views for adsorption of three PMMA fragments on Ag(100) surface: a)  $C_2H_3O_2$ , b)  $C_3H_5$ , c)  $C_6H_5O_2$ . I, II and III show initial, intermediate and final configurations for adsorption. Dark blue represents fragments. Light blue represents first, grey second and pink and red lower layers of the silver slab.

### 3.2. Adsorption Geometries

Adsorption geometries of  $C_2H_3O_2$ ,  $C_4H_5O$  and  $C_6H_{11}O_2$  fragments on Ag(100) are shown in Fig. VI-10, Fig. VI-11 and Fig. VI-12 respectively. The difference to PS fragments is that

they are larger and they contain oxygen in addition to carbon and hydrogen which makes their adsorption more complicated than for PS fragments.

For the adsorption of the  $C_2H_3O_2$  molecule, two sets of DFT calculations were carried out. In the first case, the simulations were done in two runs and in the second case in one run only. The second run was necessary to converge the configuration completely. Similar final adsorption distances are obtained for both cases and the bond between the carbon and oxygen atom becomes non-physically large (Fig. VI-10), which is an artefact due to the VMD visualization software.[215] In reality the bond is broken. This shows that the interactions between the carbon and silver atoms are strong enough to break carbon-oxygen bond.

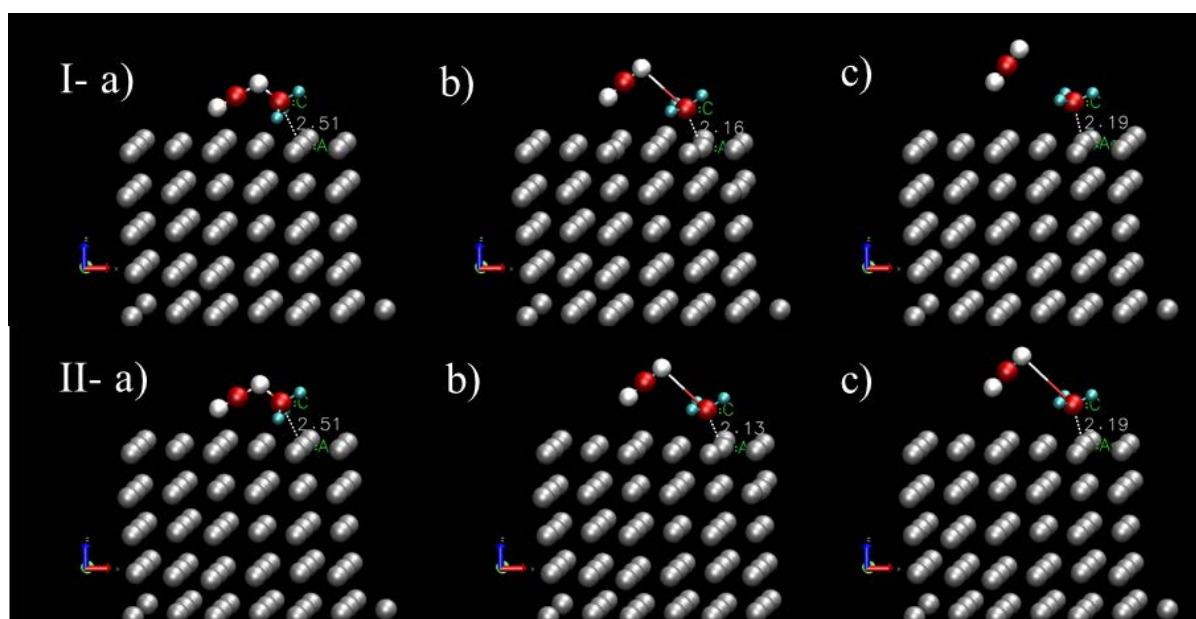


Fig. VI-10: Adsorption configurations and distances for  $C_2H_3O_2$  fragment on Ag(100) surface: a) initial, b) intermediate c) final. I and II show two different runs for DFT calculations. Red represents carbon, cyan hydrogen, white oxygen and grey represents silver atoms.

The  $C_4H_5O$  fragment was adsorbed on silver in two different orientations (Fig. VI-10). In both cases, the molecule adsorbs on the surface via a carbon atom: in the first case via the carbon atom which is bound to another carbon atom and two hydrogen atoms and in the second case via the carbon atom which is bound to another carbon atom and an oxygen atom. Through which carbon atom the molecule binds to the surface depends on the initial configuration. In the first case, the carbon atom which is bound to C and two H is closer to the surface and in the second case, the carbon bound to C and O is closer to it. They both have one 2p orbital free which makes the covalent bonding between C and Ag possible. The final adsorption distances, however, are different. The carbon which is bound to C and O is

2.2 Å above the surface, whereas the other carbon is 2.3 Å away. Shorter adsorption distance in the second case can be correlated with a higher adsorption energy on the surface. (See also section 2.3)

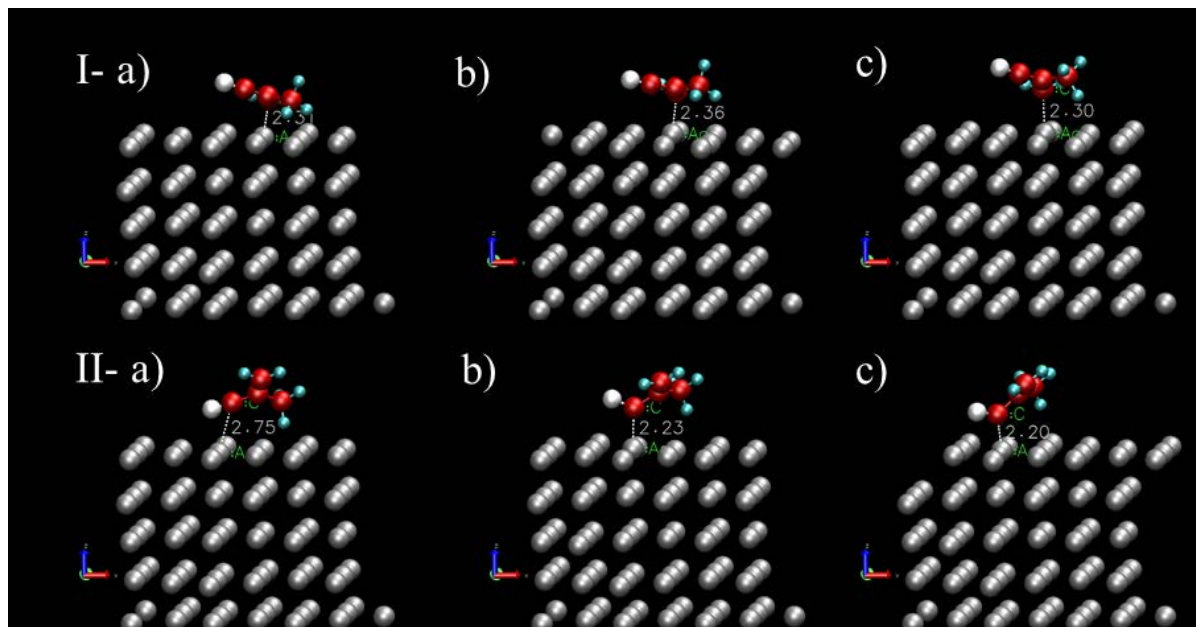


Fig. VI-11: Adsorption configurations and distances for  $C_4H_5O$  fragment on  $Ag(100)$  surface: a) initial, b) intermediate c) final. I and II show two different orientations for adsorption. Red represents carbon, cyan hydrogen, white oxygen and grey represents silver atoms.

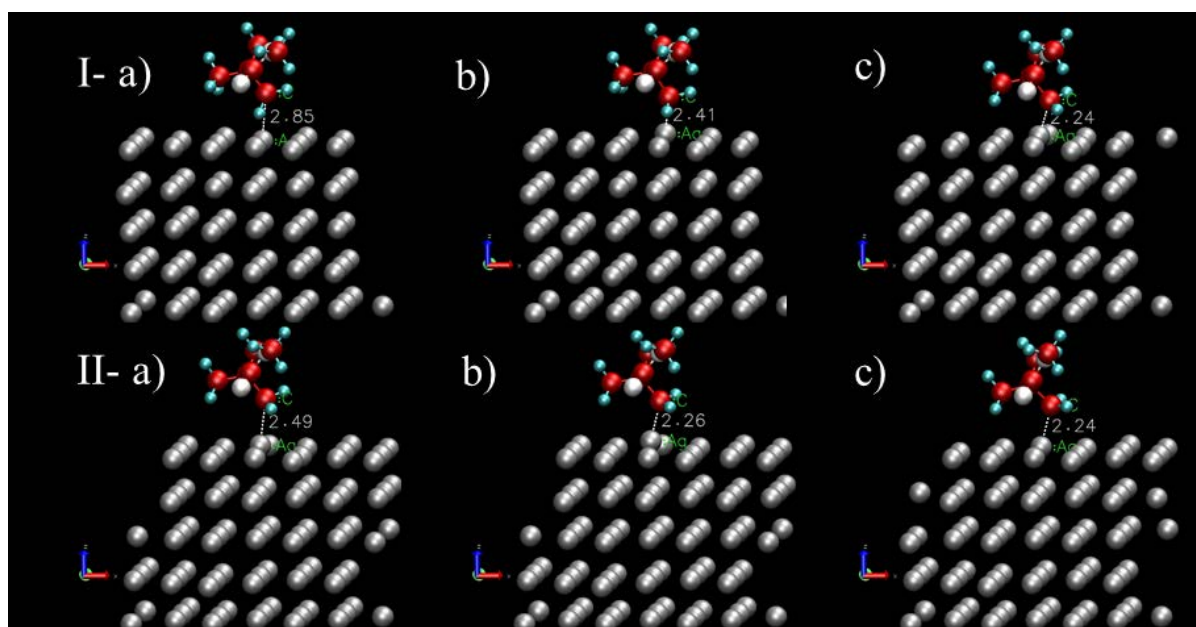


Fig. VI-12: Adsorption configurations and distances for  $C_6H_{11}O_2$  fragment on  $Ag(100)$  surface: a) initial, b) intermediate c) final. I and II show two different DFT calculations. Red represents carbon, cyan hydrogen, white oxygen and grey represents silver atoms.

DFT calculations for the adsorption of the  $C_6H_{11}O_2$  fragment were carried out with two initial adsorption distances between C and Ag: 2.85 and 2.49 Å. The final adsorption distance resulted to be the same in both cases: 2.24 Å. Since the fragment is symmetric around the central carbon atom, calculations were not repeated for the other carbon atoms with a free electron.

For adsorption of all PMMA fragments, one can observe a maximum displacement of the silver atom, which is involved in the covalent bonding during the intermediate and final configurations (Fig. VI-10b, Fig. VI-11b, and Fig. VI-12b). This displacement is either in the upwards or lateral direction depending on the size and initial configuration of the molecule on the surface.

It is interesting to note that all PMMA molecules bond to the silver surface via a carbon atom instead of oxygen which is reported to be the radical atom with a +1 charge.[174] There has been some studies to investigate the interaction of oxygen atoms or molecules with silver. Li *et al.* studied the interaction between the atomic oxygen and Ag(111) surfaces using DFT within the generalized gradient approximation.[216] They studied the effect of coverage on the adsorption of oxygen on silver and found out that the binding energy for O on Ag(111) decreases with increasing coverage and the adsorption becomes energetically unstable after 0.5 ML (monolayer) for on-surface adsorption. This indicates repulsive interaction between adatoms and a build-up of these repulsive forces between adsorbates results in decrease in binding energy. This repulsive interaction can explain the differences between adsorption of  $C_2H_3O_2$ ,  $C_4H_5O$  and  $C_6H_{11}O_2$  fragments. The repulsion between adatoms is stronger when the proportion of oxygen atoms within the molecule is larger. Only the  $C_2H_3O_2$  fragment dissociates after adsorbing on the surface, which has the highest proportion of oxygen atoms and leads to high local oxygen concentration. For the adsorption of  $C_2H_3O_2$ , there is still an energy barrier to the dissociative adsorption (or associative desorption) which keeps the  $CO_2$  molecule on the surface with a larger distance compared to carbon-silver adsorption distance. Hence, comparing  $C_2H_3O_2$ ,  $C_4H_5O$  and  $C_6H_{11}O_2$  fragments we have observed that  $C_2H_3O_2$  experiences dissociative adsorption while  $C_4H_5O$  and  $C_6H_{11}O_2$  do not.  $C_2H_3O_2$  has a higher proportion of oxygen atoms, but whether a fragment goes through dissociative or non-dissociative adsorption on the surface depends also on the metal surface. For example, CO undergoes dissociative adsorption on iron and molecular adsorption on nickel surface.[217]



We will see in the following section that these PMMA fragments follow a different adsorption pattern on different substrates.

Li *et al.* showed the effect of different metals on the interaction of O and Ag(111).[216] The interaction of O on Ag(111) was found to be notably weaker than that of O and Ru(0001) and O and Rh(111). It was also found that the binding energy decreases more rapidly with increasing coverage for O/Ag(111) which indicates a stronger repulsion between adatoms for O/Ag. The difference between these systems is also possibly due to a larger surface dipole moment for O on Ag(111) and a more ionic like bonding compared to a more covalent like bonding for O on Ru and Rh. [216]

Liu *et al.* studied the adsorption of organic molecules on metals using DFT+vdWsurf method in order to include the effect of long range van der Waals interactions.[132]. They also investigated the adsorption of oxygen containing molecules on metal surfaces. For the adsorption of olympicene-derived ketone ( $C_{19}H_{10}O$ ) on Cu(111) they showed the importance of adding vdW corrections in DFT calculations. Before inclusion of vdW interactions, the molecule was bound to the surface via the oxygen of the carbonyl group with a distance of 4 Å between the central carbon atom and the copper. After including vdW forces, this distance decreases to 2.66 Å with the molecule anchored to the copper surface, forming covalent bonds of O/Cu and C/Cu.[132]. While a direct comparison with our system is not possible (since the surface is another coinage metal and the oxygen containing molecule contains five carbon rings and a carbonyl group), this shows that inclusion of vdW interactions can change the radical atom via which the molecule binds to the surface and adsorption distances for physisorbed systems. Many vdW-inclusive methods describe well the physisorption, while they perform poorly for strongly bound systems.[132] For the PMMA molecules studied, the molecule prefers to bind to the surface through a carbon atom rather than oxygen since carbon atoms of PMMA are more reactive than the carbon atoms in olympicene-derived ketone molecule having a free electron and more flexibility. In case of olympicene-derived ketone, the carbonyl group is more reactive than the aromatic rings which explains a first bonding between O and Cu.

### 3.3. Adsorption energies and distances

Adsorption energies of  $C_2H_3O_2$ ,  $C_4H_5O$  and  $C_6H_{11}O_2$  fragments on Ag(100) were calculated for two different cases as mentioned above. The highest adsorption energy was calculated for

C<sub>2</sub>H<sub>3</sub>O<sub>2</sub> fragment: -1.99 eV and -1.96 eV for the first and second cases respectively. The small difference must be resulting from the final relaxation of the system. The adsorption distances stay the same. It is noteworthy to see the adsorption energies and adsorptions distances are related for all the fragments. The smaller adsorption distance is correlated with the higher adsorption energy. The adsorption distance is smallest (2.19 Å) for the C<sub>2</sub>H<sub>3</sub>O<sub>2</sub> fragment where the adsorption energy is highest and it is largest (2.30 Å) for the first configuration of the C<sub>4</sub>H<sub>5</sub>O fragment where the adsorption energy is lowest (-0.75 eV). For the C<sub>6</sub>H<sub>11</sub>O<sub>2</sub> fragment, the adsorption distance (2.24 Å) is between C<sub>2</sub>H<sub>3</sub>O<sub>2</sub> and C<sub>4</sub>H<sub>5</sub>O and the adsorption energy too.

Table VI-5: Calculated adsorption energies (eV) of PMMA fragments on Ag(100) for two different convergences

	<b>E<sub>ads</sub> (eV)</b>			<b>d<sub>ads</sub> (Å)</b>		
	C <sub>2</sub> H <sub>3</sub> O <sub>2</sub>	C <sub>4</sub> H <sub>5</sub> O	C <sub>6</sub> H <sub>11</sub> O <sub>2</sub>	C <sub>2</sub> H <sub>3</sub> O <sub>2</sub>	C <sub>4</sub> H <sub>5</sub> O	C <sub>6</sub> H <sub>11</sub> O <sub>2</sub>
I	-1.99	-0.75	-0.88	2.19	2.30	2.24
II	-1.97	-0.99	-0.78	2.19	2.20	2.24

#### 4. Adsorption of PS fragments on Al<sub>2</sub>O<sub>3</sub>(0001), Pt(111) and Si(111)

PS fragments (C<sub>3</sub>H<sub>3</sub>, C<sub>3</sub>H<sub>5</sub>, C<sub>6</sub>H<sub>5</sub>, C<sub>7</sub>H<sub>7</sub>, C<sub>8</sub>H<sub>9</sub> and C<sub>9</sub>H<sub>7</sub>) were placed on Al<sub>2</sub>O<sub>3</sub>(0001), Pt(111) and Si(111) surfaces randomly. DFT calculations at various adsorption sites were only carried out for the case of Ag(100) and Ag(111) since it would be too costly and time consuming to do the same on all substrates. At the same time, the results of adsorption on different adsorption sites on Ag(100) and Ag(111) did not show considerable differences in calculated adsorption energies.

##### 4.1. PS fragments on Al<sub>2</sub>O<sub>3</sub>(0001)

Table VI-6: Calculated adsorption energies (eV) and adsorption distances (Å) for PS fragments on Al<sub>2</sub>O<sub>3</sub>(0001)

	C <sub>3</sub> H <sub>3</sub>	C <sub>3</sub> H <sub>5</sub>	C <sub>6</sub> H <sub>5</sub>	C <sub>7</sub> H <sub>7</sub> (benzylum)	C <sub>7</sub> H <sub>7</sub> (tropylium)	C <sub>8</sub> H <sub>9</sub>	C <sub>9</sub> H <sub>7</sub>
E <sub>ads</sub>	-0.56	-1.18	-1.05	-0.39	-0.43	-0.21	-0.21
d <sub>ads</sub>	2.21	2.06	2.05	2.43	2.26	2.34	2.34

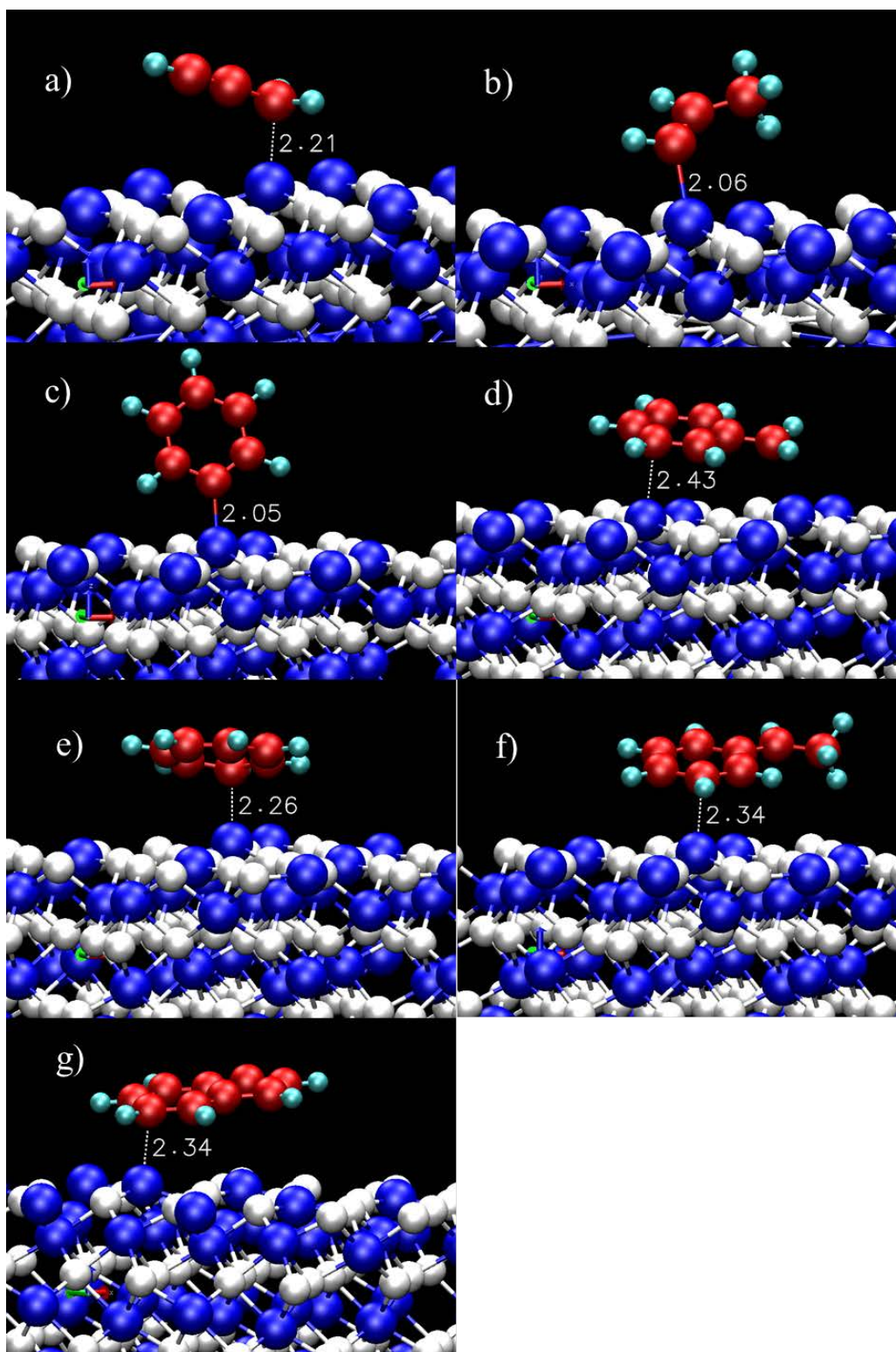


Fig. VI-13: Final adsorption configurations and distances for several PS fragments on  $\text{Al}_2\text{O}_3(0001)$  surface: a)  $\text{C}_3\text{H}_3$ , b)  $\text{C}_3\text{H}_5$ , c)  $\text{C}_6\text{H}_5$ , d)  $\text{C}_7\text{H}_7$  (benzylum), e)  $\text{C}_7\text{H}_7$  (tropylium) f)  $\text{C}_8\text{H}_9$  g)  $\text{C}_9\text{H}_7$ . Red represents carbon, cyan hydrogen, white oxygen and blue aluminum atoms.

Calculated adsorption energies and distances for adsorption for PS fragments on the  $\alpha$ -alumina surface are shown in Table VI-6. It can be seen that adsorption energies and adsorption distances are strongly correlated. The highest adsorption energy was calculated for

$C_3H_5$  (-1.18 eV) and the lowest for  $C_9H_7$  (-0.21 eV). From these calculations, we cannot conclude that the small non-cyclic fragments adsorb better on the surface since calculated adsorption energy for  $C_3H_3$  fragment is half of that of  $C_3H_5$  and also  $C_6H_5$ . However, it should be taken into account that it binds to the aluminium atom through a carbon atom with more occupied orbitals compared to  $C_3H_5$ , reducing the adsorption energy and increasing the adsorption distance. The highest adsorption energy corresponds to the lowest distance between the radical carbon atom and aluminium atom. This distance is 2.06 and 2.34 Å for  $C_3H_5$  and  $C_9H_7$  adsorption respectively. In Fig. VI-13 it can be seen that all the fragments bind to the surface through an aluminium atom. Since the fragments are placed randomly, the closest carbon atom to the surface is most of the time different than those mentioned in Chapter II, i.e. for adsorption on Ag. The carbon atom which is closest to the nearest aluminium atom gets closer to the surface compared to other carbon atoms. All of the cyclic fragments except of  $C_6H_5$ , adsorb almost flat on the  $\alpha$ -alumina surface.  $C_6H_5$  fragment adsorbs vertically.

Adsorption of aromatics on Al(111) surface was first studied by the group of Hafner since the calculations on this simple sp-metal would save computational cost compared to adsorption on transition metals where d orbitals are involved.[133] They reported a flat-lying geometry for adsorption of benzene on aluminium. The calculated adsorption energy was 0.35 eV with an adsorption distance of 3.73-3.84 Å between C and uppermost Al atoms. Their calculated adsorption energy is comparable to our case of adsorption of cyclic fragments on alumina where adsorption energy varies between 0.21-0.43 eV, except for the  $C_6H_5$  fragment which adsorbs vertically with a much higher adsorption energy of 1.05 eV. In case of flat lying adsorption, Duschek *et al.* showed weak bonding of benzene on Al(111) by valence band photoemission spectra, thermal desorption spectra and DFT calculations. Partial density of states of carbon atoms of the free and adsorbed molecules did not show much difference. The small differences were associated with no change in s orbitals, but small perturbation of p orbitals. However, this is unlike the case of adsorption on transition metals with a significant stabilization of p orbitals observed by valence band photoemission spectra. The weak bonding of benzene on Al(111) was explained by mutual polarization of the adsorbate and substrate, with no significant charge transfer between the adsorbate and the substrate.

Being different to the findings of Duschek *et al.*( 3.73-3.84 Å), our adsorption distances (2.26-2.43 Å) are much smaller. This difference might be due to the use of alumina with a

different electron configuration in the aluminium-oxygen network. For molecules the situation changes again. Blomqvist *et al.* studied adsorption of few specific small organic molecules on the oxidized Al(111) and  $\alpha$ -alumina surfaces.[218] They found weak adsorption of benzene on the oxidized aluminium and no adsorption on alumina.

## 4.2. PS fragments on Pt(111)

Table VI-7: Calculated adsorption energies (eV) and adsorption distances (Å) of PS fragments on Pt(111)

	<b>C<sub>3</sub>H<sub>3</sub></b>	<b>C<sub>3</sub>H<sub>5</sub></b>	<b>C<sub>6</sub>H<sub>5</sub></b>	<b>C<sub>7</sub>H<sub>7</sub></b> <b>(benzylum)</b>	<b>C<sub>7</sub>H<sub>7</sub></b> <b>(tropylium)</b>	<b>C<sub>8</sub>H<sub>9</sub></b>	<b>C<sub>9</sub>H<sub>7</sub></b>
E <sub>ads</sub>	-3.26	-2.93	-3.01	-2.50	-2.56	-1.44	-2.30
d <sub>ads</sub>	2.02	2.04	2.00	2.12	2.13	2.15	2.12

Table VI-7 shows the calculated adsorption energies and distances for PS fragments on the Pt(111) surface. Adsorption energies and adsorption distances are inversely proportional and the energy is very sensitive to little changes in distance (in the order of 0.01 Å). Highest adsorption energies are calculated for C<sub>3</sub>H<sub>3</sub> and C<sub>3</sub>H<sub>5</sub> fragments (-3.26 and -2.93 eV respectively), yet the difference to those of cyclic fragments are less compared to silver and alumina surfaces. High adsorption energies for cyclic fragments (-2.50, -2.56 and -2.30 for benzylum, tropylium and C<sub>9</sub>H<sub>7</sub> respectively) are possibly due to a higher interaction between carbon and platinum atoms, and that most of the atoms in the cyclic molecule are involved in adsorption. P orbitals of the cyclic fragments overlap with the d orbitals of Pt, which leads to a strong C-Pt bond and a high adsorption energy. Adsorption geometries shown in Fig. VI-14 also confirm this. Most of the cyclic fragments, except C<sub>8</sub>H<sub>9</sub>, assume a flat lying adsorption on the platinum surface. C<sub>8</sub>H<sub>9</sub>, for which the phenyl ring makes a certain angle with the surface, has the lowest adsorption energy of all (-1.44 eV).

Within transition metals, the highest calculated adsorption energy for the adsorption of benzene was on Ir(100) by Yamagishi *et al.*[219] They calculated an adsorption energy of 2.88 eV with a flat-lying geometry. Orita *et al.* calculated an adsorption energy of 2.03 eV for the adsorption of benzene on Pd(100) surface. [220] There is some variations in literature for the molecular adsorption on Pt. Morin *et al.* reported adsorption energies of 0.90 and 0.67 eV for the adsorption of benzene on bridge and hpc structures respectively[221], while Saeys *et al.* calculated 1.21 and 0.78 eV for the same structures.[222]

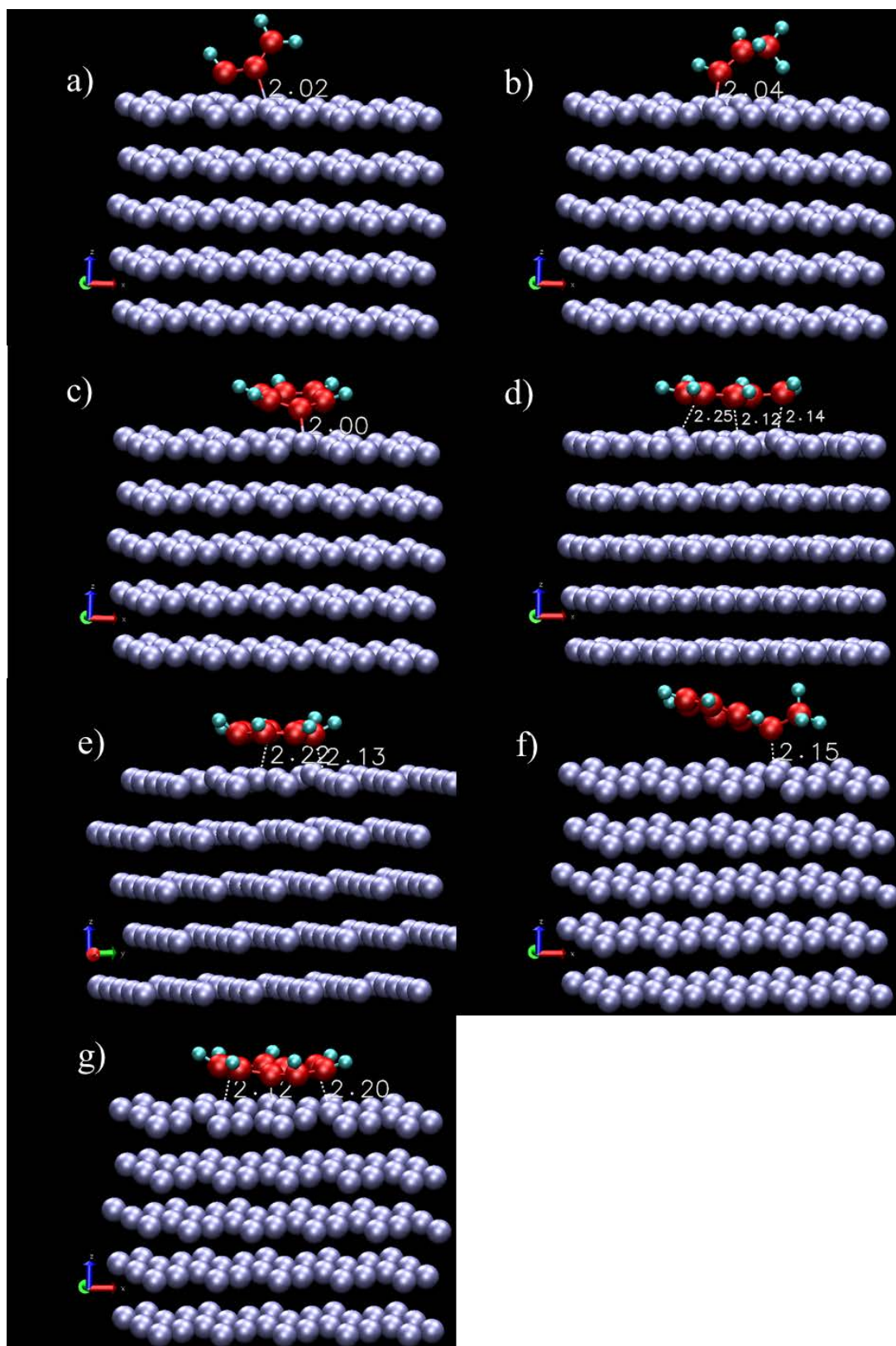


Fig. VI-14: Final adsorption configurations and distances for several PS fragments on Pt(111) surface: a)  $C_3H_3$ , b)  $C_3H_5$ , c)  $C_6H_5$ , d)  $C_7H_7$  (benzylum), e)  $C_7H_7$  (tropylium) f)  $C_8H_9$  g)  $C_9H_7$ . Red represents carbon, cyan hydrogen and ice blue platinum atoms.



### 4.3. PS fragments on Si(111)

Table VI-8: Calculated adsorption energies (eV) and adsorption distances (Å) of PS fragments on Si(111)

	<b>C<sub>3</sub>H<sub>3</sub></b>	<b>C<sub>3</sub>H<sub>5</sub></b>	<b>C<sub>6</sub>H<sub>5</sub></b>	<b>C<sub>7</sub>H<sub>7</sub></b> <b>(benzylum)</b>	<b>C<sub>7</sub>H<sub>7</sub></b> <b>(tropylium)</b>	<b>C<sub>8</sub>H<sub>9</sub></b>	<b>C<sub>9</sub>H<sub>7</sub></b>
$E_{\text{ads}}$	-3.11	-3.58	-3.47	-2.86	-1.88	-2.03	-1.83
$d_{\text{ads}}$	1.96	1.87	1.89	1.98	1.99	1.97	2.03

Adsorption energies and distances for PS fragment adsorption on Si(111) are given in Table VI-8. So far, the overall highest adsorption energies of PS fragments have been obtained on the silicon surface. This also corresponds to smaller adsorption distances of less than 2 Å. Adsorption geometries are shown in Fig. VI-15. The C<sub>3</sub>H<sub>3</sub> fragment is chemisorbed to the surface through two carbon-silicon bonds which contribute to the higher adsorption energy for this fragment. All of the cyclic fragments, except C<sub>6</sub>H<sub>5</sub>, attach to the silicon surface through many bondings between carbon and silicon atoms. For some of the cyclic molecules (benzylum, tropylium) we cannot talk about flat adsorption since the ring structure is quite disturbed owing to the large interaction between carbon and silicon for all of the carbon atoms of the cyclic fragments. For C<sub>6</sub>H<sub>5</sub> fragment however, vertical adsorption is observed.

The adsorption of benzene onto clean and H-passivated Si(001) surfaces was studied by Johnston *et al.*[223] They investigated many structures of adsorption and found the most stable one as tight-bridge structure with an adsorption energy of 1.26 eV. Although the adsorption energies are much lower than what we calculated for adsorption on Si(111) surface, for adsorption on the clean surface, like in our case, they observed large distortion of the molecules.

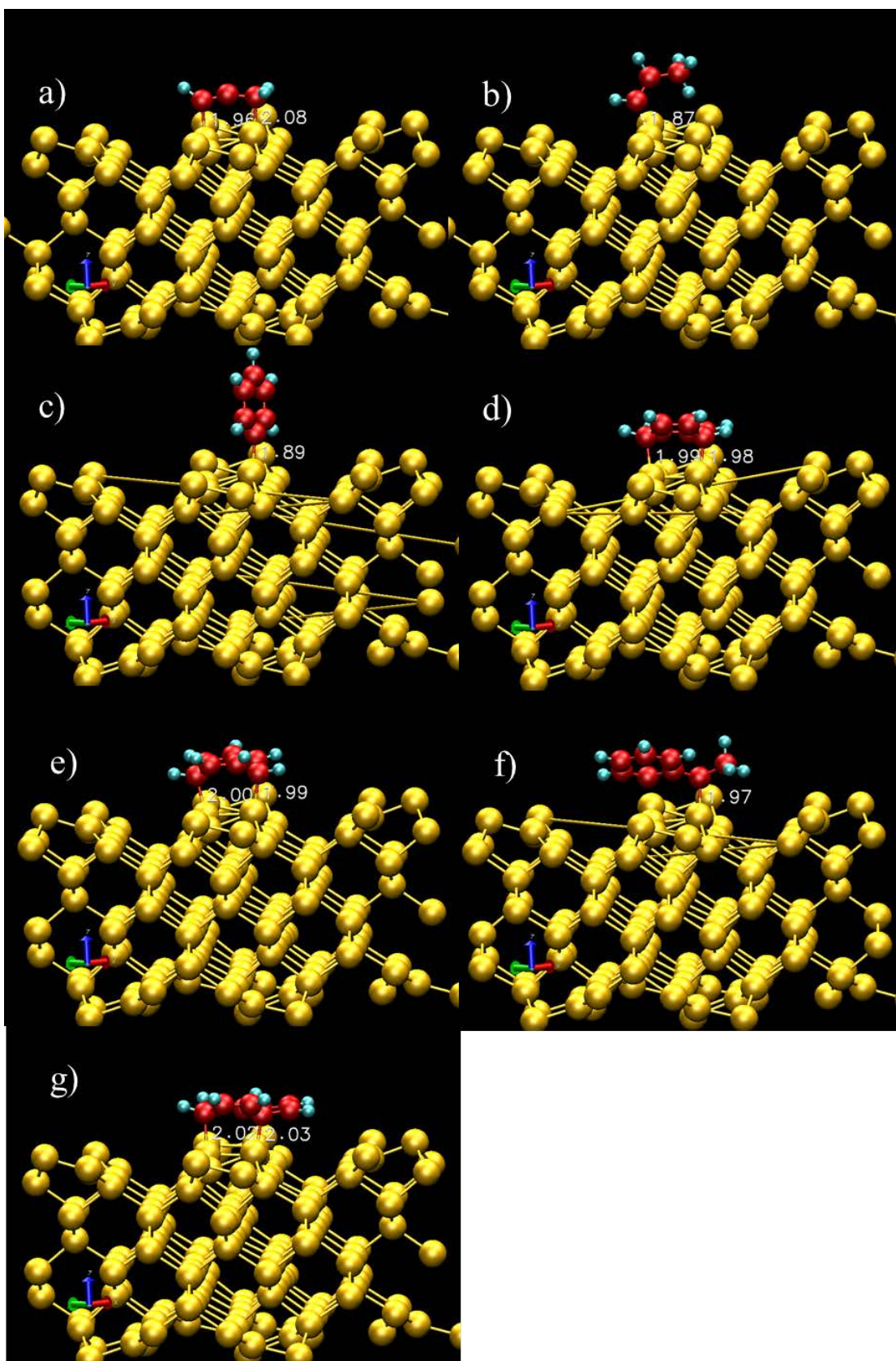


Fig. VI-15: Final adsorption configurations and distances for several PS fragments on Si(111) surface: a)  $C_3H_3$ , b)  $C_3H_5$ , c)  $C_6H_5$ , d)  $C_7H_7$  (benzylum), e)  $C_7H_7$  (tropylium) f)  $C_8H_9$  g)  $C_9H_7$ . Red represents carbon, cyan hydrogen and yellow silicon atoms.



## 5. Adsorption of PMMA fragments on Al<sub>2</sub>O<sub>3</sub>(0001), Pt(111) and Si(111)

In this section, we will investigate the final adsorption configurations of PMMA fragments on Al<sub>2</sub>O<sub>3</sub>(0001), Pt(111) and Si(111) surfaces.

### 5.1. PMMA fragments on Al<sub>2</sub>O<sub>3</sub>(0001)

Table VI-9 gives the adsorption energies and distances for the adsorption of C<sub>2</sub>H<sub>3</sub>O<sub>2</sub>, C<sub>4</sub>H<sub>5</sub>O and C<sub>6</sub>H<sub>11</sub>O<sub>2</sub> on  $\alpha$ -alumina and the final adsorption configurations are given in

Fig. VI-16. The fragments adsorb in all cases through an oxygen atom, although the initial configurations of the molecules on the substrate were random. This is probably due to the higher affinity of aluminium atom for oxygen rather than for carbon. In the case of C<sub>4</sub>H<sub>5</sub>O and C<sub>6</sub>H<sub>11</sub>O<sub>2</sub> fragments, one C atom is also involved in the adsorption, increasing their corresponding adsorption energies on the surface compared to that of C<sub>2</sub>H<sub>3</sub>O<sub>2</sub>. Their adsorption distances are not directly correlated with adsorption energies due to the fact that they are adsorbed through two atoms. The lowest adsorption energy would be expected for the adsorption of C<sub>4</sub>H<sub>5</sub>O, since the distance for adsorption (2.18 Å) is highest of all. However, the lowest adsorption energy was calculated for C<sub>2</sub>H<sub>3</sub>O<sub>2</sub> (0.81 eV), which has a lower adsorption distance (1.91 Å).

Table VI-9: Calculated adsorption energies (eV) of PMMA fragments on Al<sub>2</sub>O<sub>3</sub>

	E <sub>ads</sub> (eV)			d <sub>ads</sub> (Å)		
	C <sub>2</sub> H <sub>3</sub> O <sub>2</sub>	C <sub>4</sub> H <sub>5</sub> O	C <sub>6</sub> H <sub>11</sub> O <sub>2</sub>	C <sub>2</sub> H <sub>3</sub> O <sub>2</sub>	C <sub>4</sub> H <sub>5</sub> O	C <sub>6</sub> H <sub>11</sub> O <sub>2</sub>
Al <sub>2</sub> O <sub>3</sub>	-0.81	-0.96	-1.75	1.91	2.18	1.90

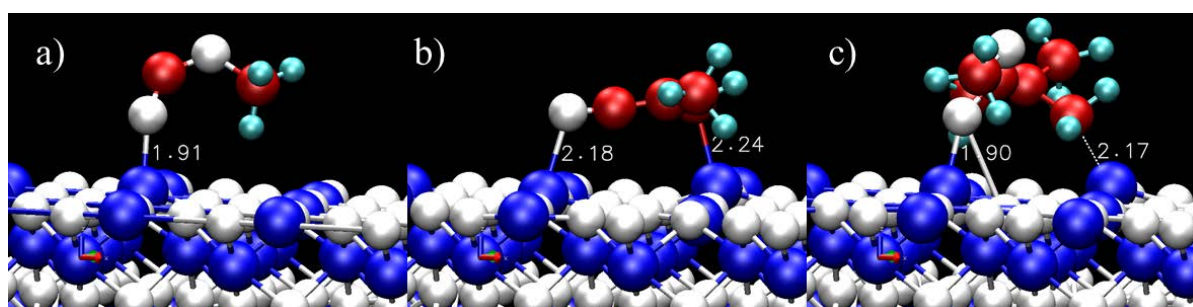


Fig. VI-16: Adsorption configurations and distances for adsorption of PMMA fragments a) C<sub>2</sub>H<sub>3</sub>O<sub>2</sub> b) C<sub>4</sub>H<sub>5</sub>O and c) C<sub>6</sub>H<sub>11</sub>O<sub>2</sub> on Al<sub>2</sub>O<sub>3</sub>(0001)

In their work for the adsorption of atomic oxygen on  $\alpha$ -alumina surface, Gamallo and Sayos obtained adsorption energies between 0.30 and 2.30 eV depending on the adsorption site.[224] Higher adsorption energies have been reported for other oxide surfaces like MgO (2.0-2.5 eV)[225] and SiO<sub>2</sub> (3.7-5.9 eV)[226]. Since  $\alpha$ -alumina is an ionic solid, the adsorption energy is reduced. Other oxygen containing molecules have also been adsorbed on  $\alpha$ -alumina surface by DFT calculations. For the adsorption of nitromethane, Sorescu *et al.* calculated adsorption energies between 0.83 and 0.86 eV[227], which is comparable to our values.

Blomqvist *et al.* found weak adsorption of phenol on the  $\alpha$ -alumina surface, while carbonic acid was bound strongly to it.[218] Unlike most transition metals, it is known that oxygen has high affinity to aluminium surface.[228]

## 5.2. PMMA fragments on Pt(111)

Adsorption energies and distances for PMMA fragment adsorption on Pt(111) are given in Table VI-10. Fragments adsorb on the surface through a carbon atom, except for the C<sub>6</sub>H<sub>11</sub>O<sub>2</sub> fragment. The fragment prefers to bind to the surface through a carbon atom, however, since they are randomly placed on the substrate and since platinum is known to have some affinity for oxygen, the adsorption is also possible through an oxygen atom. The maximum distortion of the platinum atom is experienced when it is bonded to an oxygen atom. As seen in Fig. VI-17, the platinum atom involved in adsorption is pushed down to a level that is lower than the other platinum atoms. Adsorption energies do not vary significantly for the three fragments, the highest being for C<sub>2</sub>H<sub>3</sub>O<sub>2</sub> (2.74 eV).

Table VI-10: Calculated adsorption energies (eV) of PMMA fragments on Pt(111)

	<b>E<sub>ads</sub> (eV)</b>			<b>d<sub>ads</sub> (Å)</b>		
	C <sub>2</sub> H <sub>3</sub> O <sub>2</sub>	C <sub>4</sub> H <sub>5</sub> O	C <sub>6</sub> H <sub>11</sub> O <sub>2</sub>	C <sub>2</sub> H <sub>3</sub> O <sub>2</sub>	C <sub>4</sub> H <sub>5</sub> O	C <sub>6</sub> H <sub>11</sub> O <sub>2</sub>
Pt	-2.74	-2.6	-2.65	1.99	1.99	2.13

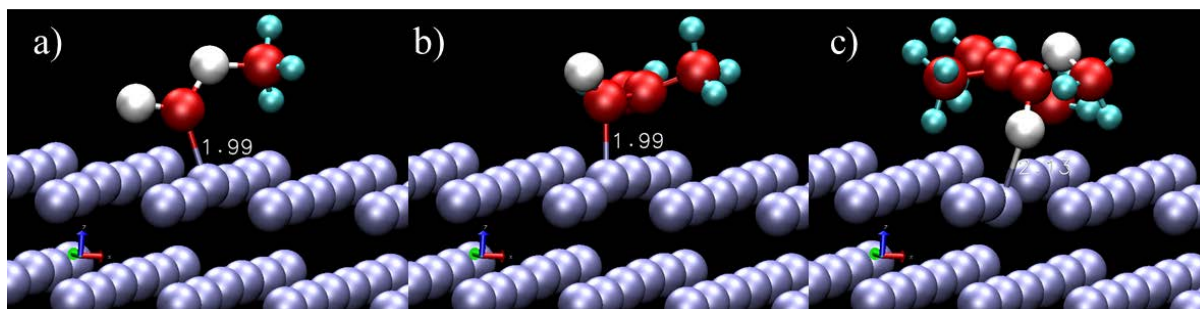


Fig. VI-17: Adsorption configurations and distances for adsorption of PMMA fragments a)  $C_2H_3O_2$  b)  $C_4H_5O$  and c)  $C_6H_{11}O_2$  on Pt(111)

### 5.3. PMMA fragments on Si(111)

Table VI-11: Calculated adsorption energies (eV) of PMMA fragments on Si(111)

	$E_{\text{ads}}$ (eV)			$d_{\text{ads}}$ (Å)		
	$C_2H_3O_2$	$C_4H_5O$	$C_6H_{11}O_2$	$C_2H_3O_2$	$C_4H_5O$	$C_6H_{11}O_2$
Si	-2.9	-2.2	-4.03	1.95	1.98	1.88

For the adsorption of PMMA fragments on silicon, relatively higher adsorption energies have been calculated. The highest is observed for the  $C_6H_{11}O_2$  fragment (4.03 eV) probably because it binds to the surface with a carbon and an oxygen atom. For the fragments containing both oxygen and carbon, the fragment tends to bind to the silicon surface via an oxygen atom. For example, unlike benzene, phenol adsorbs dissociatively on silicon and based on the experimental core level shift data, it was found that phenol is bonded to silicon via the oxygen atom.[229]

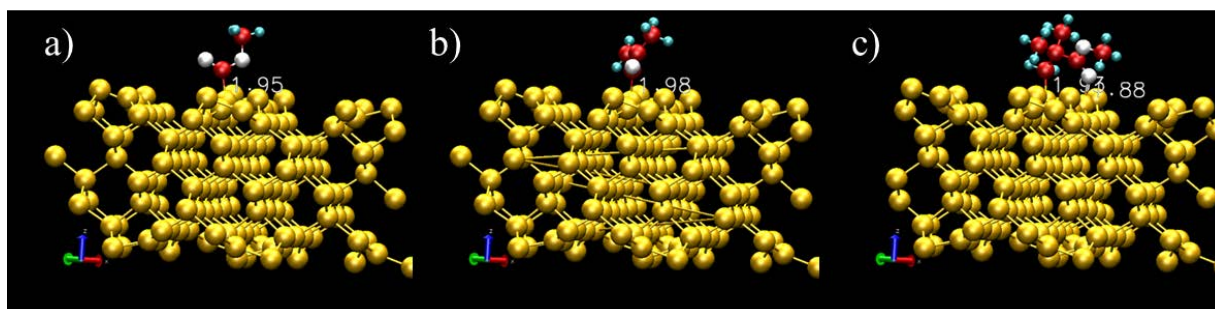


Fig. VI-18: Adsorption configurations and distances for adsorption of PMMA fragments a)  $C_2H_3O_2$  b)  $C_4H_5O$  and c)  $C_6H_{11}O_2$  on Si(111)

Fig. VI-19 shows adsorption stages of PMMA fragments on silicon. Initially they are placed parallel to the surface and after bonding to the surface they assume different adsorption configurations. Depending on the flexibility of bonds, the fragment bends around the adatom. When the oxygen atom is close enough to the surface and if the molecule gives enough flexibility to the atom, the molecule binds via its oxygen atom too. It can be observed that the oxygen atom  $C_6H_{11}O_2$  molecule is attracted by a silicon atom from the second level dimer row and their interaction brings that silicon atom to the same level as the first level dimer row. The dangling bonds on silicon increases the probability of binding the molecules to the surface.

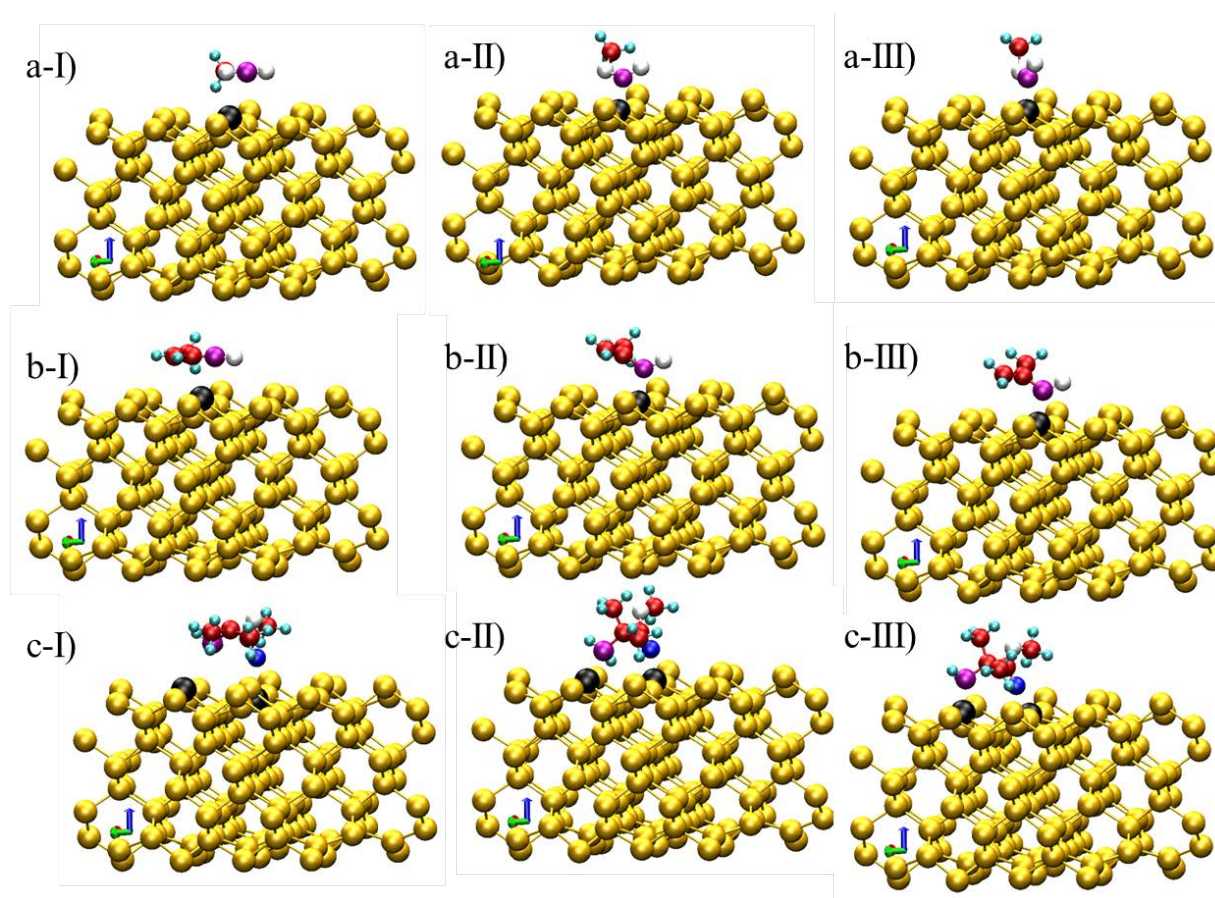


Fig. VI-19: I) initial II) intermediate and III) final stages of adsorption of PMMA fragments a)  $C_2H_3O_2$  b)  $C_4H_5O$  and c)  $C_6H_{11}O_2$  on Si(111)

## 6. Comparison of adsorption of PS and PMMA on different substrates: Al<sub>2</sub>O<sub>3</sub>(0001), Ag(100), Pt(111) and Si(111)

Table VI-12 compares the adsorption energies of PS fragments on different substrates. Highest adsorption energies have been calculated for Si for most of the fragments and lowest energies for Al<sub>2</sub>O<sub>3</sub>.

Table VI-12: Calculated adsorption energies (eV) of PS fragments on Al<sub>2</sub>O<sub>3</sub>(0001), Ag(100), Ag(111), Pt(111) and Si(111)

	C <sub>3</sub> H <sub>3</sub>	C <sub>3</sub> H <sub>5</sub>	C <sub>6</sub> H <sub>5</sub>	C <sub>7</sub> H <sub>7</sub> (benzylum)	C <sub>7</sub> H <sub>7</sub> (tropylium)	C <sub>8</sub> H <sub>9</sub>	C <sub>9</sub> H <sub>7</sub>
Al <sub>2</sub> O <sub>3</sub>	-0.55	-1.18	-1.05	-0.39	-0.43	-0.21	-0.21
Ag (100)	-1.72	-2.02	-1.70	-0.74	-0.35	-0.68	-0.98
Ag(111)	-1.46	-1.73	-1.61	-0.60	-0.29	-0.50	-0.61
Pt	-3.26	-2.93	-3.01	-2.50	-2.56	-1.44	-2.29
Si	-3.11	-3.58	-3.47	-2.86	-1.88	-2.03	-1.83

Adsorption distances can be correlated with adsorption energies. (Table VI-13) Smallest adsorption distances are observed for Si which gives the highest adsorption energies. The largest values are observed for Al<sub>2</sub>O<sub>3</sub> and Ag on which the fragments bind weaker.

Table VI-13: Calculated adsorption distances (Å) of PS fragments on Al<sub>2</sub>O<sub>3</sub>(0001), Ag(100), Ag(111), Pt(111) and Si(111)

	C <sub>3</sub> H <sub>3</sub>	C <sub>3</sub> H <sub>5</sub>	C <sub>6</sub> H <sub>5</sub>	C <sub>7</sub> H <sub>7</sub> (benzylum)	C <sub>7</sub> H <sub>7</sub> (tropylium)	C <sub>8</sub> H <sub>9</sub>	C <sub>9</sub> H <sub>7</sub>
Al <sub>2</sub> O <sub>3</sub>	2.21	2.06	2.05	2.43	2.26	2.34	2.34
Ag(100)	2.31	2.26	2.17	2.27	2.46	2.32	2.47
Ag(111)	2.30	2.15	2.25	2.27	2.61	2.34	2.47
Pt	2.02	2.04	2.00	2.12	2.13	2.15	2.12
Si	1.96	1.87	1.89	1.98	1.99	1.97	2.03

For a more detailed comparison of the adsorption characteristics on the different substrates, the C<sub>6</sub>H<sub>5</sub> fragment has been chosen. Since it has relatively high adsorption energy on most of



the substrates and a more simple structure than PMMA fragments, it will be used for electron density of states analysis.

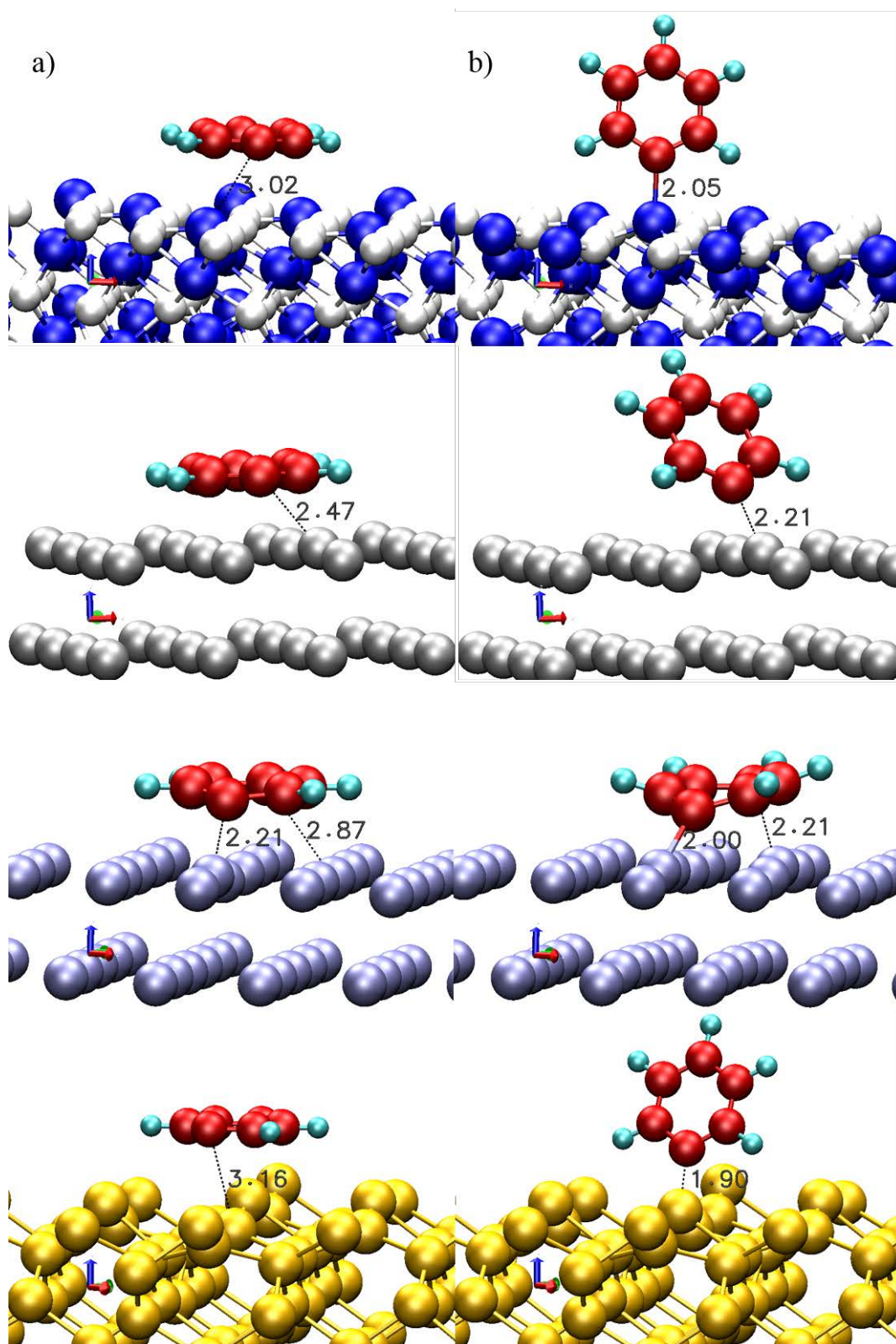


Fig. VI-20: a) initial and b) final adsorption configurations of  $C_6H_5$  on  $Al_2O_3(0001)$ ,  $Ag(111)$ ,  $Pt(111)$ , and  $Si(111)$

The distortion of the fragment upon adsorption gives an idea about its adsorption characteristics. After the C<sub>6</sub>H<sub>5</sub> fragment is placed parallel to all the surfaces, the final adsorption geometries are compared in Fig. VI-20. On alumina the fragments adsorb in a vertical configuration, and on silver close to vertical. Almost no distortion of the fragment is adsorbed. Observed adsorption configurations are in line with calculated weak adsorption energies. On silicon, the fragment undergoes some intermediate distortion with final vertical adsorption configuration. The most distortion of the fragment is observed on platinum where the fragment keeps its flat lying configuration. In case of platinum, almost all the atoms of the fragment and many upper layer platinum atoms are involved in adsorption giving it a stronger adsorption.

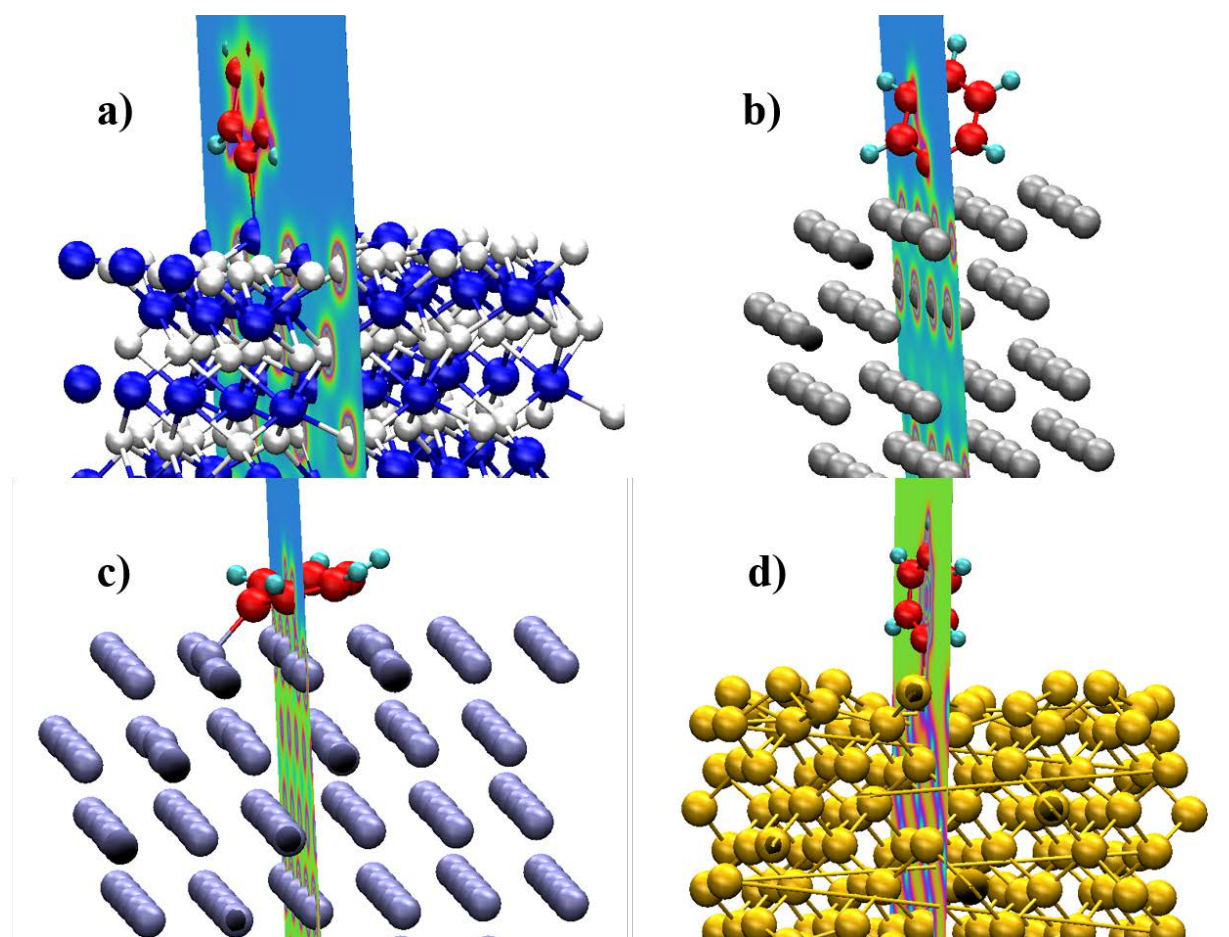


Fig. VI-21: Colour charge density difference plot side view upon adsorption of C<sub>6</sub>H<sub>5</sub> on a)Al<sub>2</sub>O<sub>3</sub>(0001), b)Ag(111), c)Pt(111), and d)Si(111)

The nature of adsorption can be followed by the overlap of orbitals. The charge density around the system of adsorption was visualized for the adsorption of C<sub>6</sub>H<sub>5</sub> on all substrates. (Fig. VI-21 and Fig. VI-22) The maximum orbital overlaps are observed for Pt and Si. There

is a very weak overlap in case of Al<sub>2</sub>O<sub>3</sub> and Ag. From these, we can conclude that the adsorption of Al<sub>2</sub>O<sub>3</sub> and Ag is physisorption and that of Pt and Si chemisorption.

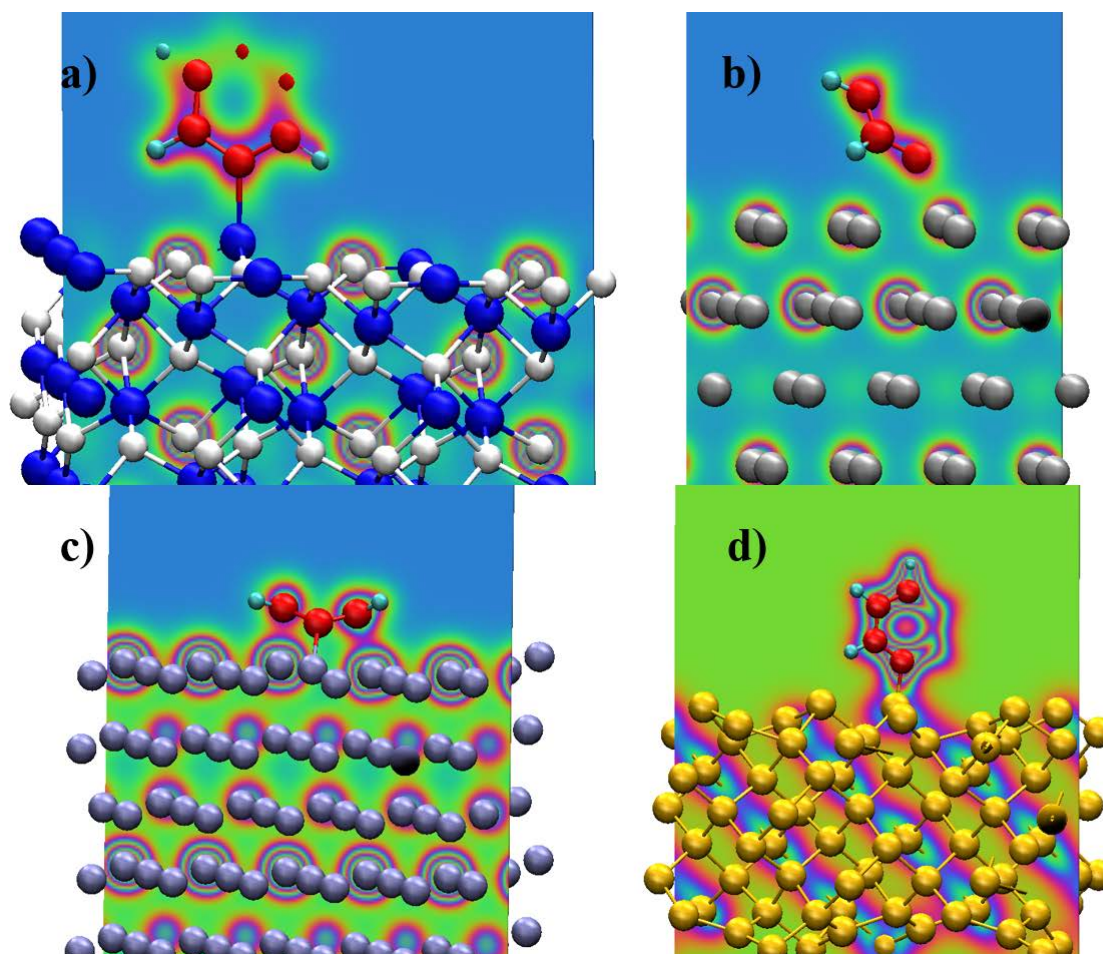


Fig. VI-22: Colour charge density difference plot front view upon adsorption of C<sub>6</sub>H<sub>5</sub> on a)Al<sub>2</sub>O<sub>3</sub>(0001), b)Ag(111), c)Pt(111), and d)Si(111)

Finally, we look at the partial density of states (DOS) of the atoms involved in adsorption, both before and after adsorption. The main difference observed in Fig. VI-23 is that the density of states of the carbon atom upon adsorption is different on different substrates. For Pt, there is a significant change in s and p orbitals for many atoms, both in the valance and conductance band stretching from -8 to 5 eV. The different states observed are mainly due to the formation of new molecular orbitals. For silicon, it can be observed that the change in the states are more localized, by moving of mainly p states just below (-1 eV,-3 eV) and above (1 eV, 3 eV) the Fermi level. For Ag, p states have been moved from conduction band to the valance band, explaining weak adsorption of molecules on silver. The least change in the density of states is observed for Al<sub>2</sub>O<sub>3</sub> by localizing p states just below the Fermi level (0 eV, -2 eV) in the valance band.



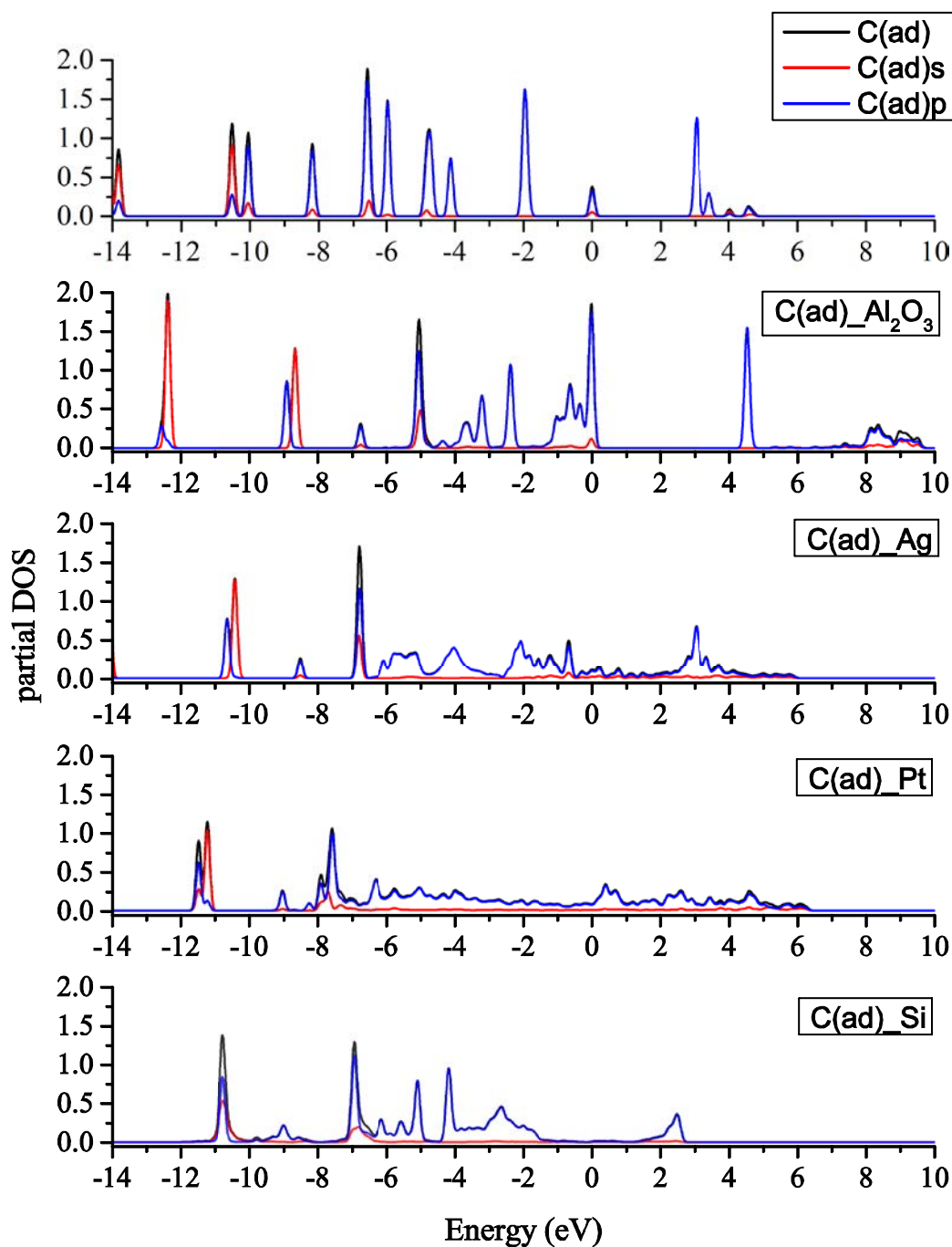


Fig. VI-23: Partial density of states of the C adatom before and upon adsorption for the adsorption of  $C_6H_5$  on  $Al_2O_3$  (0001), Ag(111), Pt(111), and Si(111)

## 7. Conclusions

For the adsorption of PS fragments on silver surfaces, aliphatic molecules have a higher adsorption energy than the cyclic ones. Although there is not a significant difference between

the adsorption of PS fragments on different adsorption sites, the adsorption energy increases by 20 % when Ag(100) is used instead of Ag(111). Their adsorption on alumina surface is much weaker compared to that on the silver characterized by smaller adsorption energies and larger adsorption distances. They adsorb strongly on the Pt(111) and Si(111) surfaces, which is also shown by the stronger orbital overlap between p orbitals of the adsorbant and d orbitals of Pt, and likewise s orbitals of Si.

The adsorption of PMMA fragments is more difficult since the fragments contain oxygen atom and are larger than the fragments of PS. For the adsorption of PS fragments, inclusion of vdW forces would not change the results significantly since especially for Pt and Si, the adsorption is of chemisorptive character. However, for PMMA fragments, being larger, the dispersion forces could change the results more significantly. The adsorption energies of PMMA fragments on different substrates yet follow the same increasing order those of PS fragments. The adsorption energy increases going from alumina to silver and then platinum and silicon.

# Conclusions and Outlook

## 1) General Conclusions

The deposition and adsorption of organic matter in the sub-monolayer range on metallic surfaces has a growing interest since its applications concerns many technologically important fields of surface science, like organic electronics, packaging, electronic and medical devices, polymeric composites, and many more. Atomic interactions between the organic adsorbant and metal substrate, especially at the interface, determine important macroscopic properties of materials. Hence, it is important to have a better fundamental understanding of the nature of these metal-organic interactions.

The main goal of this thesis was to investigate interactions of few-eV molecular fragments of studied polymers with different metal surfaces in the framework of the development of the Storing Matter technique for organic matter deposition. The technique was developed at LIST, first for the study of inorganic matter, in order to circumvent the well-known matrix effect in secondary ion mass spectrometry (SIMS), which mainly separates the analysis from the sputtering of matter. In a first step the sputtered matter is deposited on a collector and next analysed by ToF-SIMS or XPS. There have already been studies for its application to organic matter deposition. The experimental conditions have been optimized in these studies. However, some important aspects of the technique like the sticking factors of organic matter on the collector and other processes during the deposition step which could affect the ToF-SIMS results were not investigated so far. While trying to improve the Storing Matter technique for deposition of organic matter, we have investigated the interactions of sputtering polymeric fragments, with various substrates, in order to further shed light on the metal-organic interactions.

For this purpose, in this work, we used a multidisciplinary approach combining experimental techniques (sputter deposition by Storing Matter technique, time-of-flight secondary ion mass spectrometry and X-ray photoelectron spectroscopy) with density functional theory calculations and molecular dynamics simulations. The major investigated parameters were the number of primary ions and the primary ion fluence for the experimental techniques and impact energy, incidence angle, size of the organic molecules, adsorption energies and

geometries and nature of metal-organic interactions for the simulations. Taking into account these parameters, we will give general conclusions about experimental and numerical work and their implications for the development of the Storing Matter technique.

To start with, the results of MD simulations for the adsorption of simple hexane molecule and longer alkane chains showed that these molecules adsorb on metallic surfaces, only for very restricted conditions, mostly depending on the ratio of molecule size to deposition energy, rather than the incidence angle. MD simulations show that for longer molecules adsorption occurs for energies lower than 1 eV, while for shorter chains like hexane, only at lower energies of 0.01 and 0.1 eV. MD simulation results from the University of Helsinki, on the contrary, showed that the sticking is frequent for hexane fragments even at higher energies, like 5 eV. The fact that the sticking of fragments on the collector is more probable, justifies the use of sputter deposition of polymers for the Storing Matter technique since the products of the technique are rather fragments than intact molecules.

For the experimental part, polystyrene (PS) and poly(methyl methacrylate) (PMMA) were sputter deposited by Storing Matter and analysed by ToF-SIMS and XPS since these techniques give complementary information. It is well known that impurities could be problematic for the study and analysis of organic matter. Since hydrocarbon contaminations constituted a challenge during this work, especially for the Storing Matter technique, it was necessary to carry out XPS analysis in-situ.

The following conclusions can be drawn from the ToF-SIMS analysis of PS and PMMA polymers:

1. Characteristic PS and PMMA fragments can be identified in the positive ToF-SIMS fingerprint spectra.
2. For the PS deposit, either with increasing number of  $\text{Ar}^+$  primary ions or  $\text{Ar}^+$  primary ion fluence, the proportion of large fragments increase in the ToF-SIMS spectra, while the increase rate is higher with increasing fluence.
3. For the PMMA deposit, the situation is a bit different since it contains oxygen differently than PS. The intensity of PMMA specific fragments tend to increase eventually, however in the early stages of either increasing number of primary ions or primary ion fluence, the effect of preferential sputtering of oxygen can be

observed in the ToF-SIMS spectra. For the increasing number of primary ions, intensities of characteristic hydrocarbon fragments initially decrease since the oxygen is preferentially sputtered, leading to an increase in the intensities of oxygenated fragments. The trends of non-specific fragments follow that of specific hydrocarbon fragments. With fluence, there is no drop in specific hydrocarbon intensities, but a continuous increase. The rate of increase is higher for oxygenated fragments. Non-specific hydrocarbon fragments follow a similar trend to specific hydrocarbon fragments.

XPS analysis was done only for the case of increasing fluence, since the experimental setup did not allow to do it for the case of increasing number of primary ions. Similarly, the results of XPS analysis of PS and PMMA deposits can be listed as follows:

1. XPS crater analysis of PS and PMMA polymer samples, shows that both polymers degrade under Ar<sup>+</sup> primary ion bombardment with increasing ion fluence.
2. For PS, the damage on the bombarded PS sample is characterized by disappearance of shake-up component, an increase in the percentages of aliphatic compounds and a decrease in the percentages of aromatic compounds in the C1s XPS spectra.
3. For PMMA, the damage can be observed both in the C1s and O1s XPS spectra. Furthermore, in the C1s spectra, new components can be fitted with increasing fluence.
4. For the PS deposit, although the proportion of aliphatic compounds is much higher compared to those of aromatic ones, a slight increase in the amount of aromatic moieties is observed with increasing the primary ion fluence.
5. For the PMMA deposit, the oxygen content of the deposit decreases and the carbon content increases. The C1s XPS spectrum reveals a higher percentage of aliphatic carbon than components with oxygen. The aliphatic component percentage first decrease until a certain value, than increase with fluence. Components with oxygen follow the opposite trend. O1s spectra of PMMA deposit shows the C-O-C component decreases, while C=O increases in intensity.

ToF-SIMS results combined with XPS results allows us to clarify the Storing Matter processes. We have seen that both PS and PMMA polymers get damaged under  $\text{Ar}^+$  primary ion bombardment. Thus, normally we would expect that the proportion of sputtered characteristic fragments decreases with fluence, so their proportion on the collector would decrease. However, we observe an opposite trend. At this point we suggest this can only be explained by smaller fragments recombining on the collector surface. Possibly, the interactions of different fragments with the metal surface influence this too. Hence, we have carried out static DFT calculations to study the nature of interactions of various PS and PMMA fragments with the silver and other substrates (alumina, platinum, and silicon).

Following general conclusions are obtained from the adsorption of fragments on various substrates by DFT simulations:

1. For both polymers studied in this work, adsorption energies, and hence sticking probabilities, are highest for the smallest fragments.
2. For PS fragments, higher adsorption energies are obtained for small non-cyclic fragments than for larger cyclic ones.
3. For PMMA fragments the highest adsorption energies are obtained for  $\text{C}_2\text{H}_3\text{O}_2$ . This supports the results of ToF-SIMS and XPS analysis since a higher rate of increase is observed for this fragments compared to  $\text{C}_4\text{H}_5\text{O}$  and  $\text{C}_6\text{H}_{11}\text{O}_2$  fragments.
4. For the adsorption of PS and PMMA fragments, adsorption energies on Si and Pt are higher than on Ag and  $\text{Al}_2\text{O}_3$  collectors. This is supported by a larger overlap of orbitals in the charge density difference plot and the difference in their density of states (DOS) plots.

Experimental results suggest some diffusion and recombination events for the polymer fragments on the collector surface. Simulation studies further aid in describing the nature of these interactions, suggesting that small fragments adsorb better on all substrates This implies a less significant diffusion for these fragments. This finding supports the recombination reactions of small fragments, leading to an increasing proportion of larger fragments on the collector surface.

We have studied the effect of substrate on the nature of organic-metal interactions by simulations since experimentally it would be too time consuming. DFT calculations showed that using Pt or Si would be more advantageous than Ag. The advantage of using Ag is that Ag enhances cationization for ToF-SIMS analysis. The same can be expected for Pt, however this metal is too expensive to be used systematically. Silicon collectors do not enhance the emission of secondary ions.

## 2) Outlook

One of the main difficulties during the Storing Matter experimental work was the presence of contaminations. Their effect on the ToF-SIMS or XPS spectra could be reduced by doing the sputter deposition and analysis in-situ in the same chamber. Although this would not completely eliminate contaminations, it would be considerably reduce their interference, especially in the ToF-SIMS spectra, since it is extremely sensitive to contaminations.

Although we have not dealt with reducing fragmentation of polymers during sputter deposition, one innovative way of increasing the proportion of intact molecules or characteristic fragments would be the use large polyatomic projectile for the bombardment of organic samples. It is well-known that using clusters, like C<sub>60</sub><sup>+</sup> or massive Ar<sub>n</sub><sup>+</sup> reduce the surface localized damage and fragmentation.

Although simulations help us to draw conclusions about the possible mechanisms for the adsorption of molecular fragments, they do not describe the dynamics of the deposition process since DFT calculations are static and only describe quantum mechanical states. Ab-initio MD simulations could give better insights into the fundamental processes involved in the deposition processes, however this was beyond this work since it would be too costly and time consuming.

Apparently, the choice of the collector surface has a big effect on the nature of the interactions between organics and metals. Using a collector on which the organic can chemisorb, but at the same time which helps cationization for the SIMS analysis would be worth trying. A possible candidate would be Pt, except of its high cost.





# Bibliography

- [1] R. Behrisch, “1 Introduction and Overview,” in *Sputtering by Particle Bombardment I*, R. Behrisch, Ed. Springer Berlin Heidelberg, 1981, pp. 1–8.
- [2] W. R. Grove, “On the Electro-Chemical Polarity of Gases,” *Philos. Trans. R. Soc. London*, vol. 142, no. January, pp. 87–101, Jan. 1852.
- [3] R. Behrisch and W. Eckstein, “Introduction and Overview,” in *Sputtering by Particle Bombardment*, R. Behrisch and W. Eckstein, Eds. Springer, 2013, pp. 1–20.
- [4] H. F. Winters, “Chemical sputtering, a discussion of mechanisms,” *Radiat. Eff.*, no. 1–4, p. 79, 1982.
- [5] P. Sigmund, “Sputtering by Ion Bombardment Theoretical Concepts,” in *Sputtering by Particle Bombardment I*, B. Rainer, Ed. Springer Berlin Heidelberg, 1981, pp. 9–71.
- [6] R. Smith, *Atomic & Ion Collisions in Solids and at Surfaces: Theory, Simulation and Applications*. Cambridge University Press, 1997.
- [7] P. Sigmund, “Elements of sputtering theory,” in *Nanofabrication by ion-beam sputtering*, T. Som and D. Kanjilal, Eds. Pan Stanford Publishing, 2013, pp. 1–40.
- [8] M. Vicanek and H. M. Urbassek, “Energy and Angular Distributions of Sputtered Particles: A Comparison Between Analytical Theory and Computer Simulation Results,” *Nucl. Instruments Methods Phys. Res. B*, vol. 30, pp. 507–513, 1988.
- [9] P. Sigmund, *Sputtering by Ion Bombardment Theoretical Concepts*. Springer Berlin Heidelberg, 1981, p. 33.
- [10] R. Galera, J. Blais, and G. Bolbach, “Molecular sputtering and damage induced by kiloelectron ions in organic monolayer—metal systems,” *J. Mass Spectrom. Ion Process.*, vol. 107, pp. 531–543, 1991.
- [11] G. Falcone, Z. Sroubek, G. Sindona, and N. Uccella, “Sputtering theory and secondary organic ions,” *Int. J. Mass Spectrom. Ion Process.*, vol. 83, no. 3, pp. 223–230, May 1988.
- [12] Snowdon, “Distributions of sputtered diatomic molecules,” *Nucl. Instruments Methods Phys. Res. Sect. B Beam Interact. with Mater. Atoms*, vol. 9, pp. 132–144, 1985.
- [13] K. G. Standing, B. T. Chait, W. Ens, G. Mchintosh, and R. Beavis, “Time-of-flight measurements of secondary organic ions produced by 1 keV to 16 keV primary ions,” *Nucl. Instruments Methods*, vol. 198, pp. 33–38, 1982.
- [14] F. Mandl, *Statistical Physics*, 2nd ed. John Wiley & Sons, 2008.

- [15] G. Slodzian, "Some problems encountered in secondary ion emission applied to elementary analysis," *Surf. Sc.*, vol. 48, pp. 161–186, 1975.
- [16] J. Michl, "Secondary ion mass spectrometry of low-temperature solids," *Int. J. Mass Spectrom. Ion Process.*, vol. 53, pp. 255–272, 1983.
- [17] H. Grade and R. G. Cooks, "Secondary ion mass spectrometry. Cationization of organic molecules with metals," *J. Am. Chem. Soc.*, vol. 100, no. 18, pp. 5615–5621, Aug. 1978.
- [18] R. G. Cooks and K. L. Busch, "Matrix effects, Internal energies and MS/MS spectra of molecular ions sputtered from surfaces," *Int. J. Mass Spectrom. Ion Process.*, vol. 53, pp. 111–124, 1983.
- [19] A. Benninghoven, "Some aspects of secondary ion mass spectrometry of organic compounds," *Int. J. Mass Spectrom. Ion Process.*, vol. 53, pp. 85–99, 1983.
- [20] J. Zekonyte, J. Erichsen, V. Zaporozhchenko, and F. Faupel, "Mechanisms of argon ion-beam surface modification of polystyrene," *Surf. Sci.*, vol. 532–535, pp. 1040–1044, Jun. 2003.
- [21] P. Bodö and J.-E. Sundgren, "Titanium deposition onto ion-bombarded and plasma treated polydimethylsiloxane: Surface modification, interface and adhesion," *Thin Solid Films*, vol. 136, pp. 147–159, 1986.
- [22] T. Venkatesan, S. R. Forrest, M. L. Kaplan, C. A. Murray, P. H. Schmidt, and B. J. Wilkens, "Ion-beam-induced conductivity in polymer films," *J. Appl. Phys.*, vol. 54, pp. 3150–3153, 1983.
- [23] T. Venkatesan, T. Wolf, D. Allara, J. Wilkens, and G. N. Taylor, "Synthesis of novel inorganic films by ion beam irradiation of polymer films," *Appl. Phys. Lett.*, vol. 43, pp. 934–936, 1983.
- [24] Z. W. Kowalski, "Ion-bombardment modification of surface morphology of solids," *J. Mater. Sci.*, vol. 29, pp. 3542–3552, 1994.
- [25] D. Briggs and M. J. Hearn, "Interaction of ion beams with polymers, with particular reference to SIMS," *Vacuum*, vol. 36, pp. 1005–1010, 1986.
- [26] B. V King, I. S. T. Tsong, and S. H. Lin, "Mechanisms of ion-induced desorption of large molecules and clusters," *Int. J. Mass Spectrom. Ion Process.*, vol. 78, pp. 341–356, 1987.
- [27] K. Wittmaack, "Pre-equilibrium variation of secondary ion yield," *J. Mass Spectrom. Ion Phys.*, vol. 17, pp. 39–50, 1975.
- [28] C. W. Magee, "Secondary ion quadrupole mass spectrometer for depth profiling design and performance evaluation," *Rev. Sci. Instrum.*, vol. 49, no. 4, pp. 477–485, 1978.

- [29] A. Benninghoven, "Analysis of sub-monolayers on silver by secondary ion emission," *Physica Status Solidi*, vol. 34, no. 2, pp. K169–171, 1969.
- [30] A. Delcorte, "Fundamental Aspects of Organic SIMS," in *ToF-SIMS: Surface analysis by mass spectrometry*, IM Publications LLP, 2001, pp. 161–194.
- [31] A. Benninghoven, "Chemical Analysis of Inorganic and Organic Surfaces and Thin Films by Static Time-of-Flight Secondary Ion Mass Spectrometry (TOF-SIMS)," *Angew. Chem. Int. ed. Engl.*, vol. 33, pp. 1023–1043, Aug. 1994.
- [32] D. Briggs and M. J. Hearn, "Analysis of polymer surfaces by SIMS. Part 5. The effects of primary ion mass and energy on secondary ion relative intensities," *Int. J. Mass Spectrom. Ion Process.*, vol. 67, no. 1, pp. 47–56, Sep. 1985.
- [33] A. Delcorte, X. Vanden Eynde, P. Bertrand, and D. . Reich, "Influence of the primary ion beam parameters (nature, energy, and angle) on the kinetic energy distribution of molecular fragments sputtered from poly(ethylene terephthalate) by kiloelectron volt ions," *Int. J. Mass Spectrom.*, vol. 189, no. 2–3, pp. 133–146, Aug. 1999.
- [34] M. Blain, S. Della-Negra, H. Joret, Y. Le Beyec, and E. Schweikert, "Secondary-ion yields from surfaces bombarded with keV molecular and cluster ions," *Phys. Rev. Lett.*, vol. 63, no. 15, pp. 1625–1628, Oct. 1989.
- [35] M. Benguerba, a. Brunelle, S. Della-Negra, J. Depauw, H. Joret, Y. Le Beyec, M. G. Blain, E. a. Schweikert, G. B. Assayag, and P. Sudraud, "Impact of slow gold clusters on various solids: nonlinear effects in secondary ion emission," *Nucl. Instruments Methods Phys. Res. Sect. B Beam Interact. with Mater. Atoms*, vol. 62, no. 1, pp. 8–22, Nov. 1991.
- [36] C. M. Mahoney, "Cluster secondary ion mass spectrometry of polymers and related materials.," *Mass Spectrom. Rev.*, vol. 29, no. 2, pp. 247–93, 2009.
- [37] G. J. Leggett and J. C. Vickerman, "Role of electronic particle-surface interactions during the sputter degradation of polymers," *Anal. Chem.*, vol. 63, no. 6, pp. 561–568, Mar. 1991.
- [38] P. Arezki, B., Delcorte, A., Bertrand, "Substrate and structural effects on the kinetic energy of molecular fragments in SIMS of polymer overlayers," in *SIMS XII Proceedings*, H.-N. Benninghoven, A., Bertrand, P., Migeon, Ed. Elsevier, Amsterdam, 2000, pp. 199–202.
- [39] A. Delcorte, X. Vanden Eynde, P. Bertrand, J. C. Vickerman, and B. J. Garrison, "Kiloelectronvolt Particle-Induced Emission and Fragmentation of Polystyrene Molecules Adsorbed on Silver: Insights from Molecular Dynamics," *J. Phys. Chem. B*, vol. 104, pp. 2673–2691, 2000.
- [40] M. J. Hearn and D. Briggs, "Analysis of polymer surfaces by SIMS," *Surf. Interface Anal.*, vol. 11, pp. 198–213, 1988.

- [41] M. C. Davies, R. D. Short, M. a. Khan, J. F. Watts, a. Brown, a. J. Eccles, P. Humphrey, J. C. Vickerman, and M. Vert, "An XPS and SIMS analysis of biodegradable biomedical polyesters," *Surf. Interface Anal.*, vol. 14, no. 3, pp. 115–120, Mar. 1989.
- [42] G. J. Leggett and J. C. Vickerman, "An empirical model for ion formation from polymer surfaces during analysis by secondary ion mass spectrometry," *Int. J. Mass Spectrom. Ion Process.*, vol. 122, pp. 281–319, 1992.
- [43] A. Delcorte and P. Bertrand, "Energy distributions of hydrocarbon secondary ions from thin organic films under keV ion bombardment: Correlation between kinetic and formation energy of ions sputtered from tricosenoic acid," *Nucl. Instruments Methods Phys. Res. Sect. B Beam Interact. with Mater. Atoms*, vol. 117, no. 3, pp. 235–242, Sep. 1996.
- [44] A. Delcorte and P. Bertrand, "Kinetic energy distributions of secondary molecular ions from thin organic films under ion bombardment," *Nucl. Instruments Methods Phys. Res. Sect. B Beam Interact. with Mater. Atoms*, vol. 115, no. 1–4, pp. 246–250, Jul. 1996.
- [45] A. Delcorte and P. Bertrand, "Influence of chemical structure and beam degradation on the kinetic energy of molecular secondary ions in keV ion sputtering of polymers," *Nucl. Instruments Methods Phys. Res. B*, vol. 135, pp. 430–435, 1998.
- [46] G. Gillen, "The use of kinetic energy distributions to determine the relative contributions of gas-phase and surface fragmentation in kiloelectronvolt ion sputtering of a quaternary ammonium salt," *J. Mass Spectrom. Ion Process.*, vol. 105, no. 199 1, pp. 215–224, 1990.
- [47] B. Hagenhoff, "Optimisation Methods : Cationisation," in *ToF-SIMS: Surface analysis by mass spectrometry*, 2001, pp. 285–308.
- [48] D. van Leyen, B. Hagenhoff, E. Niehuis, A. Benninghoven, I. V. Bletsos, and D. M. Hercules, "Time of flight secondary ion mass spectrometry of polymer materials," *J. Vac. Sci. Technol. A*, vol. 7, p. 1790, 1989.
- [49] D. van Leyen, "Systematische Untersuchung zur Sekundärionenemission synthetischer Polymere," Münster, 1993.
- [50] A. Benninghoven, F. G. Rüdener, and H. W. Werner, *Secondary Ion Mass Spectrometry: Basic Concepts, Instrumental Aspects, Applications, and Trends*. Wiley, New York, 1987, p. 743.
- [51] S. Della-Negra, J. Depauw, H. Joret, Y. Le Beyec, and E. Schweikert, "Secondary ion emission induced by multicharged 18-keV ion bombardment of solid targets," *Phys. Rev. Lett.*, vol. 60, no. 10, pp. 948–951, Mar. 1988.
- [52] L. Calcagno, G. Compagnini, and G. Foti, "Structural modification of polymer films by ion irradiation," *Nucl. Instruments Methods Phys. Res. Sect. B*, vol. 65, pp. 413–422, 1992.

- [53] C. Mahoney, "Cluster secondary ion mass spectrometry of polymers and related materials," *Mass Spectrom. Rev.*, vol. 29, pp. 247–293, 2010.
- [54] S. Ninomiya, K. Ichiki, H. Yamada, Y. Nakata, T. Seki, T. Aoki, and J. Matsuo, "Precise and fast secondary ion mass spectrometry depth profiling of polymer materials with large Ar cluster ion beams," *Rapid Commun. Mass Spectrom.*, vol. 23, pp. 1601–1606, 2009.
- [55] A. Delcorte, L. Weng, and P. Bertrand, "Secondary molecular ion emission from aliphatic polymers bombarded with low energy ions: Effects of the molecular structure and the ion beam induced surface," *Nucl. Instruments Methods Phys. Res. Sect. B*, vol. 100, pp. 213–216, 1995.
- [56] R. Chatterjee, D. E. Riederer, Z. Postawa, and N. Winograd, "Coverage-Dependent Molecular Ejection from Ion-Bombarded C<sub>6</sub>H<sub>6</sub>/Ag {111}," *J. Phys. Chem. B*, vol. 5647, no. 98, pp. 4176–4182, 1998.
- [57] A. Benninghoven, D. Jaspers, and W. Sichtermann, "Secondary Ion emission of amino acids," *Appl. Phys.*, vol. 11, p. 35, 1976.
- [58] W. Sichtermann and A. Benninghoven, "Secondary ion formation from amino acids by proton and cation transfer," *Int. J. Mass Spectrom. Ion Process.*, vol. 40, pp. 177–184, 1981.
- [59] R. Chatterjee and D. Riederer, "Coverage-dependent molecular ejection from ion-bombarded C<sub>6</sub>H<sub>6</sub>/Ag {111}," *J. Phys. Chem. C*, vol. 5647, no. 98, pp. 4176–4182, 1998.
- [60] P. Williams and G. Gillen, "Damage processes in molecular ion sputtering from solid and liquid targets," in *Ion Formation from Organic Solids, IFOS IV*, A. Benninghoven, Ed. Chichester, UK: John Wiley, 1989, pp. 15–21.
- [61] A. Benninghoven, F. G. Rüdener, and H. W. Werner, *Secondary Ion Mass Spectrometry: Basic Concepts, Instrumental Aspects, Applications, and Trends*. Wiley, New York, 1987, p. 737.
- [62] D. Briggs and A. B. Wootton, "Analysis of Polymer Surfaces by SIMS 1. An Investigation of Practical Problems," *Surf. Interface Anal.*, vol. 4, no. 3, pp. 24–25, 1982.
- [63] G. J. Leggett and J. C. Vickerman, "Effects of damage during the SIMS analysis of poly ( vinyl chloride ) and poly ( methyl methacrylate)," *Appl. Surf. Sci.*, vol. 55, pp. 105–115, 1992.
- [64] A. Delcorte, B. G. Segda, B. J. Garrison, and P. Bertrand, "Inferring ejection distances and a surface energy profile in keV particle bombardment experiments," *Nucl. Instruments Methods Phys. Res. Sect. B*, vol. 171, pp. 277–290, 2000.
- [65] I. Gilmore and M. Seah, "Static SIMS: a study of damage using polymers," *Surf. interface Anal.*, vol. 24, no. February, pp. 746–762, 1996.

- [66] D. Briggs and I. W. Fletcher, "Cs<sup>+</sup> Ion Beam Damage of Poly ( vinyl chloride ) and Poly ( methyl methacrylate ) Studied by High Mass Resolution ToF-SIMS," *Surf. Interface Anal.*, vol. 25, no. November 1996, pp. 167–176, 1997.
- [67] M. T. Robinson and M. Torrens, "Computer simulation of atomic-displacement cascades in solids in the binary-collision approximation," *Phys. Rev. B*, vol. 9, p. 5008, 1974.
- [68] J. P. Biersack and W. Eckstein, "Sputtering studies with the Monte Carlo Program TRIM.SP," *Appl. Phys. A*, vol. 34, no. 2, pp. 73–94, 1984.
- [69] W. Eckstein and H. M. Urbassek, "Computer simulation of the sputtering process," in *Sputtering by Particle Bombardment*, Springer Berlin Heidelberg New York, 2007.
- [70] J. B. Gibson, A. N. Goland, M. Milgram, and G. H. Vineyard, "Dynamics of Radiation Damage," *Phys. Rev.*, vol. 120, p. 1229, 1960.
- [71] W. L. Gay and D. E. Harrison, "Machine Simulation of Collisions Between a Copper Atom and a Copper Lattice," *Phys. Rev.*, vol. 135, p. A1780, 1964.
- [72] B. J. Garrison, C. T. Reimann, N. Winograd, and D. E. Harrison, "Energy and angular distributions of Rh atoms ejected due to ion bombardment from Rh (111): A theoretical study," *Phys. Rev. B*, vol. 36, no. 7, pp. 3516–3521, 1987.
- [73] D. N. Bernardo, R. Bhaita, and B. J. Garrison, "keV Particle Bombardment of Solids: Molecular Dynamics Simulations and beyond," *Comput. Phys. Commun.*, vol. 80, pp. 259–273, 1994.
- [74] S. W. Rosencrance, J. S. Burnham, D. E. Sanders, C. He, B. J. Garrison, N. Winograd, Z. Postawa, and D. A.E., "Mechanistic study of atomic desorption resulting from the keV-ion bombardment of fcc{001} single-crystal metals," *Phys. Rev. B*, vol. 52, p. 6006, 1995.
- [75] J. D. E. Harrison, "CRC Critical Reviews," *Solid State Mater. Sci.*, vol. 14, no. S1, 1988.
- [76] F. H. Stillinger and T. A. Weber, "Computer simulation of local order in condensed phases of silicon," *Phys. Rev. B*, vol. 31, p. 5262, 1986.
- [77] J. Tersoff, "New empirical approach for the structure and energy of covalent systems," *Phys. Rev. B*, vol. 37, p. 6991, 1988.
- [78] T. a. Weber and F. H. Stillinger, "Inherent structures in polyatomic liquids: Simulation for Si<sub>2</sub>F<sub>6</sub>," *J. Chem. Phys.*, vol. 95, no. 5, p. 3614, 1991.
- [79] D. W. Brenner, "Empirical potential for hydrocarbons for use in simulating the chemical vapor deposition of diamond films," *Phys. Rev. B*, vol. 42, p. 9458, 1990.
- [80] D. W. Brenner, O. a Shenderova, J. a Harrison, S. J. Stuart, B. Ni, and S. B. Sinnott, "A second-generation reactive empirical bond order (REBO) potential energy

- expression for hydrocarbons,” *J. Phys. Condens. Matter*, vol. 14, no. 4, pp. 783–802, Feb. 2002.
- [81] B. J. Garrison, P. B. S. Kodali, and D. Srivastava, “Modeling of Surface Processes as Exemplified by Hydrocarbon Reactions,” *Chem. Rev.*, vol. 96, no. 4, pp. 1327–1342, 1996.
- [82] S. J. Stuart, A. B. Tutein, and J. a. Harrison, “A reactive potential for hydrocarbons with intermolecular interactions,” *J. Chem. Phys.*, vol. 112, no. 14, p. 6472, 2000.
- [83] B. J. Garrison, “Mechanism of ejection of organic molecules from surfaces by keV ion bombardment,” *J. Am. Chem. Soc.*, vol. 102, p. 6553, 1980.
- [84] B. J. Garrison, “Organic Molecule Ejection from Surface Due to Heavy Particle Bombardment,” *Am. Chem. Soc.*, vol. 104, p. 6211, 1982.
- [85] R. Chatterjee, Z. Postawa, N. Winograd, and B. J. Garrison, “Molecular Dynamics Simulation Study of Molecular Ejection Mechanisms: keV Particle Bombardment of C<sub>6</sub>H<sub>6</sub>/Ag{111},” *J. Phys. Chem. B*, vol. 103, no. 1, pp. 151–163, Jan. 1999.
- [86] B. J. Garrison, “Molecular Desorption Induced by Heavy Particle Bombardment of Solids,” *J. Mass Spectrom. Ion Phys.*, vol. 53, no. 243–254, 1983.
- [87] R. Žarić, B. Pearson, K. D. Krantzman, and B. J. Garrison, “Molecular dynamics simulations to explore the effect of projectile size on the ejection of organic targets from metal surfaces,” *Int. J. Mass Spectrom. Ion Process.*, vol. 174, no. 1–3, pp. 155–166, Mar. 1998.
- [88] B. J. Garrison, A. Delcorte, and K. D. Krantzman, “Molecule Liftoff from Surfaces,” *Acc. Chem. Res.*, vol. 33, no. 2, pp. 69–77, 2000.
- [89] J. A. Townes, A. K. White, E. N. Wiggins, K. D. Krantzman, B. J. Garrison, N. Winograd, U. V. Park, and V. Pennsylv, “Mechanism for Increased Yield with SF<sub>5</sub> + Projectiles in Organic SIMS: The Substrate Effect,” vol. 103, no. 24, pp. 10–12, 1999.
- [90] R. S. Taylor and B. J. Garrison, “Molecular Dynamics Simulations of reactions between molecules: High-energy particle bombardment of organic films,” *Langmuir*, vol. 11, pp. 1220–1228, 1995.
- [91] R. S. Taylor, L. Brummel, N. Winograd, B. J. Garrison, and J. C. Vickerman, “Molecular desorption in bombardment mass spectrometries,” *Chem. Eng. Sci.*, vol. 233, no. February, pp. 575–579, 1995.
- [92] R. S. Taylor and B. J. Garrison, “Hydrogen abstraction reactions in the keV particle bombardment of organic films,” *J. Am. Chem. Soc.*, vol. 116, pp. 4465–4466, 1994.
- [93] A. Delcorte, “Organic surfaces excited by low-energy ions: atomic collisions, molecular desorption and buckminsterfullerenes,” *Phys. Chem. Chem. Phys.*, vol. 7, no. 19, pp. 3395–406, Oct. 2005.

- [94] O. A. Restrepo and A. Delcorte, "Molecular dynamics study of metal-organic samples bombarded by kiloelectronvolt projectiles," *Surf. Interface Anal.*, vol. 43, no. 1–2, pp. 70–73, Jan. 2011.
- [95] B. Czerwinski and A. Delcorte, "Molecular Dynamics Study of Fullerite Cross-Linking under keV C 60 and Ar," *J. Phys. Chem. C*, vol. 117, pp. 3595–3604, 2013.
- [96] D. Briggs and M. J. Hearn, "Sub-micron Molecular Imaging. A Viability Study by Time-of-flight SIMS," *Surf. Interface Anal.*, vol. 13, no. July, pp. 181–185, 1988.
- [97] B. J. Garrison, N. Winograd, R. Chatterjee, Z. Postawa, A. Wucher, E. Vandeweert, P. Lievens, V. Philipsen, and R. E. Silverans, "Sputtering of atoms in fine structure states: a probe of excitation and de-excitation events," *Rapid Commun. Mass Spectrom.*, vol. 12, no. 18, pp. 1266–1272, Sep. 1998.
- [98] J. Davenas, X. L. Xu, and G. Boiteux, "New conducting and optical properties induced in polyimide by ion beam irradiation," *Synthetic Met.*, vol. 24, pp. 81–87, 1988.
- [99] J. Davenas, X. L. Xu, and D. Sage, "Relation between structure and electronic properties of ion irradiated polymers," *Nucl. Instruments Methods Phys. Res. B*, vol. 39, pp. 754–763, 1989.
- [100] J. Mort, "Polymers as electronic materials," *Adv. Phys.*, vol. 29, no. 2, pp. 367–408, 1980.
- [101] S. Storp and R. Holm, "Esca investigations of ion beam effects on surfaces," *J. Electron Spectros. Relat. Phenomena*, vol. 16, pp. 183–193, 1979.
- [102] D. E. Williams and L. E. David, *Characterization of Metal and Polymer Surfaces*, Volume 2. Academic Press, New York, 1977, p. 53.
- [103] W. J. Van Ooij, "Interpretation of the Fragmentation Patterns in Static SIMS Analysis of Polymers . Part I . Simple Aliphatic Hydrocarbons," *Surf. Interface Anal.*, vol. 11, no. June 1987, pp. 430–440, 1988.
- [104] C. Silvestre, D. Duraccio, and S. Cimmino, "Food packaging based on polymer nanomaterials," *Prog. Polym. Sci.*, vol. 36, no. 12, pp. 1766–1782, Dec. 2011.
- [105] A. Arora and G. W. Padua, "Review: nanocomposites in food packaging.," *J. Food Sci.*, vol. 75, no. 1, pp. R43–9, 2010.
- [106] J. M. Lagarón, L. Cabedo, D. Cava, J. L. Feijoo, R. Gavara, and E. Gimenez, "Improving packaged food quality and safety. Part 2: nanocomposites.," *Food Addit. Contam.*, vol. 22, no. 10, pp. 994–8, Oct. 2005.
- [107] J. Baschnagel, H. Meyer, F. Varnik, S. Metzger, M. Aichele, M. Müller, and K. Binder, "Computer Simulations of Polymers Close to Solid Interfaces :Some Selected Topics," *Interface Sci.*, vol. 11, pp. 159–173, 2003.



- [108] N. Koch, “Energy levels at interfaces between metals and conjugated organic molecules,” *J. Phys. Condens. Matter*, vol. 20, no. 18, p. 184008, May 2008.
- [109] C. Li and P. Choi, “Molecular Dynamics Study of the Adsorption Behavior of Normal Alkanes on a Relaxed Al<sub>2</sub>O<sub>3</sub> Surface,” *J. Phys. Chem. C*, vol. 111, pp. 1747–1753, 2007.
- [110] P. de Sainte Claire, K. C. Hass, W. F. Schneider, and W. L. Hase, “Simulations of hydrocarbon adsorption and subsequent water penetration on an aluminum oxide surface,” *J. Chem. Phys.*, vol. 106, no. 17, p. 7331, 1997.
- [111] I. Jang, R. Phillips, and S. B. Sinnott, “Study of C<sub>3</sub>H<sub>5</sub><sup>+</sup> ion deposition on polystyrene and polyethylene surfaces using molecular dynamics simulations,” *J. Appl. Phys.*, vol. 92, no. 6, p. 3363, 2002.
- [112] P. Traskelin, E. Salonen, K. Nordlund, A. V. Krasheninnikov, J. Keinonen, and C. H. Wu, “Molecular dynamics simulations of CH<sub>3</sub> sticking on carbon first wall structures,” *J. Nucl. Mater.*, vol. 316, pp. 52–55, 2003.
- [113] J. Winter, “Wall conditioning of fusion devices by reactive plasmas,” *J. Nucl. Mater.*, vol. 161, pp. 265–330, 1989.
- [114] G. Federici and C. H. Wu, “Modelling of the interaction of hydrogen plasma with with amorphous carbon films redeposited in fusion devices,” *J. Nucl. Mater.*, vol. 207, pp. 62–85, 1993.
- [115] D. Porezag, T. Frauenheim, T. Kohler, G. Seifert, and R. Kaschner, “Construction of tight-binding-like potentials on the basis of density-functional theory: Application to carbon,” *Phys. Rev. B*, vol. 51, no. 19, pp. 947–957, 1995.
- [116] M. Elstner, D. Porezag, G. Jungnickel, J. Elsner, M. Haugk, T. Frauenheim, S. Suhai, and G. Seifert, “Self-consistent-charge density-functional tight-binding method for simulations of complex materials properties,” *Phys. Rev. B*, vol. 58, no. 11, pp. 7260–7268, Sep. 1998.
- [117] P. Träskelin, E. Salonen, K. Nordlund, J. Keinonen, and C. . Wu, “Molecular dynamics simulations of CH<sub>3</sub> sticking on carbon surfaces, angular and energy dependence,” *J. Nucl. Mater.*, vol. 334, no. 1, pp. 65–70, Aug. 2004.
- [118] P. Träskelin, O. Saresoja, and K. Nordlund, “Molecular dynamics simulations of C<sub>2</sub>, C<sub>2</sub>H, C<sub>2</sub>H<sub>2</sub>, C<sub>2</sub>H<sub>3</sub>, C<sub>2</sub>H<sub>4</sub>, C<sub>2</sub>H<sub>5</sub>, and C<sub>2</sub>H<sub>6</sub> bombardment of diamond (111) surfaces,” *J. Nucl. Mater.*, vol. 375, no. 2, pp. 270–274, Apr. 2008.
- [119] A. R. Sharma, R. Schneider, U. Toussaint, and K. Nordlund, “Hydrocarbon radicals interaction with amorphous carbon surfaces,” *J. Nucl. Mater.*, vol. 363–365, pp. 1283–1288, Jun. 2007.
- [120] K. Tichmann, U. von Toussaint, and W. Jacob, “Determination of the sticking coefficient of energetic hydrocarbon molecules by molecular dynamics,” *J. Nucl. Mater.*, vol. 420, no. 1–3, pp. 291–296, Jan. 2012.

- [121] M. J. Frisch, G. W. Trucks, H. B. Schlegel, G. E. Scuseria, M. A. Robb, J. R. Cheeseman, G. Scalmani, V. Barone, B. Mennucci, G. A. Petersson, H. Nakatsuji, M. Caricato, H. P. Li, X.; Hratchian, A. F. Izmaylov, J. Bloino, G. Zheng, J. L. Sonnenberg, M. Hada, M. Ehara, K. Toyota, R. Fukuda, J. Hasegawa, M. Ishida, T. Nakajima, Y. Honda, O. Kitao, H. Nakai, T. Vreven, J. A. J. Montgomery, J. E. Peralta, F. Ogliaro, M. Bearpark, J. J. Heyd, E. Brothers, K. N. Kudin, V. N. Staroverov, R. Kobayashi, J. Normand, K. Raghavachari, A. Rendell, J. C. Burant, S. S. Iyengar, J. Tomasi, M. Cossi, N. Rega, M. J. Millam, M. Klene, J. E. Knox, J. B. Cross, V. Bakken, C. Adamo, J. Jaramillo, R. E. Gomperts, R. Stratmann, O. Yazyev, A. J. Austin, R. Cammi, C. Pomelli, J. W. Ochterski, R. L. Martin, K. Morokuma, V. G. Zakrzewski, G. A. Voth, P. Salvador, J. J. Dannenberg, S. Dapprich, A. D. Daniels, Ö. Farkas, J. B. Foresman, J. V. Ortiz, J. Cioslowski, and D. J. Fox, "Gaussian 09, Revision B1." GAUSSIAN Inc., Pittsburgh, 1994.
- [122] A. J. Dyson and P. V. Smith, "A molecular dynamics study of the chemisorption of C<sub>2</sub>H<sub>2</sub> and C<sub>3</sub>U<sub>3</sub> on the Si (001) - (2 x 1) surface," *Surf. Sci.*, vol. 375, pp. 45–54, 1997.
- [123] L.-T. Kong, C. Denniston, M. H. Müser, and Y. Qi, "Non-bonded force field for the interaction between metals and organic molecules: a case study of olefins on aluminum.," *Phys. Chem. Chem. Phys.*, vol. 11, no. 43, pp. 10195–203, Nov. 2009.
- [124] L. Huang and J. Kieffer, "Molecular dynamics study of cristobalite silica using a charge transfer three-body potential: Phase transformation and structural disorder," *J. Chem. Phys.*, vol. 118, no. 3, p. 1487, 2003.
- [125] L. Huang and J. Kieffer, "Thermomechanical anomalies and polyamorphism in B<sub>2</sub>O<sub>3</sub> glass: A molecular dynamics simulation study," *Phys. Rev. B*, vol. 74, no. 22, p. 224107, Dec. 2006.
- [126] J. Zhou and J. Kieffer, "Molecular Dynamics Simulations of Monofunctionalized Polyhedral Oligomeric Silesquioxane," *J. Phys. Chem. C*, vol. 112, pp. 3473–3481, 2008.
- [127] P. Philipp, Y. Yue, T. Wirtz, and J. Kieffer, "Ion-matter interactions by MD simulations making use of reactive force fields," *Surf. Interface Anal.*, vol. 43, no. 1–2, pp. 112–115, Jan. 2011.
- [128] W. R. Salaneck, S. Stafström, and J. L. Bredas, *Conjugated polymer surfaces and interfaces: Electronic and chemical structure of interfaces for polymer light emitting diodes*. Cambridge University Press, 1996.
- [129] R. Waser and M. Aono, "Nanoionics-based resistive switching memories," *Nat. Mater.*, vol. 6, pp. 833–840, 2007.
- [130] W. Lu and C. M. Lieber, "Nanoelectronics from the bottom up," *Nat. Mater.*, vol. 6, pp. 841–850, 2007.
- [131] K. Morgenstern, "Switching individual molecules by light and electrons: From isomerization to chirality flip," *Prog. Surf. Sci.*, vol. 8, pp. 115–161, 2011.

- [132] W. Liu, A. Tkatchenko, and M. Scheffler, "Modeling Adsorption and Reactions of Organic Molecules at Metal Surfaces.," *Acc. Chem. Res.*, Jun. 2014.
- [133] R. Duschek, F. Mittendorfer, R. Blyth, F. P. Netzer, J. Hafner, and M. G. Ramsey, "The adsorption of aromatics on sp-metals: benzene on Al (111)," *Chem. Phys. Lett.*, vol. 318, pp. 43–38, 2000.
- [134] S. J. Jenkins, "Aromatic adsorption on metals via first-principles density functional theory," *Proc. R. Soc. A Math. Phys. Eng. Sci.*, vol. 465, no. 2110, pp. 2949–2976, Jul. 2009.
- [135] J. P. Perdew and A. Ruzsinszky, "Fourteen easy lessons in density functional theory," *Int. J. Quantum Chem.*, vol. 110, no. 15, pp. 2801–2807, 2010.
- [136] K. Burke, "Perspective on density functional theory," *J. Chem. Phys.*, vol. 136, p. 150901, 2012.
- [137] A. Tkatchenko, L. Romaner, O. T. Hofmann, E. Zojer, C. Ambrosch-Draxl, and M. Scheffler, "Van der Waals interactions between organic adsorbates and at organic/inorganic interfaces," *MRS Bull*, vol. 35, pp. 435–442, 2010.
- [138] J. Klimes and A. Michaelides, "A perspective: Advances and challenges in treating van der Waals dispersion forces in density functional theory," *J. Chem. Phys.*, vol. 137, p. 120901, 2012.
- [139] H.-P. Steinrück, W. Huber, T. Pache, and D. Menzel, "The adsorption of benzene mono- and multilayers on Ni (111) studied by TPD and LEED," *Surf. Sci.*, vol. 218, p. 293, 1989.
- [140] F. Mittendorfer and J. Hafner, "Density-functional study of the adsorption of benzene on the (111), (100) and (110) surfaces of nickel," *Surf. Sci.*, vol. 472, pp. 133–153, 2001.
- [141] S. Yamagishi, S. J. Jenkins, and D. a. King, "Symmetry and site selectivity in molecular chemisorption: Benzene on Ni{111}," *J. Chem. Phys.*, vol. 114, no. 13, p. 5765, 2001.
- [142] W. Liu, V. G. Ruiz, G.-X. Zhang, B. Santra, X. Ren, M. Scheffler, and A. Tkatchenko, "Structure and energetics of benzene adsorbed on transition-metal surfaces: density-functional theory with van der Waals interactions including collective substrate response," *New J. Phys.*, vol. 15, no. 5, p. 053046, May 2013.
- [143] P. C. Zalm, "Secondary ion mass spectrometry," *Vacuum*, vol. 45, no. 6–7, pp. 753–772, 1994.
- [144] T. Wirtz and H.-N. Migeon, "Storing Matter: A new quantitative and sensitive analytical technique," *Appl. Surf. Sci.*, vol. 255, no. 4, pp. 1498–1500, Dec. 2008.

- [145] C. Mansilla and T. Wirtz, "Storing Matter: a new analytical technique developed to improve the sensitivity and the quantification during SIMS analyses," *Surf. Interface Anal.*, vol. 42, no. 6–7, pp. 1135–1139, Apr. 2010.
- [146] T. Wirtz, C. Mansilla, C. Verdeil, and H.-N. Migeon, "Storing Matter: A new quantitative and sensitive analytical technique based on sputtering and collection of sample material," *Nucl. Instruments Methods Phys. Res. Sect. B Beam Interact. with Mater. Atoms*, vol. 267, no. 16, pp. 2586–2588, Aug. 2009.
- [147] G. Slodzian, "Enveloppe Soleau No. 13852 deposited by Cameca on 04/05/1998 on behalf of G. Slodzian," 1998.
- [148] B. Bendler, R. Barrahma, P. Philipp, and T. Wirtz, "New neutral cesium evaporation chamber and UHV suitcase," *Surf. Interface Anal.*, vol. 43, no. 1–2, pp. 514–517, 2010.
- [149] C. Mansilla, T. Wirtz, and C. Verdeil, "Study of the useful yield of the Storing Matter technique using Ge(100) as a sputter target," *Nucl. Instruments Methods Phys. Res. Sect. B Beam Interact. with Mater. Atoms*, vol. 267, no. 16, pp. 2589–2591, Aug. 2009.
- [150] C. Mansilla and T. Wirtz, "Application of the Storing Matter technique to the analysis of semiconductor materials," *J. Vac. Sci. Technol. B Microelectron. Nanom. Struct.*, vol. 28, no. 1, p. C1C71, 2010.
- [151] C. Mansilla and T. Wirtz, "Oxidation effect on the SIMS analysis of samples sputtered and deposited by the Storing Matter technique," *Appl. Surf. Sci.*, vol. 258, no. 15, pp. 5698–5702, May 2012.
- [152] B. Kasel and T. Wirtz, "Reduction of the SIMS Matrix Effect Using the Storing Matter Technique: A Case Study on Ti in Different Matrices," *Anal. Chem.*, vol. 86, no. 8, pp. 3750–3755, 2014.
- [153] N. Becker, C. Mansilla, T. Wirtz, and H.-N. Migeon, "The Storing Matter technique applied to PVC: Effect of the primary ion fluence on the sputter-deposition," *Nucl. Instruments Methods Phys. Res. Sect. B Beam Interact. with Mater. Atoms*, vol. 269, no. 9, pp. 1029–1031, May 2011.
- [154] N. Becker, T. Wirtz, and H.-N. Migeon, "The Storing Matter technique: Application to PVC using Au and Ag collectors," *Surf. Interface Anal.*, vol. 43, no. 1–2, pp. 502–505, Jan. 2011.
- [155] N. Becker, T. Wirtz, and H.-N. Migeon, "The Storing Matter technique: application to polymer samples using Ag collectors," *Surf. Interface Anal.*, vol. 43, no. 1–2, pp. 413–416, Jan. 2011.
- [156] N. Becker and T. Wirtz, "Reduction of Matrix Effects in Polystyrene/Poly(methylene methacrylate) Blends by Metal-Assisted Secondary Ion Mass Spectrometry," *Anal. Chem.*, vol. 84, pp. 5920–5924, 2012.

- [157] P. Philipp, B. Douhard, F. Lacour, T. Wirtz, L. Houssiau, J.-J. Pireaux, and H.-N. Migeon, “The Storing Matter technique: Preliminary results on PS and PVC,” *Appl. Surf. Sci.*, vol. 255, no. 4, pp. 866–869, Dec. 2008.
- [158] N. Becker, T. Wirtz, and H.-N. Migeon, “The Storing Matter technique applied to polystyrene: a study of different methods to enhance Ag-cationization,” *Surf. Interface Anal.*, vol. 45, no. 1, pp. 541–544, Jan. 2013.
- [159] T. Wirtz, C. Mansilla, R. Barraha, and C. Verdeil, “Novel Floating Low-Energy Ion Gun for the storing matter instrument,” *Nucl. Instruments Methods Phys. Res. Sect. B Beam Interact. with Mater. Atoms*, vol. 267, no. 16, pp. 2583–2585, Aug. 2009.
- [160] D. T. Clark and A. Harrison, “ESCA applied to polymers. XXXI. A theoretical investigation of molecular core binding and relaxation energies in a series of prototype systems for nitrogen and oxygen functionalities in polymers,” *J. Polym. Sci. Polym. Chem. Ed.*, vol. 19, no. 8, pp. 1945–1955, 1981.
- [161] A. R. Leach, *Molecular Modelling – Principles and Applications*, 2nd ed. Pearson Education, Harlow, 2001.
- [162] L. G. V. Briquet, A. Jana, L. Mether, K. Nordlund, G. Henrion, and P. Philipp, “Reactive force field potential for carbon deposition on silicon surfaces,” *J. Phys. Condens. Matter*, vol. 24, no. 39, p. 395004, 2012.
- [163] M. M. Aslan, “Nanostructuring of alumina optical waveguides by hot water treatment for tuning sensor output,” *Thin Solid Films*, vol. 520, no. 6, pp. 2251–2256, Jan. 2012.
- [164] S. Shingubara, “Fabrication of Nanomaterials Using Porous Alumina Templates,” *J. Nanoparticle Res.*, vol. 5, no. 1/2, pp. 17–30, Apr. 2003.
- [165] P. Philipp, L. Briquet, T. Wirtz, and J. Kieffer, “Low-energy oxygen bombardment of silicon by MD simulations making use of a reactive force field,” *Nucl. Instruments Methods Phys. Res. Sect. B Beam Interact. with Mater. Atoms*, vol. 269, no. 14, pp. 1555–1558, Jul. 2011.
- [166] L. Angibaud, L. Briquet, P. Philipp, T. Wirtz, and J. Kieffer, “Parameter optimization in molecular dynamics simulations using a genetic algorithm,” *Nucl. Instruments Methods Phys. Res. B*, vol. 269, pp. 1559–1563, 2011.
- [167] L. Fast, J. M. Wills, B. Johansson, and O. Eriksson, “Elastic constants of hexagonal transition metals: Theory,” *Phys. Rev. B*, vol. 51, pp. 17431–17438, 1995.
- [168] A. Marmier and S. C. Parker, “Ab initio morphology and surface thermodynamics of  $\alpha$ -Al<sub>2</sub>O<sub>3</sub>,” *Phys. Rev. B*, vol. 69, p. 115409, 2004.
- [169] P. Vashishta, R. K. Kalia, A. Nakano, and J. P. Rino, “Interaction potentials for alumina and molecular dynamics simulations of amorphous and liquid alumina,” *J. Appl. Phys.*, vol. 103, pp. 083504–083513, 2008.

- [170] R. E. Newnham and Y. M. de Haan, "Refinement of the  $\alpha$ - $\text{Al}_2\text{O}_3$ ,  $\text{Ti}_2\text{O}_3$ ,  $\text{V}_2\text{O}_3$  and  $\text{Cr}_2\text{O}_3$  structures," *Zeitschrift für Krist.*, vol. 117, p. 195412, 1962.
- [171] C. Ruberto, Y. Yourdshahyan, and B. I. Lundqvist, "Surface properties of metastable alumina: a comparative study of  $k$ - and  $a$ - $\text{Al}_2\text{O}_3$ ," *Phys. Rev. B*, vol. 67, p. 195412, 2003.
- [172] H. Sun, "COMPASS: An ab Initio Force-Field Optimized for Condensed-Phase Applications Overview with Details on Alkane and Benzene Compounds," *J. Phys. Chem. B*, vol. 102, pp. 7338–7364, 1998.
- [173] "Avogadro: an open-source molecular builder and visualization tool. Version 1.XX." .
- [174] A. M. Leeson, M. R. Alexander, R. D. Short, D. Briggs, and M. J. Hearn, "Secondary Ion Mass Spectrometry of Polymers : a ToF SIMS Study of Monodispersed PMMA," *Surf. Interface Anal.*, vol. 25, no. December 1996, pp. 261–274, 1997.
- [175] K. Momma and F. Izumi, "VESTA 3 for three-dimensional visualization of crystal, volumetric and morphology data," *J. Appl. Crystallogr.*, vol. 44, pp. 1272–1276, 2011.
- [176] S. Fleming and A. Rohl, "GDIS: a visualization program for molecular and periodic systems," *Zeitschrift für Krist.*, vol. 220, no. 5–6, pp. 580–584, 2005.
- [177] G. Kresse and J. Hafner, "Ab initio molecular dynamics for liquid metals.," *Phys. Rev. B. Condens. Matter*, vol. 47, no. 1, pp. 558–561, Jan. 1993.
- [178] G. Kresse and J. Hafner, "Ab initio molecular-dynamics simulation of the liquid-metal-amorphous-semiconductor transition in germanium.," *Phys. Rev. B. Condens. Matter*, vol. 49, no. 20, pp. 14251–14269, May 1994.
- [179] G. Kresse and J. Furthmüller, "Efficiency of ab-initio total energy calculations for metals and semiconductors using a plane-wave basis set," *Comput. Mater. Sci.*, vol. 6, pp. 15–50, 1996.
- [180] G. Kresse and J. Furthmüller, "Efficient iterative schemes for ab initio total-energy calculations using a plane-wave basis set," *Phys. Rev. B. Condens. Matter*, vol. 54, no. 16, pp. 11169–11186, Oct. 1996.
- [181] J. P. Perdew, "Atoms, molecules, solids, and surfaces: Applications of the generalized gradient approximation for exchange and correlation," *Phys. Rev. B*, vol. 45, no. 23, pp. 13244–13249, 1992.
- [182] J. Perdew and Y. Wang, "Accurate and simple analytic representation of the electron-gas correlation energy.," *Phys. Rev. B. Condens. Matter*, vol. 45, no. 23, pp. 13244–13249, Jun. 1992.
- [183] P. Blöchl, "Projector augmented-wave method.," *Phys. Rev. B. Condens. Matter*, vol. 50, no. 24, pp. 17953–17979, Dec. 1994.

- [184] G. Kresse and D. Joubert, "From ultrasoft pseudopotentials to the projector augmented-wave method," vol. 59, no. 3, pp. 11–19, 1999.
- [185] K. Tonigold and A. Gross, "Adsorption of small aromatic molecules on the (111) surfaces of noble metals: A density functional theory study with semiempirical corrections for dispersion effects.," *J. Chem. Phys.*, vol. 132, no. 22, p. 224701, Jun. 2010.
- [186] T. Kawashima, T. Kurosawa, A. Satoka, S. Sheraz, J. S. Fletcher, M. Futigami, N. P. Lockyer, and J. C. Vickermann, "Examination of fragment ions of polystyrene in ToF-SIMS spectra using MS/MS," *Surf. Interface Anal.*, vol. 46, no. S1, pp. 92–95, 2014.
- [187] N. Becker, "PhD Thesis :Application of the storing matter technique to organic samples: fundamentals, applications, and evaluation of the analytical potential," University of Luxembourg, 2011.
- [188] K. Moritani, G. Mukai, M. Hashinokuchi, and K. Mochiji, "Energy-dependent fragmentation of polystyrene molecule using size-selected Ar gas cluster ion beam projectile," *Surf. Interface Anal.*, vol. 43, no. 1–2, pp. 241–244, Jan. 2011.
- [189] C. Heile, A. Muhmann, D. Lipinsky, and H. F. Arlinghaus, "Investigations of secondary ion yield-enhancing methods in combination," *Surf. Interface Anal.*, vol. 43, no. 1–2, pp. 20–23, Jan. 2011.
- [190] M. Kudo, K. Aimoto, Y. Sunagawa, N. Kato, S. Aoyagi, S. Iida, and N. Sanada, "Comparison of secondary ion intensity enhancement from polymers on silicon and silver substrates by using Au-TOF-SIMS," *Appl. Surf. Sci.*, vol. 255, no. 4, pp. 1015–1017, Dec. 2008.
- [191] A. Jana, "PhD Thesis :Sticking and deposition of atoms in the sub-monolayer range," Universite de Lorraine, 2014.
- [192] T. Wirtz, C. Mansilla, R. Barraha, and C. Verdeil, "Novel Floating Low-Energy Ion Gun for the storing matter instrument," *Nucl. Instruments Methods Phys. Res. Sect. B Beam Interact. with Mater. Atoms*, vol. 267, no. 16, pp. 2583–2585, Aug. 2009.
- [193] X. Vanden Eynde, P. Bertrand, and R. Jérôme, "Molecular Weight Effects on Polystyrene Fingerprint Time-of-Flight Secondary Ion Mass Spectrometry (ToF-SIMS) Spectra," *Macromolecules*, vol. 30, no. 21, pp. 6407–6416, Oct. 1997.
- [194] D. C. Muddiman, A. H. Brockmanj, A. Proctor, M. Houalla, and D. M. Hercules, "Characterization of Polystyrene on Etched Silver Using Ion Scattering and X-ray Photoelectron Spectroscopy: Correlation of Secondary Ion Yield in Time-of-Flight SIMS with Surface Coverage," pp. 11570–11575, 1994.
- [195] G. L. Fisher, M. Dickinson, S. R. Bryan, and J. Moulder, "C60 sputtering of organics: A study using TOF-SIMS, XPS and nanoindentation," *Appl. Surf. Sci.*, vol. 255, no. 4, pp. 819–823, Dec. 2008.

- [196] Z. Wanxi, S. Jiazhen, C. Chuangzheng, and Y. Jin, "Characterization of crosslinking density of polystyrene with the shake-up satellite peak of XPS," *Kexue Tongbao*, vol. 30, no. 6, pp. 750–753, 1985.
- [197] K. W. Bullins, T. T. S. Huang, and S. J. Kirkby, "Theoretical investigation of the formation of the tropylium ion from the toluene radical cation," *Int. J. Quantum Chem.*, vol. 109, no. 6, pp. 1322–1327, May 2009.
- [198] K. Wittmaack, "Secondary ion emission from polymer layers by atomic and molecular ion bombardment: Data evaluation based on linear-cascade sputtering theory," *Appl. Surf. Sci.*, vol. 252, no. 19, pp. 6413–6418, Jul. 2006.
- [199] D. T. Clark and Y. C. T. Fok, "Electron mean free paths in Langmuir—Blodgett multilayers," *J. Electron Spectros. Relat. Phenomena*, vol. 22, no. 2, pp. 173–185, 1981.
- [200] D. Briggs and G. Beamson, "Primary and Secondary Oxygen-Induced C1s Binding Energy Shifts in X-ray Photoelectron Spectroscopy of Polymers," *Anal. Chem.*, vol. 64, pp. 1729–1736, 1992.
- [201] A. P. Pijpers and W. A. B. Donners, "Quantitative determination of the surface composition of acrylate copolymer latex films by XPS (ESCA)," *J. Polym. Sci. Polym. Chem. Ed.*, vol. 23, no. 2, pp. 453–462, Feb. 1985.
- [202] G. Beamson and D. Briggs, "High Resolution XPS of Organic Polymers: The Scienta ESCA300 Database," *J. Chem. Educ.*, vol. 70, no. 1, p. A25, 1993.
- [203] Y. Yamamoto, K. Ichiki, S. Ninomiya, T. Seki, T. Aoki, J. Matsuo, J. Matsuo, M. Kase, T. Aoki, and T. Seki, "Evaluation of surface damage on organic materials irradiated with Ar cluster ion beam," *Ion Implant. Technol.*, vol. 298, pp. 298–301, 2011.
- [204] A. Bilic, J. R. Reimers, N. S. Hush, C. H. Rainer, and M. J. Ford, "Adsorption of benzene on copper, silver, and gold surfaces," *J. Chem. Theory Comput.*, vol. 2, pp. 1093–1105, 2006.
- [205] N. Lorente, M. Hedouin, R. Palmer, and M. Persson, "Chemisorption of benzene and STM dehydrogenation products on Cu(100)," *Phys. Rev. B*, vol. 68, no. 15, p. 155401, Oct. 2003.
- [206] T. S. Chwee and M. B. Sullivan, "Adsorption studies of C<sub>6</sub>H<sub>6</sub> on Cu (111), Ag (111), and Au (111) within dispersion corrected density functional theory," *J. Chem. Phys.*, vol. 137, no. 13, p. 134703, Oct. 2012.
- [207] F. E. Olsson, M. Persson, N. Lorente, L. J. Lauhon, and W. Ho, "STM Images and Chemisorption Bond Parameters of Acetylene, Ethynyl, and Dicarbon Chemisorbed on Copper," *J. Phys. Chem. B*, vol. 106, pp. 8161–8171, 2002.
- [208] W. Reckien, M. Eggers, and T. Bredow, "Theoretical study of the adsorption of benzene on coinage metals," *Beilstein J. Org. Chem.*, vol. 10, pp. 1775–84, Jan. 2014.



- [209] W.-K. Chen, M.-J. Cao, S.-H. Liu, Y. Xu, and J.-Q. Li, "On the coverage-dependent orientation of benzene adsorbed on Cu(100): A density functional theory study," *Chem. Phys. Lett.*, vol. 407, no. 4–6, pp. 414–418, May 2005.
- [210] K. Johnston, J. Kleis, B. Lundqvist, and R. Nieminen, "Influence of van der Waals forces on the adsorption structure of benzene on silicon studied using density functional theory," *Phys. Rev. B*, vol. 77, no. 12, p. 121404, Mar. 2008.
- [211] J. Klimeš, D. R. Bowler, and A. Michaelides, "Chemical accuracy for the van der Waals density functional," *J. Phys. Condens. Matter*, vol. 22, no. 2, p. 022201, Jan. 2010.
- [212] J. Klimeš, D. R. Bowler, and A. Michaelides, "Van der Waals density functionals applied to solids," *Phys. Rev. B*, vol. 83, no. 19, p. 195131, May 2011.
- [213] K. Lee, É. D. Murray, L. Kong, B. I. Lundqvist, and D. C. Langreth, "Higher-accuracy van der Waals density functional," *Phys. Rev. B*, vol. 82, no. 8, p. 081101, Aug. 2010.
- [214] W. Liu, J. Carrasco, B. Santra, A. Michaelides, M. Scheffler, and A. Tkatchenko, "Benzene adsorbed on metals: Concerted effect of covalency and van der Waals bonding," *Phys. Rev. B*, vol. 86, no. 24, p. 245405, Dec. 2012.
- [215] W. Humphrey, A. Dalke, and K. Schulten, "VMD - Visual Molecular Dynamics," *J. Molec. Graph.*, vol. 14, no. 1, pp. 33–38, 1996.
- [216] W.-X. Li, C. Stampfl, and M. Scheffler, "Oxygen adsorption on Ag(111): A density-functional theory investigation," *Phys. Rev. B*, vol. 65, no. 7, p. 075407, Jan. 2002.
- [217] H. S. Fogler, "Catalysis and catalytic reactors," in *Elements of chemical reaction engineering*, Prentice Hall, 2005.
- [218] J. Blomqvist and P. Salo, "Adsorption of benzene, phenol, propane and carbonic acid molecules on oxidized Al(111) and alpha-Al<sub>2</sub>O<sub>3</sub>(0001) surfaces: A first-principles study," *Condens. mat. mtrl.*, vol. 3, no. 111, p. 18, Mar. 2009.
- [219] S. Yamagishi, S. J. Jenkins, and D. A. King, "Benzene and Its Dissociation Products on Ir{100}," *J. Phys. Chem. C*, vol. 112, no. 37, pp. 1417–14427, 2008.
- [220] H. Orita and N. Itoh, "Adsorption of thiophene on Ni(100), Cu(100), and Pd(100) surfaces: ab initio periodic density functional study," *Surf. Sci.*, vol. 550, no. 1–3, pp. 177–184, Feb. 2004.
- [221] C. Morin, D. Simon, and P. Sautet, "Trends in the chemisorption of aromatic molecules on a Pt (111) surface: benzene, naphthalene, and anthracene from first principles calculations," *J. Phys. Chem. B*, no. 111, pp. 12084–12091, 2004.
- [222] M. Saeys, M.-F. Reyniers, and G. B. Marin, "Density Functional Study of Benzene Adsorption on Pt(111)," *J. Phys. Chem. B*, vol. 106, pp. 7489–7498, 2002.

- [223] K. Johnston and R. M. Nieminen, "Polymer adhesion: first-principles calculations of the adsorption of organic molecules onto Si surfaces," *Condens. mat. mtrl.*, no. 001, pp. 1–8, Apr. 2007.
- [224] P. Gamallo and R. Sayós, "A density functional theory study of atomic oxygen and nitrogen adsorption over alpha-alumina (0001).," *Phys. Chem. Chem. Phys.*, vol. 9, no. 37, pp. 5112–20, Oct. 2007.
- [225] L. N. Kantorovich and M. J. Gillan, "Adsorption of atomic and molecular oxygen on the MgO (001) surface," *Surf. Sci.*, vol. 374, no. 1–3, pp. 373–386, Mar. 1997.
- [226] C. Arasa, P. Gamallo, and R. Sayo, "Adsorption of Atomic Oxygen and Nitrogen at -Cristobalite ( 100 ): A Density Functional Theory Study," *J. Phys. Chem. B*, no. 100, pp. 14954–14964, 2005.
- [227] D. C. Sorescu, J. A. Boatz, and D. L. Thompson, "First-Principles Calculations of the Adsorption of Nitromethane and 1,1-Diamino-2,2-dinitroethylene ( FOX-7 ) Molecules on the  $\alpha$ -Al<sub>2</sub>O<sub>3</sub> ( 0001 ) Surface," *J. Phys. Chem. B*, vol. 3, no. 10, pp. 1451–1463, 2005.
- [228] J. N. Russell Jr, A. Leming, and R. E. Morris, "Phenol decomposition on Al(111)," *Surf. Sci.*, vol. 399, no. 2–3, pp. 239–247, 1998.
- [229] M. P. Casaletto, R. Zanoni, M. Carbone, M. N. Piancastelli, L. Aballe, K. Weiss, and K. Horn, "A high-resolution photoemission study," *Phys. Rev. B*, vol. 62, no. 24, pp. 128–133, 2000.

# Appendix

## Publications

Turgut, C., Wirtz, T., Belmahi, M. & Philipp, P. Fragmentation of polystyrene during sputter deposition in the storing matter instrument. *Surf. Interface Anal.* 46, 357–359 (2014).

Turgut, C., Sinha, G., Mether, L., Lahtinen, J., Nordlund, K., Belmahi, M., Philipp, P. “Experimental and numerical study of submonolayer sputter deposition of polystyrene fragments on silver for the storing matter technique,” *Anal. Chem.* 86, 11217–25 (2014).

Turgut, C., Pandiyan, S., Mether, L., Belmahi, M., Nordlund, K., Philipp, P. “Influence of alkane chain length on adsorption of an alumina surface by MD simulations,” *Nucl. Instruments Methods Phys. Res. B*, accepted.

## Oral and poster presentations

**C. Turgut**, T. Wirtz, M. Belmahi, P. Philipp. *Experimental and simulation study of PS and PMMA fragment absorption on collectors during the Storing Matter process*. **Oral presentation** at SIMS-Europe 2014, Sept 2014, Muenster, Germany.

**C. Turgut**, L. Mether, M. Belmahi, K. Nordlund, P. Philipp. *Influence of alkane chain length on adsorption on an  $\alpha$ -alumina surface by MD Simulations*. **Poster presentation** at COSIRES 2014, June 2014, Alicante, Spain.

**C. Turgut**, L. Briquet, L. Mether, M. Belmahi, K. Nordlund, P. Philipp, T. Wirtz. *Sputter deposition of Polystyrene (PS) molecular fragments on silver (Ag) in the sub-monolayer range: an experimental and simulation study*. **Oral presentation** at ECASIA’13, Oct 2013, Sardinia, Italy

**C. Turgut**, G. Sinha, J. Lahtinen, L. Briquet, L. Mether, T. Wirtz, M. Belmahi, K. Nordlund, P. Philipp. *Fragmentation of PS during sputter deposition in the Storing Matter instrument: an experimental and simulation study*. **Oral presentation** at SIMS XIX conference, Sept 2013, Jeju, South Korea.

**C. Turgut**, G. Sinha, J. Lahtinen, T. Wirtz, M. Belmahi, P. Philipp. *Sputter deposition of Poly(methylmethacrylate) (PMMA) on silver(Ag) studied by Storing Matter and XPS*. **Poster presentation** at SIMS XIX conference, Sept 2013, Jeju, South Korea.

L. Mether, **C. Turgut**, K. Henriksson, K. Nordlund, P. Philipp. *Numerical studies of hexane and alkyl deposition on silicon*. **Oral presentation** at PASI workshop, June 2013, Luxembourg

**C. Turgut**, L. Briquet, L. Mether, M. Belmahi, K. Nordlund, P. Philipp, T. Wirtz. *An experimental and simulation study on sputter deposition of polystyrene molecular fragments on Ag in the sub-monolayer range*. **Poster presentation** at PASI workshop 2013, June 2013, Luxembourg.

**C. Turgut**, L. Mether, K. Nordlund, P. Philipp, M. Belmahi. *Deposition of alkane fragments on aluminium studied by numerical simulations*. **Poster presentation** at ECOSS 2012, September, 2012, Edinburgh, UK.

**C. Turgut**, L. Mether, K. Nordlund, P. Philipp, M. Belmahi. Sputter deposition of Polystyrene (PS) molecular fragments on silver (Ag). **Poster presentation** at ECOSS 2012, September 2012, Edinburgh, UK.

**C. Turgut**, L. Mether, K. Nordlund, P. Philipp, M. Belmahi. *Sticking of Polystyrene (PS) molecular fragments on silver (Ag) using sputter deposition*. **Poster presentation** at the 13th International Conference on Plasma Surface Engineering, September 2012, Garmisch-Partenkirchen, Germany.

L. Mether, K. Henriksson, K. Nordlund, **C. Turgut**, P. Philipp. *Numerical simulations of the deposition of hexane molecules and fragments on silicon*. **Poster presentation** at the 13th International Conference on Plasma Surface Engineering, September 2012, Garmisch-Partenkirchen, Germany.

**L. Mether**, K. Henriksson, K. Nordlund, C. Turgut, P. Philipp. *Density functional theory and molecular dynamics simulations of hydrocarbon deposition on silicon*. **Poster presentation** at COSIRES 2012, June 2012, Santa Fe, New Mexico, USA.



## Résumé

Les traitements plasma présentent un outil efficace, économique et écologique pour la fonctionnalisation de surfaces. Pour cette technique, l'étude du dépôt et de l'adhésion de molécules et précurseurs dans le régime de la sous-monocouche présente un intérêt majeur, car elle définit les propriétés de la surface et l'adhésion de la couche déposée sur le substrat. L'adhésion des molécules lors de la phase initiale du dépôt est contrôlée par les espèces dans le plasma ainsi que par leurs distributions énergétiques et angulaires. Dans le cadre de ce projet, une approche multidisciplinaire combinant calculs DFT et techniques expérimentales pour la préparation et la caractérisation des dépôts dans la sous-monocouche a été utilisée. Des dépôts de PS et PMMA, préparés par bombardement d'Ar sur une surface d'Ag, ont été caractérisés par XPS et ToF-SIMS. La quantité de matière déposée augmente bien avec le temps de dépôt, ou la dose d'irradiation. Les analyses par TOF-SIMS ont également montré que la proportion des grands fragments augmente au détriment des petits. Ceci est contraire aux résultats attendus et peut seulement être expliqué par la recombinaison de petits fragments sur la surface du collecteur. Cette hypothèse est supportée par des calculs DFT qui ont montré que l'énergie d'adsorption des petits fragments est plus grande que celle des grands et, par conséquent, leur probabilité d'adsorption doit également plus élevée. Les calculs DFT ont été étendus sur d'autres substrats, notamment du Si, Pt et Al<sub>2</sub>O<sub>3</sub> et ont montrés que l'énergie d'adhésion est la plus élevée sur Si et Pt.

**Mots-clés :** ToF-SIMS, dépôt par pulvérisation, DFT, Storing Matter, adhésion, sous-monocouche.

## Abstract

Plasma surface treatments present an efficient, economical and ecological tool for surface functionalization. For this technique the deposition and adhesion of molecules and precursors in the sub-monolayer range are of utmost interest, since this layer defines the surface properties and the adhesion between deposit and substrate. The species in the plasma and their energy and angular distributions control the deposition process. To get insights into the latter, a multidisciplinary approach combining DFT calculations with experimental techniques is used for the preparation and characterisation of sub-monolayer deposits of PS and PMMA. The deposits are prepared by sputter deposition using an Ar beam and analysed by ToF-SIMS and XPS. The amount of deposited matter increases well with deposition time or fluence. ToF-SIMS analyses showed also that the proportion of large fragments on the collector surface is increasing with fluence, although the opposite was expected. This can only be explained by the recombination of smaller fragments to form larger ones. This hypothesis is supported by DFT calculations which showed that the adsorption energy, and hence the adsorption probability, is higher for the small fragments than for the large ones. DFT calculations have been extended to Si, Pt and Al<sub>2</sub>O<sub>3</sub> substrates, showing that adsorption energies are highest for Si and Pt.

**Keywords:** ToF-SIMS, sputter deposition, DFT, Storing Matter, adhesion, sub-monolayer.